Petrological insights into pre- and syn-eruptive degassing at Ambrym volcano, Vanuatu

Fionnuala Sheehan

Submitted for the degree of Doctor of Philosophy

University of East Anglia

School of Environmental Sciences

June 2016

Abstract

This study is a petrological investigation of magmatic conditions and degassing processes at Ambrym volcano, a basaltic island arc volcano recently identified as a prodigious emitter of volcanic gases. Typical activity at this volcano entails heavy degassing from quasi-permanent lava lakes, with Strombolian activity of fluctuating intensity. This is punctuated on an approximately decadal timescale by moderate sub-Plinian paroxysms, often accompanied by overflow of lava from the intracaldera cones and via flank fissures.

This study focuses primarily on basaltic scoria recently erupted from a central lava lake during a period of heavy degassing, in order to interpret volatile pathways through the system and how these relate to gas emissions at the surface. Lavas from basaltic intracaldera and flank lava flows have also been briefly examined to give a broader insight into magma storage associated with variations in volcanic activity, and detailed study has been made of a trachyandesitic lava flow erupted in 1986, a geochemically unusual event compared to the majority of larger events in historical time.

Petrography, major element modelling, mineral chemistry and dissolved volatile contents indicate that Ambrym is a water-poor, CO_2-rich system, characterised chiefly by quiescent convection-driven degassing through two central intracaldera cones. Examination of the 1986 trachyandesite suggests that it derives from interaction of basaltic magma with a body of trachydacitic melt residing in the shallow crust.

Table of contents

Abstract ..... **i**
Table of contents ..... **iii**
List of Figures ..... **vii**
List of Tables ..... **x**
Acknowledgements ..... **xiii**
Chapter 1 Introduction **1**
1.1 Volcanological setting and motivation for study 1
1.2 Broader context 2
1.3 Thesis organisation 3
Chapter 2 The Vanuatu island arc and Ambrym volcano **5**
2.1 The Vanuatu arc 5
2.1.1 Geology and structure of the arc 5
2.1.2 Fault patterns 9
2.1.3 Tectonic evolution of the Vanuatu arc 10
2.1.4 Current tectonics 12
2.1.5 The D'Entrecasteaux Zone 14
2.1.6 The subducting plate 15
2.2 Ambrym volcano 19
2.2.1 Geomorphology 19
2.2.2 Pre-caldera evolution 20
2.2.3 Tuff cone emplacement and caldera formation 21
2.2.4 Post-caldera activity 23
2.2.5 Historical eruptions 24
Chapter 3 Methods **27**
3.1 Sample preparation 27
3.1.1 X-Ray fluorescence 27

3.1.2 Thin sections 28
3.1.3 Crystal separates for melt inclusion study 28
3.2 X-ray fluorescence 28
3.3 Scanning electron microscope 29
3.4 Electron microprobe analysis (EPMA) 29
3.4.1 Quality of analyses 31
3.4.2 Ion migration and beam damage during EPMA 32
3.5 Secondary ion mass spectrometry (SIMS) 33
3.5.1 Sample preparation 33
3.5.2 Analytical conditions 33
3.5.3 Standards and corrections 34
Chapter 4 Petrology and geochemistry of recent samples: implications for magma storage 37
4.1 Introduction 37
4.1.1 Geochemistry of Ambrym volcano 37
4.1.2 Previous work 38
4.1.3 Magma evolution 40
4.1.4 Magma pathways 41
4.1.5 Existing constraints on magma storage conditions 43
4.2 Samples 46
4.3 Bulk geochemistry 47
4.4 Petrology and petrography 55
4.4.1 Mbwelesu scoria 56
4.4.2 Trachyandesite lava 63
4.4.3 Niri Mbwelesu Taten lava 69
4.4.4 Craig Cove lava 71
4.5 Phase compositions 74
4.5.1 Mbwelesu scoria 74
4.5.2 Trachyandesite lava 83
4.5.3 Niri Mbwelesu Taten lava 90
4.5.4 Craig Cove lava (AMB10) 91

4.6 Discussion 93
4.6.1 Mbwelesu scoriae and Niri Mbwelesu Taten lava 93
4.6.2 Trachyandesite 94
4.6.3 Craig Cove lava 95
4.7 Conclusions 95
Chapter 5 Geochemical modelling 97
5.1 Introduction 97
5.2 Magmatic differentiation 97
5.2.1 Fractional crystallisation 99
5.2.2 Magma mixing 100
5.2.3 Partial melting 101
5.2.4 Conclusions 102
5.3 Mineral-melt equilibria 102
5.3.1 Clinopyroxene-melt thermobarometry 103
5.3.2 Olivine-melt thermometry 108
5.3.3 Plagioclase thermobarometry and hygrometry 113
5.3.4 Glass thermometry 118
5.3.5 Oxygen fugacity 119
5.3.6 Thermobarometry summary 121
5.4 Discussion 123
5.4.1 Implications from assessment of equilibrium 123
5.4.2 Crystallisation conditions 124
5.4.3 Magma supply model 125
5.4.4 Plumbing model 127
5.5 Conclusions 128
Chapter 6 Pre-eruptive volatile contents 131
6.1 Introduction 131
6.1.1 Degassing measurements at Ambrym 131
6.2 Sample details 133
6.3 Results 134

6.3.1 Mbwelesu scoria 134
6.3.2 Trachyandesite 141
6.3.3 Post-entrapment crystallisation 144
6.4 H_2O-CO_2 solubility modelling 147
6.4.1 Model inputs and calculation parameters 148
6.4.2 Results 148
6.5 Magma flux estimate 152
6.6 Discussion 153
6.6.1 Is Ambrym truly water-poor? 153
6.6.2 Volatile supply 155
6.6.3 Volatile cycling in the subduction system 156
6.7 Conclusions 157
Chapter 7 Experimentally determined volatile solubilities 159
7.1 Introduction—the need for experiments 159
7.2 Methodology 161
7.2.1 Choice and preparation of starting material 161
7.2.2 Experimental charge preparation 162
7.2.3 Experimental conditions and set-up 166
7.2.4 Experimental products 167
7.3 Results 168
7.3.1 Crystalline phases and Fe loss 168
7.3.2 Volatile constituents 169
7.4 Discussion 180
7.4.1 H_2O-CO_2 solubilities 180
7.4.2 Halogen solubilities 180
7.5 Conclusions 185

Chapter 8 Conclusions and further work 187

8.1 Conclusions 187

8.1.1 Petrography, major element modelling, and mineral chemistry 187

8.1.2 Pre-eruptive volatile contents 189

8.1.3 Experimentally-determined volatile solubilities 190

8.2 Further work 191

8.2.1 Petrological work 191

8.2.2 Pre-eruptive volatile contents 191

8.2.3 Experimental series 192

References 193

Appendices 217

Index of appendices 217

Appendix A: Summary of the major characteristics and eruptive history of the volcanoes of Vanuatu 218

Appendix B: Activity associated with samples studied 220

Appendix C: Basaltic scoria mineral analyses 225

Appendix D: Basaltic lava flow (AMB2) mineral analyses 236

Appendix E: Trachybasaltic flank lava (AMB10) mineral analyses 237

Appendix F: Trachyandesite mineral analyses 244

Appendix G: Melt inclusion and matrix glass analyses 249

Appendix H: alkali adjustment of $K_D^{Fe\text{-}Mg}$ for olivine 257

List of Figures

Figure 2.1 Map of the Vanuatu arc showing main tectonic features. 6
Figure 2.2 Correlation of lithological sequences across Vanuatu. 8
Figure 2.3 Correlation and timing of volcanism between islands in the Central Chain 9
Figure 2.4 Schematic representation of the development of the Vanuatu arc 11
Figure 2.5 Relative plate motions in the Vanuatu-Fiji Basin region 13
Figure 2.6 Map of Ambrym island highlighting major volcanological features 20
Figure 2.7 Geology and structure of Ambrym. 23
Figure 3.1 CO_2 calibration curves for SIMS. 36
Figure 4.1 MgO vs. SiO_2 for the four major volcanic phases of Ambrym 37
Figure 4.2 Histograms of glass and whole rock analyses from entire volcanic succession 38
Figure 4.3 Relief map of Ambrym 42
Figure 4.4 Polarisation directions of very long period tremor sources. 44
Figure 4.5 Section showing earthquakes below Ambrym during the period 1975–2013 45
Figure 4.6 Simplified map of Ambrym showing sample locations 47
Figure 4.7 Whole-rock compositions for all samples 48
Figure 4.8 Alkali-FeO-MgO plot for all samples 48
Figure 4.9 Major element variation diagrams 50
Figure 4.10 Trace element diagram for all samples. 51
Figure 4.11 Trace element behaviour in Ambrym samples. 52
Figure 4.12 Photomicrographs of plagioclase glomerocryst types in basaltic scoria AMB6. 58
Figure 4.13 Photomicrographs of clinopyroxene in basaltic scoria AMB6 59
Figure 4.14 Photomicrographs of phenocrysts in 2007 scoria AMB2007 60
Figure 4.15 Photomicrographs of olivine in basaltic scoria AMB6 and AMB2007 61
Figure 4.16 Photomicrographs of melt inclusions in basaltic scoria AMB6. 62
Figure 4.17 Representative images of large phenocrysts in AMB86 65
Figure 4.18 Sieve-textured plagioclase in trachyandesite lava AMB86. 65
Figure 4.19 SEM images of clinopyroxene and olivine in trachyandesite lava AMB86 66
Figure 4.20 Photomicrographs of plagioclase in intracaldera basaltic lava AMB2 70
Figure 4.21 Photomicrograph of phenocrysts in intracaldera basaltic lava AMB1 70
Figure 4.22 Photomicrographs of phenocrysts in flank lava AMB10 73
Figure 4.23 Plagioclase compositions for scoria samples AMB6, AMB7 and AMB2007 74

Figure 4.24 Photomicrographs and EPMA traverses of plagioclase phenocrysts in basaltic scoria AMB6. 75
Figure 4.25 Labradorite overgrowth on bytownitic core in basaltic scoria AMB6 75
Figure 4.26 Clinopyroxene compositions in AMB6, AMB7 and AMB2007 77
Figure 4.27 EPMA traverse of large clinopyroxene crystal in basaltic scoria AMB6..... 77
Figure 4.28 Glass and uncorrected MI data for Mbwelesu scoria from 2005 (AMB6) and 2007 (AMB2007), and trachyandesite lava (AMB86).. 81
Figure 4.29 Plagioclase compositions for trachyandesite lava AMB86 83
Figure 4.30 Normally-zoned plagioclase in trachyandesite AMB86. 83
Figure 4.31 EPMA traverses of plagioclase phenocrysts in trachyandesite lava AMB86.. 84
Figure 4.32 Clinopyroxene compositions in trachyandesite lava AMB86 86
Figure 4.33 Ti vs. Fe^{2+}/Fe^{3+} ratio for spinel in all samples.. 87
Figure 4.34 Cl, F and S in apatite in trachyandesite lava AMB86.. 87
Figure 4.35 Fluorine and chlorine in glass and melt inclusions in basaltic scoria from 2005 (AMB6) and 2007 (AMB2007), and trachyandesite lava (AMB86). 89
Figure 4.36 Plagioclase compositions for lava sample AMB2 90
Figure 4.37 Clinopyroxene compositions in Niri Mbwelesu Taten lava AMB2 91
Figure 4.38 Plagioclase compositions for Craig Cove lava AMB10 91
Figure 4.39 Clinopyroxene compositions in Craig Cove lava AMB10. 92
Figure 5.1 Plots showing the equilibrium range for clinopyroxene and melt..... 105
Figure 5.2 Comparison of predicted values with observed values for DiHd. 106
Figure 5.3 Clinopyroxene thermobarometry results 107
Figure 5.4 Rhodes diagram showing equilibrium $K_D^{liq\text{-}ol}$ curve of 0.30 110
Figure 5.5 Results of plagioclase-melt thermobarometry. 117
Figure 5.6 Schematic illustration of the magma storage system below Ambrym 123
Figure 6.1 Melt inclusion and glass compositions, AMB6 and AMB2007. 134
Figure 6.2 Major-element variation diagrams comparing MI compositions in basaltic scoriae (AMB6, AMB2007) and trachyandesite lava (AMB86) with published data 135
Figure 6.3 Volatile concentrations in MI from basaltic scoria AMB6 and AMB2007.. 136
Figure 6.4 a) S and Cl contents in trachyandesite- and basalt-hosted melt inclusions b) Variation of Cl with SiO_2 in AMB86 trachyandesite melt inclusions 142
Figure 6.5 a) Open-system degassing pathways calculated in VolatileCalc 149
Figure 6.6 Degassing curves modelled in VolatileCalc 150
Figure 7.1 a) Sample holder and experimental capsules **b)** IHPV in working position. 167

Figure 7.2 a) Variation of melt H_2O with pressure for H_2O-CO_2 and H_2O-Cl-F experiments. **b)** Variation of melt H_2O with pressure for H_2O-CO_2 experiments. 170
Figure 7.3 H_2O and CO_2 solubilities compared to published solubility models 173
Figure 7.4 Variation of chlorine and fluorine contents in experimental glasses 175
Figure 7.5 Fluid/melt relationships of Cl and F in halogen-doped experiments 177
Figure 7.6 a) Cl vs. H_2O in experimental glasses **b)** Comparison of EPMA and SIMS chlorine data 183

List of Tables

Table 2.1 Sedimentary/geological units of the subducting plate. 16
Table 3.1 Certified standards used for XRF measurements. 29
Table 3.2 Summary table of electron microprobe analyses of natural samples. 30
Table 3.3 Beam current used for analysis of mineral phases by EPMA. 30
Table 3.4 Count times (in seconds) on peaks for each phase analysed. 31
Table 3.5 Compositions of EPMA standards used (atomic%) 31
Table 3.6 Major element compositions of basaltic standards for H_2O and CO_2 on SIMS 35
Table 3.7 CO_2 contents for basaltic glasses used in SIMS CO_2 calibrations. 35
Table 4.1 Mineral compositions and descriptions from Picard et al. (1995) for the entire volcanic succession of Ambrym 39
Table 4.2 Results of fractional crystallisation modelling from Picard et al. (1995) 40
Table 4.3 Samples described in this study 47
Table 4.4 Whole-rock major element data (wt.%) for all samples 53
Table 4.5 Whole-rock trace element data for all samples 54
Table 4.6 Modal abundances and sample vesicularity 56
Table 4.7 Average compositions of plagioclase types in AMB6, AMB7 and AMB2007. 76
Table 4.8 Averaged compositions of clinopyroxene types in all samples. 78
Table 4.9 Averaged olivine analyses for all samples except AMB2 (none analysed). 79
Table 4.10 Averaged Fe-Ti oxide compositions for all samples 80
Table 4.11 Average matrix glass and representative melt inclusion compositions from AMB6 and AMB2007 81
Table 4.12 Anorthite and forsterite compositions in island arcs. 82
Table 4.13 Averaged compositions of plagioclase types in AMB2, AMB10 and AMB86 85
Table 4.14 Averaged low-F and high-F apatite compositions in AMB86 88
Table 4.15 Average matrix glass representative melt inclusion composition in AMB86 88
Table 5.1 Mass balance calculations for generation of AMB86 by fractional crystallisation from AMB6. 99
Table 5.2 Trachydacitic olivine- and spinel-hosted melt inclusion compositions. 100
Table 5.3 Mass balance calculations for generation of AMB86 trachyandesite by mixing of AMB6 basalt with the average trachydacite melt inclusion composition 101
Table 5.4 Results of clinopyroxene-melt thermobarometry for liquid/phenocryst pairs. 108

Table 5.5 Comparison of unadjusted K_D^{liq-ol} values with those adjusted for alkali content using the procedure of Toplis (2005), and those adjusted for NBO/T, using the procedure of Kushiro & Walter (1998). 111
Table 5.6 Results of olivine-liquid thermometers 112
Table 5.7 Plagioclase thermometry, barometry and hygrometry results for AMB6, AMB2007, AMB2 and AMB10. 116
Table 5.8 Plagioclase thermometry, barometry and hygrometry results for AMB86. 118
Table 5.9 Results of glass thermometers for all samples 119
Table 5.10 T-fO_2 calculations from the Sack & Ghiorso calculator 120
Table 5.11 Oxygen fugacity calculations using the France et al. (2010) model 121
Table 6.1 SO_2 fluxes at notable strongly-degassing basaltic/silica-undersaturated volcanoes 132
Table 6.2 Number of melt inclusions analysed by SIMS in scoriae AMB6 and AMB2007 134
Table 6.3 Raw data (EPMA and SIMS) for melt inclusions in AMB6. 138
Table 6.4 Raw data (EPMA and SIMS) for melt inclusions in AMB2007. 140
Table 6.5 Raw data (SIMS) for melt inclusions in AMB6 not analysed on EPMA.. 141
Table 6.6 Raw data (EPMA) for melt inclusions in AMB86. 143
Table 6.7 Pyroxene-hosted melt inclusion compositions, corrected for post-entrapment crystallisation at 10 MPa and NNO+1.2 146
Table 6.8 Olivine-hosted melt inclusions corrected for post-entrapment crystallisation at 10 MPa and NNO+1.2. 147
Table 6.9 Calculationsof H_2O and CO_2 partitioning between melt and fluid, given the weight fraction of H_2O and CO_2 in the bulk system; i.e., fluid/(magma+fluid) 151
Table 6.10 Magma flux calculations using ϕ_{plume} data from Bani et al. (2009), Allard et al. (2009), and Bani et al. (2012). 153
Table 7.1 Starting compositions used in experiments. 162
Table 7.2 Bulk volatiles loaded in runs 1–6 (H_2O-CO_2-S). 164
Table 7.3 Compositions of bulk starting fluids (pre-experiment) for Cl-F experiments.. 165
Table 7.4 Bulk volatiles loaded in runs 15–20 (H_2O-Cl-F, one with CO_2). 166
Table 7.5 Plagioclase analyses in run #2. 168
Table 7.6 Run conditions and EPMA and SIMS data for C-O-H-S crystal-free experimental glasses. 171
Table 7.7: EPMA and SIMS data for H_2O-Cl-F experiments. 178
Table 7.8 Comparison of etnaite composition studied by Chevychelov et al. (2008) with Ambrym starting composition used in this study. 182

Table A1 Characteristics and eruptive history of Vanuatu volcanoes……218
Table C1: Coarse glomerocryst plag compositions in 2005 basaltic scoria AMB6……...225
Table C2: Fine glomerocryst plagioclase compositions in 2005 basaltic scoria AMB6…...227
Table C3: Non-glomerocrystic plagioclase in AMB6……227
Table C4: Plagioclase microphenocrysts in AMB6……...229
Table C5: Plagioclase groundmass in AMB7……230
Table C6: Large euhedral clinopyroxene traverse in basaltic scoria AMB6…….232
Table C7: Clinopyroxene analyses for AMB6 and AMB7……234
Table C8: Plagioclase and clinopyroxene phenocrysts in basaltic scoria AMB2007……235
Table D1: Plagioclase and clinopyroxene analyses in intracaldera basalt lava AMB2……..236
Table E1: Plagioclase analyses in flank trachybasalt AMB10……...237
Table E2: Clinopyroxene phenocrysts in flank trachybasalt AMB10……242
Table E3: Olivine phenocrysts in flank trachybasalt AMB10……...243
Table F1: 1986 trachyandesite plagioclase phenocryst compositions ……..244
Table F2 1986 trachyandesite plagioclase, microphenocryst/groundmass compositions…..245
Table F3: 1986 trachyandesite cpx microphenocryst/groundmass compositions……..245
Table F4: 1986 trachyandesite clinopyroxene phenocryst compositions……...246
Table F5: Olivine phenocryst and glomerocryst compositions, 1986 trachyandesite……247
Table F6: 1986 trachyandesite microphenocryst/ groundmass olivine compositions……248
Table G1: Pyroxene-hosted melt inclusions from basaltic scoria AMB6, raw data……..249
Table G2: Olivine- and spinel-hosted MI from basaltic scoria AMB6, raw data……..251
Table G3: Olivine- and spinel-hosted melt inclusions from basaltic scoria AMB2007……252
Table G4: Olivine- and spinel-hosted melt inclusions from 1986 trachyandesite lava…….253
Table G5: Matrix glass compositions in AMB6……254
Table G6: Matrix glass compositions, AMB2007 and AMB1986……255
Table G7: 1986 trachyandesite matrix glass compositions.……...256

Acknowledgements

I express my sincere thanks to all those who have assisted me and supported me over the course of this project.

I would like to thank my supervisor, Dr. Jenni Barclay, and the people who provided discussion and expertise at various stages of my research: Dr. Joaquin Cortés, Dr. Ben Edwards, Dr. Bruno Scaillet, Dr. Michel Pichavant, Dr. James Webster, Dr. Marie Edmonds, Dr. Richard Herd, and Dr. Carol Stannard.

I also thank the various technicians who made life easier and were always willing to discuss data and analytical procedures: Dr. John Brindle and Mr. Bertrand Leze at the University of East Anglia; Dr. Richard Hinton and Dr. John Craven at the Ion Microprobe Facility in Edinburgh; Dr. Chris Hayward, Dr. Chiara Petrone, and Dr. Andrew Buckley at the electron microprobe laboratory in Cambridge University; and Dr. Jean-Michel Bény at the Institut des Sciences de la Terre d'Orléans.

Thanks to Marina Alletti, Fabrice Gaillard, Jeremie Melleton, Giada Marziano and Alain Burgisser for help and friendship during time spent at the Institut des Sciences de la Terre in Orléans, France in 2008.

Finally, the biggest thanks go to my partner John McCarthy, and my parents, Annmarie and Tom, for unending support and encouragement.

This work was supported by a research fund from the Natural Environment Research Council (NERC).

Chapter 1 Introduction

1.1 Volcanological setting and motivation for study

Ambrym is one of the most active volcanoes in the Vanuatu island arc, SW Pacific. It has been continuously active since first described in 1774, displaying persistent active lava lakes in two adjacent near-summit intracaldera cones, including prodigious outgassing (Bani et al., 2009, 2012), with intermittent Vulcanian or lava flow events, punctuated by more violent central or flank eruptions on a timescale of years to decades. Interest in this volcano has increased over the last decade following satellite measurement of enormous sulphur dioxide degassing in 2005, and subsequent field analyses of gas fluxes in the plume (Bani et al., 2009) confirming extremely high fluxes of sulphur and halogens. This makes Ambrym an important target for research into volatile transport from the mantle to the atmosphere. Ambrym is also a rare example of persistent lava lake activity, recorded in only a handful of other locations: Kilauea (Hawai'i), Erebus (Antarctica), Erta' Ale (Ethiopia), Masaya (Nicaragua), Nyiragongo (Democratic Republic of the Congo), and Villarica (Chile).

Additionally, Ambrym features a bimodal shallow storage system, with basaltic and trachyandesitic magmas erupted from vents only ~2 km apart in the space of 2 years (Legrand et al., 2005), in 1988 and 1986 respectively (Cheney, 1988; Charley, 1988). The origin of andesitic magmas is an ongoing source of uncertainty in igneous petrology (e.g., Eichelberger, 1974; Reubi & Blundy, 2009), and is of fundamental importance in understanding the generation of evolved crust at convergent margins. A young, primarily basaltic arc volcano such as Ambrym is an ideal laboratory for the study of processes leading to development of an andesitic magma, without complicating factors such as non-volcanic basement or a thick volcanic succession.

Only a handful of studies have documented petrological characteristics of samples from Ambrym (Picard et al., 1995; Robin et al., 1993; Gorton, 1977), and no attempt has been made to quantitatively model conditions of magma storage. This study establishes a detailed petrological framework for recent magmas, to facilitate the interpretation, quantification and modelling of storage conditions and volatile components. Detailed petrographic descriptions and petrological analyses have been carried out for basaltic scoria and lava flows from the currently active central conduit; the 1986 trachyandesite; and a trachybasaltic flank lava. These data have been used to quantify and model the evolution and changing storage conditions of these magmas.

In addition to degassing and lava lake activity, Ambrym undergoes intermittent paroxysms with an average recurrence interval of 4 years. Paroxysms at basaltic volcanoes cause intermittent elevation of volcanic hazard associated with systems which are otherwise typically considered to be relatively safe to approach (e.g., Allard et al., 2006; Allard, 2010; Bertagnini et al., 2011; Pino et al., 2011). Prominent examples of this type of volcano include Stromboli and Etna (Italy), and Yasur (Vanuatu): all popular tourist destinations, with concomitant implications for hazard. Ambrym is another such system. Ambrym is becoming more popular as an adventure destination with an attendant increase in hazard, both for tourists and for the island inhabitants who guide them to the active intracaldera vents. Significant increases in activity can impact the wider island community, who live in villages concentrated along the coasts, while episodes of heavy degassing create acid rain, which damages crops, and human and livestock health (Cronin & Sharp, 2002).

Hazards associated with these fluctuating modes of magmatism may be mitigated given improved understanding of the driving mechanisms of variations in activity. The cause of transition to paroxysmal activity at basaltic volcanoes is not fully resolved. This study is a first step towards characterising magma conditions related to varied modes of activity at Ambrym. Linking processes in the magma storage region to changes in eruptive style and volatile emissions at the surface may then be used to improve prediction of eruptive behaviour.

1.2 Broader context

Focus on, and understanding of, subduction zone volcanism has increased in a series of leaps following several major eruptive events in both island arc and continental margin settings in recent decades; *e.g.*, Mount St Helens, USA, 1980 (e.g., Lipman & Mullineaux, 1981); Pinatubo, Philippines, 1991 (e.g. Bluth et al., 1992; Gerlach et al., 1996); and Soufrière Hills, Montserrat, 1995–present (e.g., Young et al., 1998).

Subduction zones are particularly prominent centres of volatile recycling (Wallace, 2005), and attract significant interest due to the associated climate and hazard implications (e.g. Johnston et al., 2011; Lindsay, 2005). A large proportion of studies have focused on silicic systems, which are often highly explosive (e.g., Rose & Durant, 2009), and often markedly enriched in volatiles and economically desirable metals (e.g. Payne & Peters, 2015), which make them a research priority from hazard mitigation and economic perspectives. Somewhat less attention has been directed towards basaltic subduction zone magmas, due in

part to their generally less violent eruptive styles, but also to technical barriers to laboratory study of basaltic melts, such as iron loss to noble metal capsules at basaltic temperatures, and quench crystallisation due to faster diffusion of melt components in basaltic liquid, which is less polymerised than silicic compositions (e.g., Berndt et al., 2002).

There is, however, increasing evidence for strong outgassing from basaltic arc volcanoes (*e.g.*, Aiuppa et al., 2006; Bani et al., 2009), which together with explosive basaltic volcanism invites closer investigation with regard to hazard mitigation and volatile cycles in the crust and upper mantle. Volatile-focused studies of basaltic systems have increased from a relatively small proportion of all papers on volatile-bearing phase equilibria and pre-eruptive volatile contents several decades ago (*e.g.*, Helz, 1973; Holloway & Burnham, 1972; Sigurdsson & Shepherd, 1974) to being an important constituent of the literature in the modern field (*e.g.*, Dixon et al., 1995; Dixon, 1997; Danyushevsky, 2001; Pichavant et al., 2002, 2009; Barclay & Carmichael, 2004; Scaillet & Pichavant, 2005; Di Carlo et al., 2006; Lesne et al., 2011a, 2015). Investigation of the roles of volatile constituents other than H_2O and CO_2, such as sulphur, chlorine and fluorine (Costa et al., 2004; Chevychelov et al., 2007, 2008; Stelling et al., 2008; Webster, 1997), and how these species interact in both basaltic and silicic magmas, has also received increased attention in recent years. This study adds to the body of mixed-volatile experimental data, including H_2O, CO_2, S, Cl and F, for alkalic island arc basaltic magmas.

1.3 Thesis organisation

This thesis comprises three distinct but related investigations: a petrological characterisation of recent scoriae and lavas, evaluation of pre-eruptive volatile contents and degassing via melt inclusions, and experimental investigation of mixed-volatile solubilities in a recent natural basalt composition.

Chapter 2 discusses the tectonic setting and geological history of the Vanuatu arc, and gives an overview of the evolution of Ambrym volcano, including geochemical evolution, eruptive behaviour and eruptive history. Vanuatu is located in a tectonically complex region, with unusual features including unusually high subduction rates, explosive basaltic volcanism, and occasional exotic magma compositions. This review of the tectonic and geochemical context of the arc aids interpretation of the evolution and present-day behaviour of Ambrym volcano.

Chapter 3 provides details of sample preparation, analytical techniques, analytical conditions and data processing and quality control.

Chapter 4 introduces the samples studied during this research. The samples are described from field locality and associated activity of the volcano at the time of sample eruption, via hand sample and petrographic description, to detailed investigation of mineral and glass compositions using electron microprobe analysis. The combination of field, petrographic and geochemical observations provide a preliminary model for the magma storage region.

Chapter 5 models magma storage conditions using mineral-melt equilibria, putting quantitative constraints on theories of magma storage and transport suggested by the data presented in Chapter 4. The relationship between the basaltic and trachyandesitic magmas is also evaluated using least-squares calculations and major element modelling.

Chapter 6 investigates magma conditions recorded by silicate melt inclusions in olivine, clinopyroxene and spinel. Degassing histories recorded in melt inclusions add information on the path traversed by the magma en route to the surface which places further constraints on interpretations from petrography and geochemistry. The tectonic, petrological and geochemical framework laid down in the preceding three chapters also helps to form a framework in which to interpret data from melt inclusions.

Chapter 7 reports results from a mixed-volatile (COHS and H_2O-Cl-F) experimental series. Unfortunately, the COHS runs were compromised by a contaminated starting glass, but provide useful solubility information nonetheless. H_2O-Cl-F experiments offer new insights into volatile behaviour at Ambrym, as well as some results which are difficult to explain.

Chapter 8 draws together the findings of each line of investigation and discusses ideas for further work which emerged in the course of this research.

Chapter 2 The Vanuatu island arc and Ambrym volcano

2.1 The Vanuatu arc

The Vanuatu arc is a volcanic archipelago c. 1750 km east-northeast of Australia, stretching c. 1250 km from north to south (Fig. 2.1). Current volcanism is associated with eastward subduction of the Indo-Australian plate beneath the Pacific plate. The arc includes nine historically active subaerial volcanoes, with 137 confirmed eruptions recorded since the first European exploration in 1774 (Global Volcanism Program, 2013). The subduction trench is on average ~6 km deep, but reaches up to 7 km depth in places (Greene et al., 1994), and is 143 ± 3 km lateral distance from the volcanic front (Dubois et al., 1988). The arc is complicated by the subduction of an aseismic ridge known as the D'Entrecasteaux Zone (DEZ) near 16º S, in the vicinity of Ambrym volcano; there is a gap in the trench in this region, from c. 15° to 17° S (Greene et al., 1994). The Benioff zone varies from a depth of 94 km near Tanna island in the south, to 172 km near Vanua Lava island in the north (Syracuse et al., 2010).

The earliest reports of volcanism in the archipelago were made by Captain James Cook, the first European to visit Vanuatu, who described eruptive activity on Tanna and Ambrym islands in 1774 (Beaglehole, 1961). Atkin (1868) reported vigorous activity of Lopevi volcano in 1864, with "an avalanche of hot stones and ashes" spilling from a breach in the crater rim, and also reported activity at Tanna and Ambrym at that time.

The volcanoes of Vanuatu are predominantly basaltic to andesitic stratovolcanoes, with the exceptions of the basaltic shields of Ambrym and Aoba, and the submarine caldera of Kuwae. Pyroclastic deposits, Strombolian activity and hydrovolcanism (maars and coastal tuff cones) are common features. Several of the larger volcanoes have summit calderas, some with crater lakes. A summary of the major characteristics and eruptive histories of the volcanoes of Vanuatu is given in Appendix A.

2.1.1 Geology and structure of the arc

The Vanuatu arc is divided into three longitudinal segments (Fig 2.1): the Western Belt (Espiritu Santo, Malekula and the Torres islands; Oligocene–Miocene age), the Eastern Belt (Maewo and Pentecost; Miocene–Pliocene age) and the Central Chain (Ambrym, Ambae and Gaua/Santa Maria; Pliocene–Holocene age) (Greene et al., 1994).

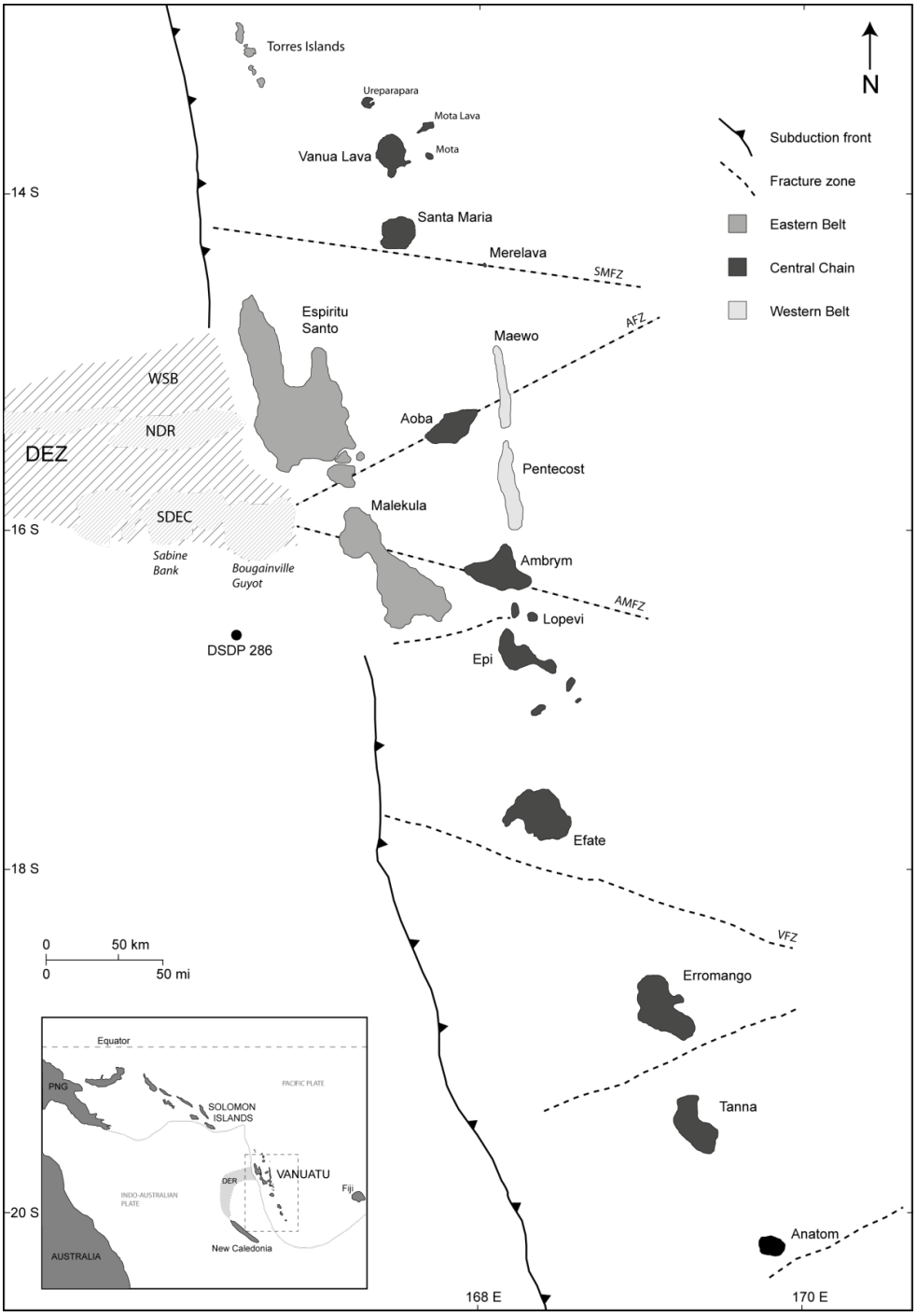

Figure 2.1 Map of the Vanuatu arc showing the three island belts and main tectonic features. Inset: position of the Vanuatu arc relative to Australia and the other major island groups of Melanesia. PNG=Papua New Guinea. DEZ=D'Entrecasteaux Zone. NDR=North D'Entrecasteaux Ridge; grey areas are topographic highs: SDEC=South D'Entrecasteaux Chain. Sabine Bank and Bougainville Guyot are two major seamounts of the SDEC seamount chain. WSB=West Santo Basin. SMFZ, AFZ, AMFZ, VFZ=Santa Maria, Aoba, Ambrym, and Vulcan Fracture Zones. The location of DSDP drill site 286 is shown, just south of the DEZ.

The island belts are composed of igneous rocks (both extrusive and intrusive), volcanogenic sediments, clastic carbonates, mudstones, and limestones, including reef carbonates deposited on all three belts since the Pliocene (Fig. 2.2) (Macfarlane et al., 1988).

Western Belt

The Western Belt comprises a succession of Oligocene to Early Miocene volcanics, volcaniclastic sediment, and basaltic to andesitic intrusions, overlain by Late Miocene to Pleistocene marine sediments and capped by reef limestones (Fig. 2.2; Macfarlane et al., 1988).

The lower sequence is derived from volcanism along an ancient, now inactive, south-west dipping arc, known as the Vitiaz arc. The lavas are dominated by andesitic compositions, but range from olivine basalt to rhyodacite pumice. Geochemically, they are similar to a modern-day lower-K_2O lava series found in the Central Chain, and like this series are transitional between tholeiitic and calc-alkaline (Maillet et al., 1995). The early volcanics and sediments were later intruded by hornblende andesites and diorites, followed by block faulting and uplift in the mid-Miocene (Mitchell & Warden, 1971).

In the Late Miocene, turbidites were sourced from the volcaniclastic deposits. Further faulting and erosion of occasional tuff deposits was followed by a marine transgression in the Pliocene (Mitchell & Warden, 1971) during which foraminiferal sediment, shallow marine deposits, terrigenous sediment, and finally reef limestones were laid down. The mid to late Miocene was dominated by uplift and erosion (Macfarlane et al., 1988).

Eastern Belt

The Eastern Belt comprises deepwater clastics deposited during the Miocene, with subordinate volcanics, overlain by late Miocene to Pliocene pelagic and hemipelagic sediments and volcanics, and Pliocene to Pleistocene limestone (Fig. 2.2; Macfarlane et al., 1988).

Early lavas of the Eastern Belt underwent faulting and intrusion of gabbros and norites prior to the mid-Miocene, followed by tectonic emplacement of serpentinites, eruption of pillow basalts, and breccia emplacement during the Upper Miocene to Lower Pliocene (Mitchell & Warden, 1971). Slices of ultramafic and mafic rocks, interpreted as fragmented ophiolite of Eocene-Oligocene age (Gorton, 1977), were emplaced into the Pentecost volcanic pile during the Pliocene.

Most of the Eastern Belt volcanics were erupted from submarine fissures from late Miocene to mid-Pliocene, and include pillow lavas, basic intrusions and pyroclastics of ankaramitic, picritic and mafic basalt compositions near the base, to feldspar-phyric basalts and basaltic andesites towards the upper part of the succession (Maillet et al., 1995). Eastern Belt volcanism ceased c. 3.5 Ma (Maillet et al., 1995).

Central Chain

The Central Chain comprises volcanic rocks and reef carbonates dating from the late Miocene to the Holocene (Fig. 2.2; Macfarlane et al., 1988). Volcanic activity began c. 5.8–5.3 Ma (seen on Erromango island; Bellon et al., 1984), while Eastern Belt activity was still ongoing. With the exception of Erromango and Futuna, which have histories reaching back to the end-Miocene/Pliocene, volcanism has been contemporaneous across all islands of the Central Chain, from the early Pliocene to the Holocene (Fig. 2.3). Central Chain lavas range from picritic (e.g., on Aoba island; Sorbadere et al., 2011) to rhyodacitic (e.g., Ambrym pyroclastic series; Robin et al., 1993), with the majority of compositions in the basaltic range.

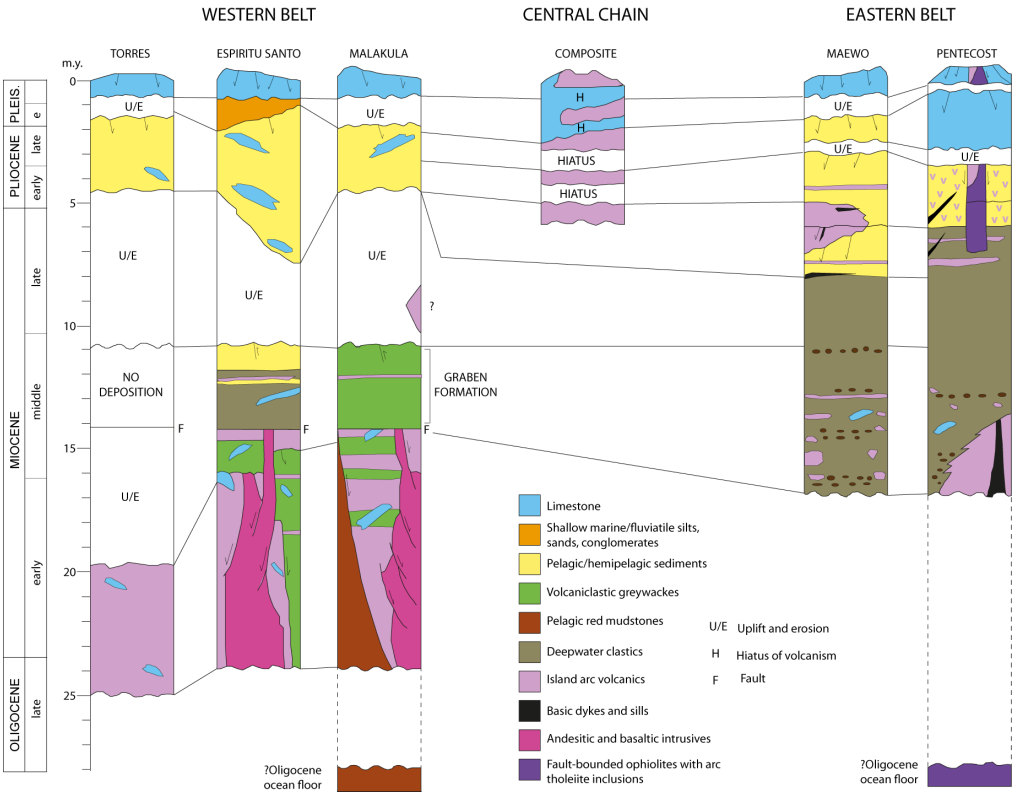

Figure 2.2 Correlation of lithological sequences across the Western Belt, Central Chain and Eastern Belt of Vanuatu (after Macfarlane et al., 1988).

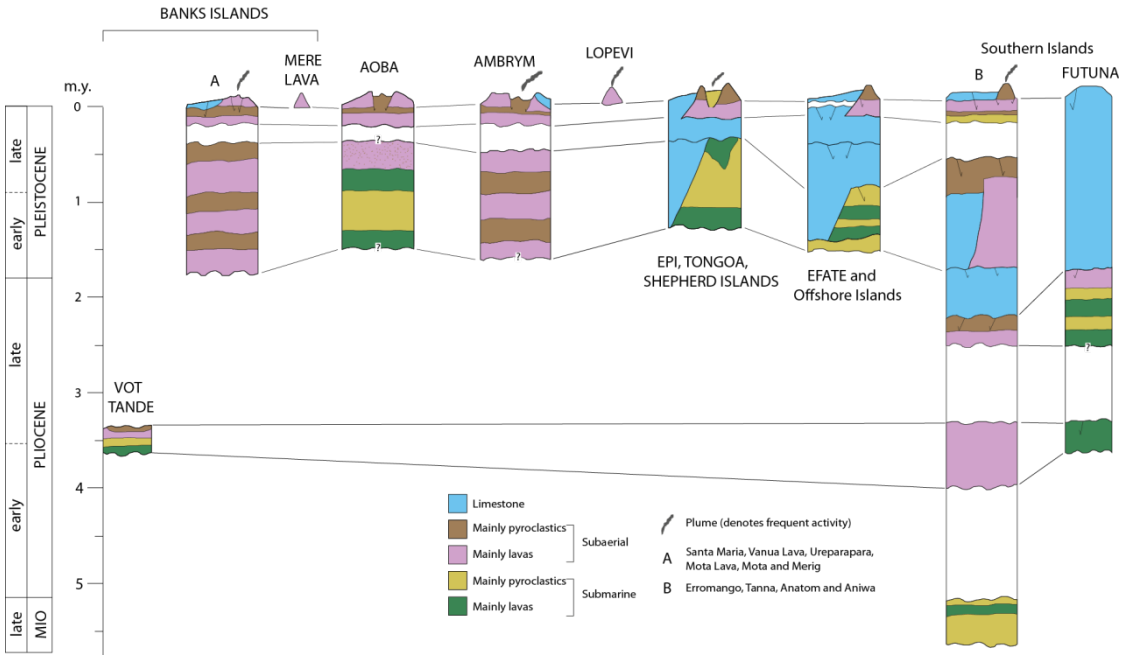

Figure 2.3 Correlation and timing of volcanism between islands in the Central Chain, from north to south (after Macfarlane et al., 1988).

2.1.2 Fault patterns

Onshore faults are predominantly arc-parallel (NNW–SSE) and extensional, bounding tilted fault blocks. These are probably a result of upbowing associated with subduction of the D'Entrecasteaux Zone (Greene et al., 1988). Offshore faults are arc-parallel, arc-oblique or arc-transverse (Greene et al., 1988). The oblique faults were likely shifted from an originally arc-parallel alignment following collision with the D'Entrecasteaux Zone.

There are also ENE-, WSW-, EW- and ESE-trending transverse faults which are possible conduits for magmatism, such as major wrench faults passing beneath Ambrym, Aoba and Mere Lava (Ambrym Fracture Zone, Aoba Fracture Zone and Santa Maria Fracture Zone; Fig. 2.1). It can be seen from Figure 2.1 that the fractures exert a control on the morphology of both Ambrym and Aoba, which are elongate in the direction of their respective fracture zone orientations. The Santa Maria fracture zone is marked by a line of submarine and subaerial volcanoes. These three fracture zones post-date the arc-parallel normal faults which bound the horst and graben blocks (Greene et al., 1994).

Within the central segment of the arc, arc-parallel grabens, probably active since the Miocene, form thickly sedimented central basins (the North Aoba Basin and South Aoba

Basin) with the islands of Espiritu Santo and Malekula to the west, and Maewo and Pentecost to the east, raised on horsts to either side (Greene et al., 1994).

2.1.3 Tectonic evolution of the Vanuatu arc

The Vanuatu arc began to form in the Oligocene as a rear-arc belt to a now-extinct oceanic arc known as the Vitiaz Arc, the previous locus of which is marked by the Vitiaz trench to the northeast of Vanuatu[1]. From 25–14 Ma, mainly submarine basaltic to andesitic volcanism built up eruptives and volcanogenic sediments, which eroded into fault-controlled basins (Fig. 2.4a). At this time, this area, which would later form the Western Belt, was shallowly submerged, though locally emergent and reef-fringed, with greywackes forming in arc-summit basins. Limestone blocks slumped into some of these greywackes from adjacent reef platforms. The Vitiaz arc, largely basaltic, was periodically active from 25–22 Ma, and possibly at 15 Ma (Kroenke, 1984). Coarse clastic sediments were eroding off the Vitiaz arc from c. 16 Ma and being deposited as deepwater submarine fans across the future site of the Eastern Belt (Greene et al., 1988).

From 14–11 Ma was a quiescent period characterised by heavy erosion of the Western Belt and Vitiaz Arc, and deposition into fault-controlled basins of volcaniclastic submarine fans onto the area of ocean floor that would later become the Eastern Belt (Fig. 2.4b).

From 11–8 Ma, the Western Belt was subaerially exposed and eroding still further, with minor volcanic activity, while the Vitiaz Arc had ceased activity and begun to subside (Fig. 2.4c). Faulting and uplift were occurring along the Western Belt. Reversal of subduction direction had also begun by the end of this period—collision of the Ontong-Java Plateau with the Solomon arc around 22–20 Ma caused southerly subduction of the Pacific plate to cease for a time before resuming intermittently c. 15 Ma, followed by a reversal of subduction direction in the Solomon-Vitiaz arc c. 8 Ma (Petterson et al., 1997).

From 8–7 Ma, separation of the Vitiaz arc from the Vanuatu arc area began, with initiation of seafloor spreading between the two. Westward subduction ended and eastward subduction initiated c. 300 km to the west with Eastern Belt volcanism occurring at the site of earlier deepwater sedimentation (Fig. 2.4d; Greene et al., 1988). The Western Belt islands were receiving calcareous, shallow-water, and volcanic sediment in central grabens, and the

[1] Prior to c. 12 Ma, the Vitiaz arc formed part of a continuous subduction front between the Pacific and Indo-Australian plates, in line with the Solomon Islands and Fiji (Fig. 2.5). At that time, the Pacific plate was subducting beneath the Indo-Australian plate at the Vitiaz arc in a south-westerly direction.

islands were tilting southeast. Sediments eroded from the Western Belt were being deposited on the site of the Eastern Belt.

From 7–2 Ma (Fig. 2.4e), seafloor spreading opened up the North Fiji Basin and rotated the developing Vanuatu arc to its present position (cf. Louat & Pelletier, 1989; Colley & Hindle, 1984). At this time, the Eastern Belt was still volcanically active but the Western Belt was subsiding. Around 6 Ma, volcanic activity moved from the Eastern Belt to the Central Chain with extrusion of submarine basalt and andesite at the site of what is now Erromango island (Louat & Pelletier, 1989). Central Chain activity in this period occurred at Erromango (c. 6 Ma) and Tanna (c. 2.5 Ma), and in the backarc at Vot Tande (3.5 Ma) and Futuna (2.6 Ma). There was no volcanism in the central and northern segments of the Central Chain in this period. Collision with the D'Entrecasteaux Zone (DEZ) began c. 4–3 Ma (Fig. 2.4e).

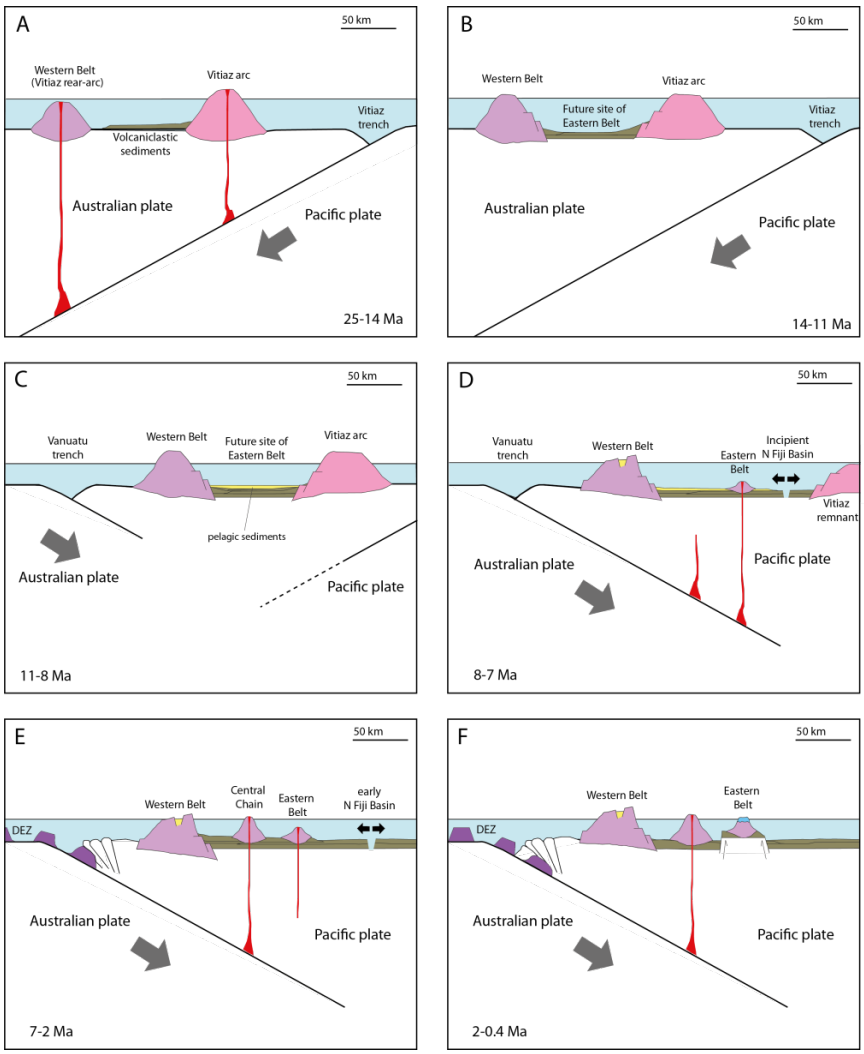

Figure 2.4 Schematic representation of the development of the Vanuatu arc, following the timing given in Greene et al. (1988). See text for a detailed description of events. Sedimentary and structural features are shown schematically and are not intended to represent detailed lithological or structural geometries.

From c. 2 Ma, magmatism ended in the Eastern Belt and increased in the Central Chain, spreading to the north and south as the Central Chain developed. Subaerial and submarine volcanism developed at the Banks Islands, Aoba, Ambrym, Epi-Tongoa, Efate, Erromango, Tanna and Anatom. Meanwhile, Vot Tande and Futuna (1.8 Ma) ceased activity. The locus of Central Chain activity has moved closer to the trench over time, as the angle of subduction has increased to the current angle of 70° (Peate et al., 1997). Continued collision with the D'Entrecasteaux Zone has given rise to arc-transverse transcurrent faults in the central region of the arc, creating the wedge-shaped structural blocks that can be seen in Figure 2.1. A compressional tectonic regime since 2 Ma has caused uplift of the Eastern and Western Belts (Greene et al., 1988).

2.1.4 Current tectonics

The major tectonic processes currently operating in the Vanuatu region are:

1) Convergence of the Pacific and Indo-Australian plates and consumption of the Indo-Australian plate along the Vanuatu arc;
2) Subduction of the D'Entrecasteaux Zone (DEZ), which is discussed in detail in section 2.1.5;
3) Extension in the back-arc and in the North Fiji Basin, a young (<10 Ma) marginal basin connecting the Vanuatu and Tonga arcs.

The subduction rate at the Vanuatu arc varies from 15–16 cm yr^{-1} in the northern segment of the arc, to 12 cm yr^{-1} in the southern segment, falling to 1.5 cm yr^{-1} at the far southern end where the trench curves around to an approximately E–W orientation (Fig. 2.5) (Louat & Pelletier, 1989). The subduction rate opposite the D'Entrecasteaux Zone is not as well constrained as in other parts of the arc, but is calculated at roughly 9 cm yr^{-1} (Louat & Pelletier, 1989)[2]. The high convergence rate in the northern segment means the Pacific plate in the northern part of the arc is being very rapidly consumed, causing rotation which is bringing the Vanuatu arc and Solomon arc into alignment.

The Vot Tande and Coriolis back-arc troughs (to the east of the northern and southern arc segments, respectively; Fig. 2.5) are regarded as expressions of the early stages of back-

[2] A compression rate of 1 cm yr^{-1} is 'arbitrarily' assigned to the back-arc thrust zone opposite the DEZ, combined with a 10 cm yr^{-1} convergence rate calculated from the RM-2 global plate motion model of Minster & Jordan (1978) to give an overall convergence rate of 9 cm yr^{-1} for the DEZ region (Louat & Pelletier, 1989).

arc extension, caused by the combined effects of subduction to the west (at the Vanuatu arc) and extension to the east (in the North Fiji Basin), and to a lesser extent, collision of the D'Entrecasteaux Zone with the Vanuatu arc (Maillet et al., 1995).

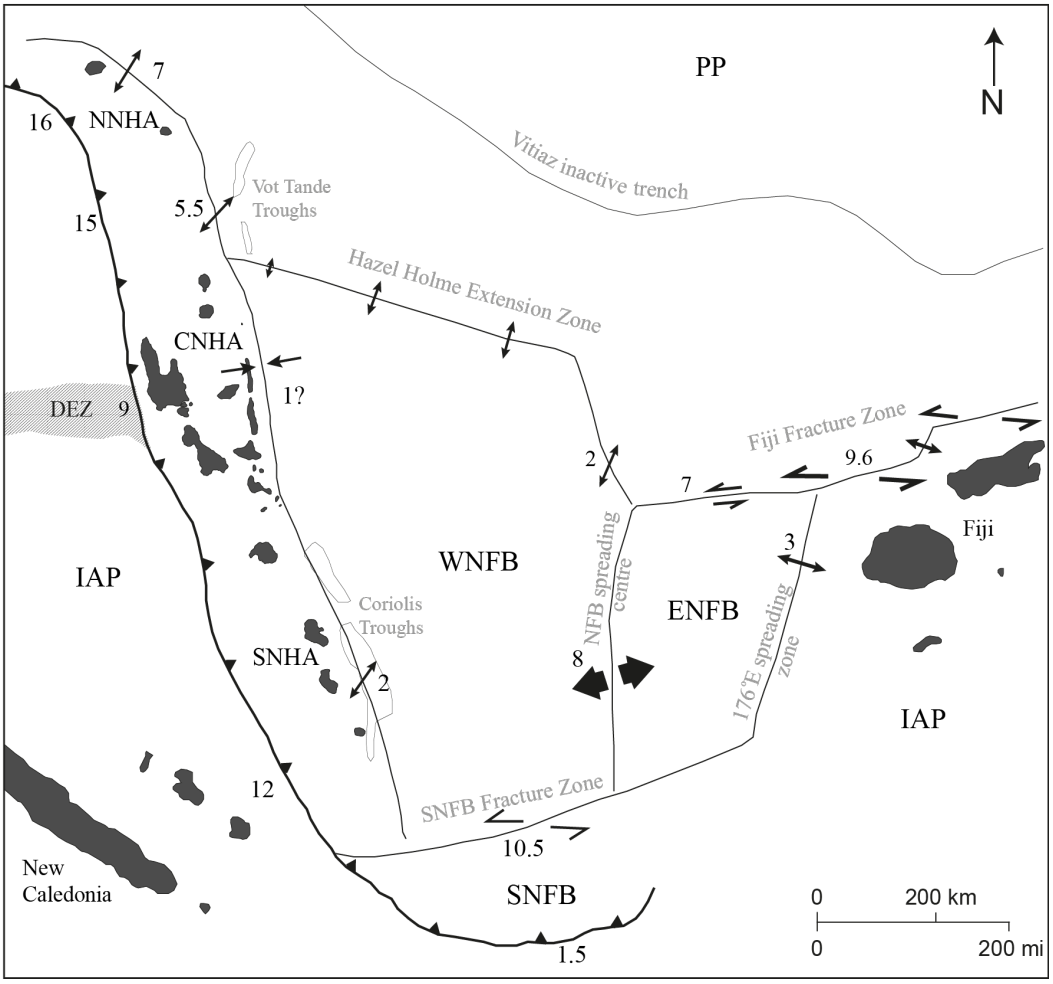

Figure 2.5 Relative plate motions in the Vanuatu-Fiji Basin region, after Louat & Pelletier (1989). IAP=Indo-Australian Plate. PP=Pacific Plate. DEZ=D'Entrecasteaux Zone. NNHA, CNHA, SNHA=North, Central and South New Hebrides Arc. WNFB, ENFB, SNFB=West, East and South North Fiji Basin. Numbers and arrows indicate the sense of movement and rate in cm yr^{-1} of relative plate motions at each boundary. Diverging arrows=spreading, converging arrows=convergence, laterally diverging arrows=shear extension. The size of the arrows represents the relative magnitude of movement rates. Positions of back-arc troughs are based on Maillet et al. (1995) in combination with bathymetric images from the online image repository of the National Geophysical Data Center of the National Oceanic and Atmospheric Administration.

The backarc region is tectonically complex, with multiple microplates bounded by spreading ridges and fracture zones, all moving relative to the surrounding crust at varying speeds (Fig. 2.5). Louat & Pelletier (1989) consider the boundary of the Pacific plate proper to be along the Fiji Fracture Zone and the Hazel Holme Fracture Zone, with the intervening crust between these fracture zones and the Vanuatu trench being composed of several microplates.

These are the Vanuatu arc microplate, and the West, East and South North Fiji Basin microplates (WNFB, ENFB, and SNFB; Fig. 2.5). The Louat & Pelletier (1989) model indicates rotational movement along several boundaries in the NFB caused by variations in rates of motion along plate boundaries. One example is the faster spreading rate towards the south of the North Fiji Basin spreading centre (between the WNFB and ENFB) compared to the north.

2.1.5 The D'Entrecasteaux Zone

The D'Entrecasteaux Zone is believed to be the remnant of an Eocene-Oligocene island arc (Maillet et al., 1989). It curves around from New Caledonia, trending east-west as it approaches Vanuatu (see inset, Fig. 2.1) where it is c. 100 km wide, with a ridge to the north (the North D'Entrecasteaux Ridge) which is interpreted as back-arc or fore-arc crust, and a chain of seamounts to the south (South D'Entrecasteaux Chain), with a deep basin in between the two (Maillet et al., 1989; Fig. 2.1). The North D'Entrecasteaux Ridge comprises Pliocene to Pleistocene sediment atop Eocene basaltic basement of mid-ocean ridge basalt (MORB) affinity (Maillet et al., 1989). Peate et al. (1997) report highly variable radiogenic strontium ratios for D'Entrecasteaux Zone samples, indicating extensive seawater alteration. The Bougainville Guyot, the South D'Entrecasteaux Chain seamount nearest to the Vanuatu arc, is a middle Eocene andesitic volcano capped with limestones (Collot & Fisher, 1992) and is currently colliding with the arc. D'Entrecasteaux Ridge material is accreting onto the forearc to create Wousi Bank, a submarine ridge west of Espiritu Santo (Greene et al., 1994).

Collision of the D'Entrecasteaux Zone with the Vanuatu arc was initiated ~3.0–1.5 Ma near 16º S and has migrated northward at a rate of 2–4 cm yr^{-1} due to its oblique approach to the arc front (Greene et al., 1994). The rate of ridge-arc convergence at the D'Entrecasteaux Zone has been variously estimated as 4.2 cm yr^{-1} (Taylor et al., 1995), 9 cm yr^{-1} (Louat & Pelletier, 1989), 11–20 cm yr^{-1} (Taylor et al., 1985, cited in Greene et al., 1988) and 10 cm yr^{-1} (Collot & Fisher, 1992). The obliquity of collision means that the D'Entrecasteaux Zone is also moving 2.5 cm yr^{-1} northwards relative to the arc (Collot & Fisher, 1992).

Taylor et al. (1995) concluded that there is a strong coupling between the D'Entrecasteaux Zone and the arc; in particular, a compressional tectonic regime is seen in the back-arc region in the vicinity of the D'Entrecasteaux Zone, in contrast to the rear-arc rift pattern that characterises the rest of the backarc region. Focal mechanisms of a belt of earthquakes on the eastern side of the central islands indicate thrust faulting in the back-arc

region along a west-dipping thrust zone (Louat & Pelletier, 1989). This thrust zone is bounded to the north and south by areas where strike-slip earthquake events have been recorded (Collot et al., 1985). This compressional zone bounded by strike-slip faulting events is interpreted as a block of the arc being 'shunted' eastwards by the impinging D'Entrecasteaux Zone. Taylor et al. (1995) modelled convergence rates along the arc and found a convergence rate deficit in the central region which cannot be adequately accounted for by a 'stick-slip' model of motion (only a small fraction of the deficit can be attributed to elastic strain accumulation), and requires that the central arc segment should undergo a net eastward movement relative to the arc as a whole at a rate of 3.6–8.3 cm yr^{-1}, consistent with back-arc compression in the central region and strike-slip faults bounding the central segment to north and south. The cause of this 'shunting' of the central segment is most likely the collision with the D'Entrecasteaux Zone. Subduction of the D'Entrecasteaux Zone is also considered likely to be at least partially responsible for the uplift and tilt of the Western (Espiritu Santo and Malekula) and Eastern (Pentecost and Maewo) Belts, and for the break in the trench in the central Vanuatu arc region (Taylor et al., 1995; Luyendyk et al., 1974; Greene et al., 1988).

Volcanoes near the collision zone (Ambrym, Aoba and Gaua) display anomalous geochemistry, such as alkaline lavas (as opposed to tholeiitic/calc-alkaline in the rest of the arc), anomalous radiogenic isotope ratios, slightly elevated large-ion lithophile elements concentrations, and Indian MORB-type $^{206}Pb/^{204}Pb$ ratios which are very low for arc magmas (Peate et al., 1997). Collision with the D'Entrecasteaux Zone is believed to have significantly influenced the development of high-K_2O (HK) shoshonitic volcanism in the Central Chain (Baker & Condliffe, 1996) by producing a system of transverse wrench faults across the arc. HK and shoshonitic magmatism occurs only on those islands located on transverse faults, in contrast to the low-K_2O (LK) to medium-K_2O (MK) calc-alkaline suites of most of the other islands.

2.1.6 The subducting plate

The sediment column and a short section of basement of the downgoing plate was cored during Deep Sea Drilling Project (DSDP) Leg 30 at DSDP site 286, located c. 50 km west of the arc, and c. 50 km south of the D'Entrecasteaux Zone (16º32' S, 166º22' E; Fig. 2.1). The cored sequence was divided into five units (three sedimentary units atop two basement units of the underlying oceanic plate; Table 2.1) and described by Andrews et al. (1973). The basement is interpreted as sea-floor basalt (Unit 4) intruded by gabbro (Unit 5) at an unknown

time, and overlain by a thick sequence of rapidly-deposited Eocene volcaniclastics most probably derived from the Loyalty Islands (Unit 3). There followed a period in which sea level was shallow enough to allow carbonate deposition. This period is represented by a sequence of upper-Eocene to upper-Oligocene nanno-ooze and nanno-chalk with accessory-to-moderate ash content, again believed to derive from the Loyalty Islands (Unit 2). More recently, Peate et al. (1997) have suggested that the Eocene volcaniclastics may have derived from the South D'Entrecasteaux Chain, based on isotopic compositions and unusual trace element ratios common to both, as well as the fact that the D'Entrecasteaux Zone volcanic activity occurred at the same time as deposition of the volcaniclastics.

A subsequent decline in volcanic activity led to sea-floor subsidence, and as a consequence, the foram-dominated sedimentation regime shifted to deposition of biogenic sediments with minor ash input towards the end-Eocene and Oligocene period. Continued subsidence brought the seafloor further below the carbonate compensation depth during the Oligocene. After a hiatus in sedimentation during the Miocene (with the possible exception of an ash and micronodule-rich red clay unit of uncertain age) the sequence was dominated in the Pliocene and Pleistocene by distally-sourced glassy ash, containing reworked fossils indicative of erosion of nearby Miocene- and Pliocene-age shelf deposits (Unit 1). These uppermost volcaniclastic sediments were derived from the Central Chain of the Vanuatu arc—and as such the arc is digesting its own products, in what Peate et al. (1997) dub "intra-arc cannibalism"—and also contain abundant nannofossils, radiolarians and microcarbonate particles.

Unit	Age	Thickness (m)	Description
1a	Pliocene–Pleistocene	64	Glassy ash with radiolaria, nannofossils, micarb
1b	?Miocene	19	Glassy ash with zeolite and micronodule rich clay
2	U. Eocene–U. Oligocene	114	Nanno ooze, nanno chalk with small to moderate glassy ash component
3a	Mid-Eocene to U. Eocene	133	Vitric siltstone
3b	Mid-Eocene to U. Eocene	81	Volcanic conglomerate
3c	Mid-Eocene to U. Eocene	238	Vitric siltstone, minor vitric sandstone, very minor volcanic conglomerate
4	?	10	Altered tholeiitic basalt
5	?	47	Intrusive gabbro, altered; plag, px replaced by smectite, chlorite

Table 2.1 Sedimentary/geological units of the subducting plate, cored at Deep Sea Drilling Project site 286 (Andrews et al., 1973).

Subduction input

There is evidence that some of the sediment atop the downgoing plate is accreting onto the arc front (Greene et al., 1994) but it has proven difficult to quantify how much, if any, is being carried down into the subduction zone. The resolution of the seismic reflection data used to image the forearc sediments is not sufficient to determine with certainty the fate of the uppermost 50–100 m of sediment, but otherwise indicates that most of the sediment pile is entering the subduction zone. Peate et al. (1997) report significant sediment subduction along the Vanuatu arc; however, the trace element compositions of erupted lavas (Ba/La ratios) do not reflect incorporation of bulk sediments. Trace element and radiogenic isotope analyses indicate that the slab component of the magmas is fluid rather than melt (Peate et al., 1997); *i.e.*, fluid from the oceanic crust which has picked up an additional, fluid-transferred component from subducted sediment.

$^{87}Sr/^{86}Sr$ and $\delta^{18}O$ in Ambrym lavas indicate a contribution of slab-derived fluid or melt to the magma source (Peate et al., 1997; Eiler et al., 2000). Eiler et al. (2000) report that $\delta^{18}O$ is atypically enriched in lavas from Vanuatu, compared to the majority of island arcs; the same enrichment is seen in lavas from New Caledonia and the Tabar-Lihir-Tanga-Feni island group (NNE of New Britain), suggesting a common source. Ambrym olivine shows $\delta^{18}O$ values elevated above MORB and above other ocean arc samples analysed in the same study, and may provide a constraint on sediment input. $\delta^{18}O$ vs. $^{87}Sr/^{86}Sr$ for Vanuatu arc lavas describes a trend which can be explained by mixing between a MORB component (low $\delta^{18}O$, $^{87}Sr/^{86}Sr$) and a slab component (high $\delta^{18}O$, $^{87}Sr/^{86}Sr$). The trend is hyperbolic, rather than the linear trend expected for assimilation at an oceanic arc—a linear trend is expected because the arc basement would have similar isotopes to present lavas, being from the same source. According to the classification system of Hawkesworth et al. (1997), the trace element abundances indicate a primarily fluidic slab component, rather than slab melt.

Of particular interest from the perspective of this study is the possibility of a link between subducted material and volatile output from the arc volcanoes. Sulphur, chlorine and fluorine are most likely to derive from seawater percolation into the oceanic crust and sediments. The source of high carbon dioxide outgassing is less well understood, and at other volcanoes worldwide has been linked to mass assimilation of crustal carbonate, e.g., Merapi (Deegan et al., 2010), Popocatépetl (Goff et al., 2001), Vesuvius and Etna (Marziano et al., 2008). Although there are reef limestones in the Vanuatu area, they do not appear to form part of the crustal section below Ambrym, and no evidence of assimilated carbonates such as xenoliths, elevated CaO content or exotic carbonate-influenced mineralogy, is seen.

Possible carbon sources at Ambrym include carbonate nanno ooze and chalk on the downgoing plate, carbonate caps on subducting features (such as the limestone-capped Bougainville Guyot) at the D'Entrecasteaux Zone, and carbonate alteration veins in the subducting basaltic oceanic crust. The subducting crust at the Vanuatu arc is of Eocene age, meaning it is probably too young to have developed significant carbonate veining via hydrothermal alteration; probably c. 1.3–2.4 wt.% bulk CO_2 at most (estimated after Alt & Teagle, 1999). Carbonate veins up to 1 cm thick are reported as common in the basement basalt (of which 10 m was cored) at DSDP site 286, along with some 'sparse, small' calcium carbonate amygdules and occasional dolomite veining (Stoeser, 1975) but the total proportion of carbonate is not estimated. Overall, there does not appear to be any unusually carbon-rich material entering the subduction zone at Ambrym, suggesting that mantle-derived carbon could be the primary source of CO_2 in the fluid phase.

Mantle input

High $^3He/^4He$ ratios (R_A of up to 10.05)[3] measured in waters and gases near a major fault structure on Ambrym (Jean-Baptiste et al., 2009, 2015) indicate a primary mantle melt component in the source region, which would be consistent with the theory that the CO_2 signal at Ambrym likely has a strong mantle-derived component.

Analysis of a range of isotope systems—Nd, Pb, Sr, Hf, $\delta^{18}O$—has shown that Indian Ocean type MORB is present beneath the central segment of the Vanuatu arc (Pearce et al., 2007; Peate et al., 1997; Turner et al., 1999): lavas from the Central Chain volcanoes (Ambrym, Aoba, and Gaua/Santa Maria) plot in the Indian MORB fields for Pb isotopes, compared to lavas from north and south of the DEZ, which plot in the P-MORB field (Peate et al., 1997). The cause of this is believed to be an upwelling of Indian Ocean type MORB beneath the central segment of the arc as a result of disruption due to collision with the D'Entrecasteaux Zone (Crawford et al., 1995; Peate et al., 1997; Turner et al., 1999). This Indian-MORB type character has been demonstrated to date from the onset of D'Entrecasteaux collision (ca. 1.5–3 Ma), before which central Vanuatu displayed characteristics of Pacific MORB (Briqueu et al., 1994).

[3] $R_A = (^3He/^4He)_{observed}/(^3He/^4He)_{air}$, and $(^3He/^4He)_{air} = 1.4 \times 10^{-6}$

2.2 Ambrym volcano

2.2.1 Geomorphology

Ambrym is a roughly triangular, N105ºE-elongate island of c. 35 × 50 km area, rising 1800 m above the adjacent sea-floor (Fig. 2.6) in the central part of the Vanuatu island arc, near the D'Entrecasteaux collision zone (Fig. 2.1). It is classified as a pyroclastic shield, being composed of a basaltic shield overlain by a 24-km-wide basaltic to dacitic tuff cone with an estimated volume of more than 20 km^3 dense rock equivalent (Robin et al., 1993). The tuff cone is cut by a 12 km diameter caldera, one of the largest basaltic examples known, containing two currently active cones towards the western side. These are Marum and Benbow, reaching 1200 m and 1160 m in height above sea level respectively. Marum is host to several adventitious cones; Mbwelesu, Niri Mbwelesu, and Niri Mbwelesu Taten. There are also a number of phreatomagmatic cones in the eastern part of the caldera, including a recent maar, Lewolembwi crater, which is surrounded by a c. 2 km diameter tuff ring (Robin et al., 1993).

The caldera is circular in outline, and contains a gently eastward-sloping ash plain of 550–700m altitude, composed of lava flows, tephra and volcanic sand, bordered by the caldera scarp which rises from a few tens of metres up to 450 m high (Robin et al., 1993). The scarp is shallowed by ash deposits from the two active cones towards the west; gravity data indicates that the entire caldera is predominantly ash-filled (McCall et al., 1970). The caldera rim cuts through an ancient edifice (Dalahum), the remainder of which rises 450 m above the caldera floor. This height is taken as a minimum displacement of the north caldera wall and an indication of the extent of overall subsidence. The infrequent exposures of lava on the ash plain are ropy, massive or rubbly basalt similar to that historically erupting from Marum and Benbow (McCall et al., 1970). Recent lava flows have breached the caldera rim in five places and follow ravines to the sea.

The major physical features of the island are shown in Figure 2.6.

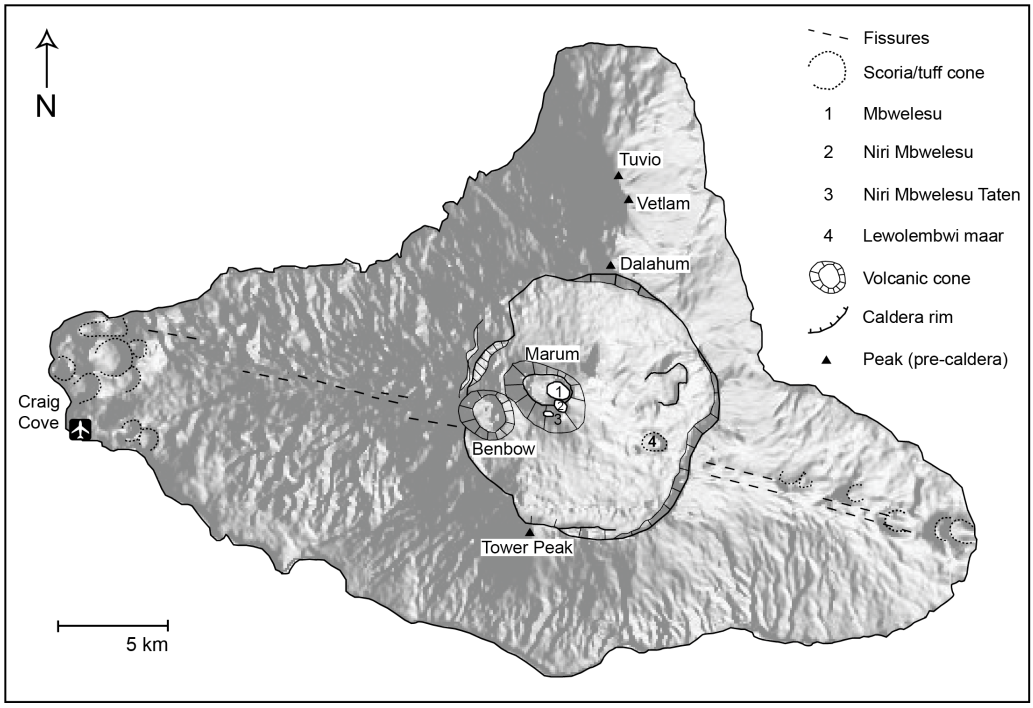

Figure 2.6 Map of Ambrym island highlighting the major volcanological features and the airfield at Craig Cove. Satellite image from NASA Earth Observing System satellite Terra.

2.2.2 Pre-caldera evolution

Development of the island began with the growth of a wide (>19 km diameter) composite cone, roughly contemporaneous with three steeper, narrower cones known as Tuvio, Dalahum (a.k.a. Rahoum) and Tower Peak, aligned N10ºE. The remains of these cones are still evident, and are composed of rubbly or blocky lavas intercalated with ash, lapilli tuffs and minor agglomerates, with stream-bed conglomerate deposits in places indicating erosive gaps between eruptive phases (McCall et al., 1970). The early cone stage was followed by a shield-building phase, during which a series of low-viscosity, pahoehoe-type basaltic lava flows constructed a gently-sloping (2–3º) shield-shaped edifice. Monzier et al. (1991) estimate the shield volcano summit at c. 400 m in height.

An aeromagnetic survey by McCall et al. (1970) indicates that the pattern of volcanism on Ambrym is a result of intersection of an east-west lineation with the approximately north-south axis of the Vanuatu arc.

Geochemistry of the early edifice

The most primitive rocks on Ambrym are found in the medium-K basaltic lavas of Tuvio and Vetlam, with high MgO (9.8–12.8 wt.%), Ni and Cr, and the lowest Zr, Y and Nb contents (Picard et al., 1995) of the whole succession. These lavas include plagioclase-glomeroporphyritic basalts.

The lavas of the shield-building phase are medium-K to high-K basaltic magmas (Picard et al., 1995) similar to recent basalts.

2.2.3 Tuff cone emplacement and caldera formation

The shield-building phase was followed by construction of the tuff cone and formation of the caldera, either by a hydromagmatic eruption (Monzier et al., 1991) or by quiet subsidence due to drainage of the magma chamber through flank fissure eruptions (McCall et al., 1970). The caldera-forming event has been dated to 50 AD (± 100 y), using radiocarbon-dating of charcoal from late pre-caldera strata (McCall et al., 1970).

The constituent deposits of the tuff cone have been divided into four sequences (Monzier et al., 1991; Robin et al., 1993), collectively named the Ambrym Pyroclastic Series, showing a progressive upwards decrease in the role of water. No lava flows are interstratified with the tuffs, as demonstrated by the lack of stepped topography and the widespread gully incision seen on the extra-caldera slopes (Robin et al., 1993).

The first sequence of the tuff cone comprises mainly dacitic Plinian deposits—coarse ash and lapilli (50%), vitreous clasts and cauliflower bombs (15%), accidental clasts (20%), and pumice (15%)—and phreatomagmatic deposits, with intercalated base surge deposits.

Sequence II forms the main part of the tuff cone, and consists of mainly basaltic Surtseyan type deposits of vitric tuffs with intercalated agglomerates, interbedded with ash flows in the upper part of the sequence. Phenocrysts (plagioclase and clinopyroxene) form up to 50% of some coarse ash or lapilli layers of this sequence (Picard et al., 1995).

Sequence III consists of basaltic ash-flow deposits with highly vesicular glassy droplets and pumiceous lapilli.

Sequence IV comprises Strombolian basaltic deposits, reaching maximum thickness near the Tower Peak vent at the southern rim of the caldera from which they are believed to have emitted.

Most studies favour caldera formation by collapse following a cataclysmic Plinian/phreatomagmatic event, tapering off to Surtseyan and finally Strombolian activity

(Monzier et al., 1991; Robin et al., 1993; Picard et al., 1995). Picard et al. (1995) note that the heterogeneity of the tuff cone deposits indicates mechanical mixing of a variety of magmas, from medium-K to high-K, and basaltic to rhyodacitic compositions. The simultaneous eruption of variably porphyritic basaltic liquids and magmas of variably evolved compositions suggests rapid emptying of a partially differentiated basaltic reservoir (Monzier et al., 1991).

McCall et al. (1970) argue for passive collapse of the chamber roof following drainage of magma through lateral dykes to feed flank eruptions. Those authors point to the lack of debris derived from the pre-caldera edifice, which would be expected if a cataclysmic explosion had created the caldera by blasting out a great volume of the summit, and emphasise that there are no unusual deposits nor a noticeable break in the eruptive sequence marking the caldera formation. However, great volumes of blasted rock are not required if the collapse followed drainage of the magma reservoir by prolonged eruption rather than evisceration, and the tuff cone—which was not recognised until twenty years later (Monzier et al., 1991)—provides the 'unusual deposits' as well as containing a significant volume of non-juvenile material stripped out of the old edifice during eruption. McCall et al. (1970) found no significant petrographic differences between pre- and post-caldera lavas, with all of the lavas being basaltic, with phenocrysts including plagioclase, diopsidic pyroxene, olivine and titanomagnetite. They did recognise that a change in bulk geochemistry might not necessarily be apparent in the mineralogy and stated intentions to carry out a geochemical study. Later studies show that there was in fact a geochemical shift, from MK-dominated to HK-dominated, following caldera formation (Picard et al., 1995). Along with the volume of pyroclastics emplaced at that time, uniquely large in the evolutionary history of the volcano, this indicates that the event marked a fundamental shift in geochemistry and activity at the volcano.

Németh & Cronin (2007a) follow the McCall et al. (1970) model of 'quiet' formation of the caldera due to magma drainage via flank fissures, and suggest that the 'tuff cone' model is a misinterpretation based on patchy field observations of a composite volcanic field. This may be a fair criticism of the sample set—the sample location maps of Monzier et al. (1991) and Picard et al. (1995) indicate only 6–8 locations for sampling of the tuff series: 4–6 sites on the NW coast, a single site on the southern coast, and one in the northeast—but other evidence suggests that the tuff cone model is valid. The significantly steeper angles of dip compared to the underlying shield (2–3°) suggest that the steeper central edifice is built of tuff rather than lava flows. Németh & Cronin (2007a) also suggest that the pyroclastic unit identified as a dacite is simply altered mafic material or reworked caldera sediment. However, mineral phase analyses of the dacite were published by Picard et al. (1995) and clearly demonstrate an

evolved silicic mineralogy, namely iron-rich olivine ($Fo_{42–44}$), two pyroxenes ($Wo_{41–42}En_{34–36}Fs_{21–24}$ and $Wo_{43–45}En_{36–40}Fs_{16–19}$), a TiO_2-rich titanomagnetite (12–14% TiO_2) and reverse-zoned andesine plagioclase ($An_{34–45}$) with An_{35} microlites in a glassy matrix.

It seems that the argument for quiet subsidence is based largely on incomplete evidence or incorrect assumptions, and the edifice morphology, petrographic evidence for varying involvement of water in the pyroclastic deposits, range of compositions of juvenile material, and marked geochemical shift associated with caldera formation all point towards a cataclysmic rather than a passive event.

Geochemistry of the tuff cone

The first sequence of the tuff cone is mainly medium-K dacite composition, with subordinate medium-K andesite and basalt; Sequences II through IV are medium-K to high-K basalts.

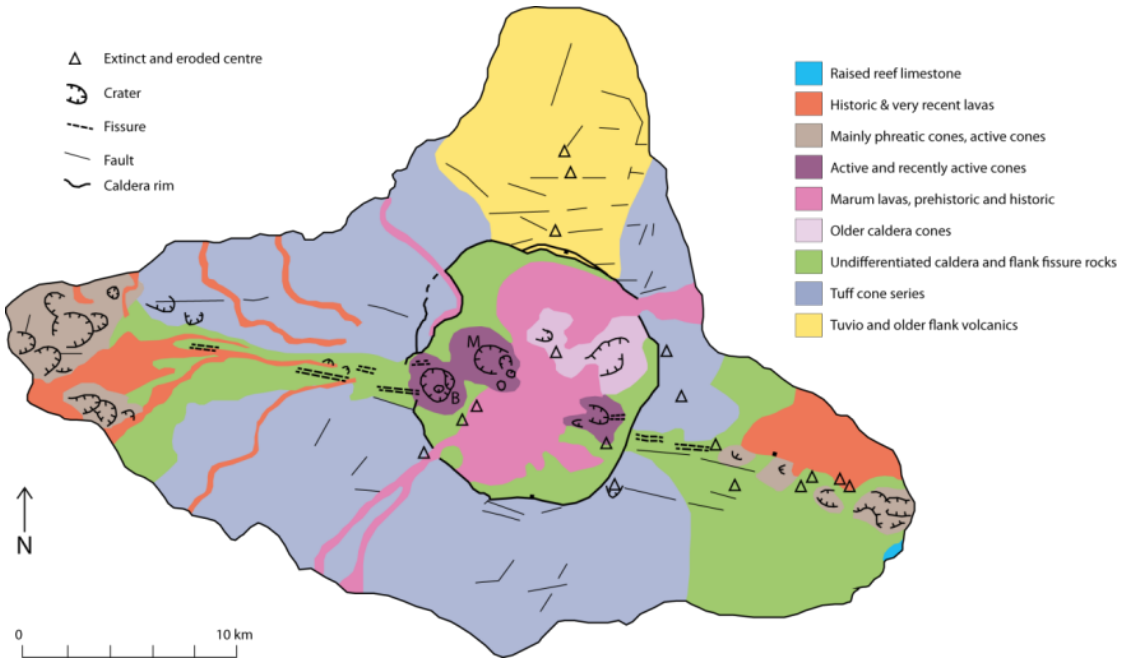

Figure 2.7 Geology and structural features of Ambrym, after Monzier & Robin (1996).

2.2.4 Post-caldera activity

Post-caldera activity occurs mainly from the two basaltic intracaldera cones, Marum and Benbow. Drainage of the episodic lava lakes in Marum and Benbow occasionally feeds lava flows, usually of a'a type, onto the caldera floor, and low-level eruption of basaltic scoria and ash is common. Lava flows sometimes extend beyond the rim of the caldera. Given the 50 AD

(± 100 y) date for caldera collapse, post-caldera ash and lava production must have at an earlier time been more prolific than at present, to account for the infilling of the ash plain and the construction of Marum and Benbow over the short period since caldera formation (McCall et al., 1970).

Other than this, post-caldera activity occurs on N105°E oriented flank fissures and intracaldera fractures (Fig. 2.7). The eruptive pattern seems to have undergone a major change from N10ºE to N105ºE alignment since the caldera formed (McCall et al., 1970), with fissure eruptions a feature since caldera formation, marking the axis of extension of the island to east and west. The N105°E alignment corresponds to the alignment of the Ambrym Fracture Zone (Fig. 2.1). The caldera centre lies at the approximate intersection of the old N10ºE alignment and the more recent N105ºE rifts. Lewolembwi maar, in the eastern part of the caldera, is located on a N105°E fissure.

Geochemistry of the post-caldera activity

Post-caldera activity is dominated by medium-K to high-K basalts, as well as a more evolved high-K trachyandesite erupted in 1986 in the eastern part of the caldera. Picard et al. (1995) report five samples of olivine-rich post-caldera medium-K basalts, and 25 samples of plagioclase-rich high-K basalts. Olivine-rich basalt flows have been found near the floor of Lewolembwi maar (Picard et al., 1995).

2.2.5 Historical eruptions

Marum and Benbow are characterised chiefly by quasi-continuous Strombolian activity, with infrequent sub-Plinian and Vulcanian activity and lava flows (Wiart, 1995). Flank eruptions along the N105°E-trending fissure system, small-volume lava flows from the crater, and phreatomagmatic eruptions near the coast have occurred a number of times in recorded history. Flank fissure eruptions are responsible for building the island out into its triangular shape towards the eastern- and western-most points. Activity also occurs along N105°E fissures within the caldera. Clusters of phreatomagmatic cones occur on the eastern and western points of the island where fissure magma interacts with seawater or low-lying wet sediment (Fig. 2.6). These cones are typically c. 1 km across with rims < 100 m high (Németh & Cronin, 2007b). The most recent of these cones date from eruptions in 1894 and 1913. Coral fragments in some of the cones, notably at Lonwolwol and in the Craig Cove area, illustrate seawater input during eruption.

Historical activity may be summarised, following Eissen et al. (1989), under five types, in approximate order of decreasing frequency: 1) Intermittent Strombolian-type activity, limited to the caldera with a small amount of extra-caldera ashfall, but no lava flows. This occurs almost every year. 2) Eruptions preceded by lava lake formation, usually involving a Vulcanian column, and followed by intra-caldera lava flows. 3) Similar to 2) but with lava overflow from the caldera (*e.g.*, 1863, 1913, 1942). 4) Flank fissure eruptions (1894, 1913, 1929, 1936), which may evolve towards type 5. 5) Pyroclastic cone formation on the lower flanks or in coastal areas (hydrovolcanic tuff cones), sometimes with lava flows (1888, 1915, 1929). A number of these modes may occur consecutively in the course of a single eruption, such as in 1913–14 and 1929.

The earliest historical record of eruption was made by Captain Cook in 1774 who noted that Ambrym was in eruption at the time of his exploration of the region (Beaglehole, 1961). The Global Volcanism Program lists 56 eruptions since 1774. Eruptions of Volcanic Explosivity Index (VEI) 2 or less dominate the record. There have been five VEI 1 eruptions, of which 4 are tentative ratings, thirty-seven VEI 2 eruptions, of which 3 are tentative ratings, seven VEI 3, one VEI 4+, one VEI 6+ (the caldera-forming event of 2 ka), three of uncertain VEI, and two uncertain (poorly-reported) events. Events >VEI 3 are briefly described below.

A ‘very large’ eruption reportedly occurred around 1820 on the west flank, estimated from the age of the elderly man who remembered it (Purey-Cust, 1896, cited in Gregory, 1917), involving radial fissure eruption, lava flows, and damage to land and property. In 1894 a fissure eruption of the west flank caused an unknown number of fatalities, and in 1913, also on the west flank, the Presbyterian mission hospital at Lonwolwol was blasted ‘sky-high’ by a phreatomagmatic eruption (Gregory, 1917), killing 21 people and injuring c. 121 (Witham, 2005). An elongate sea inlet now occupies the former site of the hospital. These eruptions were both rated VEI 3. The eruption of 1950 (VEI 4+) with a tephra output of 8×10^8 m^3, led to evacuation, property damage and lahars. In 1961 a VEI 3 event involved central vent eruption, flank eruption, and lava lake activity. Damage to land and property again occurred in 1972 with a VEI 3 eruption. Further VEI 3 events occurred in 1973 and 1980. An eruption of Benbow in February 1988 (VEI 3) launched an ash cloud c. 10 km high, but caused no reported damage (Scientific Event Alert Network Bulletin 13:02).

Fatalities and damage to property tend to be associated with flank eruptions, as the central vents are located in a broad unpopulated ash plain where they have little impact on the population, except for the adverse effects of strong degassing. The situation of the main centres of activity at such a remove from the general population, as well as the frequent

presence of tropical clouds around the summit, also means that lower-level activity may often go unrecorded.

The active intracaldera vents are characterised by high gas output (S, Br, I, F), with 'colossal' sulphur and bromine degassing quantitatively measured for the first time in early 2005 (Bani et al., 2009). Satellite (Ozone Mapping Instrument, OMI) data showed Ambrym to be the strongest global point source of SO_2 for the first months of that year (Bani et al., 2009), emitting up to 65% of the previously estimated annual global volcanic SO_2 output (Andres & Kasgnoc, 1998). Daily SO_2 images from OMI, available from May 2007 onwards, show Ambrym to be a regular high emitter of SO_2, compared to sporadic emissions from the other active Vanuatu volcanoes Ambae, Gaua and Yasur. In late 2009, the sulphur dioxide output of Ambrym was estimated at 15,000 tonnes per day using OMI measurements. By comparison within the arc, Yasur, which is also in a continuous state of low-level activity, very rarely registers on the satellite images for SO_2 emission, and even then at much lower concentrations. This suggests uniquely prodigious gas output from Ambrym compared to the rest of the arc.

Southeasterly trade winds blow the plume to the west where most of the islanders live. Historical reports document strong degassing prior to satellite or ground-based measurements. In February 1979, acid rain destroyed most of the vegetation on the SW of the island and caused skin burns to some islanders (Witham, 2005). High levels of HCl and sulphur compounds were reported in the gas plume; this produced acid rain which caused burning and yellowing of crops and pastures, and burning and gastric upsets to inhabitants (Cronin & Sharp, 2002). Acid rain was also measured in 1997 (Vetch & Haefali, 1997) and burning of vegetation was again recorded in 1989 (Eissen et al., 1989). Incidence of skeletal fluorosis among the island population (Crimp et al., 2006; Cronin & Sharp, 2002) attests to the ongoing high level of degassing. Measurements of fluoride levels in drinking water on Ambrym during a quiescent period exceeded the levels recommended by the World Health Organisation, posing a serious risk of chronic dental and skeletal fluorosis to the inhabitants (Cronin and Sharp, 2002). Crimp et al. (2006) measured drinking water fluoride contents of more than eight times the recommended limit, and observed 'severe' dental fluorosis in young children. The problem is exacerbated by collection of rainwater, which scavenges fluoride from the plume, for domestic use by the population. Mild fluorosis was evident in samples of bones and teeth from cattle, which contained approximately 2–6 times the normal level.

Chapter 3 Methods

3.1 Sample preparation

Eight lava samples (representing three lava flow events) and four scoria samples (representing two different periods of activity) were collected from Mbwelesu crater rim, the caldera ash plain, and outcrops near the western coast at Craig Cove during two separate field seasons in 2005 and 2008. Thin-sections, powder pellets and glass beads were made for each sample, and crystal separates picked from two basaltic scoria samples and one trachyandesite lava sample.

Preparation of experimental samples is discussed separately in the experimental chapter (Chapter 7).

3.1.1 X-Ray fluorescence

Scoria samples were washed thoroughly in deionised water and dried at 100 ºC in a drying oven overnight. Lava samples were trimmed of weathered rims using a rock cutting saw and crushed inside thick polythene bags using a geological hammer. The resulting fragments were milled to a fine powder in either an agate or tungsten carbide ring mill.

For major element analyses, 0.5–1.0 g of rock powder was mixed with ~8 g of 66:34 lithium tetraborate: lithium metaborate flux. Powder and flux masses were carefully noted to accurately calculate the dilution factor of the mixture. The flux/powder mixture was then fused in a platinum crucible using a Phoenix fusion machine, with 30 seconds pre-melt, 180 s melting time, 200 s swirling at temperature to ensure thorough mixing, and automatic pouring into platinum disc moulds. This sequence is designed to avoid sodium loss by heating slowly and at a low temperature. The flame is at 1250 ºC and temperature of melt is estimated at 800–900 ºC. The crucible was cleaned in citric acid solution in an ultrasonic bath between samples. Completed discs were then labelled and stored in a desiccator when not in use.

For trace element analyses, rock powder was mixed with Herzog Mahlhilfe wax tablets in the ratio 2.5 g rock to 1 wax tablet. To generate sufficient material for a powder pellet, 10 g rock powder and 4 tablets were used for each sample. These were milled together in a ring mill and pressed into pellets using a hydraulic press. The finished pellets were inserted into plastic collars for physical protection and ease of handling.

3.1.2 Thin sections

A total of 14 polished thin sections were examined during this study. 11 polished thin sections of 10 basaltic samples had been prepared prior to the beginning of this research project. Further sections of trachyandesite lava (1) and basaltic scoria (2) were prepared following collection during a field season in 2008. These samples were sent to the British Geological Survey for preparation as polished sections.

3.1.3 Crystal separates for melt inclusion study

Phenocrysts were separated from crushed rock samples by several methods:

- Picking under stereo microscope, for more easily-crushed samples and larger or more visible crystals, *i.e.*, large plagioclase and olivine crystals which stand out due to distinctive colour and morphology.
- Heavy liquid separation using polysodium tungstate, for smaller or glass-coated olivine crystals, which were difficult to see, and also for spinel.
- Dissolution of the matrix with hydrofluoric acid—this was necessary for the harder trachyandesite lava, which was resistant to heavy liquid separation due to the presence of oxide minerals in the matrix attached to phenocrysts.

The separated phenocrysts were set in Epofix^{TM} epoxy resin mounts each containing c. 20–50 crystals and polished to 1 μm to expose melt inclusions, without prior petrographic examination. No rehomogenisation was performed.

The polished samples were mapped in reflected light on an optical microscope and examined for cracks, bubbles or other post-entrapment features by a combination of reflected and transmitted light.

3.2 X-ray fluorescence

Whole-rock major and trace elements were analysed by X-ray fluorescence on a Brucker AXS S4 Pioneer spectrometer in the Geotechnical Microanalysis Laboratory at the University of East Anglia, using glass beads for major element analysis, and pressed powders for trace elements. Six repeats of each sample were run to confirm repeatability of the data.

The standards used for calibration are listed in Table 3.1. Detection limits for trace elements analysed were 10 ppm for Rb, Sr, Y, Zr, Nb, Th, U, Sc, V, Cr, Ni, Cu, Zn, Mo, and As, and 20 ppm for Ba, La, Ce, and Pb.

Standard	Description	Provider
1c	Argillaceous limestone	NIST
368	Dolomite	BCS
376	Potash feldspar	BCS
AC-E	Ailsa Craig Granite	SARM
AGV-1	Andesite, Guano Valley, OR	USGS
BCR-2	Basalt, Columbia River, OR	USGS
BE-N	Basalt, Essey-la-Côte, France	SARM
BX-N	Bauxite, Mine de Marou, France	SARM
DTS-1	Dunite, Twin Sisters area, WA	USGS
DTS-2	Dunite, Twin Sisters Range, WA	USGS
G-2	Granite, Bradford, RI	USGS
GS-N	Granite, Senones, France	SARM
GXR-1	Jasperoid, Drum Mountain, UT	USGS
GXR-2	Loams, Park City, UT	USGS
GXR-3	Hot-spring deposit, Humboldt County, NV	USGS
LKSD-3	Lake sediments, Calabogie Lake, Ontario	NRC
MRG-1	Gabbro, Mount Royal, Montreal, QC	NRC
SARM-2	Syenite, Phalaborwa, Transvaal	SACMT
STSD-2	Stream sediment, Hirok Stream, BC	NRC
UB-N	Serpentine, Col des Bagenelles, France	SARM

Table 3.1 Certified standards used for XRF measurements of Na, Mg, Al, Si, P, K, Ca, Ti, Mn & Fe in the University of East Anglia Geotechnical Microanalysis Laboratory. NIST=National Institute of Standards & Technology, US Department of Commerce. BCS= British Chemical Standards, Bureau of Analysed Samples Ltd, UK. SARM= Service d'Analyse des Roches et des Materiaux, CNRS, France. USGS= United State Geological Survey. NRC= Natural Resources Canada (CANMET). SACMT= South Africa Council of Mineral Technology.

3.3 Scanning electron microscope

The JEOL JSM 5900LV wavelength-dispersive scanning electron microscope in the Geotechnical Microanalysis Laboratory at UEA was used for reconnaissance and imaging of polished and carbon-coated thin sections and resin mounts.

3.4 Electron microprobe analysis (EPMA)

Mineral phase and glass compositions were determined on a Cameca-SX100 electron microprobe at the University of Cambridge Department of Earth Sciences. Natural samples, experimental glasses, and crystal separates were mounted in epoxy resin and polished to 1 μm by sequential polishing with SiC paper and diamond paste, with cleaning in an ultrasonic bath

between grit sizes. The samples were carbon coated in-house at the EPMA laboratory prior to analysis, to the standard thickness of 15–20 nm. Table 3.2 shows the number of analyses performed on the phases in each sample.

	Basalt					Trachyandesite
	Scoria			Intracaldera lava	Flank lava	Lava
Sample	AMB6	AMB7	AMB2007	AMB2	AMB10	AMB86
Plag	161	69	12	4	86	79
Cpx	46	14	5	6	8	49
Ol	28	1	6	-	13	49
Spinel	23	3	7	-	1	17
Glass	23	-	5	-	-	17
MI in ol	21	-	3	-	-	6
MI in sp	2	-	9	-	-	11
MI in cpx	29	-	-	-	-	-
Pyrrhotite	-	-	-	-	-	6
Apatite	-	-	-	-	-	12

Table 3.2 Summary table of electron microprobe analyses of natural samples, showing number of analyses performed on each constituent phase (after screening for quality) including matrix glass and melt inclusions. Plag=plagioclase, Cpx=clinopyroxene, Glass=matrix glass, MI=melt inclusions.

The accelerating voltage was 15 keV for all analyses. For minerals, the major elements were analysed using a 10 nA beam current and trace elements using a 100 nA beam current, except for clinopyroxene and pyrrhotite (Table 3.3).

K-alpha spectral lines were used for all elements except Sr in plagioclase (L-alpha, to avoid interference with Si), and Sr and Ba in apatite (L-beta, to avoid interference with rare earth elements).

For glass analyses, the beam current was 4 nA on Na, Mg, Si, Al, K, Ca, Ti, and Fe, and 60 nA on F, Cl, S, P, Cr, Mn, and Ni. Na was analysed first for the shortest count time (20 s) and low beam current to reduce the effects of alkali migration.

Beam sizes used were 10 μm for glass, 5 μm for apatite, 20 μm for pyrrhotite, and 0 μm (nominal; actual size of c. 3 μm) for plagioclase, clinopyroxene, olivine, and spinel.

Average detection limits for F, Cl and S in glass were ~320, ~60, and ~50 ppm respectively.

Matrix effects were corrected for using the Φ(ρz) matrix correction program XPHI.

	10 nA	20 nA	60 nA	100 nA
Plagioclase	Na, Si, Ca			Mn, Mg, K, Sr, Ti, Fe
Olivine	Na, Si, Mg, Fe			Mn, K, Ca, Ti, Al, Cr, Ni
Spinel	Fe, Ti			Ca, Cr, Mn, Ni, Si, Mg, Al
Apatite	P, Ca, Na			K, Cl, Ba, Mn, F, Mg, Fe, Sr, Si
Clinopyroxene	Na, Si, Mg, Fe, Ca		Mn, K, Ti, Al, Cr, Ni	
Pyrrhotite		Fe, S, Ni		

Table 3.3 Beam current used for analysis of mineral phases by EPMA.

Peak count times for elements analysed in each phase are given in Table 3.4. The count time is short for the major elements and longer for elements expected to occur in lower concentrations in a given mineral.

	20 s	30 s	60 s	90 s	180 s
Glass	Na, Mg, Si, K, Ca, Ti, Fe, Al	Cr, Mn, Ni	Cl, S, P		F
Plag	Na, Mg, Si, K, Ca, Ti, Fe, Al	Mn	Cl, S, P		F
Apatite	Na, Ca, P	Mg, Si, K, Fe, Cl, S, Mn, Ba, Sr		F	
Cpx	Na, Mg, Si, Ca, Fe	K, Ti, Al, Cr, Mn, Ni			
Olivine	Na, Mg, Si, Fe	K, Ca, Ti, Al, Cr, Mn, Ni			
Spinel	Ti, Fe	Mg, Si, Ca, Al, Cr, Mn, Ni			
Pyrrh		Fe, S, Ni			

Table 3.4 Count times (in seconds) on peaks for each phase analysed.

The standards used were jadeite (Na), periclase (Mg), diopside (Si, Ca), corundum (Al), potassium feldspar (K), rutile (Ti), fayalite (Fe), fluorite (F), halite (Cl), celestine (S), apatite (P), pyrite (for pyrrhotite analyses; S, Fe) and pure Cr, Mn, and Ni. The compositions of the standards are listed in Table 3.5.

	O	Si	Ti	Al	Fe	Mg	Ca	Na	Other
Jadeite	47.5	27.8	-	13.2	0.2	-	-	11.3	-
Periclase	39.7	-	-	-	-	60.3	-	-	-
Diopside	44.5	25.9	-	-	-	11.2	18.4	-	-
Corundum	47.1	-	-	52.9	-	-	-	-	-
Kspar	46.1	30.3	-	9.7	0.3	-	-	0.8	K: 12.8%
Rutile	40.1	-	59.9	-	-	-	-	-	-
Fayalite	31.4	13.8	-	-	54.8	-	-	-	-
Fluorite	-	-	-	-	-	-	51.1	-	F: 48.665%
Halite	-	-	-	-	-	-	-	39.3	Cl: 60.7%
Celestine	34.7	-	-	-	-	-	-	-	S: 17.4%, Sr: 47.1%, Ba: 0.8%
Apatite	38.1	-	-	-	-	-	39.7	-	F: 3.4%, P: 18.4%, Cl: 0.4%
Pyrite	-	-	-	-	46.5	-	-	-	S: 53.5
Cr	-	-	-	-	-	-	-	-	Cr: 100.%
Mn	-	-	-	-	-	-	-	-	Mn: 100.%
Ni	-	-	-	-	-	-	-	-	Ni: 100.%

Table 3.5 Compositions of EPMA standards used (atomic%).

3.4.1 Quality of analyses

Analytical error is estimated at c. 5% relative, except for Na for which error is estimated at c. 10% relative.

The quality of individual analyses was monitored using major element and cation totals. Analyses with major element totals less than 98.0 wt.% or greater than 101.5 wt.% have been discarded, as have those with cation totals calculated on the basis of 4 (olivine), 6

(clinopyroxene) or 8 (plagioclase) oxygens, which fall outside the ranges 3±0.02 (olivine), 4±0.05 (clinopyroxene[4]) and 5±0.025 (plagioclase). Spinel analyses were excluded from major element screening as they have totals of ~92–95 wt.% due to analysis of all Fe as FeO.

Apatite analyses were corrected by subtracting the oxygen equivalents of F and Cl from the analytical total (moles of F × $^{16}/_{38}$ and moles of Cl × $^{16}/_{71}$).

3.4.2 Ion migration and beam damage during EPMA

As the melt inclusions and matrix glasses are water-poor with relatively high Ca/(Na+K), they should not have been significantly affected by alkali depletion[5], particularly since the appropriate precautions were taken during analysis.

[4] Assumption of a cation sum of 4.00 for clinopyroxene is justified provided that the mineral contains less than 20% jadeite and > 0.7 calcium cations per unit formula, both of which criteria apply to all clinopyroxenes in this study (Cawthorne & Collerson, 1974).

[5] The extent of alkali depletion and depth to which it affects the sample both increase as Ca/(Na+K) decreases, and may increase with water content (Humphreys et al., 2006).

3.5 Secondary ion mass spectrometry (SIMS)

The Cameca ims-4f spectrometer at the University of Edinburgh was used over two five-day sessions to analyse CO_2, H_2O, Cl and F contents in 56 experimental glasses, 49 olivine-, clinopyroxene- and spinel-hosted melt inclusions and 14 matrix glass spots in natural basalt and trachyandesite samples. For some experimental runs (#15, #16 and #17), only selected charges (A, D and E; those being charges of moderate Cl content, very high Cl content, and combined Cl-F respectively) were analysed due to time constraints.

To avoid any possible effect of ion migration during electron microprobe analysis[6], melt inclusions were analysed first on SIMS and later in EPMA, although for some of the smaller inclusions, the large SIMS spot size did not leave a sufficient area of undamaged glass for subsequent EPMA analysis.

3.5.1 Sample preparation

Samples were mounted in Epofix™ epoxy resin, polished, and mapped in reflected light. Crystal mounts were polished for 10–20 seconds on 0.3 micron alumina to enhance melt inclusion relief. The polished sample mounts were gold-coated to a thickness of < 20 nm.

3.5.2 Analytical conditions

Analyses were performed using a 5 nA O^- primary beam with a nominal 10 keV impact energy generated by a duoplasmatron source. Sputtered ions were accelerated to 4.5 keV. Energy filtering was applied to reduce interference from molecular species—an offset of 50 eV was applied for ^{12}C measurements, and of 75 eV for ^{1}H, ^{35}Cl and ^{19}F measurements. ^{1}H, ^{35}Cl and ^{19}F were analysed using a 25 μm image field; ^{12}C was analysed using a 150 μm image field

Each analysis site was pre-sputtered with a 15 μm (nominally 50 μm) raster for 2 minutes to remove surface contamination, unless using a previously analysed spot, in which case a 30 s raster was considered sufficient. Peak positions were checked prior to each analysis. ^{12}C was analysed in 20 counting cycles (of which the first 10 were discarded) and

[6] Humphreys et al. (2006) examined the effect of EPMA irradiation on silicate glasses and found that migration of ions towards or away from electrons implanted by the beam causes enrichment or depletion of certain ions (particularly alkalis and the OH^- ion). Hydrous glasses are more susceptible to beam damage than anhydrous glasses (Morgan & London, 2005).

^{1}H, ^{35}Cl and ^{19}F were analysed in 10 counting cycles (of which the first 5 were discarded) at each site. Both measurements were performed on the same spot, with a shorter sputter time for H-Cl-F due to pre-sputtering already carried out prior to ^{12}C analysis. Repeat analysis of ^{24}Mg and ^{30}Si was used to check for internal consistency. Analyses with low Si counts or anomalous Mg counts were rejected.

Routine detection limits for volatiles and halogens were c. 0.02 wt.% H_2O, < 5 ppm CO_2, < 1 ppm F and Cl.

Background counts were monitored by regularly analysing volatile-free standards, quartz, or olivine host crystals. Background counts were averaged for each day's session and subtracted from the raw data.

Carbon backgrounds were typically 50–80 ppm with a residual, after correction, of about 10 ppm. Occasional anomalous results occurred (two out of 43 analyses of CO_2-free experimental glasses returned CO_2 contents above 100 ppm) but are not believed to represent unreliability of the dataset as a whole. In general, if the vacuum is poor, results will show an overall high concentration and not fall below a certain level, e.g., 200 ppm (R. Hinton, pers comm, 2015).

Some analyses of CO_2-free experimental glasses suffered the effects of epoxy outgassing (verified by correlation with poor vacuum pressures), giving spurious high-CO_2 data. Subsequent re-analysis of these samples gave CO_2 results around background or lower.

3.5.3 Standards and corrections

Repeat analyses of standards were performed throughout the two analysis sessions. No secondary standards were used. Two basalt glass standards, TPF and CFD, were used as standards for H_2O (Table 3.6).

Rhyolite standards NIST SRM-610 (Jochum et al., 2011), RB480 and RB497 (Brooker et al., 2000) were used as standards for F, Cl and CO_2, as appropriate basaltic standards were not yet in place in the ion microprobe laboratory. Appropriate basaltic standards (Table 3.6) were later analysed, and the results were used to apply a correction to the concentrations calculated using the rhyolitic standards. Calibration curves for carbon were generated by plotting $^{12}C/^{30}Si$ (corrected for $SiO_2^{standard}$ vs. SiO_2^{sample}) against CO_2 concentration. A representative calibration curve (of five used), constructed using the basalt standards listed in Table 3.7, is shown in Figure 3.1.

	H_2O		CO_2		
	TPF	CFD	Sims[a]	Pichavant[b]	Shishkina[c]
SiO_2	46.1	47.95	48.6	49.4	50.07
TiO_2	1.02	0.57	2.01	0.79	0.9
Al_2O_3	22.1	18.45	16	15.75	18.36
FeO	0.27	5.61	10.4	7.67	9.35
MnO	-	-	0.17	0.15	0.17
MgO	9.8	11.19	7.01	7.96	7.02
CaO	10.6	11.46	9.8	12.73	11.32
Na_2O	5.42	2.19	3.16	2.27	2.45
K_2O	-	-	0.63	1.85	0.22
P_2O_5	-	-	0.31	0.43	0.15
H_2O	4.63	1.07	-	-	-
LOI	n.d.	n.d.	n.d.	0.62	n.d.
Total	-	-	98.09	99.1	100

Table 3.6 Major element compositions of basaltic standards used to calibrate H_2O and CO_2 analyses. [a]Sims et al. (2002), MORB glass sample, analysed by XRF. [b]Pichavant et al. (2009) experimental starting composition, analysed by ICP-AES. [c]Shishkina et al. (2010) starting composition analysed by XRF (normalised to 100).

Sample	CO_2 (ppm)	Analytical method	Sample type and reference study
2390-5 2768-6	144 183	Cameca IMS 6f SIMS	East Pacific Rise MORB; Le Roux et al. (2006).
St1 St2 St6	691±11 1136 ±74 871±16	Combustion and IR spectroscopy	Basalt from Mutnovsky volcano; Shishkina et al. (2010).
17-2 S5-14 S4-13 S2-3	2552±192 1284 922 636	FTIR	Stromboli golden pumice; Pichavant et al. (2009).

Table 3.7 CO_2 contents and analytical method for basaltic glasses used in SIMS CO_2 calibrations.

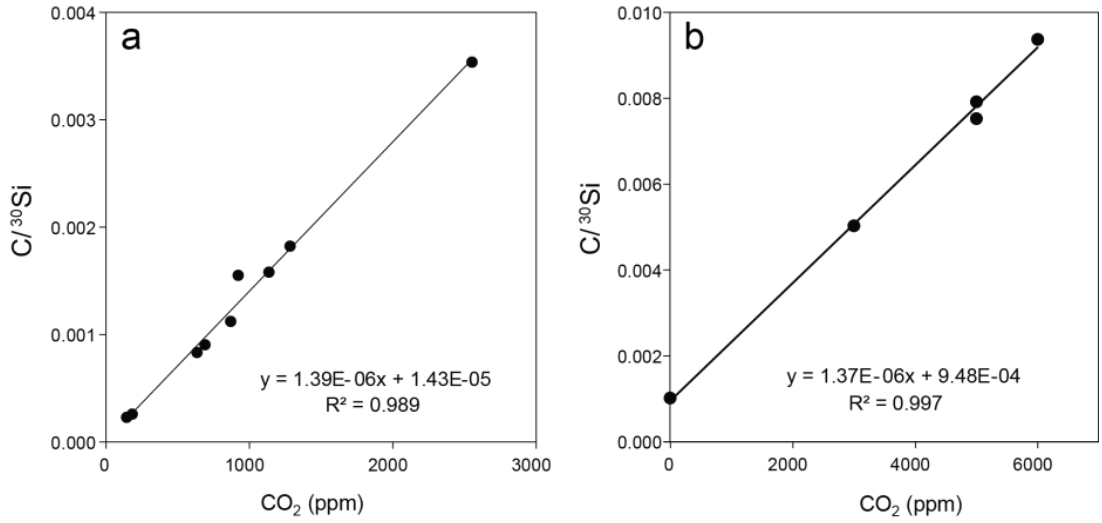

Figure 3.1 CO_2 calibration curves for natural basaltic glasses (a) and experimental basaltic glasses (b). Experimental Glasses manufactured by M. Berg. In this curve SiO_2 has been corrected to an arbitrary value of 50 wt.% to represent a typical basalt. Calculations for individual samples are made using individual SiO_2 contents.

1-sigma errors based on repeat analyses of standards are of the order of 6% for CO_2, and 2–10% for H_2O, decreasing as dissolved H_2O contents increase (from 0.24–4.7 wt.%). Fluorine errors are better than 3% at 700 ppm, up to 10% at 100 ppm, and Cl errors are 1% at 5000 ppm, rising to 5% at 130 ppm.

Chapter 4 Petrology and geochemistry of recent samples: implications for magma storage

4.1 Introduction

This chapter presents petrological descriptions and analyses for a suite of recently-erupted products from Ambrym volcano. The objectives are to interpret the magmatic history recorded by each sample type, and to determine relationships between samples, such as whether they derive from a common parental magma, and to determine the processes involved in their petrogenesis, such as fractional crystallisation or magma mixing. These investigations, in conjunction with examination of the eruptive history of the volcano and previous studies, will be used to construct a model of the magma storage system.

4.1.1 Geochemistry of Ambrym volcano

Ambrym volcano is characterised by four distinct volcanic phases (Fig. 4.1; Picard et al., 1995): the earliest (Pleistocene) edifices, Tuvio, Vetlam and Dalahum, in which the most primitive products are found, with 12.8 wt.% MgO and 49.1 wt.% SiO_2; the significantly less primitive basaltic shield with ≤ 5.2 wt.% MgO; a basaltic-to-rhyodacitic pyroclastic series (tuff cone) associated with caldera subsidence ~2 Ka; and post-caldera, primarily basaltic activity, from 2 Ka to present. Samples analysed in this study derive from the post-caldera suite.

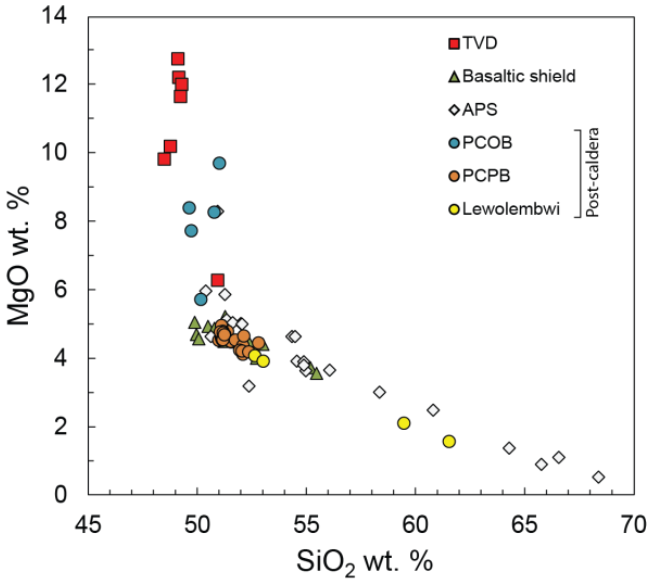

Figure 4.1 MgO vs. SiO_2 for the four major volcanic phases of Ambrym (data from Picard et al., 1995), from oldest to youngest in key (post-caldera products are Recent). TVD=Tuvio-Vetlam-Dalahum edifices. APS=Ambrym Pyroclastic Series (tuff cone). PCOB=post-caldera olivine basalts. PCPB=post-caldera plagioclase basalts. Lewolembwi samples are from the eastern part of the caldera. Note significant overlap between shield basalt, PCPB and APS compositions; partially obscured by the high number of datapoints near the kink in the trend.

Samples taken from Ambrym volcano are compositionally bimodal, with peaks at 50–53 wt.% SiO_2 and 66 wt.% SiO_2 (Picard et al., 1995; Fig. 4.2a). The system is primarily basaltic (Fig. 4.2b). Trachyandesite erupted in 1986 is the sole silicic post-caldera product, and one of only a handful of evolved products throughout the entire history of the volcano. Andesitic to rhyodacitic pyroclastics are found in the (mainly basaltic) tuff cone, and a glassy andesitic lava flow believed to relate to caldera formation occurs at the northern rim of the caldera (Picard et al., 1995). The 1986 trachyandesite is the only recorded relatively evolved product not related to tuff cone or caldera formation.

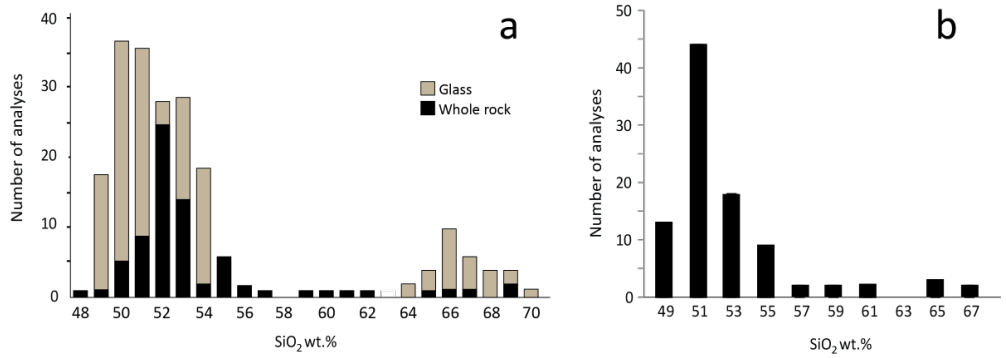

Figure 4.2 a: Histogram of 137 glass analyses from vitric clasts of Ambrym Pyroclastic Series and 68 whole rock analyses from the entire volcano; class interval 1% (Picard et al., 1995). **b:** Histogram of 96 whole rock analyses from entire volcano, data from Picard et al., (1995), Robin et al. (1993), and Gorton (1977). Class interval=2%, label represents median value (e.g., 49 represents 48–50 wt.%).

4.1.2 Previous work

The petrography and mineralogy of Ambrym eruptive products have previously been described only in brief (Gorton, 1977; Picard et al., 1995) or on the outcrop to hand sample scale (Robin et al., 1993). The primary petrological reference for Ambrym is Picard et al. (1995), which reports whole rock major and trace element data for 80 samples covering the entire volcanic succession, from ancient pre-shield edifices to post-caldera lavas (see Chapter 2 for a detailed volcanological history). Picard et al. (1995) identify three trends: a medium-K (MK) to high-K (HK), tholeiitic-to-calc-alkaline basaltic trend, and two basaltic to dacitic/rhyodacitic trends, one MK and one HK.

Published mineralogical descriptions of Ambrym samples show a predominance of plagioclase-rich basalts with a typical phenocryst phase assemblage of bytownite/labradorite, diopside/augite, olivine, and spinel (Gorton, 1977; Marshall, 1914; Picard et al., 1995). Less common clinopyroxene-rich and olivine-rich basalts are also reported. Picard et al. (1995) briefly describe the mineralogy of the entire volcanic succession, from the ancient Tuvio-

Vetlam-Dalahum (TVD) volcanoes, through the basaltic shield and the tuff cone sequence, to the post-caldera lavas; these descriptions are summarised in Table 4.1. Plagioclase displays normal zoning in all samples except the dacitic member of the tuff cone.

	Plag[1]	Cpx	Ol[2]	Fe-Ti ox	Groundmass	Texture
TVD (basalts, LK to MK)	82–55	Diopside–augite	83–79	Yes	Plag, px	GP, PA
Basal shield (basalt, MK to HK)	91-67	Diopside–augite	84–51	Yes	Microlitic	Isolated or GP plag phenocrysts
Tuff cone, andesitic to rhyodacitic (MK)	45–34, reverse zoned	$Wo_{41–42}En_{34–36}Fs_{21–24}$ and $Wo_{43–45}En_{36–40}Fs_{16–19}$	44–42 (rare; MP)	12–14% TiO_2	Vitric glass, rare andesine microlites An_{35}	
Tuff cone, basaltic (MK to HK)	91–80	$Wo_{43–44}En_{40.5–44}Fs_{12–16}$	80–72	4–6.5% TiO_2	Glassy	
Post-caldera ol basalts (MK)	83–66 (rare phenocrysts)	Diopside–augite	79–58 (phenocrysts)	Not mentioned	Microlitic, ol-($Fo_{42–45}$) and cpx- rich	
Post-caldera plag basalts (HK)	92–65	Diopside–augite	78–55	Yes	Microlitic, plag rich $An_{70–60}$	GP

Table 4.1 Mineral compositions and descriptions from Picard et al. (1995) for the entire volcanic succession of Ambrym, in order of oldest to youngest. TVD=Tuvio-Vetlam-Dalahum (ancient pre-shield cones). GP=glomeroporphyritic. PA= plagioclase aggregates. MP=microphenocrysts. [1]An mole% of plagioclase. [2]Fo mole% of olivine. MK=medium-K_2O, HK=high-K_2O.

Marshall (1914) describes three 'basaltic' lava samples from flank eruptions at the western end of the island; whole rock analyses do not appear to have been carried out. According to Marshall (1914), the most common type of lava in that locality contains large (up to 1 cm) rounded aggregates of bytownite with magnetite, glass and olivine inclusions, smaller augite and olivine phenocrysts, and groundmass bytownite, augite/diopside and olivine ± magnetite octahedrons, in magnetite- or ilmenite-bearing glass. Another sample is dominated by augite and magnetite-dust-bearing olivine phenocrysts with bytownite-labradorite microphenocrysts in a groundmass of feldspar, augite and magnetite. This description shows that lavas at the western end of the island feature a similar phase assemblage to intracaldera basalts but are dominated by large bytownite aggregates, and appear to have a different oxidation history, as demonstrated by magnetite dust in olivine, and matrix-glass ilmenite; ilmenite is not reported in any other sample from Ambrym.

4.1.3 Magma evolution

The sole published model for the evolution of magma composition at Ambrym volcano is found in Picard et al. (1995), and models derivation of whole-rock major-element trends by fractional crystallisation using a least-squares mixing program (Mason, 1987). Details of the calculations are given in Table 4.2. Picard et al. (1995) also note that fractionation plays an important role, as indicated by a great variation in K_2O over small intervals of $[La/Yb]_n$.

Trend	Stage	Parent melt	Fractionating phases				Residual melt	SSR
TVD to APS1	1	TVD olivine basalt	An_{70} (21%)	Augite (17%)	Fo_{81} (16%)	Fe-Ti oxide (0.1%)	APS1 plag basalt	0.06
	2	Plag basalt	An_{76} (30%)	Augite (26%)	Fe-Ti oxide (9%)	Fo_{79} (4%)	APS1 rhyodacite	0.02
APS2		Basaltic glass	An_{65} (31%)	Augite (23%)	Fe-Ti oxide (9%)	Fo_{79} (3%)	Rhyodacitic glass	
Basal shield	1	Olivine basalt	Augite (15%)	Fo_{79} (7%)	An_{72} (6%)	Fe-Ti oxide (1%)	Plag basalt	0.01
	2	Plag basalt	An_{72} (16%)	Augite (9%)	Fe-Ti oxide (3%)	Fo_{75} (1%)	Andesite	0.07
Post-caldera	1	High-Mg olivine basalt	Augite (9%)	Fo_{79} (6%)	An_{72} (5%)		Low-Mg olivine basalt	0.05
	2	Low-Mg olivine basalt	An_{72} (14%)	Augite (13%)	Fe-Ti oxide (2%)	Fo_{79} (2%)	Plag basalt	0.01
	3	Plagioclase basalt	An_{68} (25%)	Augite (17%)	Fe-Ti oxide (8%)	Fo_{79} (1%)	Andesite	0.04

Table 4.2 Results of fractional crystallisation modelling from Picard et al. (1995) for three main identified trends: 1) Medium-K ancient TVD basalts to earliest tuff cone deposits (Ambrym Pyroclastic Series 1; APS1). 2) Basal shield series, 3) Post-caldera series. SSR=sum of squares of residuals.

Each of the three main trends modelled have a first stage with sharply decreasing MgO and increasing FeOt, TiO_2 and K_2O (refer ahead to Section 4.3 for variation diagrams) which Picard et al. (1995) modelled by fractionation of olivine ($Fo_{79–81}$), plagioclase ($An_{70–72}$), clinopyroxene and Fe-Ti oxide, and a second (more evolved) stage showing a shallower decrease of MgO, and decreasing FeOt, TiO_2 and CaO, which Picard et al. (1995) modelled by fractionation of olivine (Fo_{75-79}), plagioclase ($An_{72–76}$), clinopyroxene and Fe-Ti oxide.

Generation of the more differentiated rocks (Ambrym Pyroclastic Series sequence 2, and Stage 3 of the post-caldera trend) are modelled by fractionation of plagioclase (An_{68-65}), clinopyroxene, Fe-Ti oxides and minor olivine (Fo_{79}).

This model has some weaknesses. Modelled forsterite and anorthite compositions are incongruous with their host rock or relative position in the modelled sequence in several cases. For example, fractionation of An_{76} and Fo_{79} is invoked in order to generate rhyodacite,

from a plagioclase basalt itself generated by fractionation of An_{70} and Fo_{81}: these are incongruously primitive mineral compositions to directly precede a rhyodacite, and this sequence also requires the evolved basalt to revert to crystallisation of higher-anorthite plagioclase as it evolves towards a rhyodacitic composition, while the olivine fractionating from a 6 wt.% MgO plagioclase basalt has become only marginally less forsteritic than that crystallising from a high-MgO (12 wt.%) basalt earlier in the sequence.

In addition, the model relies on large amounts (8–9%) of Fe-Ti oxide fractionation to generate the more silicic rocks. Such high percentages of Fe-Ti oxides are not observed: phase percentages are not given but normative oxide minerals (magnetite, haematite and ilmenite) sum to 1.5–6%, with the lowest proportions occurring in the most evolved compositions, where the model relies most heavily on them. Fe-Ti oxides have a large influence on major-element modeling due to their high Fe content, and small changes of proportions can give a "mathematically correct but geologically irrelevant" result (Defant & Nielsen, 1990). It is possible, however, that these have been removed via density settling.

It is evident that while the Picard et al. (1995) model can mathematically reproduce observed compositions, some of the proposed mechanisms are geologically unrealistic. There is a clear need for a more rigorous model of magma evolution at Ambrym volcano, taking mineral compositions and petrographic evidence into account.

4.1.4 Magma pathways

The volume of historically erupted magma at Ambrym volcano is low, but the presence of quasi-permanent lava lakes and long-lived high gas output require sustained heat and gas fluxes. Such activity may imply endogenous growth (Francis et al., 1993; Oppenheimer and Francis, 1998), or magma recycling (Harris et al., 1999), with heat transfer from basaltic recharge.

The morphology of the island clearly records significant growth along the fissure zones extending to the east and west. Flank eruptions, extending towards the eastern and western extremities, in some cases propagating offshore (see Section 2.2.5), demonstrate that magma frequently migrates through the edifice as well as ascending through the central vents. Other volcanoes with persistent lava lakes and flank fissures show a direct link between summit and flank magma sources—such as Nyiragongo volcano, where a lava lake active for 50 years drained after a fissure eruption in 1977 (Tazieff, 1977), and Nyamuragira volcano, where a lava lake was drained by a flank eruption in 1938 (Verhoogen, 1948). There are no reports of

lava lake drainage following flank eruptions in the historical record of Ambrym; flank eruptions typically occur in conjunction with increased activity (paroxysms) at the central vents. This suggests that flank eruptions are driven by increased activity throughout the entire system rather than drainage of the central conduit. The last flank eruption was in 1937, so opportunities to observe the response of the central vents to flank eruptions have not occurred during the course of modern monitoring efforts. The association of heightened central vent activity with flank eruptions suggests that during these events, heightened pressure in a common source drives magma towards both flanks and summit vents. The distinct mineralogy of the flank lavas—notably, the high content of large plagioclase glomerocrysts or megacrysts—suggests that the flank lavas pass through a region of plagioclase cumulates or stagnant plagioclase-rich magma en route to the surface, or are driven by glomerocryst-rich magma recharge.

Surface expressions of recent magmatism appear to be less common on the eastern arm of the island (Fig. 4.3), although this may be an artefact of lower reportage or fewer field measurements due to lower population and difficulty of access in that sector. The approximately equal size of the two flanks shows that growth has been equal for most of the lifetime of the fissure system. The 1986 trachyandesite storage region may be a region where magma stalls, reducing eastern flank surface activity, and enabling differentiation of basaltic magma to trachyandesitic composition. An alternative formation mechanism for the trachyandesite melt is the development of lenses of silicic melt in the volcanic crust by remelting of basaltic crust with heat supplied by dyke intrusion (e.g., Gunnarsson et al., 1998).

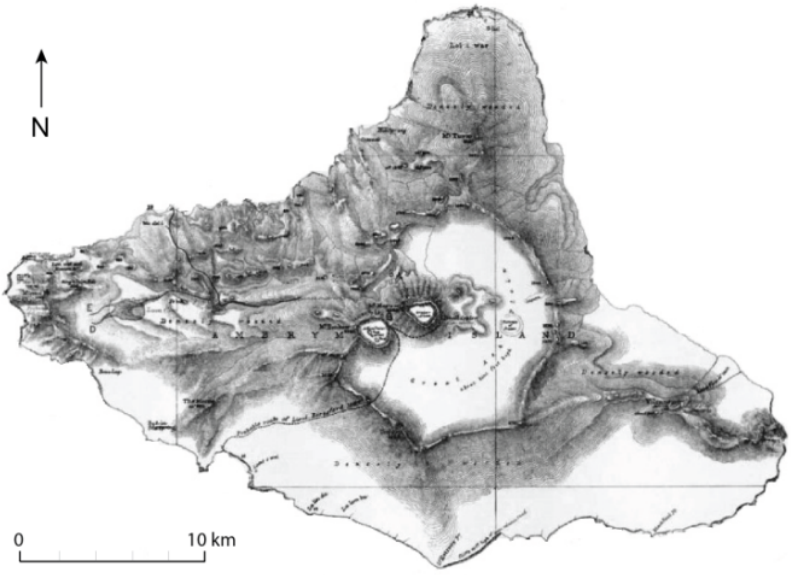

Figure 4.3 Relief map of Ambrym (Purey-Cust, 1896) showing **a** dense coverage of flank eruption sites in the west to north-west sector and significantly fewer in the east. The apparent lack of eruptive activity along the south and north-east coasts may be an artefact of poor survey coverage in those areas.

4.1.5 Existing constraints on magma storage conditions

Existing constraints on magma storage conditions at Ambrym primarily derive from geophysical investigations and seismic studies.

A study of very long period tremor (VLPT) from July to November 2000 (Legrand et al., 2005) demonstrated the existence of two distinct tremor sources, associated with the western (basaltic) and eastern (trachyandesitic) intracaldera vents respectively (Fig. 4.4). The tremor source associated with current intracaldera basaltic activity is located c. 3.7 km below the western part of the caldera floor, and the eastern source is c. 3.5 km below the eastern part of the caldera floor. Assuming a uniform crustal density (ρ) of 2700 kg m^{-3}, this translates to a pressure of 98 MPa for the basalt storage region and 93 MPa for the trachyandesite storage region. Allard et al. (2015) report a cluster of melt inclusion entrapment pressures around 130 ± 20 MPa (~4–5 km), based on dissolved H_2O-CO_2 contents, which may relate to the same magmatic activity captured by VLPT recordings.

The VLPT data also reveal that the source beneath the eastern part of the caldera is more active despite a lack of surface activity other than the 1986 trachyandesite eruption, in contrast to the persistent and visible surface activity at the basaltic cones in the western part of the caldera. This may be explained by the correspondence of the study period to a phase of low activity at Marum and Benbow, during which no thermal alerts were recorded by the Moderate Resolution Imaging Spectroradiometer (MODIS*)* aboard the NASA Terra satellite.

Legrand et al. (2005) defined these tremors as ‘quasi-continuous non-destructive sources’—a confined ‘breathing’ or shifting activity of magma in the system. The dominance of either source was observed to switch from one to the other on a timescale of months: the eastern source was dominant from July to October 2000, and the western source became dominant in November 2000, shortly after which the study period ended. The two sources seemed to be related in such a way that only one or the other was active at any given time during the study.

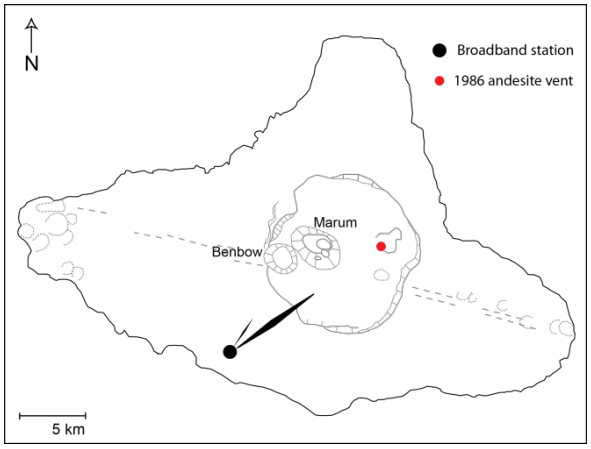

Figure 4.4 Polarisation directions of very long period tremor sources recorded by Legrand et al. (2005) from a broadband station located near the SW coast (filled black circle). The long black arrows indicate the polarisation directions; the length is proportional to the number of events. Figure simplified from Legrand et al. (2005).

The active basaltic intracaldera region consists of two cones, Marum and Benbow (Fig. 4.4). Acoustic survey (Bani et al., 2010) reveals that strong activity at Marum is preceded by increased acoustic events at both Marum and Benbow, indicating a shared shallow plumbing system. During phases of high Strombolian activity, Marum displays variation between Strombolian explosions and quiescence, whereas Benbow displays continuous Strombolian explosions, indicating that Benbow lies closer to the shared magma source. Vergniolle et al. (2013) suggest that a shared magma reservoir in which the roof slopes towards Marum can account for the continuous low-level activity at Benbow, and alternation between quiescence and activity at Marum; for example, following the end of a Strombolian phase in October 2008, degassing resumed immediately at Benbow, but only after a period of 12 days at Marum.

The results of a magnetic survey (McCall et al., 1970) show the upper surface of an anomalous source body beneath the caldera at c. 300 m above sea level, suggesting a perched magma chamber beneath the active cones.

At deeper levels, U.S. Geological Survey earthquake data for the period 1975–2013 show two major clusters of earthquakes, between 10–35 km and 170–210 km depth below Ambrym (Fig. 4.5a). A series of seismic gaps indicated by earthquake locations may record levels of magma storage within the shallow crust (Fig. 4.5b).

Blot (1981) designated earthquake activity at 150–200 km depth as the ‘deep root’ of the volcano, based on correlation of earthquakes from this depth with increased eruptive activity. Blot (1981) noted that delay times between deep earthquakes and eruptions clustered at around 200 days and 315 days, and suggested that these may relate to explosive or gas-rich events, and magma ascent and lava flows, respectively—adding that paroxysmal activity often occurs on a timescale of months following the beginning of an active phase with increased gas output. These observations indicate that deep seismic events are related to magma release.

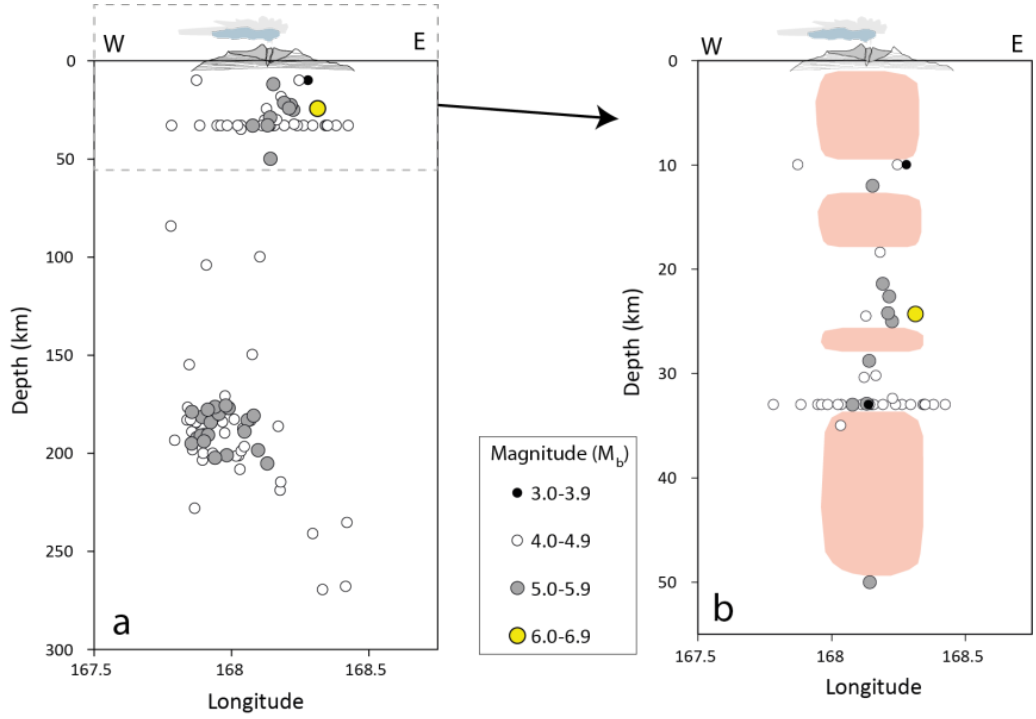

Figure 4.5 Earthquakes below Ambrym during the period 1975–2013, displayed on an east-west transect. Earthquakes located by the U.S. Geological Survey National Earthquake Information Center. Magnitude is in M_b; some values have been converted from M_w or M_S following Scordilis (2006). Earthquake locations are located by longitude; the illustration of the volcanic edifice is also matched to actual longitudinal position. a) Data to 300 km depth. Ambrym volcano is shown with vertical exaggeration of ×6 compared to the sub-sea-level depth scale. The dashed box outlines the area shown in panel b. b) Shallow earthquake data (0–55 km). Pink areas show inferred hot zones where magma storage may occur. Ambrym volcano is shown to scale with sub-sea-level depths.

Picard et al. (1995) calculated segregation depths of the source magmas by plotting sample compositions on the Ol–Jd+CaTs–Qz molecular normative projection (Jaques & Green, 1980; Falloon & Green, 1988; Falloon et al., 1988), indicating that the most primitive basalts of Ambrym (found in the oldest edifices, Tuvio-Vetlam-Dalahum) last equilibrated at ~45–60 km (1500–2000 MPa); the basal shield volcano magma last equilibrated at c. 30–35 km depth (1000–1200 MPa); and post-caldera magmas last equilibrated at depths of 30–45 km (1500–1000 MPa). This approximately correlates with the ~10–35 km earthquake cluster visible in the USGS data (Fig. 4.5).

Optical pyrometry measurements of the quasi-permanent lava lake at Marum record temperatures of up to 964 °C (Vetch & Haefali, 1997). No other measurements that constrain temperatures have been made.

These studies provide broad constraints on the configuration of the magma system, from a deep root at 150–200 km (Blot, 1981), to magma segregation at 60–30 km (Picard et al., 1995), the likely presence of magma at 50–35 km, ~27 km and ~15 km (earthquake data; Fig.

4.5), and some kind of activity clustered around 3–4 km (Allard et al., 2015; Legrand et al., 2005). Existing data also show that the 1986 storage region has indicators of unrest and movement, and is somehow linked to activity at the Marum-Benbow vent complex (Legrand et al., 2005), which is a two-vent expression of a single sloping shallow magma chamber (Bani et al., 2010; Vergniolle et al., 2013).

4.2 Samples

Twelve rock samples representing the main post-caldera lava compositions and modes of activity at Ambrym, spanning the period 1929 to 2007, were analysed in this study:

- Mbwelesu scoria/reticulite: four samples of scoria/reticulite from Strombolian activity in 2005 and 2007 at Mbwelesu (the main active vent in Marum, one of two active basaltic cones in the western part of the caldera; Fig. 4.6). Three of the samples were erupted in 2005: one is glassy (AMB6) and two are microcrystalline (AMB7, AMB8). The last sample is a reticulite ejected in 2007 (AMB2007).
- Niri Mbwelesu Taten lava: five samples from two intracaldera lava flows erupted in 1988 and 1989, originating from Niri Mbwelesu Taten, a smaller adventitious vent on the flank of Marum.
- Trachyandesite lava: one sample of lava from an apparently monogenetic lava flow in the eastern region of the caldera.
- Craig Cove lava: two samples of lava from flank eruptions near the west coast.

Sample names and details are given in Table 4.3 and sample collection locations are indicated in Figure 4.6. Sample preparation and analytical techniques are detailed in Sections 3.2–3.4. Samples AMB1–10 were collected by Dr. Ben Mason during a 2005 field season focused primarily on gas plume analysis. Samples AMB86 (trachyandesite) and AMB2007 (scoria/reticulite) were collected by F. Sheehan during a three-day field season in 2008, in which collection of a trachyandesite sample was the main objective.

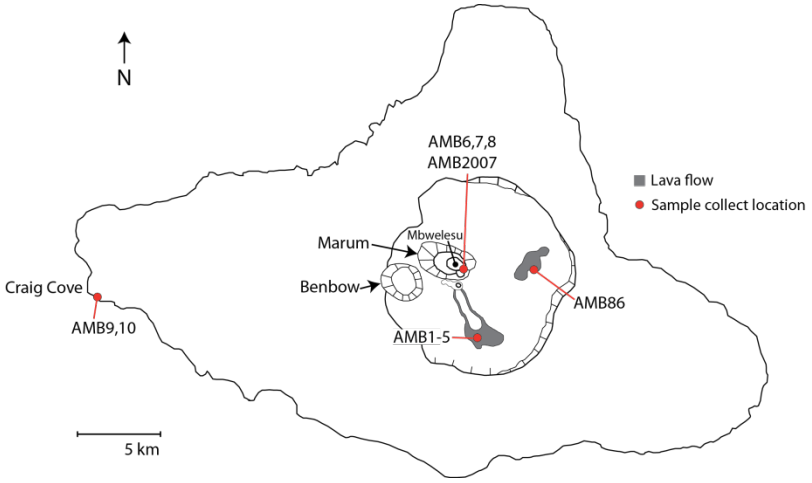

Figure 4.6 Simplified map of Ambrym showing sample locations. Sample details are given in Table 4.3 below.
See Figs. 2.6 and 2.7 for detailed geomorphology and geology.

Sample	Rock type	Eruption date	Collection location	Collected
AMB1–3	Basaltic lava flow	1988/89	Ash plain south of Marum	2005
AMB4,5	Basaltic lava flow	1988	Ash plain south of Marum	2005
AMB6–8	Basaltic scoria	?July 2005	Mbwelesu crater rim	2005
AMB2007	Basaltic-andesitic scoria	2007	Mbwelesu crater rim	2008
AMB9	Trachybasaltic lava flow	1929	Western tip of island	2005
AMB10	Basaltic-trachyandesitic lava flow	Pre-1929	Western tip of island	2005
AMB86	Trachyandesitic lava flow	1986	16°15’37S 168°10’05E	2008

Table 4.3 Samples described in this study; sample name, rock type, eruption date, collection location and collection date.

4.3 Bulk geochemistry

The majority of the samples (eleven out of twelve) are high-K, high-Al, low-Ti basalt to basaltic (trachy)andesite, with SiO_2 contents of c. 50–53 wt.%, and $Na_2O + K_2O$ contents of 4.4–5.2 wt.%. The 1986 lava from the eastern part of the caldera is a high-K trachyandesite, with 59.9 wt.% SiO_2 and 7.7 wt.% $Na_2O + K_2O$ (Table 4.4; Fig. 4.7). The samples plot just within the sub-alkaline field of the total alkali and silica (TAS) diagram as defined by Irvine & Baragar (1971). All major-element data (wt.%) have been normalised to 100%, LOI-(loss on ignition) free, with all iron as FeOt.

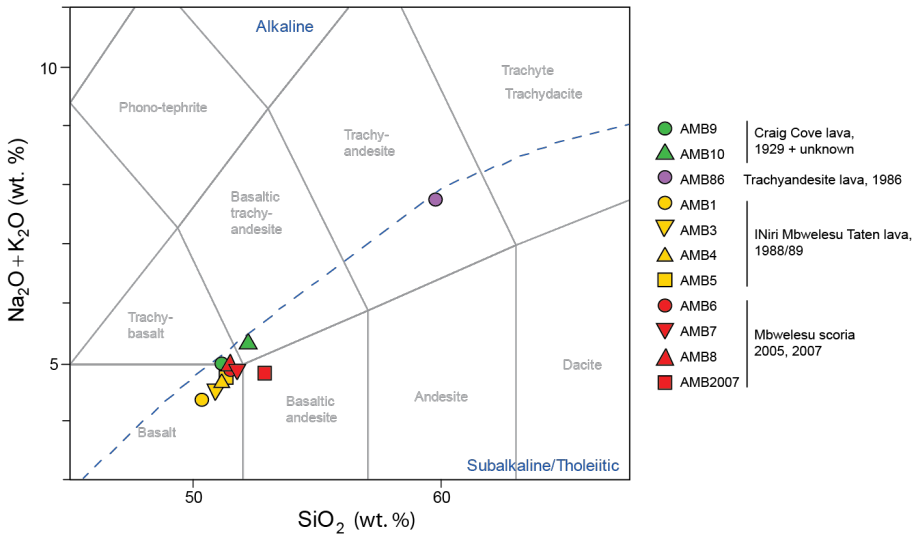

Figure 4.7 Whole-rock compositions for all samples (XRF data, normalised to 100%). Classification diagram after LeBas et al. (1986). The dividing line between alkaline and subalkaline series is that of Irvine & Baragar (1971).

The Ambrym magma series displays characteristics of both tholeiitic and calc-alkaline series, with initial Fe- and Ti-enrichment but crossing back into the calc-alkaline field (Fig. 4.8).

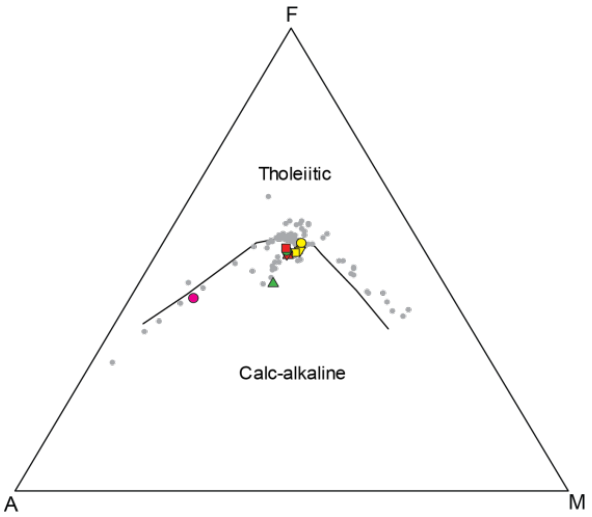

Figure 4.8 Alkali-FeO-MgO plot (after Irvine & Baragar, 1971), using normalised wt.% values, for all samples. Symbols as in Fig. 4.6. Grey datapoints show published data covering the entire volcanic succession (Picard et al., 1995; Robin et al. 1993; Gorton, 1977).

Whole-rock data shows that scoria samples ejected during lava lake activity are slightly more evolved than 1988/89 lava flow samples (Table 4.4). The Niri Mbwelesu Taten lavas contain up to 2.3 wt.% less SiO_2 and 0.8 wt.% more MgO than the scoria, these differences being most pronounced in the least phenocrystic sample (AMB1); i.e. where the whole rock composition is closest to a true liquid.

Major element variation diagrams of all published whole rock data for Ambrym (Fig. 4.9) show the importance of olivine, calcic plagioclase, and clinopyroxene crystallisation in driving the evolution of the volcanic series, with fractionation of olivine followed by

fractionation of olivine+plagioclase+clinopyroxene driving the progression from lowest to highest SiO_2. The Al_2O_3 (wt.%) vs. SiO_2 (wt.%) plot shows a group of high-Al_2O_3 samples (Fig. 4.9g), attributed to plagioclase accumulation by Picard et al. (1995). One of the flank lava flows sampled in this study (Craig Cove lava AMB10) plots in this high-Al_2O_3 field. K_2O, Na_2O and P_2O_5 are incompatible in Ambrym melts and correlate positively with SiO_2.

Trace element concentrations for all samples (Table 4.5) relative to normal mid-ocean ridge basalt (NMORB) exhibit enrichment of large ion lithophile elements (Fig. 4.10), and Nb depletion. Enrichment in fluid-mobile large ion lithophile elements (K, Rb, Ba, Sr, U, Pb) may represent fluid migration from slab dehydration (Wilson, 1989). Pb enrichment may indicate crustal contamination of the mantle source. The spider diagram resembles an ocean island basalt signature, rather than the characteristic flat high field strength element pattern associated with island arc systems. The mantle domain beneath the central part of the Vanuatu arc has a previously-documented unusual character, attributed to influx of mantle of Indian MORB type as a result of collision with the D'Entrecasteaux Zone (Crawford et al., 1995; Jean-Baptiste et al., 2015; Peate et al., 1997; Turner et al., 1999).

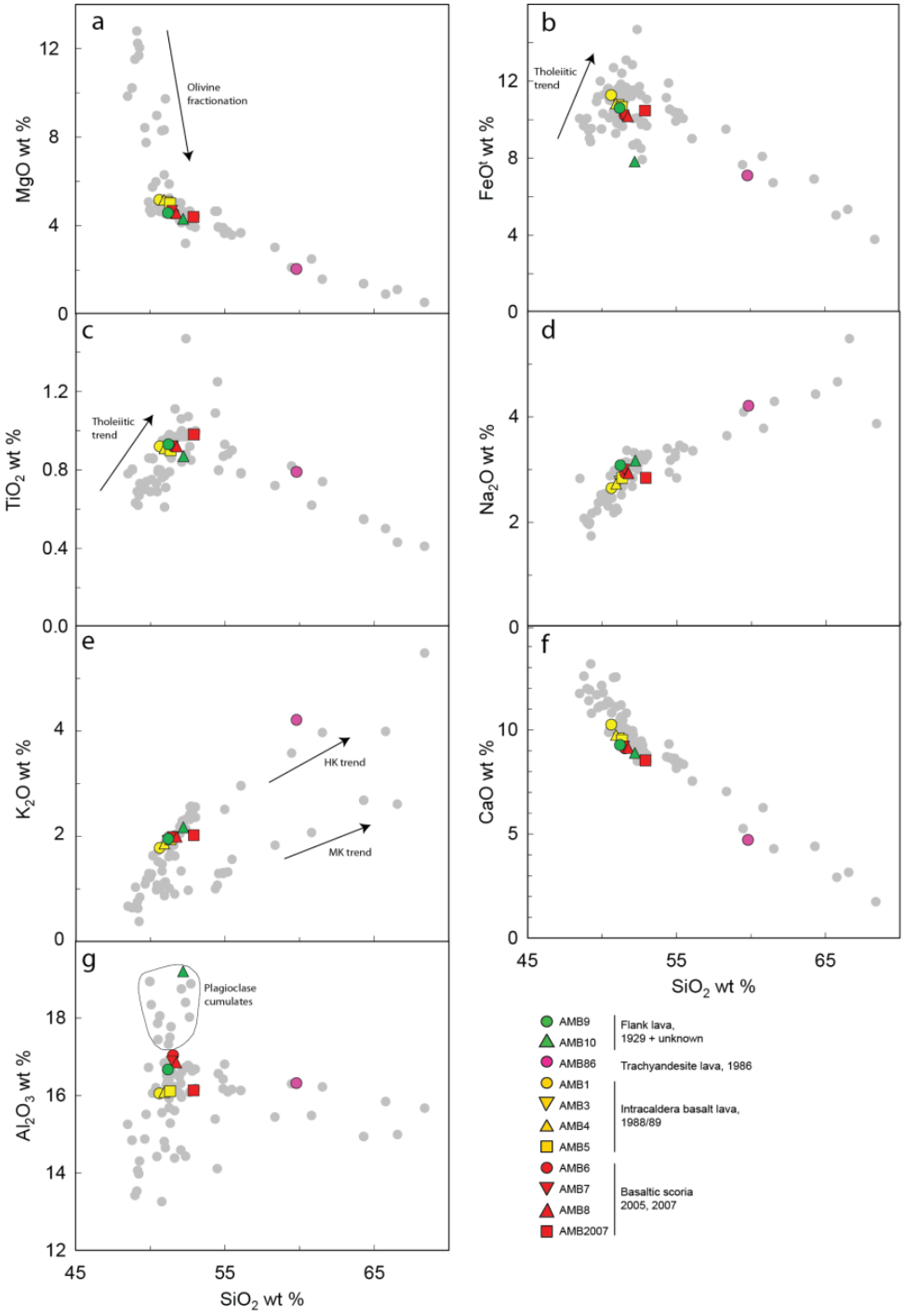

Figure 4.9 Major element variation diagrams comparing samples from this study (coloured symbols) with published data for Ambrym samples (grey symbols) from; Picard et al. (1995), Robin et al. (1993) and Gorton (1977), with SiO_2 as a differentiation index. The 'plagioclase cumulates' field is from Picard et al. (1995); note that the Craig Cove lava sample AMB10 plots in this field.

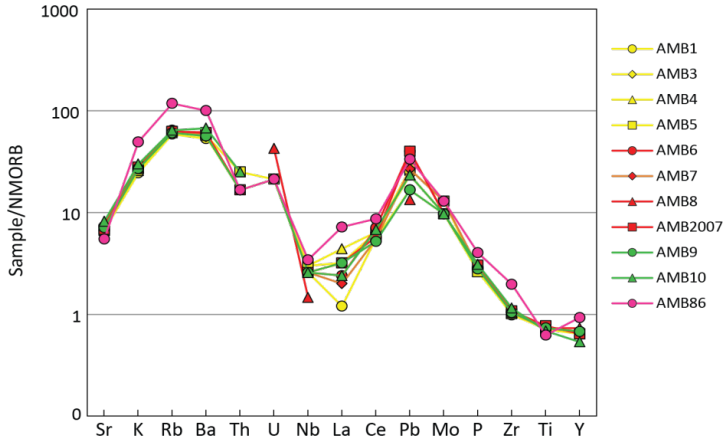

Figure 4.10 Trace element diagram for all samples. Normalisation data from Sun & McDonough (1989). Datapoints are missing where concentration=0 (e.g., Th for AMB8). Apparent variations between basaltic samples for U, Nb, La, and Pb are spurious, occurring for concentrations which are almost all below the detection limit.

Trace element variation is also consistent with fractional crystallisation of olivine, clinopyroxene and plagioclase, with enrichment of incompatible elements (K, Rb, Ba) in the trachyandesite relative to the basalt to basaltic trachyandesite samples, and lower Sr, consistent with the ubiquitous plagioclase crystallisation (Fig. 4.11a–d). Incompatible element ratios (K/Rb) remain approximately constant across all samples, consistent with fractionation-controlled evolution (Fig. 4.11d). Enrichment of the trachyandesite in K and Rb are consistent with the lack of amphibole, biotite or potassium feldspar in the crystallising assemblage. Sr enrichment in the high-Al_2O_3 samples confirms the role of plagioclase accumulation (Fig. 4.11b).

Transition elements display variations (Fig. 4.11e–h) consistent with evolution via crystallisation of olivine (Fig. 4.11e), Fe-Ti oxides (V initially increasing, then decreasing; Fig. 4.11f) and clinopyroxene (Co, Cr, Cu and Sc decreasing; Fig. 4.11g,h).

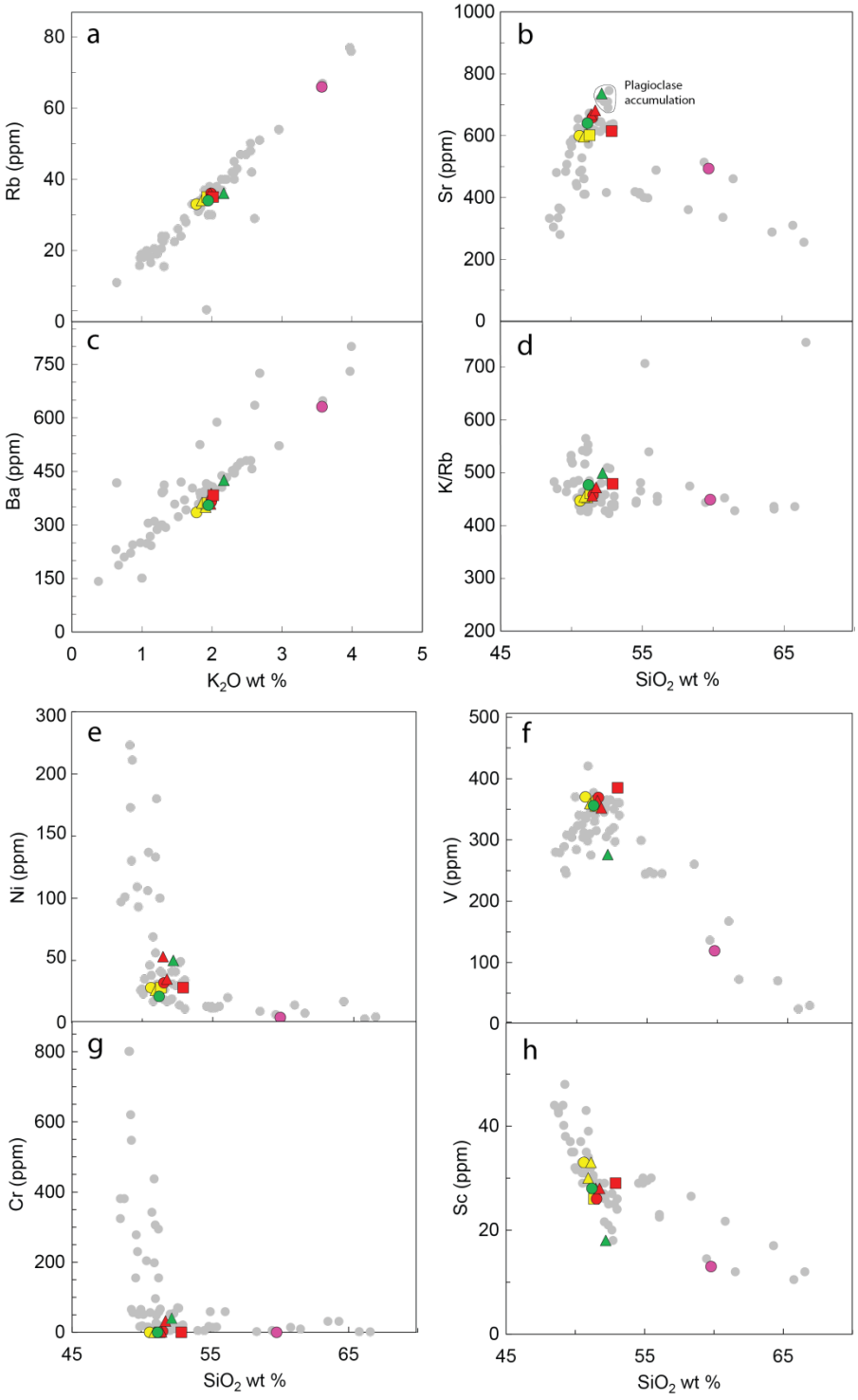

Figure 4.11 Symbols as in Fig. 4.9. **a–d)** Incompatible element behaviour in Ambrym samples. **e-h)** Behaviour of olivine- (Ni), clinopyroxene- (Cr, Sc) and spinel- (V) compatible elements in Ambrym samples.

	Niri Mbwelesu Taten lava					Mbwelesu scoria				Craig Cove lava		Trachyandesite lava
	1988/89					2005			2007	1929	Pre-1929	1986
Sample:	AMB1	AMB2	AMB3	AMB4	AMB5	AMB6	AMB7	AMB8	AMB2007	AMB9	AMB10	AMB1986
Rock type:	Basalt	Basalt	Basalt	Basalt	Basalt	Basalt	Basalt	Basalt	Basaltic andesite	Trachybasalt	Basaltic trachyandesite	Trachyandesite
wt.%												
SiO_2	50.62	51.25	51.14	50.94	51.34	51.54	51.48	51.76	52.91	51.20	52.21	59.80
TiO_2	0.92	0.90	0.91	0.91	0.90	0.92	0.92	0.92	0.98	0.93	0.87	0.79
Al_2O_3	16.05	16.16	16.12	16.08	16.11	17.04	16.87	16.85	16.13	16.67	19.20	16.32
FeOt	11.28	10.64	10.76	10.84	10.66	10.22	10.22	10.17	10.47	10.60	7.82	7.10
MnO	0.22	0.21	0.21	0.21	0.21	0.20	0.20	0.20	0.21	0.21	0.15	0.20
MgO	5.16	4.99	5.06	5.16	5.00	4.57	4.66	4.56	4.39	4.58	4.30	2.04
CaO	10.25	9.50	9.59	9.75	9.51	9.11	9.20	9.13	8.53	9.27	8.89	4.71
Na_2O	2.65	2.91	2.77	2.73	2.84	2.93	3.00	2.93	2.84	3.08	3.17	4.21
K_2O	1.78	1.94	1.91	1.86	1.94	1.99	1.98	1.99	2.02	1.95	2.17	3.57
P_2O_5	0.32	0.31	0.31	0.30	0.30	0.33	0.32	0.34	0.35	0.32	0.36	0.47
LOI	n.d.	-0.16	0.44	0.91	0.21	-0.46	0.00	0.83	n.d.	n.d.	n.d.	n.d.
Total*	99.67	99.8	98.43	98.5	98.86	98.63	98.61	98.43	97.43	98.84	97.89	98.69
Mg#	0.64	0.65	0.65	0.65	0.65	0.64	0.64	0.64	0.62	0.63	0.69	0.53
CaO/Al_2O_3	0.64	0.59	0.59	0.61	0.59	0.53	0.55	0.54	0.53	0.56	0.46	0.29

Table 4.4 Whole-rock major element data (wt.%) for all samples, analysed by XRF on glass beads. Loss on Ignition values were measured at 1050 °C. Mg# and CaO/A_2O_3 values are given as differentiation indices.

	Niri Mbwelesu Taten lava				Mbwelesu scoria				Craig Cove lava		Trachyandesite lava
	1988/89				2005			2007	1929		1986
Sample:	AMB1	AMB3	AMB4	AMB5	AMB6	AMB7	AMB8	AMB2007	AMB9	AMB10	AMB86
Rock type:	Basalt	Basalt	Basalt	Basalt	Basalt	Basalt	Basalt	Basalt	Basalt	Basalt	Andesite
ppm											
Ti	5516	5482	5478	5397	5531	5532	5542	5845	5580	5206	4738
Sc	33	33	30	26	26	28	28	29	28	18	13
V	370	364	359	355	369	364	352	385	356	276	119
Cr	0	0	0	0	3	1	32	0	0	40	0
Ni	28	26	26	28	32	53	35	28	21	50	4
Cu	173	173	141	163	111	297	228	169	201	230	24
Zn	104	105	106	107	116	110	103	104	110	83	107
As	7	7	11	10	23	10	10	14	6	6	10
Rb	33	35	34	35	36	36	35	35	34	36	66
Sr	599	606	596	601	658	669	681	614	640	736	493
Y	19	19	18	18	19	19	21	18	19	15	26
Zr	73	75	76	75	77	79	77	80	77	85	146
K	14740	15853	15420	16120	16494	16413	16527	16782	16207	17975	29604
Nb	6	6	7	7	6	6	3	6	6	6	8
Mo	3	3	3	4	3	4	0	3	3	3	4
Ba	335	350	362	361	365	359	387	383	355	425	631
La	3	8	11	8	6	5	n.d.	8	8	6	18
Ce	42	48	48	47	53	41	n.d.	43	39	51	65
Pb	5	7	7	8	12	8	4	12	5	7	10
Th	0	2	0	3	0	2	0	2	2	3	2
U	0	1	0	1	0	1	2	0	1	0	1
K/Rb	447	453	454	461	458	456	472	479	477	499	449
Ba/Rb	10	10	11	10	10	10	11	11	10	12	10

Table 4.5 Whole-rock trace element data for all samples, analysed by XRF on pressed powder pellets. Detection limits were 10 ppm for Rb, Sr, Y, Zr, Nb, Th, U, Sc, V, Cr, Ni, Cu, Zn, Mo, and As, and 20 ppm for Ba, La, Ce, and Pb.

4.4 Petrology and petrography

All samples are porphyritic, with major phenocryst phases of plagioclase, clinopyroxene, olivine, and Fe-Ti oxides, in order of decreasing abundance. Plagioclase forms the largest and most texturally complex phenocrysts, often glomerocrystic, and also dominates groundmass assemblages. Microphenocrystic (~100–200 μm) plagioclase and clinopyroxene, ± olivine, are found in all samples. The groundmass of all samples (except scoriae AMB6 and AMB2007, which are glassy) comprises plagioclase, clinopyroxene, olivine, Fe-Ti oxides, and glass. Apatite is present as rare inclusions within clinopyroxene in the Niri Mbwelesu Taten lava (AMB2), and as a significant accessory phase in the trachyandesite lava (AMB86). Pyrrhotite is also present as a minor phase in the trachyandesite lava.

Vesicle-free modal abundances and vesicularities are listed in Table 4.6. Vesicularity was determined on one thin section per sample using ImageJ image analysis freeware (http://imagej.nih.gov/ij/index.html). Modal abundances were estimated by least-squares regression analysis using the MINSQ Excel^{TM} spreadsheet (Herrmann & Berry, 2002). Results from calculations were converted from weight percent to volume percent using density of 2.6 g cm^{-3} for plagioclase, 3.3 g cm^{-3} for clinopyroxene, 3.4 g cm^{-3} for olivine and 2.75 g cm^{-3} for glass. These results were compared to estimates from point counting (602 points on one thin section) for sample AMB6, and from image analysis for sample AMB86. The comparison shows a good fit except in AMB86 where the least squares method overestimates glass and underestimates plagioclase.

	Phase proportions, vesicle-free basis								
	Plagioclase		Clinopyroxene		Fe-Ti oxides	Olivine	Apatite	Glass	Ves
	ph	mp	ph	mp	mp	ph			
Mbwelesu scoria									
AMB6^{PC}	15.4	4.0	2.9	1.0	0.7	0.4	-	75.6	42.4
AMB6^{ls}	18.0	0.9	0.3	0.0	0.0	2.0	-	78.9	-
AMB7	10.0	30.0	3.0	5.0	0.5	0.5	-	50.0	42.2
AMB8	10.0	31.0	3.0	5.0	0.5	0.5	-	50.0	43.7
AMB2007	5.0	1.0	2.0	0.1	1.0	0.5	-	90.4	84.8
Intracaldera basalt lava									
AMB1	3.0	67.0	4.5	20.0	5.0	0.5	-	0.0	58.7
AMB2	3.0	68.0	4.0	18.0	5.0	2.0	-	0.0	44.4
AMB3	5.0	68.0	4.0	17.0	5.0	1.0	-	0.0	20.2
AMB4	10.0	55.0	15.0	15.0	5.0	1.0	-	0.0	3.1
AMB5	10.0	50.0	16.0	19.0	5.0	0.5	-	0.0	1.3
Flank lava									
AMB9	15.0	70.0	5.0	5.0	0.5	0.5	-	4.0	5.8
AMB10	40.0	40.0	5.0	5.0	3.0	4.0	-	3.0	7.8
AMB86^{IA}	17.8		4.0		2.7	2.6	-	72.8*	58.6
AMB86^{LS}	25.8		2.5		1.4	2.8	0.9	66.7*	-
AMB86$_{GM}{}^{IJ}$	40.4		2.0		1.1	2.3	-	27.1	

Table 4.6 Modal abundances in volume percent (on a vesicle-free basis), and sample vesicularity. Ph=phenocrysts, mp=microphenocrysts, Ves=vesicularity.. Modal abundances were estimated using least-squares regression analysis, except where indicated by superscripts: PC=point count, LS=least squares, IA=image analysis. *=groundmass.

4.4.1 Mbwelesu scoria

Scoria samples were collected from the rim of Mbwelesu[7] vent in 2005 and 2008. Three of the scoria samples (AMB6, AMB7, AMB8) derive from 2005 activity following a period of very strong degassing (Bani et al., 2009). These are basaltic and vary from glassy (AMB6) to microcrystalline (AMB7 and AMB8). A further sample from activity in April/May 2007 (collected in 2008) is glassy basaltic andesite (AMB2007). Scoria samples from 2005 and 2007 are believed to derive from a single persistent magma source, as lava lake activity was continuous during the intervening period, and glass and phenocryst compositions are closely similar. Full descriptions of the 2005 and 2007 activity are given in Appendix B.

The 2005 scoria samples (AMB6, AMB7, AMB8) are dark grey and ~40% vesicular. Prominent plagioclase glomerocrysts (~10%) and plagioclase-clinopyroxene±olivine

[7] The main active vent in Marum, one of two active basaltic cones inside the caldera; refer to Fig. 4.6.

glomerocrysts (~1%), of ~0.5–3 mm length, as well as isolated glassy, bottle-green clinopyroxene phenocrysts (~3%) from <0.5 mm up to ~2–3 mm in length are visible in hand sample. Phenocrysts mainly occur in glomerocrystic glomerocrysts. Plagioclase-only glomerocrysts (Fig. 4.12a,c,d) are the most common, followed by plagioclase-clinopyroxene±olivine glomerocrysts (Fig. 4.12b), and rare clinopyroxene glomerocrysts (Fig. 4.13c). Clinopyroxene also occurs as individual rounded or euhedral crystals (Fig. 4.13a), as does olivine (Fig. 4.14). Fe-Ti oxides occur as small (<150 μm) subhedral phenocrysts, inclusions in clinopyroxene and olivine, and rounded groundmass grains. The groundmass of AMB6 is pale brown glass, varying to dark brown opaque material or cryptocrystalline groundmass in places. AMB7 and AMB8 have microcrystalline groundmass. The blocky, angular groundmass crystals are on the order of 3–30 μm in size and in order of decreasing abundance are made up of plagioclase, clinopyroxene, olivine and Fe-Ti oxides.

Sample AMB2007 is a reticulite, ~85% vesicular and very fragile, with fragments of Pelé's hair found among the scoria on the crater rim. Phenocrysts of up to 1 mm in size of plagioclase (~5%) and bottle-green clinopyroxene (~2%) occur in clusters of 1–2 mm diameter, and often display rounded outlines. Plagioclase crystals show complex zoning, with large numbers of convolute, concentric, rounded zones in the large phenocrysts. Small glomerocrysts (up to 500 μm) of smaller plagioclase crystals also occur. Clinopyroxene (up to 1200 μm) is pale green and euhedral to heavily rounded. Olivine is euhedral to rounded, up to 600 μm, and occurs in clusters of up to 1 mm with subhedral Fe-Ti oxide crystals of up to 200 μm. The matrix consists of pale brown glass.

Plagioclase

Plagioclase crystals in the scoria occur as 4 principal types:

1.) 'Coarse' glomerocrysts (aggregates of large crystals) c. 1000–3000 μm diameter, with crystals of c. 250–1500 μm along the long axis, and c. 90–1000 μm width. These glomerocrysts display two different textures. One is of jumbled, lath-shaped crystals with blurred Carlsbad twinning, and recrystallised grain boundaries (Fig. 4.12a). The other comprises blocky, rounded crystals with conspicuous fritted cores (Fig. 4.12b) or zones (Fig. 4.12c), and these glomerocrysts often include large ragged clinopyroxene crystals (Fig. 4.12b). Both textures may occur in a single glomerocryst.

2.) ‘Fine’ glomerocrysts (aggregates of smaller crystals), of 300–800 μm diameter (Fig. 4.12d). Crystals range from c. 100–400 μm along the long axis, and c. 50–100 μm width. The crystals are typically blocky and sharp-edged. Constituent crystals in the fine glomerocrysts are markedly more distinct in outline than those in the coarse glomerocrysts, and are often attached longitudinally along crystal faces or perpendicular to a crystal face of the neighbouring crystal (Fig. 4.12d).

3.) Microphenocrysts of 50–200 μm, either blocky and rectangular (which may be related to fine glomerocryst crystals), or ragged and irregularly shaped.

4.) Groundmass crystals c. 5–30 μm size, interlocking with clinopyroxene, olivine, Fe-Ti oxide and interstitial glass in microcrystalline samples AMB7, AMB8.

All four types occur in the 2005 samples but only coarse glomerocrysts (Fig. 4.14a) and rare groundmass microlites occur in the 2007 scoria.

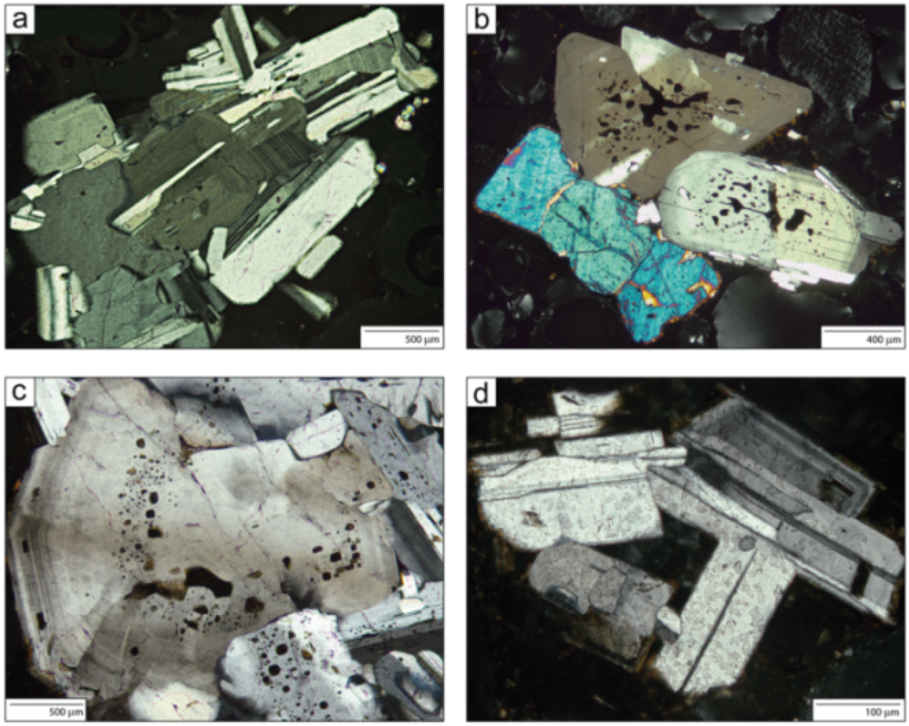

Figure 4.12 Photomicrographs under crossed nicols of plagioclase glomerocryst types in basaltic scoria AMB6. **a)** A coarse glomerocryst of lath-shaped crystals with blurred Carlsbad twinning and recrystallised inner grain boundaries. **b)** Rounded, blocky coarse glomerocryst plagioclase crystals with sieve-textured cores, and large rounded to ragged clinopyroxene crystals. **c)** Rounded, blocky coarse glomerocryst crystal with heavily fritted zone and embayed concentric zoning. **d)** Fine glomerocryst type, showing blocky, sharp-edged crystals.

Clinopyroxene

Clinopyroxene in AMB6 occurs as large euhedral phenocrysts (up to 1500 μm; Fig. 4.13a), rounded to ragged glomerocryst crystals associated with olivine and plagioclase (~200–800 μm; Fig. 4.12b, Fig. 4.13b), blocky to ragged individual phenocrysts (c. 200–700 μm), rare glomerocrysts of subhedral crystals (300–900 μm; Fig. 4.13c), and ragged or rounded subhedral crystals (~100–300 μm). Groundmass clinopyroxene, where present, occurs as diamond-shaped or angular anhedral crystals of ~5–20 μm. The large euhedral phenocrysts contain frequent Fe-Ti oxide inclusions, occasional plagioclase inclusions, and rare olivine inclusions (Fig. 4.13a,b).

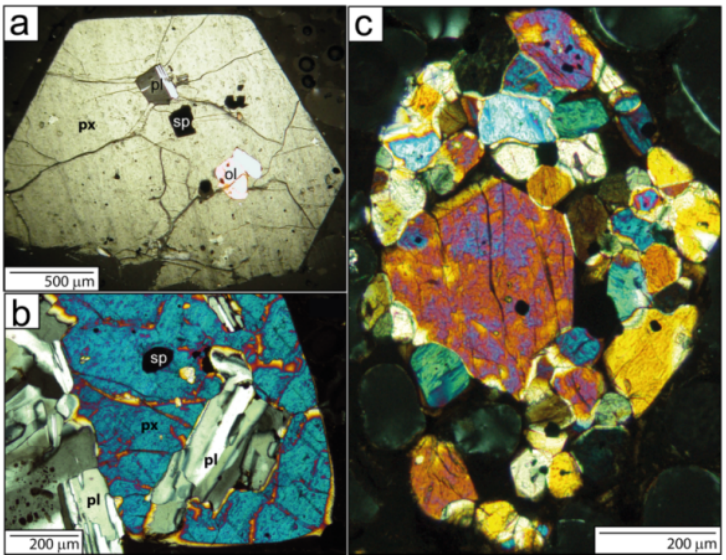

Figure 4.13 Photomicrographs of clinopyroxene in basaltic scoria AMB6, under crossed nicols. **a)** Large euhedral clinopyroxene with plagioclase, Fe-Ti oxide and olivine inclusions. **b)** Rounded clinopyroxene attached to large plagioclase glomerocryst, with glomerocryst plagioclase and Fe-Ti oxide inclusions. **c)** Clinopyroxene aggregate.

Clinopyroxene in the 2007 scoria (AMB2007) occurs as large rounded crystals of 500–1500 μm in glomerocrysts or with inclusions of plagioclase (Fig. 4.14b), glomerocrysts of small crystals of up to 1000 μm (Fig. 4.14c), and angular (Fig. 4.14c, top left) and large euhedral (Fig. 4.14d) crystals of up to 1000 μm. All types occur in conjunction with rounded, stubby Fe-Ti oxide crystals of 50–250 μm, and Fe-Ti oxide inclusions of 10–50 μm.

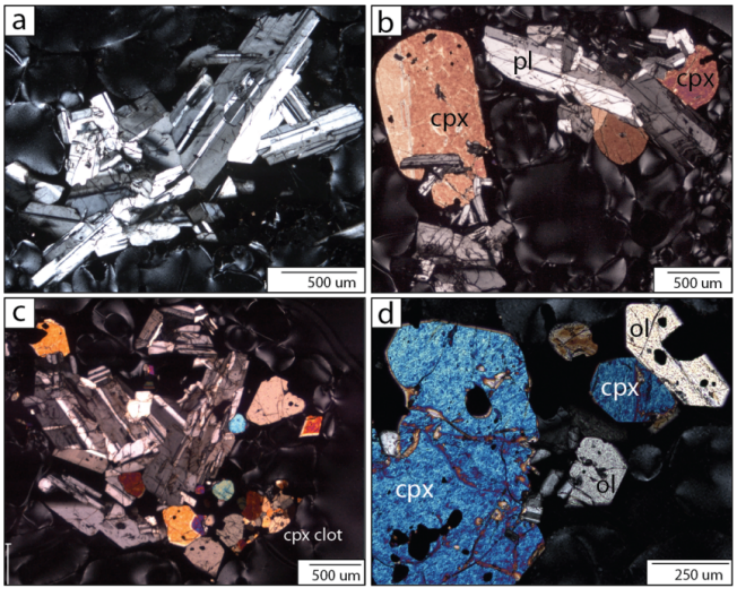

Figure 4.14 Photomicrographs of phenocrysts in 2007 scoria (AMB2007) under crossed nicols. **a)** Plagioclase glomerocryst. **b)** Rounded clinopyroxene with plagioclase inclusions and aggregated with plagioclase/ **c)** Plagioclase glomerocryst with clinopyroxene. **d)** Euhedral clinopyroxene and olivine phenocrysts with Fe-Ti oxide inclusions.

Olivine

Olivine mainly occurs as large (up to 400 μm) rounded or euhedral to subhedral crystals with Fe-Ti oxide inclusions, almost always in association with other large phenocrysts (Fig. 4.15a) or in glomerocrysts (Fig. 4.15b). Occasional isolated rounded grains and angular crystals are also present. In the groundmass, olivine occurs as subhedral to euhedral crystals of 10–30 μm. No zoning is visible in any of these types.

In 2007 scoria (AMB2007) olivine occurs as single or clustered rounded to euhedral crystals of 100–600 μm (Fig. 4.15c,d) and angular and rounded groundmass crystals (10–20 μm).

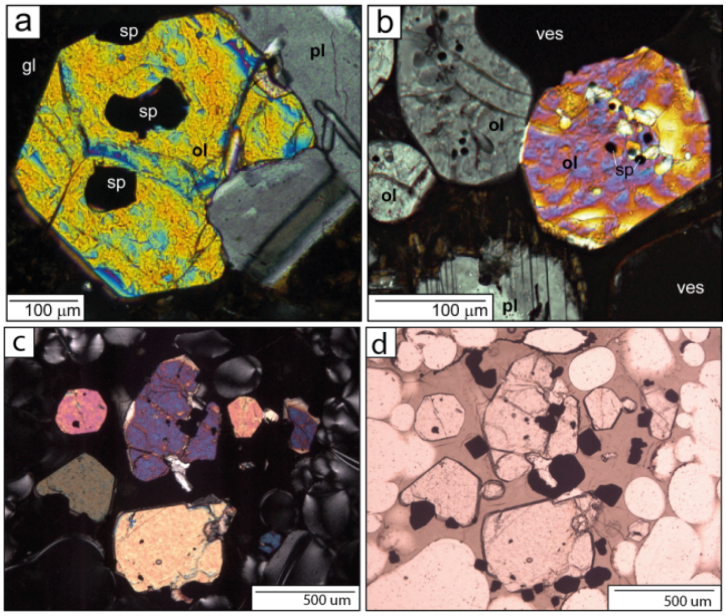

Figure 4.15 Photomicrographs of olivine in basaltic scoria AMB6 (a and b) and AMB2007 (c and d), under crossed nicols. **a)** Large euhedral olivine (ol) with Fe-Ti oxide (sp) inclusions, associated with plagioclase glomerocryst (pl). **b)** Olivine glomerocryst crystals, again associated with plagioclase (at lower left) and with abundant Fe-Ti oxide inclusions. **c)** Olivine and Fe-Ti oxide cluster in AMB2007 under crossed polars; **d)** same cluster under plane polarised light.

Fe-Ti oxides

Fe-Ti oxide phenocrysts occur as rounded to subhedral crystals up to c. 200 μm, and in association with olivine or clinopyroxene in crystal aggregates (Figs. 4.13–4.15). Most olivine phenocrysts contain several inclusions of Fe-Ti oxide up to c. 100 μm in size (Fig. 4.15a,b). Fe-Ti oxides are also occasionally found as individual subhedral microphenocrysts of c. 40–50 μm size. In the groundmass of microcrystalline samples AMB7 and AMB8, they are present as angular anhedral grains <5 μm, interlocking with the other groundmass phases.

Melt inclusions

Melt inclusions occur abundantly in large plagioclase crystals (Fig. 4.12b,c), and to a lesser extent in olivine, clinopyroxene and Fe-Ti oxides. In plagioclase, the inclusions are often irregular in shape or in elongate form along crystal growth faces. In olivine, inclusions are typically pale brown, glassy and ovoid, and usually < 100 μm in diameter (Fig. 4.16). Fe-Ti oxide-hosted inclusions are usually ovoid to squarish, and can be difficult to distinguish from embayments due to the opacity of the phase.

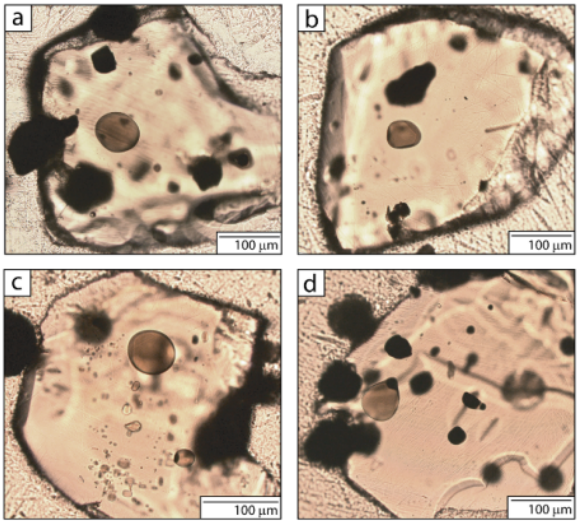

Figure 4.16 Photomicrographs of melt inclusions (brown ovoids) and Fe-Ti oxides (opaque grains) in individually polished olivine crystals from basaltic scoria AMB6, mounted in temporary polishing medium (Crystalbond 509). **a)** Large ovoid melt inclusion and a scattering of smaller inclusions throughout the crystal. **b)** Sub-ovoid melt inclusion. **c)** Large ovoid melt inclusion and numerous smaller inclusions throughout the crystal. **d)** Melt inclusion containing trapped Fe-Ti oxide grain (left) and inclusion bisected by a large crack (right).

Petrographic interpretation

Phenocryst associations in the scoria samples indicate that plagioclase and Fe-Ti oxides, which contain no inclusions of other minerals, crystallised initially in the absence of the other phases. Inclusions of Fe-Ti oxides, plagioclase and olivine are found in euhedral clinopyroxene, and Fe-Ti oxide inclusions are ubiquitous in olivine.

The coarse plagioclase glomerocrysts are the largest and most mature crystals, thus most likely to be the oldest phase. They lack any interstitial matrix such as would be seen in a magmatic enclave or inclusion, so appear to be mature synneusis products. Those crystals with rounded, fritted cores or zones (Figs. 4.12b,c, 4.15a) record at least one major dissolution event such as thermal or chemical disequilibrium, or both (*e.g.*, Clynne, 1999; Murphy et al., 2000), followed by a long uninterrupted period of overgrowth of 200–500 µm of clear plagioclase. Crystals without fritted zones (Fig. 4.12a) represent a population that did not experience the dissolution event; these perhaps represent the same period as the clear overgrowths on the fritted population.

The fine plagioclase glomerocrysts record a different growth history to the coarse glomerocrysts, having clean, sharp outlines, no fritting, and simple zoning (Fig. 4.12d). The euhedral shape and lack of disequilibrium textures indicate that these crystals grew in equilibrium with the matrix. In contrast to the irregular intergrowth of the large glomerocryst crystals, the smaller glomerocryst crystals have well-defined outlines and are frequently aligned along crystal faces, suggesting recent synneusis.

Clinopyroxene phenocrysts in the 2005 scoria exhibit sector zoning, which in extrusive rocks is generally attributed to rapid growth (Brophy et al., 1999; Paterson & Stephens, 1992;

Watson & Liang, 1995). The presence of both euhedral and rounded clinopyroxene indicates two populations of clinopyroxene phenocrysts. The heavily rounded clinopyroxene tends to be associated with large plagioclase glomerocrysts (Figs. 4.12b, 4.13b, 4.14b,c) while the euhedral phenocrysts occur alone, which suggests resorption of earlier glomerocrystic pyroxene and euhedral growth of younger free-floating phenocrysts.

The presence of both euhedral and rounded olivine phenocrysts similarly suggests two populations of olivine.

The presence of resorbed/sieved and non-resorbed phenocryst types in both plagioclase and clinopyroxene demonstrates the coexistence of more mature with more recently-grown phenocrysts, perhaps as a result of magma convection in the storage region, or magma mixing between resident and recharge magma.

4.4.2 Trachyandesite lava

Trachyandesite sample AMB86, a rare occurrence of more siliceous lava from this predominantly basaltic volcano, derives from a 1986 lava flow in the eastern part of the caldera (Cheney, 1986), distinct from the long-lived basaltic activity at the western intracaldera cones. A description of the eruption is given in Appendix B.

Samples of the 1986 trachyandesite lava flow were collected ~1 km from the point of eruption, at 16° 15’37 S, 168° 10’05 E (Fig. 4.6). The flow is hummocky and deeply weathered, with a friable, altered zone extending deep into the interior from the exposed rock surface.

The trachyandesite is medium-grey, hard and coherent, and is ~50% vesicular. In hand sample it is seen to contain abundant (~18%) plagioclase phenocrysts of 1–3 mm and occasional (~4%) green clinopyroxene crystals of ~1 mm, in a microcrystalline matrix.

The phenocryst assemblage is dominated by plagioclase (Fig. 4.17a, b), followed by clinopyroxene, olivine and Fe-Ti oxides, with accessory apatite and pyrrhotite (Fig. 4.17c–f). All six mineral phases occur both individually and combined in clusters, which are dominated by plagioclase, clinopyroxene and olivine, with microphenocrystic apatite, rounded-to-subhedral Fe-Ti oxide inclusions, and amorphous blebs of pyrrhotite included within mafic phases or along margins between mafic crystals. These multi-mineralic glomerocrysts occur as both large (c. 700–2000 μm; Fig. 4.17c, d) and small (c. 100–200 μm) variants. In addition to glomerocrysts and phenocrysts are microphenocrysts (~30–100 μm) of blocky or lath-shaped plagioclase, angular clinopyroxene and olivine, and rounded or cruciform Fe-Ti

oxides, in a matrix of glass and fine crystallites of plagioclase, clinopyroxene, olivine and Fe-Ti oxides. Plumose intergrowths of plagioclase and clinopyroxene, and skeletal or hopper microphenocrysts with blocky extensions, are common. Some plagioclase and clinopyroxene phenocrysts show thin (~5 μm) outer rims of slightly lower greyscale intensity in backscattered electron images.

Plagioclase

Plagioclase phenocrysts occur mainly as angular, lath-shaped crystals up to ~800×2500 μm in size (Fig. 4.17a), with a sparser population of stubby angular crystals of <400 μm, often sieve-textured (Fig. 4.18). In glomerocrysts, plagioclase crystals have the same angular morphology and are up to 900×400 μm in size. Glomerocryst crystals display rounded or irregular margins where they are in contact with other phases but otherwise have euhedral crystal faces (*e.g.*, Fig. 4.17b–d). Irregularly-shaped inclusions occur frequently in crystal cores and are glassy or microcrystalline. The microcrystalline variety is dominated by microlites of plagioclase and clinopyroxene/olivine as well as Fe-Ti oxide grains.

Microphenocrystic plagioclase occurs as blocky or lath-shaped crystals of ~5–60 μm length. Groundmass plagioclase is acicular, c. 1–2 μm wide by 10–30 μm long, often with swallowtail textures.

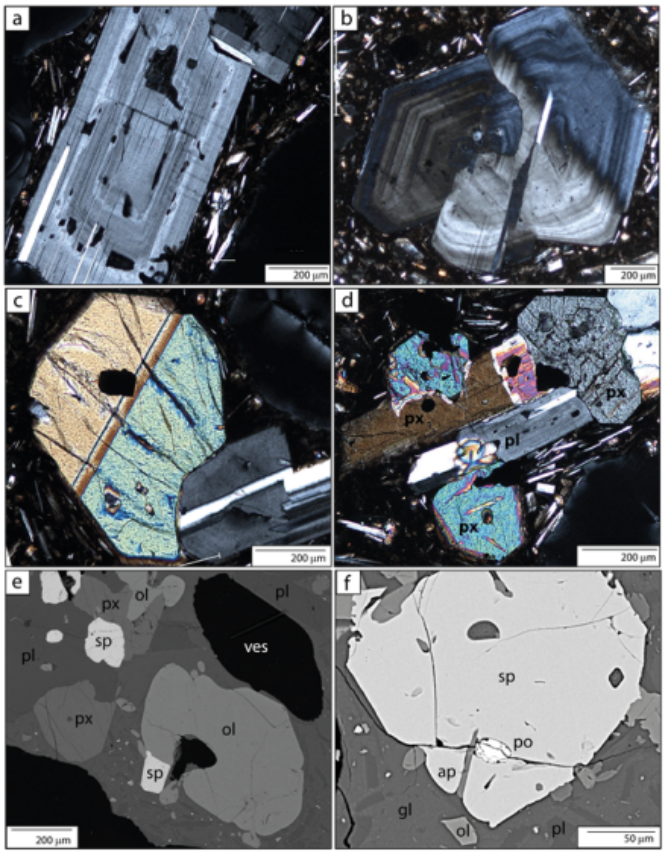

Figure 4.17 Representative images of large phenocrysts in the 1986 trachyandesite lava (AMB86) in XP (a–d) and BSE images (e–f). **a)** Zoned, sieve-textured plagioclase, with patchy zoning in the core and melt inclusions along growth faces. **b)** Zoned plagioclase. **c)** Clinopyroxene-plagioclase glomerocryst. **d)** Augite-plagioclase-olivine glomerocryst, displaying embayments and dissolution, with multiple apatite and Fe-Ti oxide inclusions and zoned, sieved plagioclase. **e)** Multi-mineralic glomerocryst of rounded, embayed olivine, with clinopyroxene, plagioclase and Fe-Ti oxides. **f)** Large Fe-Ti oxide with pyrrhotite (white, cracked ovoid grain; po) and apatite (mid-grey needle adjacent to pyrrhotite grain; ap) inclusions.

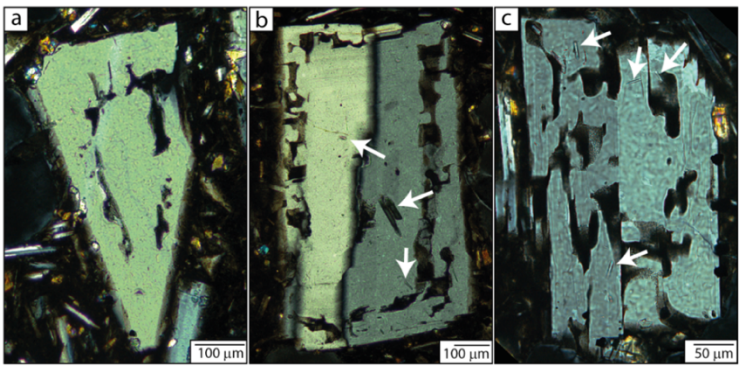

Figure 4.18 Sieve-textured plagioclase in trachyandesite lava AMB86. White arrows in panels b and c highlight some of the numerous apatite inclusions present.

Clinopyroxene

Clinopyroxene occurs as equant or stubby subhedral to euhedral phenocrysts up to ~600 µm across, almost always associated with Fe-Ti oxides and often associated with plagioclase or in polymineralic glomerocrysts (Fig. 4.17, Fig. 4.19). The crystals tend to be angular and subhedral. Some glomerocryst crystals display ragged to rounded outlines. The majority of clinopyroxene crystals exhibit no visible zoning, although sector zoning (Fig. 4.19a), resorbed

cores with overgrowth (Fig. 4.19b) and concentric oscillatory zoning (Fig. 4.19d) can be seen in some microphenocrysts, which are generally 100–200 μm in size.

In the groundmass, clinopyroxene is angular, square-to-rectangular or diamond-shaped, approximately 10–30 μm in maximum dimension, and often displays hopper or swallow-tail morphologies.

Olivine

Phenocrystic olivine is primarily found in clusters with other phenocrysts, or clustered (two or three crystals) with Fe-Ti oxides. It mainly occurs as rounded, resorbed or embayed crystals up to 500 μm in size (*e.g.*, Fig. 4.17e). Microphenocrysts are generally euhedral or angular with sharp crystal boundaries and semi-skeletal morphologies (Fig. 4.19a). Smaller microphenocrysts and groundmass crystals are predominantly angular, or skeletal with euhedral outline, and similar in appearance to groundmass clinopyroxene, often with hopper or swallow-tail textures indicative of rapid or quench crystallisation. Cuspate margins are seen on faces of some olivine phenocrysts (Fig. 4.19c).

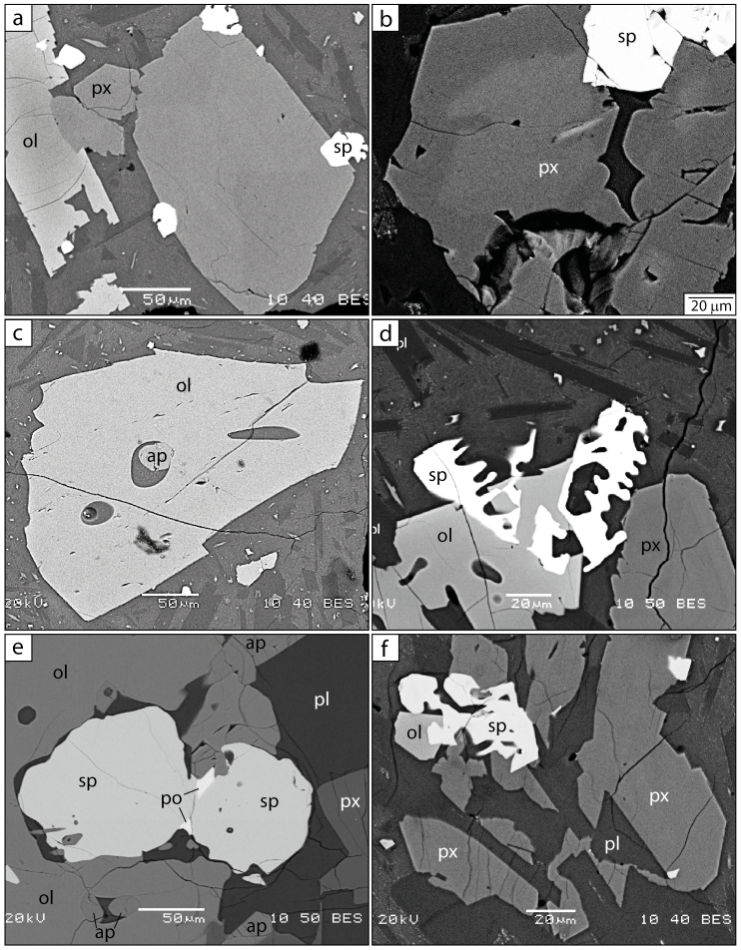

Figure 4.19 SEM images of clinopyroxene and olivine in trachyandesite lava AMB86. **a)** Sector zoned clinopyroxene (largest crystal, mid-grey) with hopper-like olivine, attached Fe-Ti oxide crystals, and groundmass plagioclase (dark grey laths). **b)** Zoned clinopyroxene microphenocryst with resorbed core. **c)** Olivine phenocryst with cuspate margins, large melt inclusions or embayments, and apatite inclusion. **d)** Multimineralic cluster of skeletal Fe-Ti oxides, olivine and concentrically-zoned clinopyroxene. **e)** Multimineralic cluster with bleb-like pyrrhotite occupying triple junctions. **f)** Mineral cluster displaying graphic intergrowth of plagioclase with clinopyroxene.

Fe-Ti oxides

Fe-Ti oxides exhibit striking skeletal, lobate, and cruciform textures (Figs. 4.19a,d,f). Large, irregular sub-rounded oxides also occur, often within glomerocrysts (Figs. 4.17e, 4.19e). Fe-Ti oxides also occur as rounded to subhedral groundmass grains of <10 μm (see for example the groundmass of Fig. 4.19d).

Apatite

Apatite occurs primarily as inclusions in other phases (Fig. 4.18b,c; 4.19c) or in association with multimineralic glomerocrysts (Fig. 4.19e). Apatite inclusions in olivine phenocrysts tend towards a stubby euhedral or rounded type (Fig. 4.19c, e), rather than the long prisms and acicular crystals associated with plagioclase (Fig. 4.18b, c), clinopyroxene and Fe-Ti oxides (Fig. 4.17f). Plagioclase and clinopyroxene phenocrysts often contain multiple inclusions of 10–40 μm prismatic apatite crystals (Fig. 4.18b,c). Elongate microphenocrystic apatite (up to 100 μm length) is also present (c. 2% of groundmass).

Pyrrhotite

Pyrrhotite occurs in association with Fe-Ti oxides and clinopyroxene, as blebs between grain boundaries within crystal glomerocrysts, or within the crystals themselves (Fig. 4.19e). The largest bleb observed is a ~30 μm ovoid bleb inside an Fe-Ti oxide phenocryst (Fig. 4.17f).

Petrographic interpretation

Inclusion relationships indicate that olivine and clinopyroxene are late-crystallising phases as they do not occur as inclusions in any other phases. Apatite inclusions are common in plagioclase phenocrysts (e.g., Fig 4.18b,c), and plagioclase, apatite and pyrrhotite are found in clinopyroxene. A pyrrhotite bleb adhering to an apatite crystal demonstrates that pyrrhotite exsolved subsequent to apatite crystallisation. Pyrrhotite is found in Fe-Ti oxide crystals, and Fe-Ti oxide is found in clinopyroxene and olivine.

The majority of plagioclase phenocrysts display clear euhedral overgrowth around resorbed and patchy-textured or sieved cores, indicating resorption followed by equilibration with the host melt; the irregularly-shaped melt inclusions common along zone margins in some plagioclase phenocrysts (Fig. 4.18), for example, have the characteristic appearance of resorption melt inclusions (cf. Reubi & Blundy, 2008). Some sieved crystals lack euhedral

overgrowth or infill of dissolved areas, which indicates that the euhedral population has spent longer re-equilibrating with the magma following resorption, while the others were more resorbed.

The majority of clinopyroxene phenocrysts are subhedral to euhedral and appear unzoned or sector-zoned (indicating rapid growth), or display faint concentric zoning only towards the margins (Fig. 4.19d). Rare clinopyroxene cores with rounded, irregular outlines (Fig. 4.19b) record resorption and overgrowth, or rapid growth followed by euhedral infill. Microphenocrystic clinopyroxene textures occur in two populations indicative of different cooling rates. Blocky, swallow-tail morphologies are very similar to those experimentally produced (in Etna basalt at 500 MPa) by cooling rates of 0.5 ºC min^{-1}, and plumose textures are identical to those experimentally produced by cooling rates of 15 ºC min^{-1} (Mollo et al., 2010). Clinopyroxene can thus be divided into four populations: equilibrium phenocrysts, possibly inherited resorbed and overgrown phenocrysts, relatively slowly-grown microphenocrysts, and rapid-growth microphenocrysts.

Olivine is dominated by skeletal and hopper morphologies characteristic of rapid growth. Some of the olivine phenocrysts display cuspate margins (Fig. 4.19c), which are characteristic of thermal resorption (Thornber & Huebner, 1985), smooth rounded edges, which are characteristic of resorption due to chemical disequilibrium (Fig. 4.19e), and embayments, which in conjunction with rounded crystal shapes are characteristic of dissolution (Donaldson & Henderson, 1988).

Skeletal Fe-Ti oxide morphologies are strikingly similar to those experimentally produced by Mollo et al. (2010) by rapid cooling rates (0.5 ºC min^{-1}) in Etna basalt at 500 MPa.

Globular pyrrhotite included in glomerocrysts (Fig. 4.19e) has the appearance of immiscible sulphide liquid (Luhr, 1990). The morphology of the interstitial pyrrhotite in crystal aggregates is characteristic of intercumulus melt (cf. O'Driscoll et al., 2010), which indicates entrainment of cumulates. Disaggregated cumulate glomerocrysts may thus account for some of the phenocrysts and observed disequilibrium textures.

The combination of rapid growth and resorption textures implies a thermally and chemically dynamic system immediately prior to eruption, with growth of new equilibrium crystals and chemical/thermal resorption of disequilibrium phases. Resorption textures, particularly seen in plagioclase and, to a lesser extent, clinopyroxene, indicate mixing of more mafic magma into a more evolved melt rather than a gradual evolution towards those compositions. Alternatively, cyclical disequilibrium due to convection of buoyant, heated

magma, driven by arrival of hotter mafic magma at the base of the storage region, could cause resorption and overgrowth without mechanical mixing of distinct magma batches (Couch et al., 2001). Latent heat of crystallisation can also constitute a significant thermal input—approximately 2–3 °C per 1% crystallisation (Couch et al., 2003)—which could contribute to thermal disequilibrium.

4.4.3 Niri Mbwelesu Taten lava

Samples AMB1–5 derive from basaltic intracaldera a'a lava flows erupted in 1988/89 from a newly-formed adventitious vent (Niri Mbwelesu Taten) on the southern flank of Marum (Cheney, 1988; Charley, 1988). The flow extends 5 kilometres south-west through the gullied lower slopes of Marum cone and across the caldera floor in blocky, rubbly tongues. Full descriptions of the 1988/89 eruptions are given in Appendix B.

The lavas are medium-to-dark grey and display variable vesicularity and phenocryst content. Samples AMB1–3 have lower phenocryst contents (8–10% on a vesicle-free basis) and higher vesicularity (20–60%), and AMB4 and AMB5 have higher phenocryst contents (~26% on a vesicle-free basis) and low vesicularity (<5%).

In contrast to the scoria samples, plagioclase glomerocrysts are rare in these lavas. The phenocryst assemblage consists of plagioclase laths up to 2 mm (3–10%; Fig. 4.21a,b), occasional ragged, sector-zoned clinopyroxene up to 1 mm (<5%), occasional euhedral or hopper olivine (~1%; Fig. 4.21c,d), and rare plagioclase-pyroxene glomerocrysts of xenolithic appearance (Fig. 4.19e,f), in a microcrystalline groundmass of plagioclase laths (75%), diamond-shaped clinopyroxene (10%), subhedral olivine (5%) and rounded Fe-Ti oxide grains (10%).

Plagioclase

Plagioclase occurs as sieve-textured crystals up to 400 μm (Fig. 4.20a), clear lath-shaped crystals up to 700 μm (Fig. 4.20b), and lath-shaped phenocrysts of 200–800 μm with overgrowth around a rounded core. Groundmass plagioclase consists of laths of 5–100 μm.

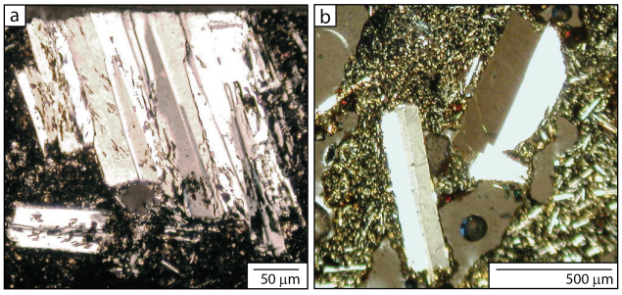

Figure 4.20 Photomicrographs of plagioclase in intracaldera basaltic lava AMB2. **a)** Sieve-textured plagioclase. **b)** Clear lath-shaped plagioclase.

Clinopyroxene

Clinopyroxene is predominantly angular and ragged-edged, 200–500 μm in size, with reaction rims of lower birefringence around a ragged core (Fig.4.21a,b). Diamond-shaped to rectangular microphenocrysts (40–100 μm) are common. Sector zoning is prominent in both phenocrysts and microphenocrysts. Ragged, patchy clinopyroxene aggregates c. 100 μm across occur frequently in the groundmass.

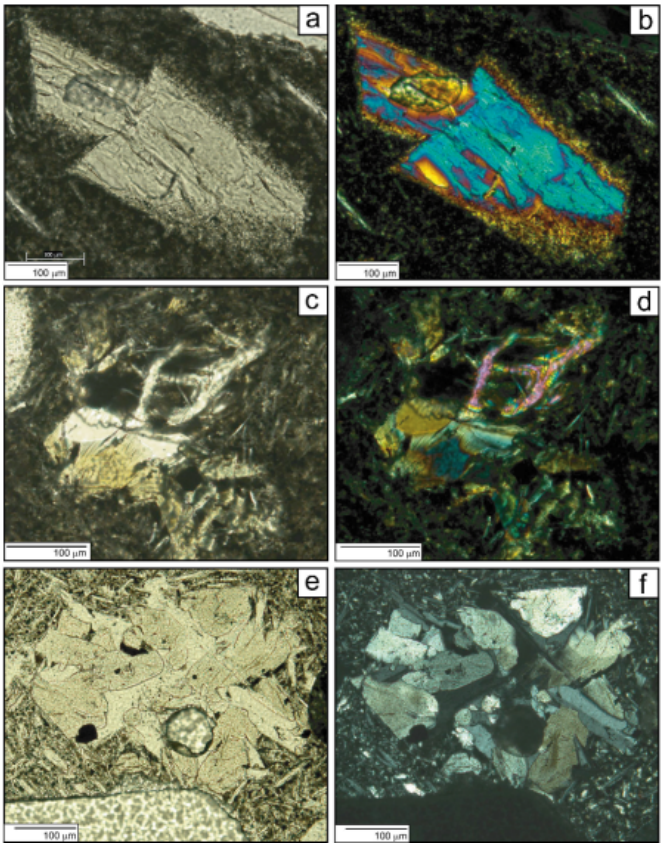

Figure 4.21 Photomicrograph of phenocrysts in intracaldera basaltic lava (AMB1), under PPL (a, c, e) and XP (b, d, f). **a, b)** Ragged clinopyroxene with reaction rim. **c, d)** Hopper olivine. **e, f)** Pyroxene-plagioclase glomerocryst; possible xenolith/autolith.

Olivine

Phenocrystic olivine occurs as rare euhedral phenocrysts of ~200 μm or hopper crystals of 100–200 μm (Fig. 4.21c,d). Olivine occurs as subhedral to euhedral crystals of up to 30 μm in the groundmass.

Fe-Ti oxides

Fe-Ti oxides are not a conspicuous phenocryst phase in the intracaldera basaltic lava samples but occur throughout the groundmass as rounded grains up to c. 10–20 μm (e.g. groundmass of Fig. 4.21e).

Petrographic interpretation

These lavas contain only a minor cargo of phenocrysts and are dominated by groundmass phases, indicating that they represent a predominantly liquid magma. The low number of phenocrysts may be due to removal by crystal settling during shallow storage.

The phenocrysts typically display indistinct rims, with plagioclase often sieve-textured. These may be xenocrysts, perhaps derived from disaggregated xenoliths (Fig. 4.21e,f), which have undergone dissolution once mixed into this magma; or phenocrysts which have undergone resorption during ascent, which can produce sieve texture in plagioclase (Nelson & Montana, 1992; Vance, 1965).

4.4.4 Craig Cove lava

Two lava flow samples were collected from a beach adjacent to Craig Cove airfield, on the western coast. One flow dates to 1929, and the other is of uncertain age but underlies the 1929 flow (B. Mason 2010, pers. comm.); it possibly dates from the previous western flank eruption in 1913. The lava flows derive from either a fissure or a short-lived crater which opened near the coast. A full description of the 1929 eruption is given in Appendix B.

The 1929 flow (AMB9) is medium-to-dark grey, and ~5% vesicular, containing abundant (c. 10%) 0.5–3 mm plagioclase clusters, some of which include bottle-green pyroxene crystals of 0.5–1 mm, in a microcrystalline matrix.

The older flow (AMB10) is blue-grey, crumbly and weathered, with oxidised surfaces extending through the sample in gaps and cracks. The most striking feature is the population of large plagioclase phenocrysts, up to ~1 cm long, forming ~15% of the rock. These usually

occur in groups of two or three crystals in a criss-crossing arrangement, with zoning apparent even in hand sample. The groundmass is microcrystalline.

AMB10 was selected for more detailed examination due to its striking megacrystic plagioclase, as well as heavily oxidised olivine phenocrysts.

Plagioclase

AMB10 contains abundant aggregates of megacrystic euhedral plagioclase (up to 2200 μm across and 7500 μm in length), which display conspicuous zoning, embayments, and heavily sieved zones of melt inclusions (Fig. 4.22a, b), which are concentrated along zone margins, twinning surfaces and cracks. Plagioclase also occurs as smaller glomerocrysts (~1500–2500 μm) of sharply rectangular crystals (Fig. 4.22a). Individual phenocrysts with overgrowth around a sieved zone and occasional skeletal crystals (Fig. 4.22c) are also present (up to ~700 μm).

Clinopyroxene

Clinopyroxene occurs mainly as rounded glomerocrysts up to 1000 μm across (Fig. 4.22a,e). The shape of the glomerocrysts suggests that they may have replaced olivine; in one case, a large (c. 700 μm) embayed and rounded crystal of olivine is seen in the centre of a clinopyroxene glomerocryst (lowermost pyroxene glomerocryst in Fig. 4.22a, towards bottom left). Clinopyroxene also occurs as clear, slightly rounded, subhedral crystals attached to the large plagioclase glomerocrysts, with minor magnetite dust in places along crystal rims. No zoning is visible in the clinopyroxene phenocrysts. Groundmass clinopyroxene is present as squarish angular microlites of 20–50 μm.

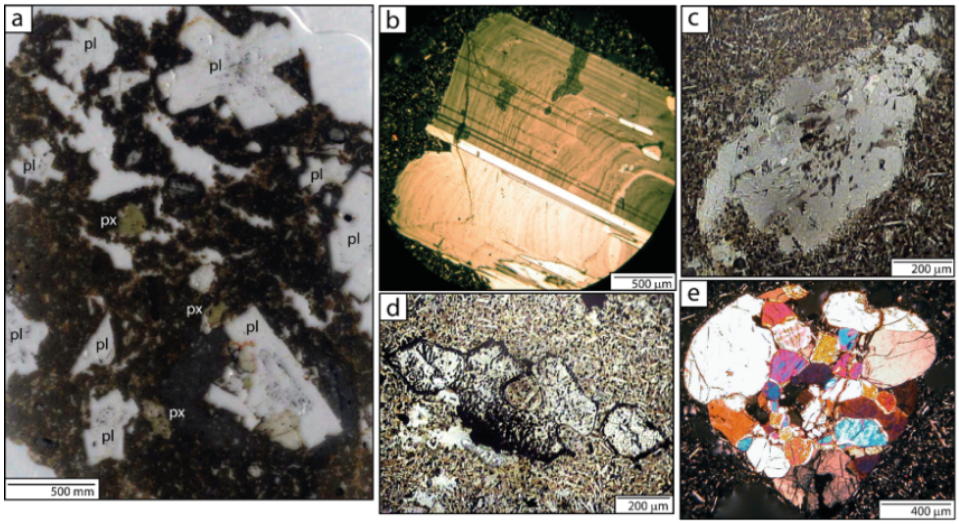

Figure 4.22 Photomicrographs of phenocrysts in flank lava AMB10. **a)** Thin section displaying plagioclase (pl) megacrysts, small glomerocrysts (e.g., top left) and clinopyroxene ± olivine glomerocrysts (px). **b)** Zoned plagioclase megacryst with rounded resorption surfaces and re-entrants (XP). **c)** Sieve-textured plagioclase (PPL). **d)** Heavily-embayed olivine-oxide symplectite (PPL). **e)** Clinopyroxene glomerocryst with rounded outline (XP).

Olivine

Olivine is more prominent in AMB10 than in the intracaldera scoria and lavas, and displays more complex textures. It is seen as large, isolated euhedral phenocrysts of up to 1 mm, which are heavily embayed, oxidised and fragmented, with rims and trails of magnetite dust (Fig. 4.22d). Olivine is also found as an apparent relict phase in the centre of a large (2 mm) clinopyroxene glomerocryst. Groundmass olivine is present as square/diamond-shaped microlites of 30–50 μm size.

Fe-Ti oxides

Fe-Ti oxides occur as rounded microphenocrysts (up to 200 μm), inclusions in mafic phases, and abundant groundmass grains (<5 μm; black grains in Fig. 4.22c,d).

Petrographic interpretation

The plagioclase megacrysts and resorbed, oxidised olivines in lava AMB10 indicate that the magma passed through a storage region distinct from that traversed by the intracaldera samples. Embayed olivine and heavily sieve-textured plagioclase indicate significant disequilibrium, perhaps caused by xenocrystic/antecrystic origin or decompression, and oxidation of olivine and clinopyroxene (as evidenced by oxide ‘dust’ or symplectites) indicate a significant change in oxygen fugacity, perhaps as a result of degassing.

4.5 Phase compositions

Representative samples were chosen for electron microprobe analysis. AMB6 and AMB7 represent (respectively) glassy and microcrystalline Mbwelesu scoria types from 2005, while AMB2007 represents 2007 Mbwelesu scoria. AMB2 represents the Niri Mbwelesu Taten lava flows, AMB10 represents flank lava flows, and AMB86 is the trachyandesite lava flow.

A total of 831 electron microprobe analyses (after screening for quality; see Section 3.4.1) of mineral phases, matrix glass and melt inclusions in the selected samples were made (see Table 3.3 for distribution of analyses). Details of the analytical set-up are given in the methods chapter, and the full datasets are provided in Appendices C–G.

4.5.1 Mbwelesu scoria

Plagioclase

Anorthite contents in the scoria (AMB6, AMB7, AMB2007) range from An_{89}–An_{36}. There is significant compositional overlap (Fig. 4.23) between the plagioclase crystal types described in Section 4.4.1.

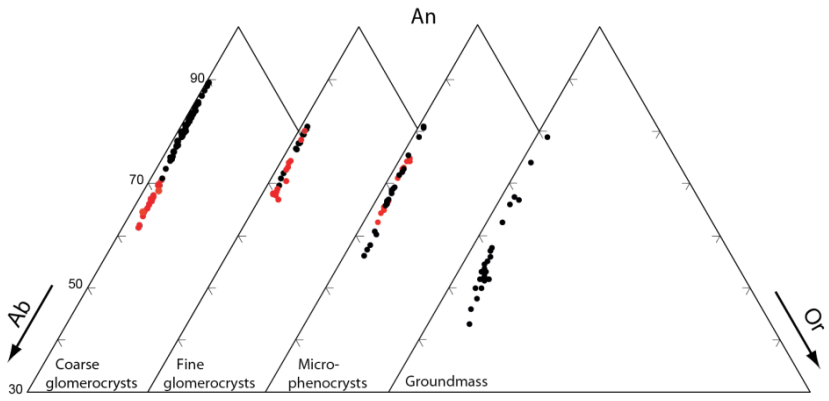

Figure 4.23 Plagioclase compositions for scoria samples AMB6, AMB7 and AMB2007. Note left-hand scale starts at An_{30}. Black=core, red=rim.

Coarse glomerocryst crystal cores have compositions of $An_{89–75}$, with rims of $An_{71–67}$. These crystals display normal zoning, with both stepped and gradual profiles (Fig. 4.24). In some cases, zoning is slightly oscillatory but with an overall decrease in An content from core to rim. The anorthite contents of fine glomerocryst crystals are $An_{81–68}$. Normal zoning is also seen in the fine glomerocryst crystals; with cores from $An_{81–71}$ and rims from $An_{80–68}$, mainly toward the lower end of the range (Table 4.7). Microphenocrysts show a compositional range of $An_{81–56}$, including a distinct population of blocky to elongate laths of ~50–70 μm with

compositions in the range $An_{68–56}$. Zoning is generally normal but is asymmetrical across some crystals, believed to be a function of crystallographic orientation or fragmentation of larger crystals. Groundmass crystals (present in AMB7 only) cover a range of compositions from $An_{79–46}$.

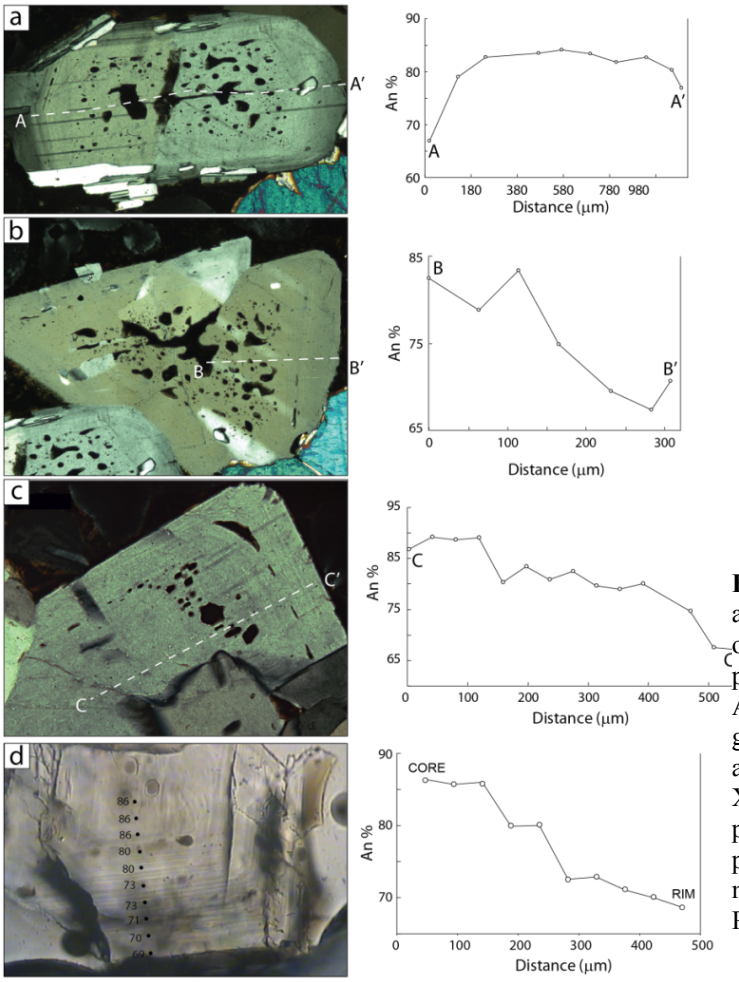

Figure 4.24 Photo-micrographs and electron microprobe traverses of normally-zoned plagioclase phenocrysts in basaltic scoria AMB6. Panels a–c show coarse glomerocryst crystals of rounded and fritted type, photographed in XP. The crystal in panel d is a picked fragment mounted and polished for EPMA analysis of melt inclusions, photographed in PPL.

Other notable plagioclase occurrences include a labradorite mantling bytownite (Fig. 4.25), and ~$An_{82–77}$ plagioclase inclusions in clinopyroxene.

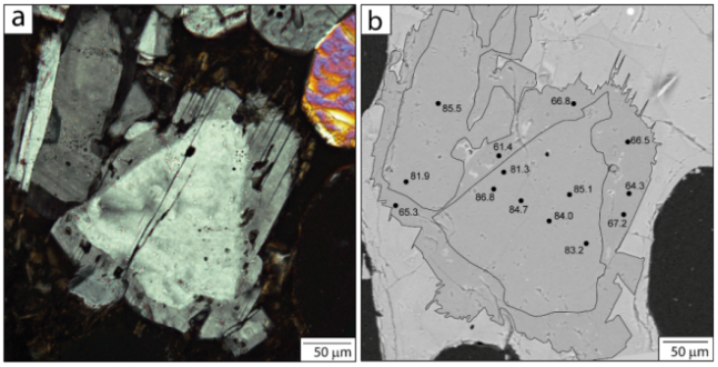

Figure 4.25 Labradorite overgrowth around a ragged bytownitic core in basaltic scoria AMB6. a) Core clearly visible under crossed polars. b) BSE image showing spot compositions in An mol% as analysed by EPMA.

	AMB6										AMB7		AMB2007	
	Coarse glomerocryst cores		Coarse glomerocryst rims		Fine glomerocryst cores		Fine glomerocryst rims		Microphenocrysts		Groundmass		Coarse glomerocrysts	
n	54		22		10		11		42		40		9	
SiO_2	47.30	*1.12*	51.10	*0.92*	48.61	*0.91*	49.28	*1.24*	50.51	*1.27*	52.19	*2.61*	48.61	*1.61*
TiO_2	0.02	*0.01*	0.04	*0.01*	0.03	*0.00*	0.03	*0.01*	0.04	*0.02*	0.08	*0.05*	0.04	*0.02*
Al_2O_3	31.83	*1.02*	29.47	*0.52*	30.65	*0.62*	30.54	*1.06*	30.25	*0.90*	28.66	*2.17*	31.21	*1.13*
FeO	1.10	*0.05*	1.21	*0.09*	1.13	*0.03*	1.20	*0.07*	1.29	*0.16*	1.62	*0.33*	1.10	*0.10*
MnO	0.00	*0.01*	0.00	*0.01*	0.01	*0.01*	0.01	*0.01*	0.01	*0.01*	0.01	*0.02*	0.01	*0.01*
MgO	0.12	*0.02*	0.16	*0.01*	0.14	*0.01*	0.14	*0.02*	0.17	*0.06*	0.21	*0.09*	0.13	*0.02*
CaO	16.25	*0.85*	13.42	*0.58*	15.01	*0.72*	14.64	*1.05*	13.97	*0.91*	12.56	*2.06*	15.79	*1.33*
Na_2O	1.94	*0.44*	3.50	*0.36*	2.49	*0.36*	2.76	*0.48*	3.23	*0.48*	4.01	*1.10*	2.45	*0.70*
K_2O	0.17	*0.06*	0.39	*0.06*	0.25	*0.04*	0.28	*0.07*	0.35	*0.07*	0.58	*0.28*	0.23	*0.10*
SrO	0.15	*0.01*	0.16	*0.02*	0.17	*0.02*	0.16	*0.01*	0.17	*0.02*	0.17	*0.02*	0.13	*0.03*
Total	98.88	*0.70*	99.47	*0.83*	98.49	*0.24*	99.04	*0.81*	100.01	*0.48*	100.08	*0.36*	99.65	*0.53*
Cations on the basis of 8 oxygens														
Si	2.21	*0.05*	2.35	*0.03*	2.27	*0.04*	2.29	*0.06*	2.32	*0.05*	2.38	*0.11*	2.25	*0.07*
Al	1.75	*0.05*	1.60	*0.03*	1.69	*0.04*	1.67	*0.06*	1.64	*0.05*	1.54	*0.12*	1.70	*0.07*
Fe^{2+}	0.04	*0.00*	0.05	*0.00*	0.04	*0.00*	0.05	*0.00*	0.05	*0.01*	0.06	*0.01*	0.04	*0.00*
Mg	0.01	*0.00*	0.01	*0.00*	0.01	*0.00*	0.01	*0.00*	0.01	*0.00*	0.01	*0.01*	0.01	*0.00*
Ca	0.81	*0.04*	0.66	*0.03*	0.75	*0.04*	0.73	*0.05*	0.69	*0.05*	0.62	*0.10*	0.78	*0.07*
Na	0.18	*0.04*	0.31	*0.03*	0.23	*0.03*	0.25	*0.04*	0.29	*0.04*	0.35	*0.10*	0.22	*0.06*
K	0.01	*0.00*	0.02	*0.00*	0.01	*0.00*	0.02	*0.00*	0.02	*0.00*	0.03	*0.02*	0.01	*0.01*
Total	5.009	*0.005*	5.012	*0.008*	5.005	*0.004*	5.008	*0.007*	5.015	*0.004*	5.006	*0.009*	5.02	*0.00*
An	81.44	*4.27*	66.43	*3.31*	75.74	*3.55*	73.31	*4.82*	69.02	*4.63*	61.41	*10.78*	77.06	*6.64*
Ab	17.56	*3.94*	31.30	*3.01*	22.77	*3.31*	25.01	*4.41*	28.90	*4.23*	35.26	*9.29*	21.63	*6.10*
Or	1.00	*0.34*	2.27	*0.31*	1.49	*0.26*	1.69	*0.45*	2.07	*0.44*	3.33	*1.57*	1.31	*0.55*

Table 4.7 Average compositions of plagioclase types in basaltic scoria samples AMB6 (glassy, 2005), AMB7 (microcrystalline, 2005), and AMB2007 (glassy, 2007). Figures in italics are one standard deviation. The full analytical datasets are given in Appendix C.

Clinopyroxene

Clinopyroxene glomerocryst crystals, euhedral phenocrysts, and rounded phenocrysts cluster in the augite field, around ~$En_{43–44}Wo_{41–42}Fs_{14–15}$ (Fig. 4.26; Table 4.8). Concentric growth zonation can be seen in some of the large euhedral clinopyroxenes, which EPMA data shows to be slight oscillatory zoning (Fig. 4.27). Sector zoning is seen in euhedral and rounded subhedral crystals. Microphenocrysts and groundmass crystals show a wider compositional range than the phenocrysts (over the range $En_{26–42}Wo_{38–46}Fs_{18–31}$), with higher iron and aluminium contents.

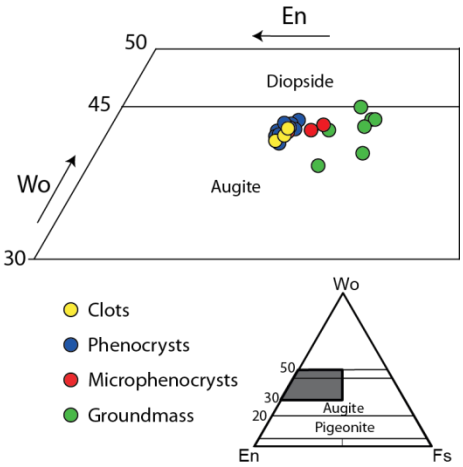

Figure 4.26 Clinopyroxene compositions in AMB6, AMB7 and AMB2007. The grey shaded area of the small triangle shows the area of the En-Wo-Fs triangle enlarged.

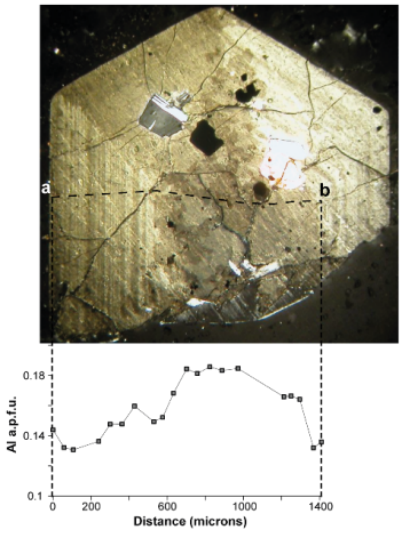

Figure 4.27 Electron microprobe traverse across a large, sector-zoned, euhedral clinopyroxene crystal from basaltic scoria AMB6. The traverse shows oscillatory zoning, and higher Al in the central sector. This image is a composite to show plagioclase and olivine inclusions (which are at extinction when clinopyroxene zoning is visible) more clearly.

	AMB6&7						AMB2007		AMB2		AMB10		AMB86							
	GL(21)		Ph (64)		MP&GM (14)		GL (4)		MP (2)		GL (8)		GL (4)		Ph (18)		MP (12)		GM (15)	
SiO_2	50.36	*0.64*	50.25	*0.42*	46.89	*1.21*	50.72	*0.25*	50.46	*0.55*	50.27	*0.36*	51.77	*0.45*	51.82	*0.49*	49.92	*1.36*	49.76	*1.26*
TiO_2	0.5	*0.05*	0.5	*0.05*	1.28	*0.19*	0.53	*0.04*	0.56	*0.02*	0.58	*0.04*	0.47	*0.06*	0.46	*0.1*	0.78	*0.23*	0.89	*0.22*
Al_2O_3	3.86	*0.66*	3.65	*0.36*	6.84	*1.35*	3.65	*0.27*	2.52	*0.05*	3.67	*0.26*	1.89	*0.21*	2.02	*0.47*	3.75	*1.29*	3.69	*0.88*
FeOt	8.88	*0.32*	8.95	*0.34*	12.39	*0.9*	8.95	*0.35*	10.33	*0.35*	8.29	*0.19*	10.34	*0.74*	10.57	*0.28*	11	*1.06*	11.89	*0.53*
MnO	0.24	*0.02*	0.23	*0.02*	0.29	*0.03*	0.24	*0.03*	0.55	*0.02*	0.2	*0.02*	0.51	*0.11*	0.54	*0.04*	0.43	*0.15*	0.49	*0.07*
MgO	14.75	*0.34*	14.74	*0.3*	12.24	*0.95*	14.87	*0.27*	13.64	*0.34*	15.08	*0.17*	14.46	*0.78*	14.22	*0.46*	13.57	*0.82*	13.44	*0.62*
CaO	20.48	*0.26*	20.35	*0.34*	18.83	*1.23*	20.6	*0.11*	19.86	*0.11*	20.19	*0.16*	19.67	*0.41*	19.15	*0.38*	19.27	*1.16*	18.29	*1.01*
Na_2O	0.33	*0.02*	0.33	*0.02*	0.43	*0.06*	0.35	*0.01*	0.33	*0.02*	0.36	*0.01*	0.29	*0.03*	0.3	*0.03*	0.31	*0.04*	0.35	*0.1*
Total	99.44	*0.4*	99.04	*0.51*	99.5	*0.94*	99.94	*0.21*	98.28	*0.4*	98.78	*0.4*	99.4	*0.46*	99.09	*0.28*	99.04	*0.49*	98.83	*0.9*
Cations on the basis of 6 oxygens																				
Si	1.87	*0.02*	1.88	*0.01*	1.77	*0.04*	1.88	*0.01*	1.92	*0.01*	1.88	*0.01*	1.94	*0.01*	1.95	*0.02*	1.88	*0.05*	1.89	*0.04*
Ti	0.01	*0.00*	0.01	*0.00*	0.04	*0.01*	0.01	*0.00*	0.02	*0.00*	0.02	*0.00*	0.01	*0.00*	0.01	*0.00*	0.02	*0.01*	0.03	*0.01*
Al	0.17	*0.03*	0.16	*0.02*	0.3	*0.06*	0.16	*0.01*	0.11	*0*	0.16	*0.01*	0.08	*0.01*	0.09	*0.02*	0.17	*0.06*	0.17	*0.04*
Fe^{+3}	0.08	*0.02*	0.08	*0.02*	0.14	*0.03*	0.08	*0.01*	0.04	*0.01*	0.07	*0.01*	0.03	*0.01*	0.01	*0.01*	0.05	*0.03*	0.04	*0.03*
Fe^{+2}	0.2	*0.02*	0.2	*0.02*	0.25	*0.03*	0.2	*0.01*	0.28	*0*	0.19	*0.01*	0.3	*0.03*	0.33	*0.01*	0.3	*0.06*	0.34	*0.03*
Mg	0.82	*0.02*	0.82	*0.02*	0.69	*0.05*	0.82	*0.02*	0.77	*0.01*	0.84	*0.01*	0.81	*0.04*	0.8	*0.02*	0.76	*0.04*	0.76	*0.03*
Ca	0.82	*0.01*	0.81	*0.01*	0.76	*0.05*	0.82	*0.00*	0.81	*0.01*	0.81	*0.01*	0.79	*0.01*	0.77	*0.02*	0.78	*0.04*	0.74	*0.04*
Total	4	*0*	4	*0*	4	*0*	4	*0*	4	*0*	4	*0*	4	*0*	4	*0*	4	*0*	4	*0*
FER	0.41	*0.15*	0.4	*0.1*	0.55	*0.2*	0.41	*0.03*	0.15	*0.05*	0.39	*0.07*	0.09	*0.03*	0.02	*0.04*	0.17	*0.15*	0.13	*0.1*
Wo	44.6	*0.8*	44.4	*0.8*	44.7	*2.5*	44.6	*0.4*	43.3	*0.6*	44.0	*0.1*	41.7	*1*	40.8	*1*	42.3	*3*	40.4	*2.5*
En	44.7	*0.8*	44.7	*0.7*	40.4	*2.4*	44.8	*0.6*	41.4	*0.7*	45.8	*0.5*	42.7	*1.9*	42.1	*1.1*	41.4	*1.8*	41.3	*1.5*
Fs	10.8	*0.9*	10.9	*0.8*	15	*2*	10.7	*0.3*	15.3	*0*	10.2	*0.6*	15.7	*1.4*	17.1	*0.6*	16.3	*2.9*	18.3	*1.6*
Mg#	81	*1*	80	*1*	73	*3*	81	*1*	73	*0*	82	*1*	73	*3*	71	*1*	72	*4*	69	*2*

Table 4.8 Mean compositions of clinopyroxene types in all samples. Italics = one standard deviation. MP & GM= microphenocrysts and groundmass. Full analytical datasets are given in Appendices C (basalts) and D (trachyandesite). Mg# = $100Mg/(Mg+Fe^{2+})$. FER=Fe ratio, Fe^{3+}/Fe^{2+}, calculated using stoichiometry. GL=glomerocrysts, Ph=phenocrysts, MP=microphenocrysts, GM=groundmass.

Olivine

Olivine in AMB6 has a homogeneous composition of $Fo_{74.9\pm0.4}$ despite variations in size and morphology (Table. 4.9). AMB2007 contains marginally more forsteritic olivine ($An_{75.5\pm0.3}$), with little compositional variation between the differing textural groups, from large glomerocrystic phenocrysts to rare groundmass microlites (<30 μm).

	AMB6		AMB2007		Craig Cove lava		Trachyandesite			
	All types		Glomerocrysts and GM		Glomerocrysts/ Phenocrysts		Glomerocrysts/ Phenocrysts		Groundmass	
n	29		6		13		26		17	
SiO_2	38.58	*0.19*	38.56	*0.17*	39.16	*0.35*	36.05	*0.42*	35.01	*0.44*
FeO	22.93	*0.44*	22.24	*0.35*	19.05	*1.04*	36.10	*1.14*	39.12	*1.42*
MnO	0.48	*0.04*	0.46	*0.02*	0.40	*0.02*	1.17	*0.05*	1.24	*0.08*
MgO	38.29	*0.21*	38.44	*0.12*	41.21	*0.91*	26.37	*0.89*	23.46	*1.45*
CaO	0.31	*0.07*	0.32	*0.03*	0.26	*0.03*	0.22	*0.04*	0.42	*0.39*
Total	100.76	*0.43*	100.17	*0.47*	100.28	*0.47*	99.98	*0.47*	99.42	*0.42*
Cations on the basis of 4 oxygens										
Si	1.00	*0.00*	1.00	*0.00*	1.00	*0.00*	1.01	*0.01*	1.00	*0.01*
Fe^{2+}	0.50	*0.01*	0.48	*0.01*	0.41	*0.02*	0.85	*0.03*	0.94	*0.04*
Mn	0.01	*0.00*	0.01	*0.00*	0.01	*0.00*	0.03	*0.00*	0.03	*0.00*
Mg	1.48	*0.01*	1.49	*0.00*	1.57	*0.03*	1.10	*0.03*	1.00	*0.05*
Ca	0.01	*0.00*	0.01	*0.00*	0.01	*0.00*	0.01	*0.00*	0.01	*0.01*
Total	3.000	*0.004*	2.997	*0.003*	2.999	*0.004*	2.999	*0.005*	2.995	*0.008*
Fo	74.85	*0.40*	75.50	*0.29*	79.40	*1.23*	56.55	*1.60*	51.64	*2.39*
Fa	25.15	*0.40*	24.50	*0.29*	20.60	*1.23*	43.45	*1.60*	48.36	*2.39*

Table 4.9 Averaged olivine analyses for all samples except AMB2 (none analysed). Figures in italics are one standard deviation for n analyses. GM=groundmass. Full analytical datasets are given in Appendices C (basalts) and D (trachyandesite).

Fe-Ti oxides

Fe-Ti oxide compositions are essentially homogeneous within the basaltic scoria, and can be classified as spinel, with roughly 6 wt.% Al_2O_3, 5 wt.% MgO, 4 wt.% TiO_2, 0.5 wt.% Cr_2O_3, and an Fe^{2+}/Fe^{3+} ratio of 0.6 (Table 4.10). Total iron was recalculated to Fe^{2+} and Fe^{3+} following the method of Carmichael (1967), assuming the minerals to be stoichiometric. Very slightly elevated Cr_2O_3 (0.6 wt.%) was found in a spinel inclusion within an olivine crystal.

	AMB6&7		AMB2007		AMB2		AMB10	AMB86	
n	16		7		2		1	17	
SiO_2	0.16	*0.03*	0.14	*0.01*	0.14	*0.01*	0.07	0.14	*0.06*
TiO_2	4.41	*0.07*	4.48	*0.09*	4.25	*0.13*	4.53	12.90	*1.29*
Al_2O_3	6.04	*0.11*	6.11	*0.12*	6.11	*0.07*	6.09	3.30	*0.36*
Cr_2O_3	0.45	*0.07*	0.43	*0.12*	0.54	*0.06*	5.00	0.01	*0.01*
Fe_2O_3	54.83	*0.66*	53.55	*0.28*	54.92	*0.06*	50.14	39.55	*2.49*
FeO	28.80	*0.31*	28.28	*0.16*	28.51	*0.11*	26.71	39.08	*1.27*
MnO	0.34	*0.03*	0.31	*0.01*	0.30	*0.00*	0.43	0.64	*0.07*
MgO	4.65	*0.24*	4.70	*0.03*	4.73	*0.00*	5.76	2.21	*0.28*
Total	99.68	*0.86*	98.01	*0.41*	99.49	*0.03*	98.72	97.83	*0.84*
Cations recalculated on the basis of 4 oxygens									
Si	0.01	*0.00*	0.01	*0.00*	0.01	*0.00*	0.00	0.01	*0.00*
Ti	0.12	*0.00*	0.12	*0.00*	0.11	*0.00*	0.12	0.36	*0.04*
Al	0.26	*0.00*	0.26	*0.01*	0.26	*0.00*	0.26	0.15	*0.02*
Cr	0.01	*0.00*	0.01	*0.00*	0.01	*0.00*	0.14	0.00	*0.00*
Fe^{3+}	1.48	*0.01*	1.47	*0.01*	1.49	*0.00*	1.36	1.12	*0.06*
Fe^{2+}	0.87	*0.01*	0.86	*0.00*	0.86	*0.00*	0.80	1.23	*0.05*
Mn	0.01	*0.00*	0.01	*0.00*	0.01	*0.00*	0.01	0.02	*0.00*
Mg	0.25	*0.01*	0.26	*0.00*	0.25	*0.00*	0.31	0.12	*0.01*
Total	3.00	*0.00*	3.00	*0.00*	3.00	*0.00*	3.00	3.00	*0.00*
Fe^{2+}/Fe^{3+}	0.6	*0.0*	0.6	*0.0*	0.6	*0.0*	0.6	1.1	*0.1*
Mg#	22.4	*1.7*	22.9	*0.2*	22.8	*0.1*	27.8	9.2	*1.2*
Cr#	4.6	*0.6*	4.3	*1.2*	5.3	*0.5*	34.4	0.2	*0.2*

Table 4.10 Averaged Fe-Ti oxide compositions (n=number of analyses) for basaltic scoria from 2005 (AMB6&7) and 2007 (AMB2007), intracaldera basaltic lava (AMB2), basaltic flank lava (AMB10), and trachyandesite lava (AMB86). Figures in italics=1σ. Mg# = $Mg/(Mg+Fe^{2+})*100$, Cr# = $Cr/(Cr+Al)*100$. Fe_2O_3 is calculated using stoichiometry and charge balance.

Matrix glass and melt inclusions

The matrix glass in the basaltic scoria is basaltic trachyandesitic and is almost identical in glassy samples AMB6 and AMB2007, from 2005 and 2007 respectively (Fig. 4.28; Table 4.11). Sulphur content is slightly higher in the 2007 glass (78–153 ppm) than in 2005 (from below detection limit to 96 ppm). Fluorine and chlorine contents in the glass are indistinguishable between the two samples.

The major element compositions of melt inclusions in AMB6 and AMB2007 plot between the whole rock and matrix glass compositions (Fig. 4.28) with the exception of two higher-SiO_2 outliers. There is some variation between major element compositions of melt inclusions from different host minerals. Olivine- and pyroxene-hosted melt inclusions tend towards less alkalic compositions, and plagioclase-hosted inclusions tend towards more alkalic compositions, possibly an effect of post-entrapment crystallisation; this will be investigated in Chapter 6. Elevated S (up to 1506 ppm) and Cl (up to 845 ppm) contents were found in many inclusions, with F slightly higher (up to 993 ppm) than in the matrix glass.

	AMB6		AMB2007		5_mi7 (AMB6)		olmi1 (AMB2007)	
n	23		3		3		3	
SiO_2	53.01	*0.32*	53.09	*0.10*	52.35	*0.05*	52.23	*0.09*
TiO_2	1.13	*0.05*	1.10	*0.06*	0.77	*0.01*	0.61	*0.03*
Al_2O_3	14.66	*0.17*	14.42	*0.24*	15.15	*0.38*	14.2	*0.19*
FeOt	11.88	*0.49*	11.78	*0.19*	12.20	*0.42*	12.8	*0.17*
MnO	0.24	*0.02*	0.24	*0.02*	0.26	*0.01*	0.29	*0.03*
MgO	4.45	*0.51*	4.58	*0.09*	3.85	*0.14*	5.11	*0.03*
CaO	8.32	*0.55*	8.50	*0.23*	9.29	*0.05*	9.88	*0.12*
Na_2O	3.27	*0.12*	3.34	*0.02*	3.49	*0.16*	2.82	*0.02*
K_2O	2.50	*0.14*	2.38	*0.08*	1.92	*0.06*	1.47	*0.03*
P_2O_5	0.44	*0.02*	0.42	*0.01*	0.36	*0.00*	0.31	*0.01*
F ppm	521	*178*	684	*91*	717	*52*	713	*24*
Cl ppm	323	*43*	333	*23*	571	*9*	442	*10*
S ppm	37	*29*	119	*38*	1082	*31*	702	*11*
Total*	99.13	*0.48*	99.09	*0.35*	98.72	*0.51*	98.6	*0.23*

Table 4.11 Average (**normalised to 100% anhydrous**) of matrix glass compositions of basaltic scorias AMB6 and AMB2007, and representative melt inclusion compositions from each sample. Figures in italics=one standard deviation. *Original analytical totals.

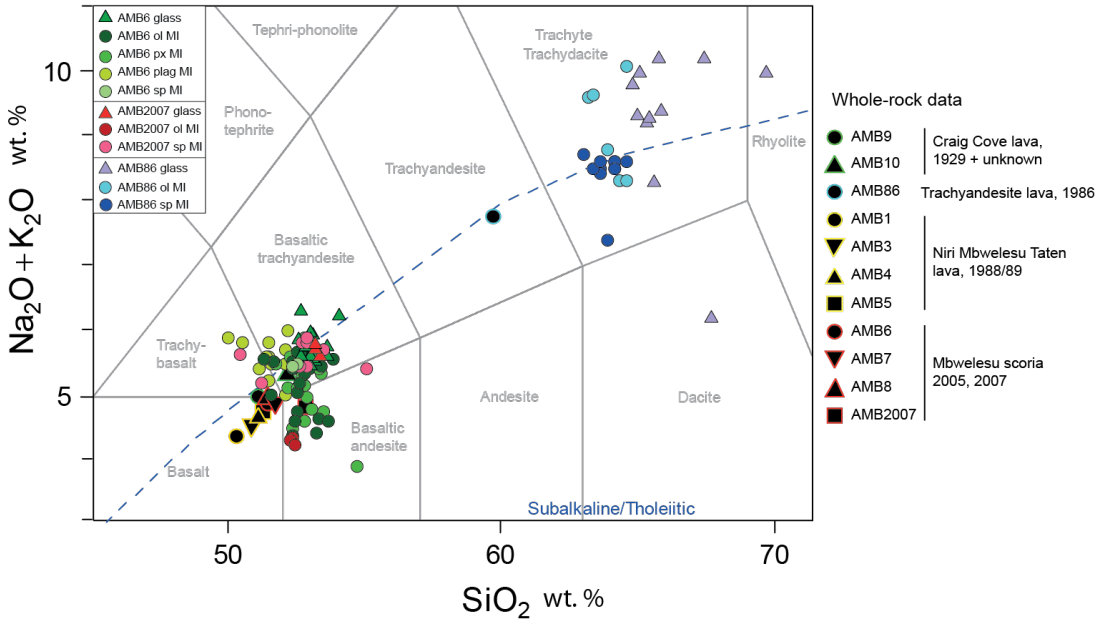

Figure 4.28 Glass and uncorrected MI data for Mbwelesu scoria from 2005 (AMB6) and 2007 (AMB2007), and trachyandesite lava (AMB86), with whole-rock data for comparison. The main cluster of pyroxene-hosted MI in AMB6 lie in the same field as the matrix glass but are obscured here by other datapoints.

Interpretation

Normal zoning in plagioclase indicates evolution of the magma by fractional crystallisation. The minor oscillations recorded by plagioclase zoning may be due to repeated local disequilibrium such as circulation within the magma storage region. The 'fine'

glomerocrysts fall within the compositional range of the microphenocrysts (Fig. 4.23), which along with the morphological similarity between these two types indicates a shared origin followed by aggregation of some, but not all, crystals by synneusis.

The compositional similarity of glomerocryst, euhedral and rounded phenocrystic clinopyroxene suggests a single population with some phenocrysts experiencing resorption, and glomerocrysts derived from synneusis or crystal settling. Concentric oscillatory zoning is considered a growth texture rather than a record of extrinsic variation (Shore & Fowler, 1996). Microphenocrysts show higher Na and Al contents indicating rapid disequilibrium growth.

The homogeneity of olivine compositions from resorbed or euhedral crystals through to groundmass indicates re-equilibration of olivine with the melt as it evolves.

Compared to other island arcs and the rest of the Vanuatu arc, olivine and plagioclase phenocryst compositions analysed in this study fall approximately in the centre of the compositional range, though tending towards the lower side of the average for forsterite compositions (Table 4.12).

	Anorthite mol.%			Forsterite mol.%		
	n	Range	Mean	N	Range	Mean
Lesser Antilles[1]	53	61–98	83±11	42	65–92	81±8
Izu-Bonin[2]	87	56–91	87±7	69	70–98	77±7
Vanuatu[3]	166	40–96	81±11	95	39–93	77±11
Tonga[4]	115	64–96	80±8	93	67–93	84±5
Marianas and Yap[5]	35	76–98	88±7	19	71–91	83±7
Scotia[6]	120	69–96	81±6	84	71–88	84±5
Kurile[7]	61	61–97	81±9	42	60–91	85±8

Table 4.12 Anorthite and forsterite compositions in island arcs. [1]Pichavant & McDonald (2007), Arculus & Wills (1980), Bardintzeff (1984), Fichaut (1989), Pichavant et al. (2002), Gourgaud et al. (1989), Coulon et al. (1984), Smith & Roobol (1990), Parkinson et al. (2003), Sen et al. (1988). [2]Tamura et al. (2007), Ishizuka et al. (2008), Gill et al. (1992), Van der Laan et al. (1992), Ikeda et al. (1989), Tamura (1994), Koyaguchi (1986), Tsuya (1955), Hamuro (1985), Geshi et al. (2002), Arai & Takahashi (1988). [3]Handley et al. (2007), Marcelot et al. (1979, 1983), Maillet et al. (1986), Coulon & Maury (1981), Baker (1994), Coulon et al. (1979), Eissen (1991). [4]Hawkins & Melchior (1985), Hawkins & Allan (1994), Bryan & Ewart (1971), Cawood (1985), Frenzel et al. (1990), Falloon et al. (2007). [5]Michibayashi et al. (2009), Marlow et al. (1992), Stern (1979), Dixon & Batiza (1979), Woodhead (1988), Beccaluva et al. (1980), Lazko & Gladkov (1991), Shiraki et al. (2000). [6]Saunders & Tarney (1979), Pearce et al. (1995), Fretzdorff et al. (2002). [7]Kovalenko et al. (2004), Takazawa et al. (1996), Morishita & Kodera (1998), Morishita & Arai (2001), Takahashi & Arai (1989), Takahashi (1991, 2001), Komatsu (1975), Niida (1984), Shiotani & Niida (1997), Honma (1997), Ikeda et al. (1990), Volynets et al. (1990), Sugawara et al. (1995).

Glass analyses show that the apparent difference on the TAS diagram (Fig. 4.7) between whole rock scoria from 2005 (AMB6–8) and 2007 (AMB2007) is an effect of their respective phenocryst contents. Melt inclusion compositions are consistent with fractional crystallisation, lying as they do between whole rock and glass compositions. Low values for H_2O by difference in melt inclusions suggest low dissolved H_2O content.

4.5.2 Trachyandesite lava

Plagioclase

Anorthite contents in the trachyandesite lava AMB86 (Fig. 4.29, Table 4.13) are $An_{65–48}$ for phenocrysts (with one high-An outlier of An_{74} in a zoned crystal core; Fig. 4.30), $An_{60–49}$ for glomerocryst crystals, and $An_{59–39}$ for groundmass crystals.

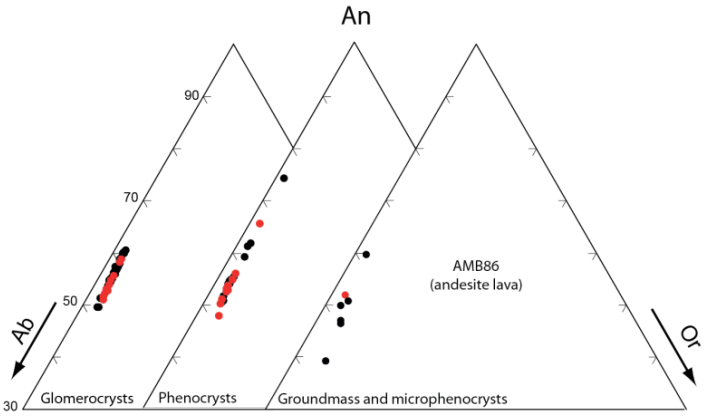

Figure 4.29 Plagioclase compositions for trachyandesite lava AMB86. Note left-hand scale starts at An_{30}. Black=core, red=rim.

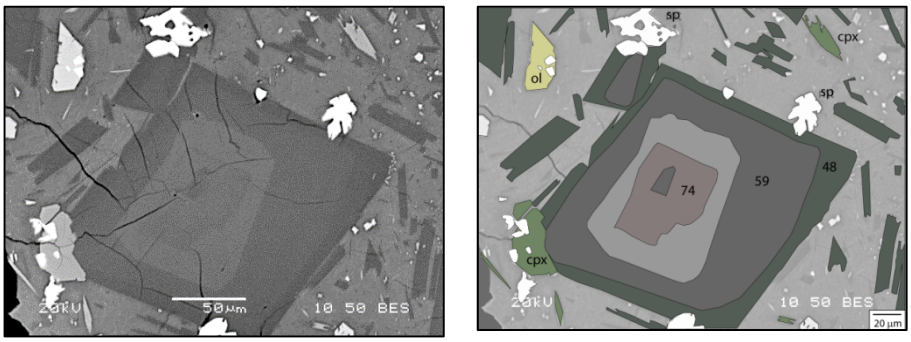

Figure 4.30 Normally-zoned plagioclase in trachyandesite AMB86; SEM image (left,)and digitised, annotated version (right). The near-core composition (An_{74}) is the highest An content recorded in the trachyandesite lava by a significant margin. The innermost and third innermost zones were not visible on the electron microprobe SEM. The brightness of the zones, in which brighter zones are more calcic, indicates that the core is less calcic, and the third zone from the centre is more calcic than the An_{74} zone, so this crystal appears to exhibit oscillatory rather than normal zoning. The greyscale brightness of the core appears comparable to that of the An_{59} zone.

There is no systematic variation of phenocrystic anorthite content with size. Phenocrysts show reverse, normal and oscillatory zoning. The normally-zoned crystals have cores of $An_{74–58}$ and rims of $An_{62–55}$. Reverse zoned crystals were found to have cores of $An_{62–50}$ and rims of $An_{65–52}$. For most phenocrysts, only a single core and single rim analysis were obtained so finer scale zoning is not recorded. Detailed traverses of large phenocrysts reveal oscillatory zoning (Fig. 4.31). In light of this, crystals analysed only at ‘core’ and ‘rim’ should be only tentatively designated reverse or normal zoned, as analyses may have sampled an oscillation in anorthite content rather than a large zone.

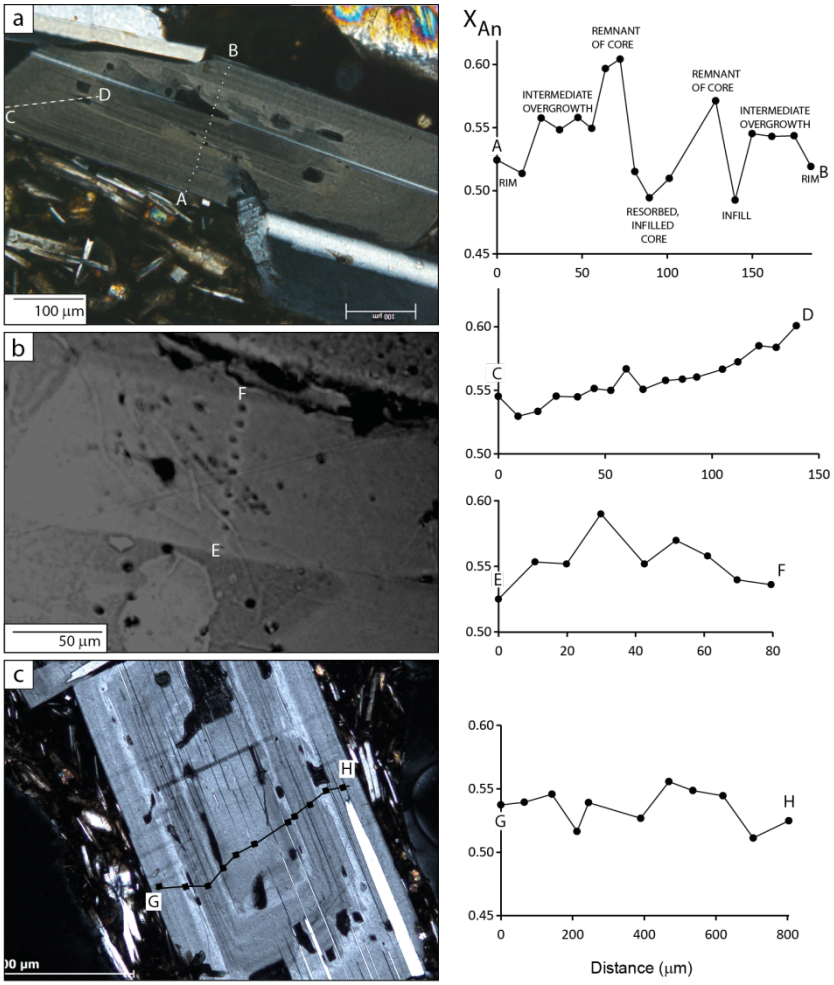

Figure 4.31 EPMA traverses of large plagioclase phenocrysts in trachyandesite lava AMB86. The upper two panels are cross-polarised **(a)** and reflected-light **(b)** images of adjacent, overlapping areas, with transects A–B and most of C–D included in both. The EPMA scars of the traverses can be seen in the reflected light image and faintly in the XP image. **c)** Back-scattered electron image of a different crystal, with microprobe traverse overlain.

	AMB2		AMB10								AMB86			
	Phenocrysts		Coarse glomerocrysts		Fine glomerocrysts		Skeletal		Grmass		Phenocrysts/glomerocrysts		Groundmass	
n	5		9		76		2		1		18		6	
SiO_2	49.32	*1.54*	51.30	*0.51*	51.10	*0.62*	48.74	*0.12*	54.67		53.58	*1.61*	56.37	*1.83*
Al_2O_3	30.23	*1.13*	29.63	*0.32*	28.87	*0.39*	30.45	*0.04*	27.62		28.17	*0.87*	26.46	*1.27*
FeOt	1.23	*0.29*	1.09	*0.04*	1.20	*0.03*	1.21	*0.07*	1.45		0.68	*0.13*	0.81	*0.11*
MgO	0.14	*0.06*	0.16	*0.01*	0.17	*0.01*	0.14	*0.01*	0.17		0.08	*0.02*	0.09	*0.03*
CaO	14.67	*1.21*	13.30	*0.37*	13.27	*0.44*	14.84	*0.34*	11.28		11.76	*1.23*	9.89	*1.33*
Na_2O	2.78	*0.65*	3.65	*0.20*	3.41	*0.22*	2.56	*0.18*	4.96		4.60	*0.67*	5.50	*0.68*
K_2O	0.24	*0.08*	0.45	*0.04*	0.45	*0.05*	0.29	*0.03*	0.81		0.41	*0.10*	0.79	*0.28*
SrO	0.17	*0.02*	0.16	*0.01*	0.17	*0.02*	0.15	*0.02*	n.d.		0.19	*0.03*	0.19	*0.03*
Total	98.69	*0.35*	99.80	*0.20*	98.57	*0.30*	98.31	*0.14*	100.99		99.52	*0.43*	100.31	*0.69*
Cations on the basis of 8 oxygens														
Si	2.29	*0.06*	2.35	*0.02*	2.37	*0.02*	2.27	*0.01*	2.46		2.45	*0.06*	2.55	*0.07*
Al	1.65	*0.06*	1.60	*0.02*	1.58	*0.02*	1.67	*0.00*	1.47		1.52	*0.06*	1.41	*0.07*
Fe^{2+}	0.04	*0.01*	0.04	*0.00*	0.04	*0.00*	0.04	*0.00*	0.05		0.03	*0.00*	0.03	*0.00*
Mg	0.01	*0.00*	0.01	*0.00*	0.01	*0.00*	0.01	*0.00*	0.01		0.01	*0.00*	0.01	*0.00*
Ca	0.73	*0.06*	0.65	*0.02*	0.66	*0.02*	0.74	*0.02*	0.54		0.58	*0.06*	0.48	*0.07*
Na	0.25	*0.06*	0.32	*0.02*	0.31	*0.02*	0.23	*0.02*	0.43		0.41	*0.06*	0.48	*0.06*
K	0.01	*0.00*	0.03	*0.00*	0.03	*0.00*	0.02	*0.00*	0.05		0.02	*0.01*	0.05	*0.02*
Total	4.99	*0.00*	5.00	*0.00*	4.99	*0.00*	4.99	*0.00*	5.02		5.01	*0.00*	5.01	*0.00*
An	73.42	*6.21*	65.06	*1.88*	66.42	*2.23*	74.89	*1.76*	53.18		57.19	*6.23*	47.66	*6.90*
Ab	25.14	*5.79*	32.34	*1.72*	30.89	*1.96*	23.38	*1.61*	42.29		40.42	*5.70*	47.85	*5.56*
Or	1.44	*0.45*	2.60	*0.20*	2.69	*0.28*	1.72	*0.15*	4.53		2.39	*0.56*	4.50	*1.53*

Table 4.13 Averaged compositions of plagioclase types in lava flow samples AMB2 (intracaldera basaltic lava flow, 1988), AMB10 (basaltic flank lava, date unknown), and AMB86 (trachyandesite lava, 1986). Figures in italics are one standard deviation. Full analytical datasets are given in Appendices C (basalts) and D (trachyandesite).

Clinopyroxene

Clinopyroxene phenocrysts cover a range of $En_{40–44}Wo_{38–42}Fs_{17–19}$ (Fig. 4.32; Table 4.8). A glomerocryst of 400–500 μm diameter euhedral crystals shows compositions of $En_{40–44}Wo_{40–42}Fs_{15–18}$, while microphenocrysts (100–400 μm) span a wider compositional range ($En_{37–45}Wo_{37–44}Fs_{14–22}$), as do groundmass crystals ($En_{38–45}Wo_{34–43}Fs_{18–21}$).

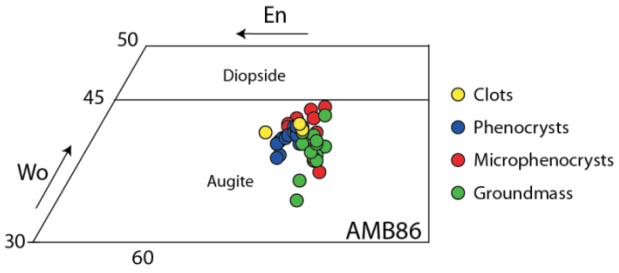

Figure 4.32 Clinopyroxene compositions in trachyandesite lava AMB86. Enlarged area of the En-Wo-Fs triangle is the same as that shown in Fig. 4.26.

Olivine

Olivine compositions show a distinction between glomerocryst crystals/phenocrysts, with cores of $Fo_{59–56}$ and rims of $Fo_{57–51}$, and groundmass crystals, with compositions of $Fo_{56–45}$ (Table 4.9).

Fe-Ti oxides

Fe-Ti oxides in the trachyandesite can be classed as spinel, and are more variable and more reduced than in the basaltic scoria, with 9.4–13.7 wt.% TiO_2 and Fe^{2+}/Fe^{3+} of 1.1±0.1 (Fig. 4.33; Table 4.10). Cr_2O_3 and NiO contents are negligible. The trachyandesite spinels have higher TiO_2 and lower FeOt, MgO (2 wt.%) and Al_2O_3 (3 wt.%) than their basaltic counterparts. The compositional difference between spinel types (glomerocryst crystals vs. groundmass) in the trachyandesite (Fig. 4.28) follows a progression from lowest Ti-Fe^{2+}/Fe^{3+} (relatively oxidised) in spinels included within phenocrysts and constituent in glomerocrysts, to highest Ti-Fe^{2+}/Fe^{3+} (relatively reduced) in spinels attached to phenocryst rims and in the groundmass.

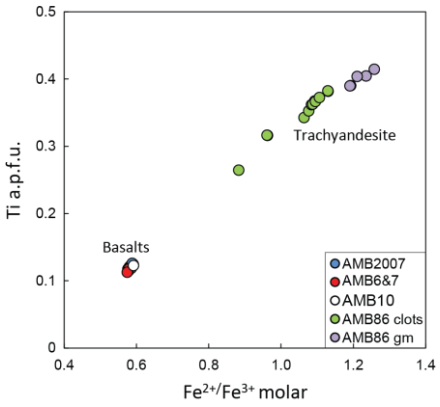

Figure 4.33 Ti vs. Fe^{2+}/Fe^{3+} ratio (calculated by charge balance) for spinel in all samples. Spinel compositions in the more mafic samples cluster very tightly but show a broad, linear spread in the trachyandesite. 'Glomerocrysts' denotes crystals included in phenocryst aggregates, 'gm' denotes groundmass crystals.

Pyrrhotite

Pyrrhotite, found only in the trachyandesite lava sample, shows compositions of ~$Fe_{48–46}S_{54–52}$. Ni content is below the detection limit.

Apatite

Apatite compositions in the trachyandesite form two clusters (Fig. 4.34), of lower and higher fluorine. The higher-F apatites occur as 20–50 μm subhedral crystals included within large plagioclase and clinopyroxene phenocrysts, whereas the lower-F crystals tend to be groundmass crystals or inclusions in microphenocrysts (Table 4.14), although some are inclusions in phenocrysts. Sulphur content is low (2–249 ppm) and shows no correlation with F or Cl.

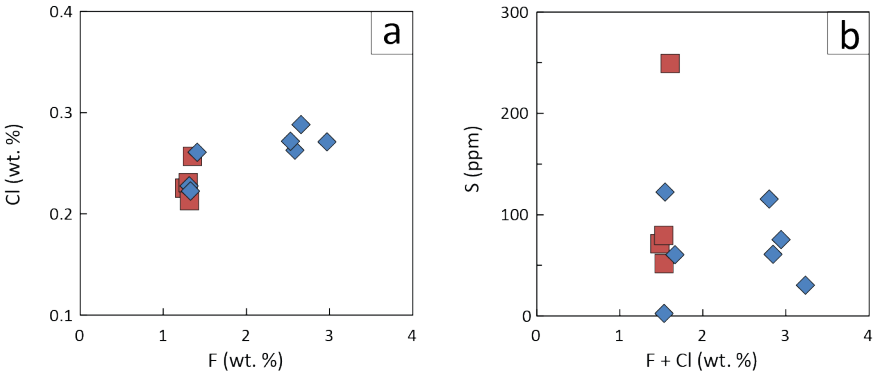

Figure 4.34 Cl, F and S in apatite in trachyandesite lava AMB86. **a:** Chlorine vs. fluorine. **b:** Sulphur vs. total fluorine and chlorine. Red=free-floating apatite microphenocrysts and inclusions in microphenocrystic clinopyroxene. Blue=apatite inclusions in phenocrystic plagioclase and clinopyroxene.

	Low-fluorine		High-fluorine	
	n=7		n=4	
CaO	53.75	*0.29*	54.39	*0.29*
P_2O_5	43.00	*0.58*	41.35	*0.61*
SiO_2	0.21	*0.04*	0.24	*0.13*
FeO	0.52	*0.08*	0.78	*0.47*
MgO	0.24	*0.01*	0.23	*0.03*
MnO	0.12	*0.01*	0.11	*0.04*
Na_2O	0.05	*0.01*	0.04	*0.02*
F_{corr}	1.33	*0.05*	2.69	*0.20*
Cl_{corr}	0.23	*0.02*	0.27	*0.01*
SO_2	0.02	*0.02*	0.01	*0.01*
S ppm	91	*78*	70	*35*
$Total_{recalc}$	99.64	*0.67*	100.20	*0.80*

Table 4.14 Averaged low-F and high-F apatite compositions in AMB86 trachyandesite lava. Analyses were corrected for the presence of F and Cl by subtracting the oxygen equivalents of F and Cl from the analytical total. F_{corr} and Cl_{corr} are the corrected F and Cl contents and $Total_{recalc}$ is the total recalculated after corrections. Figures in italics are one standard deviation.

Matrix glass and melt inclusions

Groundmass glass in the trachyandesite is predominantly trachydacitic (Fig. 4.28; Table 4.15), and quite variable, covering a range of 64.5–69.5 wt.% SiO_2 (anhydrous). Sulphur content ranges from below detection limit to 183 ppm. Chlorine is significantly higher than in the basaltic scoria matrix glass, and fluorine slightly higher (Fig. 4.35).

	Matrix glass		Melt inclusion	
N	11		2	
SiO_2	65.89	*1.54*	62.98	*0.10*
TiO_2	0.79	*0.05*	0.63	*0.03*
Al_2O_3	14.40	*0.95*	16.85	*0.14*
FeOt	5.48	*1.14*	4.45	*0.12*
MnO	0.16	*0.05*	0.13	*0.01*
MgO	0.90	*0.38*	0.67	*0.04*
CaO	2.60	*0.74*	3.96	*0.18*
Na_2O	4.12	*0.82*	4.90	*0.01*
K_2O	5.16	*0.80*	4.74	*0.01*
P_2O_5	0.33	*0.17*	0.41	*0.00*
F ppm	798	*232*	896	*14*
Cl ppm	986	*247*	1166	*1*
S ppm	59	*55*	367	*17*
Total*	100.65	*0.92*	101.67	*0.18*

Table 4.15 Average (normalised to 100% anhydrous) of matrix glass compositions of trachyandesite lava AMB86, and representative olivine-hosted melt inclusion composition. Figures in italics=one standard deviation.

*Original analytical totals.

Silicate melt inclusions were analysed in olivine and spinel. Their compositions are trachydacitic and less variable than matrix glass compositions, with 62.8–64.5 wt.% SiO_2 on

an anhydrous basis (Fig. 4.28, Table 4.15). There is a clear compositional gap between the melt inclusions and the trachyandesite whole-rock. Spinel-hosted melt inclusion compositions mainly cluster closely, while olivine-hosted inclusions are more scattered, with higher alkali content. Olivine-hosted melt inclusion compositions have lower MgO and FeO than the spinel-hosted inclusions, indicating post-entrapment modification, which will be addressed in Chapter 6.

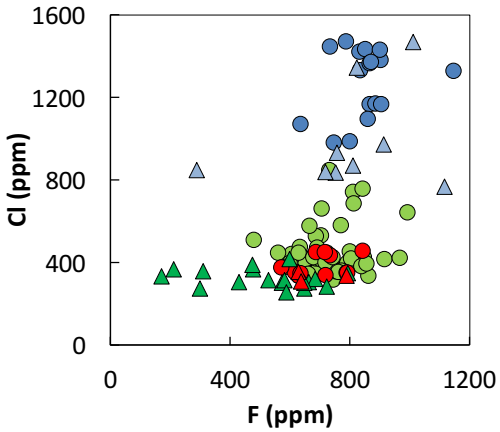

Figure 4.35 Fluorine and chlorine contents of matrix glass (triangles) and melt inclusions (circles) in basaltic scoria from 2005 (AMB6; green) and 2007 (AMB2007; red), and trachyandesite lava (AMB86; blue).

Interpretation

The trachyandesite contains a distinct crystal population which is more evolved than the basaltic crystals. Clinopyroxene, olivine and spinel compositions are clearly distinct from those in the basalts, while plagioclase is generally more evolved (~An_{60-50}). Melt inclusions in olivine and spinel phenocrysts are trachydacitic, which indicates growth of these phases from a trachydacitic melt. Rare calcic cores in plagioclase may be derived from mixing with a more mafic magma or entrained cumulate, or an antecrystic inheritance from a mafic parent. The presence of rare basaltic phenocryst remnants (augite, bytownite) alongside fayalitic olivine with trachydacite inclusions, in dacitic-to-rhyolitic glass, indicates that the trachyandesite formed by mixing of phenocrystic basalt, or basaltic cumulates, with trachydacitic melt. The low F content of melt inclusions imply that melt inclusion hosts crystallised from a degassed melt.

Spinel with associated pyrrhotite tends to occur partly included in olivine, and spinel-hosted melt inclusions are also trachydacitic; these observations indicate that spinel, olivine and pyrrhotite all derive from a trachydacitic melt.

Olivine displays higher-forsterite (glomerocrysts and resorbed phenocrysts) and lower-forsterite (microphenocrysts and groundmass) populations. Both rapid-growth and resorption

textures occur in olivine crystals of similar composition, possibly indicating convection-related thermal or compositional disequilibrium.

Calculated ferrous/ferric iron ratios in spinel and clinopyroxene (Section 4.5.2) demonstrate that the trachyandesite is more reduced than the basalts. Groundmass spinel is more reduced than spinel inclusions within other phases, indicating progression towards more reducing conditions during crystallisation. The linear progression (Fig. 4.33) indicates crystallisation of spinel in a continuous, progressively more reduced, interval rather than mixing of phenocrysts and groundmass crystallised in two distinct redox environments.

Fluorine contents of apatite, given the essentially constant $D_F^{melt\text{-}apatite}$ of ~3.4 in silicate melts (Mathez & Webster, 2005), imply two stages of apatite crystallisation at melt contents of 0.7–0.9 wt.% F (early-crystallised inclusions in phenocrysts) and 0.4 wt.% F (groundmass and inclusions in microphenocrysts) respectively. The matrix glass contains 0.08±0.02 wt.% F. Melt inclusion (olivine- and spinel-hosted) fluorine contents are 0.07–0.09 wt.%, indicating that they do not represent the melt from which early apatite crystallised. Two possible explanations for this are that: i) apatite composition was controlled by changes in the melt or fluid phase F content, or: ii) initial apatite crystallisation caused a decrease in melt F content.

4.5.3 Niri Mbwelesu Taten lava

Plagioclase phenocrysts in intracaldera basaltic lava sample AMB2 have compositions of $An_{79–65}$ (Fig. 4.36; Table 4.13), but only a small number of plagioclase crystals (5) were successfully analysed in this sample. The highest An content (An_{80}) is displayed by a sieved, blocky 200 μm crystal, and the lowest by a lath-shaped microphenocryst (An_{64}).

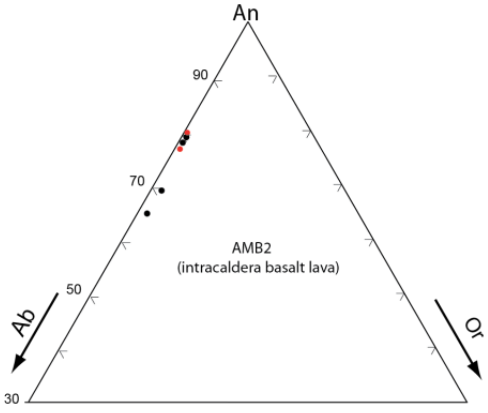

Figure 4.36 Plagioclase compositions for lava sample AMB2. Note that left-hand scale starts at An_{30}. Black=core, red=rim.

Clinopyroxene compositions fall in the diopside to augite field (Fig. 4.37). Phenocrysts are more Mg-rich, around ~$En_{41–42}Wo_{42–46}Fs_{13–17}$ (Fig. 4.37; Table 4.8). Microphenocrysts are

$En_{40–44}Wo_{38–43}Fs_{17–19}$ and groundmass crystals are diopsidic (over the range $En_{36–39}Wo_{45}Fs_{16–19}$), with higher iron and aluminium contents.

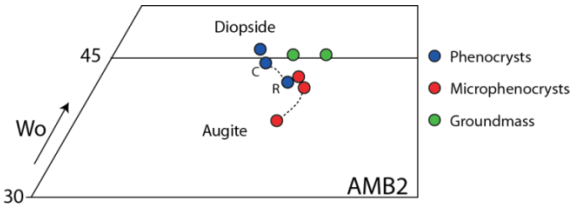

Figure 4.37 Clinopyroxene compositions in Niri Mbwelesu Taten lava AMB2. Dotted lines connect multiple analyses of same crystal; C=core, R=rim. Enlarged area of the En-Wo-Fs triangle is the same as that shown in Fig. 4.21.

No olivine was successfully analysed. Two Fe-Ti oxide crystals were analysed and show the same composition as those in the basaltic scoria (Fig. 4.33; Table 4.10).

Interpretation

Overlapping plagioclase and clinopyroxene phenocryst compositions, and identical olivine and spinel phenocryst compositions, indicate a similar source for these lava flows and the Mbwelesu scoria (AMB6, AMB7, AMB2007), although whole rock data indicate a slightly more mafic composition.

4.5.4 Craig Cove lava (AMB10)

The anorthite contents of both large and small glomerocryst plagioclase in AMB10 (Fig. 4.38, Table 4.13) fall in the range of $An_{74–62}$. The glomerocrystic plagioclase displays reverse and oscillatory zoning, with labradoritic cores and bytownitic rims. The highest anorthite content observed, An_{75}, occurs in a sieve-textured plagioclase phenocryst. A single groundmass crystal analysis (the only such analysis with an acceptable cation total) is significantly more sodic (An_{53}) than the glomerocryst plagioclase (Appendix E).

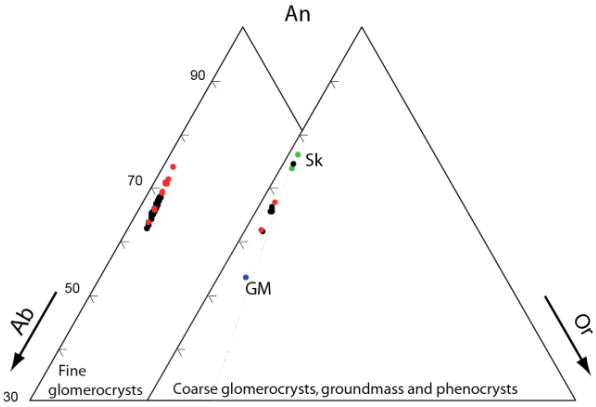

Figure 4.38 Plagioclase compositions for Craig Cove lava AMB10. Glomerocrysts: black=core; red=rim. Green (Sk)=skeletal phenocrysts; blue (GM)=groundmass.

Glomerocryst clinopyroxene compositions cluster around $En_{42}Wo_{44}Fs_{14}$ (Fig. 4.39), with $\sigma < 0.4$ for each component (n=8), and are slightly Chromian compared to clinopyroxene in all other samples (Cr_2O_3=0.13wt.%) . Other phenocrysts and groundmass were not analysed.

Rounded mafic glomerocryst olivine has a composition of ~Fo_{78}, and large euhedral, embayed phenocrysts have compositions of $Fo_{78–82}$ (Table 4.9). Groundmass olivine is less than 5 μm in size, not large enough for microprobe analysis. Forsterite content varies in an unsystematic manner across embayed phenocrysts, by up to several mole percent.

Only one Fe-Ti oxide analysis has been obtained for this rock sample, of an inclusion in olivine in a mafic glomerocryst. This analysis (Table 4.10) can be classed as spinel, and shows effectively identical TiO_2 and Al_2O_3 contents to the basaltic intra-caldera lava and scoria, with slightly higher Mg and significantly higher Cr_2O_3 (5 wt.%), with lower total iron but the same Fe^{2+}/Fe^{3+} ratio of 0.6.

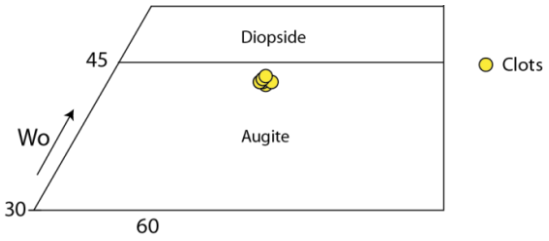

Figure 4.39 Clinopyroxene compositions in Craig Cove lava AMB10. Enlarged area of the En-Wo-Fs triangle is the same as that shown in Fig. 4.21.

Interpretation

The high proportion of sieved plagioclase megacrysts and heavy resorption of olivine in this lava suggests transport of these phases from their original region of crystallisation to a storage region in which they were in disequilibrium. The combination of Cr-rich spinel, skeletal bytownitic ($An_{74–76}$) plagioclase and embayed, relatively high-Fo olivine ($Fo_{78–82}$) suggests the mixing of a more mafic assemblage with the megacrystic plagioclase glomerocrysts (~An_{65}). Higher-Fo olivine with Cr-rich spinel may be a relic of a high-Mg basaltic precursor to the high-Al basalt (analogous to Kliuchevskoi; Almeev et al., 2013). Sieved labradorite megacrysts and reverse zoning of the smaller glomerocryst plagioclase (bytownite rims around labradorite) may indicate derivation of these phases from higher pressures—plagioclase composition is more albitic at higher pressures for high-Al, low-H_2O basaltic melts (Longhi et al., 1993) similar to this composition—followed by partial resorption and/or bytownitic overgrowth when transported to a lower pressure storage region prior to eruption. Another possibility is higher-anorthite overgrowth due to increased concentration of water in the residual melt with crystallisation (Almeev et al., 2012, Danyushevsky et al., 1997).

4.6 Discussion

4.6.1 Mbwelesu scoriae and Niri Mbwelesu Taten lava

The Mbwelesu scoriae (AMB6, AMB7, AMB2007) display an assemblage in which plagioclase and spinel crystallisation preceded cotectic plagioclase-spinel-clinopyroxene-olivine crystallisation. Normal zoning of phenocrysts, and progression to more evolved compositions in microphenocrysts and groundmass, is consistent with fractional crystallisation, with minor oscillations suggesting small-scale variations in magmatic environment perhaps due to convection within the magma storage region. Melt inclusion compositions are also consistent with fractional crystallisation, having trapped a composition intermediate between whole rock and matrix glass.

Early spinel crystallisation and minor high-anorthite plagioclase—the record is dominated by labradoritic to bytownitic plagioclase—indicating that water was present (Sisson & Grove, 1993) early in the crystallisation history. However, the high proportion of plagioclase throughout the volcanic history does not follow the prediction (Sisson & Grove, 1993) that the presence of water should lead to a reduced proportion of plagioclase.

Resorption textures such as rounding and fritting indicate episodes of thermal or chemical dissolution which, along with the constancy of magma composition from the intracaldera cones, indicates that the system is periodically replenished, causing temporary states of cognate disequilibrium. Glomerocrysts and sieve-textured plagioclase in particular indicate recharge. Long-term high-level degassing (cf. Section 2.2.5) indicates sustained supply of fresh magma despite low erupted volume. Sustained magma supply may drive magma convection by heating from below, with resorption occurring in the heated region.

The slightly more primitive composition of the Niri Mbwelesu Taten lavas (AMB1–5) suggests that the 1988/89 eruption sampled a slightly more primitive magma, perhaps a replenishing pulse from depth, although identical olivine and spinel compositions to the Mbwelesu scoria indicate a common parent for the two magmas. These lavas appear closer to a true liquid, with low phenocryst content. Those phenocrysts present have the appearance of disequilibrium.

Clinopyroxene aggregates are seen in the scoria (Fig. 4.13c), intracaldera lava (Fig. 4.21f) and flank lava (Fig. 4.22e), possibly recording disaggregated pyroxene-rich cumulates in erupting lavas throughout the edifice. These glomerocrysts show rounded boundaries, suggesting partial resorption once incorporated into mobile magma.

4.6.2 Trachyandesite

The trachyandesite magma bears a more evolved phenocryst population, with microphenocrysts and groundmass newly crystallised from a more evolved magma, along with multi-mineralic cumulate-textured glomerocrysts and rare vestiges of more mafic compositions found in high-anorthite cores of large plagioclase phenocrysts (now resorbed or overgrown) and possible minor inheritance of clinopyroxene. Resorption textures in plagioclase and clinopyroxene crystals indicate that some of these crystals may be inherited or entrained from a different magma or cumulate. Plagioclase in particular suggests mixing of mafic phenocrysts into an evolved liquid, e.g., a high-An (An_{74}) core with a sudden jump to An_{59} then An_{48} records a sudden disequilibrium (Fig. 4.30), and patchy zoning where andesine has infilled labradorite (Fig. 4.31).

There is textural evidence for both rapid growth and resorption just prior to eruption. Spinel compositions and the presence of pyrrhotite indicate a reduced magma (note: pyrrhotite may have arrived in cumulate glomerocrysts), progressively more reduced as crystallisation proceeded.

Olivine- and spinel-hosted melt inclusions are trachydacitic, demonstrating that the host minerals crystallised from a trachydacitic liquid, close to the matrix glass composition of the trachyandesite. The scatter of olivine MI compositions suggests that they may represent late-stage entrapment of evolved, heterogeneous matrix glass, or may have undergone post-entrapment crystallisation (PEC); the spinel-hosted MI are more closely clustered and may record a more homogeneous magmatic liquid (or lower susceptibility to PEC). The bulk composition may represent a hybrid of trachydacitic melt with more mafic inherited crystals alongside phases (phenocrysts, microphenocrysts and groundmass) crystallised in situ. The relationship between the basalt and the trachyandesite will be further investigated via geochemical modelling in Chapter 5.

Two possible sources (other than fractional crystallisation) for a trachydacitic melt are extraction of silicic partial melt from basaltic crust, or segregation of silicic melt from crystallising basaltic bodies stalled in the crust. Segregation lenses of silicic melt within the edifice may form in basaltic/gabbroic sill-like bodies from tearing and filling of the solidification front (Marsh et al., 2008). Silicic eruptions of 0.01–0.30 km^3 volume at Torfajökull, Iceland are believed to have formed by this method (Gunnarsson et al., 1998). The estimated volume of the 1986 trachyandesite flow is in the same order of magnitude at 0.01 km^3 (using an area of ~2.1 km^2, measured from satellite imagery, and average flow thickness of 5 m, estimated from field observation).

Indications from geophysical data that the trachyandesite region is still active (Legrand et al., 2005) suggests that future silicic eruptions may be forthcoming in the eastern part of the caldera, with attendant hazard implications given the potential higher explosivity of evolved magmas.

4.6.3 Craig Cove lava

The flank lava appears to record flushing of plagioclase megacrysts from depth, potentially by a high-Mg basalt.

4.7 Conclusions

Major and trace element patterns for Ambrym volcano demonstrate the importance of fractional crystallisation in magma evolution, showing evidence of fractionation of olivine, plagioclase, clinopyroxene and Fe-Ti oxides, which corresponds to the observed phase assemblage. Mineral compositions, textures and zoning patterns in the basalts also reflect fractional crystallisation, showing normal zoning and compositional progressions with crystal size congruous with evolution via progressive fractionation.

The studied samples cluster at a break in slope where olivine crystallisation gave way to olivine, clinopyroxene and plagioclase crystallisation. Trace elements demonstrate that the suite of studied samples share a parent magma, with almost identical patterns, differing only in elevation of incompatible elements in the trachyandesite.

The mafic samples represent a long-lived plagioclase basalt composition which has remained effectively constant since the beginning of the post-caldera period c. 2 Ka (see Section 2.2.5), indicating that the predominant magma generation mechanism is in a stable state, on a timescale of Ka. Textures and zoning indicate crystal convection, most likely to be thermally driven by injections of higher-temperature basaltic magma into shallow magma reservoirs.

Trachydacitic olivine- and spinel-hosted melt inclusions and relatively mafic plagioclase and clinopyroxene compositions indicate derivation of the trachyandesite by mixing of basalt with trachydacite.

Chapter 5 Geochemical modelling

5.1 Introduction

This chapter investigates magma storage conditions and shallow-level magma evolution at Ambrym using mass balance modelling and mineral-melt equilibria. New constraints, based on the petrological data presented in Chapter 4, are placed on temperature, pressure, oxygen fugacity, water content and crystallisation paths using mineral-melt equilibria. These constraints can be used to test models for magma storage suggested by petrography and geochemistry.

This chapter will build on constraints from petrography and petrology and collect the results and conclusions in a summary model of the system.

5.2 Magmatic differentiation

Of the samples studied, the majority represent a similar, approximately basaltic composition with minor compositional differences primarily controlled by variations in crystal cargo. The trachyandesite represents a clearly distinct composition with more evolved mineralogy. Trace element variations reflect these observations, being almost identical within the more basaltic subset of samples, and similar but more enriched in incompatible elements for the trachyandesite (Fig. 4.9).

Ambrym lava compositions tend to cluster around 50–53 wt.% SiO_2 and 4–5 wt.% MgO over a long timescale, returning to this as the dominant composition in every volcanic phase since the shield stage of the early volcanic history (Fig. 4.1). Flank eruptions appear to sample the same source as the central vents, in some cases picking up cumulates of plagioclase and more mafic mineralogies such as Cr-spinel and relatively high-forsterite olivine. Ancient olivine basalts from the earliest phase of volcanism represent a distinct primitive composition, but later, rare occurrences of high-MgO basalt are otherwise similar to plagioclase basalts and notably contain olivine of lower forsterite content (Fo_{79}, as in the plagioclase basalts) than equilibrium with the high-MgO whole rock would require, suggesting olivine accumulation (Picard et al., 1995). More evolved compositions are limited to the tuff-cone-forming event and the modern trachyandesite.

The combination of constant composition and long-term prodigious degassing from the central vents indicate that a supply of compositionally constant basaltic magma is fed to the

surface via an open-system conduit. In contrast, the trachyandesite eruption represents a single emission of geochemically distinct lava at a site which showed no previous or subsequent activity, although the shallow storage region is inferred from very long period tremor (VLPT) recordings (Legrand et al., 2005) to be still active beneath the surface. Clarification of the relationship between the basalt and trachyandesite sources remains a major outstanding question at Ambrym.

Recordings of very long period tremor showed a possible connection between the central basaltic and eastern trachyandesitic storage regions within the caldera, whereby one source became dominant when the other entered a period of quiescence (Legrand et al., 2005; see Section 4.1.5). This suggests that magma may be periodically diverted into the eastern storage region from a source shared with the central vents.

Trace element patterns also suggest a close link between the basaltic and trachyandesitic magmas (Section 4.3). Enrichment in incompatible elements (Ba, Rb, Th, Nb, Zr, Y, La and Ce), and decrease in Sr and Eu (Table 4.4), may be consistent with fractional crystallisation or mixing of cogenetic magmas. Mixing of cogenetic products could involve basalt mixing with the fractionated product of its own parent magma (e.g., Sakuyama, 1981) or partial melts of gabbroic cumulates. Ratios of incompatible elements (K/Rb, Ba/Rb and Zr/Rb) remain approximately constant from basalt to trachyandesite (e.g., Fig. 411d), supporting fractional crystallisation rather than derivation of trachyandesite by partial melting of the subvolcanic crust.

It is difficult to distinguish between fractionation and mixing using major or trace elements, as either process may result in a linear trend; although fractional crystallisation will cause notable inflections in some of the patterns, these may not be obvious or present in evolution from a relatively evolved (53 wt.% SiO_2) basalt to a trachyandesite with the same, though more evolved, phase assemblage. Rare calcic cores in plagioclase phenocrysts in the trachyandesite could derive either from a fractional crystallisation parent, or a mafic mixing component. Similarly, fayalitic olivine in the trachyandesite could represent phenocrysts from an evolved mixing component, or late-stage crystallisation from evolved residual liquid produced by fractional crystallisation.

The potential hypotheses—fractional crystallisation, magma mixing, or partial melting of the crust, or combinations thereof—are evaluated below, using petrological observations and geochemical modelling.

5.2.1 Fractional crystallisation

The fractional crystallisation hypothesis may be tested by removing phenocryst fractions from a nominal parent basalt composition and comparing the resulting liquid with the trachyandesite. Basaltic scoria AMB6 is chosen here as the nominal parent composition, as it is the most well-characterised sample and derives from the central vents which have a demonstrated connection with the trachyandesite source. It also sits within the field of the dominant basaltic composition at Ambrym. The compositions and proportions of crystallisation necessary to produce a trachyandesitic liquid can also be compared to observed phase proportions to assess the viability of the model.

The least-squares mass balance calculation program XLFRAC (Stormer & Nicholls, 1978) indicates that removal from AMB6 basalt (whole rock) of plagioclase (26% of initial mass), augite (15%), spinel (5%) and olivine (3%), of phenocryst compositions observed in the basalt (Table 5.1), can produce the trachyandesite whole rock composition with a sum of squares of residuals (SSR) of 0.072, where an SSR value of less than 2 represents a satisfactory fit (Stormer & Nicholls, 1978).

	Initial magma[a]	Plag	Cpx	Spinel	Olivine	Normalised derivative magma[b]	Trachy-andesite AMB86[c]	R^2
Removed		25.5	14.5	5.3	3			
Observed		19.4	3.9	0.7	0.4			
SiO_2	52.41	49.37	51.1	0.16	38.48	60.58	60.69	0.010
TiO_2	0.94	0.03	0.51	4.72	0.02	0.99	0.80	0.038
Al_2O_3	17.33	31.27	3.51	6.48	0.04	16.51	16.57	0.004
FeOt	10.39	1.15	9.19	83.52	22.98	7.12	7.21	0.009
MgO	4.65	0.14	14.93	5.05	38.15	2.03	2.07	0.001
CaO	9.27	15.13	20.4	0.08	0.31	4.74	4.78	0.001
Na_2O	2.98	2.65	0.34	0.00	0.01	4.32	4.27	0.003
K_2O	2.02	0.26	0.01	0.00	0.02	3.70	3.62	0.007
Total								0.072

Table 5.1 Mass balance calculations demonstrating generation of 'normalised derivative magma' by removal of observed phenocryst fractions from basalt AMB6, and closeness of fit to natural trachyandesite AMB86. Table includes phase compositions used in mass balance calculations. Spinel is normalised to 100. The 'Removed' and 'Observed' rows show the modelled percentage of crystallisation required to produce the trachyandesite liquid (total=48.3%) and the actual phenocryst proportions in AMB6 (total=24.4%), respectively. [a] AMB6WR (normalised for selected 8 oxides, all Fe as FeO). [b] Composition calculated by removal of crystal fractions in XLFRAC. [c] AMB86 (normalised, all Fe as FeO).

Comparison of the required proportion of fractionating phenocrysts (~48% total) with the observed proportion (~24% total) shows a significant discrepancy. Fractionation using

observed modes results in an SSR value of 96, with the spinel discrepancy having the largest effect (an increase in SSR of 61). These results show that while it is possible to generate the trachyandesite composition from the basalt, this requires removal of a further ~24% of the initial magma, for example via crystal settling, in order for sufficient fractionation to occur.

5.2.2 Magma mixing

There is a large compositional gap between the most evolved basaltic to basaltic-trachyandesitic glasses of the more mafic samples, and the least evolved trachyandesite-hosted melt inclusions (Fig. 4.28), none of which fall close to the trachyandesite bulk composition. This strongly suggests the absence of a true liquid of trachyandesitic composition.

Melt inclusions in the trachyandesite are more evolved (trachydacitic; ~63–65 wt.% SiO_2; Table 5.2) than the bulk rock (~60 wt.% SiO_2). At the same time, rare calcic cores in plagioclase phenocrysts, and clinopyroxene phenocrysts of comparable composition to those found in the basaltic scoria, indicate the involvement of a basaltic component. This suggests that the trachyandesite derives from mixing of a basaltic component with a more evolved liquid, most likely the trachydacitic melt inclusion composition.

Host	Olivine (n=6)		Spinel (n=11)	
	Mean	σ	Mean	σ
SiO_2	63.73	0.66	63.56	0.44
Al_2O_3	16.29	0.80	14.87	0.34
TiO_2	0.65	0.05	0.66	0.10
FeO	5.00	1.16	6.75	0.64
MnO	0.15	0.04	0.21	0.03
MgO	0.74	0.16	1.39	0.21
CaO	3.68	0.35	3.51	0.35
Na_2O	4.82	0.33	4.13	0.52
K_2O	4.31	0.46	4.32	0.17
P_2O_5	0.36	0.05	0.32	0.06
F ppm	817	105	866	106
Cl ppm	1106	75	1358	132
S ppm	306	50	342	60

Table 5.2 Trachydacitic olivine- and spinel-hosted melt inclusion compositions.

The majority (71%) of analysed melt inclusions form a cluster which falls along the trend from basalts to trachyandesite to matrix glass (Fig. 4.28), which indicates that these compositions sample a volumetrically significant true melt. Both olivine- and spinel-hosted melt inclusions fall in this cluster, indicating that the majority of melt inclusion compositions have not been significantly altered by post-entrapment crystallisation.

Mass balance calculations on mixing of basalt with the 63–65% SiO_2 liquid trapped by melt inclusions in the trachyandesite (using an average of the main compositional cluster of melt inclusions) indicates that addition of the melt inclusion trachydacite melt to Mbwelesu basalt in the ratio 31:69 produces the trachyandesite bulk composition with an SSR value of 1.00 (where a value <2 indicates a good fit; Table 5.3).

	AMB6	MI average	Derivative magma	AMB86	Squares of residuals
SiO_2	52.41	64.18	60.47	60.21	0.070
TiO_2	0.94	0.66	0.75	0.8	0.002
Al_2O_3	17.33	15.10	15.8	16.43	0.396
FeOt	10.39	6.65	7.83	7.95	0.014
MgO	4.65	1.29	2.35	2.05	0.090
CaO	9.27	3.51	5.33	4.74	0.339
Na_2O	2.98	4.38	3.94	4.23	0.085
K_2O	2.02	4.22	3.53	3.59	0.004
Total	100	100	100	100	1.000

Table 5.3 Mass balance calculations for generation of AMB86 trachyandesite by mixing of AMB6 basalt with the average trachydacite melt inclusion composition. All compositions are normalised to the eight oxides listed, with all Fe as FeOt. The derivative magma is AMB6 + 0.44 × MI average.

If Mbwelesu basalt comprises 69% of the mixed magma, the basaltic phenocryst cargo in the trachyandesite should be 69% of the modes observed in the basalt, i.e., 13% plagioclase, 3% clinopyroxene, 0.5% spinel and 0.3% olivine. Recast as percentages of observed modes in the trachyandesite, basaltic phenocryst compositions should account for 76% of plagioclase analyses, 68% of clinopyroxene analyses, 18% of spinel analyses, and 11% of olivine analyses. No basaltic spinel or olivine compositions were found, perhaps reflecting settling out prior to mixing, due to higher density of these phases.

5.2.3 Partial melting

Mineral and melt inclusion compositions suggest that if partial melting played a role, it was in the generation of a trachydacitic melt which mixed with a basalt to generate the trachyandesitic composition. Trachydacite is known to have occurred previously in the volcanic history with no related intermediate compositions (see Section 2.2.3) which demonstrates that conditions conducive to trachydacite generation are present in the subvolcanic crust. A possible source for trachydacite is partial melting of solidified, unerupted magma below the edifice (Annen and Sparks, 2002; Lange & Carmichael, 1996). The young arc crust beneath Ambrym consists of oceanic crust and volcanics, with only a minor occurrence of reef limestone cropping out at the south-eastern coastal margin (see Fig. 2.7); assimilation of exotic crustal rocks can therefore be ruled out. Any crustal material (e.g.,

plutonic roots; Reubi and Blundy, 2009) incorporated into the rising magma would be a derivative of the parent magma source and may not be easily distinguishable by trace element concentrations. The lack of trace element data for the trachydacitic glass precludes further conclusions.

5.2.4 Conclusions

These combined lines of evidence indicate that the trachyandesitic bulk composition derives from mixing of the dominant basalt magma composition with trachydacite, probably generated by partial melting of basaltic/gabbroic crust, with the majority of plagioclase and clinopyroxene phenocrysts inherited from the basaltic member, and olivine and spinel contributed from the trachydacitic member. The trachydacitic melt inclusions in olivine and spinel require precipitation of these phases prior to mixing with the basaltic input. The textural relationships of apatite and pyrrhotite to olivine and spinel—present as inclusions or interstitial blebs—indicates that these too pre-date mixing.

5.3 Mineral-melt equilibria

Evaluation of temperatures and pressures of crystallisation via mineral-melt equilibria further constrain models suggested by geochemistry, petrography and major element modelling, by clarifying P-T-XH_2O-fO_2 conditions associated with different stages of the crystallisation history. Mineral-melt equilibria also provide insights into the crystallisation history via evaluations of equilibrium, including whether mineral phases crystallised from a more primitive or more evolved melt than the whole rock or matrix glass in which they erupted.

Nominal melts used here for mineral-melt equilibria are whole rock, matrix glass, and melt inclusions. Whole rock, melt inclusion and glass compositions in this sample suite form a trend indicating a liquid line of descent via removal of observed phenocryst phases, which justifies the use of whole rock as a melt composition. The mineral-melt pairs chosen for calculations are those which satisfy tests for equilibrium, detailed below.

Calculations have been performed on an anhydrous to low-H_2O basis based on low H_2O measurements in melt inclusions, reported in Chapter 6.

5.3.1 Clinopyroxene-melt thermobarometry

Two sets of clinopyroxene-melt thermobarometers were applied, to evaluate consistency of the results. The temperature and pressure models of Putirka et al. (2003) were chosen as the most reliable, due to having the highest precision (R^2=0.96 and 0.97 respectively) and lowest error (33 °C and 170 MPa respectively) of currently available models, and are well-calibrated for basaltic compositions:

$$\mathrm{P(kbar)} = -88.3 + 2.82\times10^{-3}T9(K)ln\left[\frac{Jd^{cpx}}{[Na^{liq}Al^{liq}(Si^{liq})^2]}\right] + 2.19\times10^{-2}T(K) - 25.1ln\left[Ca^{liq}Si^{liq}\right] + 7.03\left[Mg^{liq}\right] + 12.4ln\left[Ca^{liq}\right]$$

$$\frac{10^4}{T(K)} = 4.60\times10^{-1}ln\left[\frac{Jd^{cpx}Ca^{liq}Fm^{liq}}{DiHd^{cpx}Na^{liq}Al^{liq}}\right] - 6.54\times10^{-1}ln\left[Mg^{liq}\right] - 3.26\times10^{-1}ln\left[Na^{liq}\right] - 6.32\times10^{-3}[P(kbar)] - 0.92ln\left[Si^{liq}\right] + 2.74\times10^{-1}ln[Jd^{cpx}]$$

The barometer is based on the large change in molar volume involved in jadeite formation (i.e., the large partial molar volumes of Na and Al in liquid compared to the small molar volume of jadeite), while the thermometer is based on the temperature-sensitivity of the jadeite-diopside/hedenbergite exchange between clinopyroxene and coexisting melt.

A clinopyroxene-only barometer and thermometer (Equation 32a and Equation 32d of Putirka, 2008) with errors of 310 MPa and 58 °C respectively, were also applied as an independent test of results from the clinopyroxene-melt calculations:

$$P(kbar) = 3205 + 0.384T(K) - 518lnT(K) - 5.62\left(X_{Mg}^{cpx}\right) + 83.2\left(X_{Na}^{cpx}\right) + 68.2\left(X_{DiHd}^{cpx}\right) + 2.52\ln\left(X_{Al(VI)}^{cpx}\right) - 51.1\left(X_{DiHd}^{cpx}\right)^2 + 34.8(X_{EnFs}^{cpx})^2 \quad \text{(Eq. 32a)}$$

$$T(K) = \frac{93100 + 544P(kbar)}{61.1 + 36.6\left(X_{Ti}^{cpx}\right) + 10.9\left(X_{Fe}^{cpx}\right) - 0.95\left(X_{Al}^{cpx} + X_{Cr}^{cpx} - X_{Na}^{cpx} - X_{K}^{cpx}\right) + 0.395\left[ln\left(a_{En}^{cpx}\right)\right]^2} \quad \text{(Eq. 32d)}$$

Note that these models are independent of melt H_2O content.

Assessment of equilibrium

The models incorporate two tests for crystal-liquid equilibrium. The first compares the clinopyroxene-liquid Fe-Mg partition coefficient[8] ($K_D^{liq\text{-}cpx}$) to the experimentally-determined equilibrium value of 0.27±0.03 (Putirka, 2008). The second compares predicted equilibrium

[8] $K_D(Fe\text{-}Mg)^{liq\text{-}cpx} = \frac{\left(\frac{Fe}{Mg}\right)_{cpx}}{\left(\frac{Fe^{2+}}{Fe^{3+}}\right)_{liq} \times \left(\frac{Fe}{Mg}\right)_{liq}}$

clinopyroxene composition (constrained from experimental data) with measured values for pyroxene components EnFs, DiHd, and CaTs (Fig. 5.2), calculated using a normative procedure (Putirka et al., 2003). Calculated crystallisation temperatures can also be compared with the calculated clinopyroxene saturation temperature for the liquid (Eq. 34 of Putirka, 2008); if valid, they should be lower than the saturation temperature.

$$\frac{10^4}{T(K)} = 6.39 + 0.076\left(H_2O^{liq}\right) - 5.55\left[X_{CaO}^{liq} X_{SiO_2}^{liq}\right] - 0.386\ln\left(X_{MgO}^{liq}\right) - 0.046P(kbar) + 2.2\times10^{-4}[P(kbar)]^2 \quad \text{(Eq. 34)}$$

Clinopyroxene-liquid thermobarometry results given in this chapter include only those pairs which have $K_D^{liq\text{-}cpx}$ values within the equilibrium range of 0.27±0.03; for disequilibrium crystals, calculations from clinopyroxene-only models are given.

The equilibrium value for $K_D^{liq\text{-}cpx}$ was calibrated to the assumption that Fe^{3+} is zero in the liquid and very small in the clinopyroxene, and no correction for iron speciation was made in the calibrations, so there is no increase in precision or accuracy by including iron speciation in the calculations (K. Putirka, pers. comm., 2013). The calculation of $K_D^{liq\text{-}cpx}$ does incorporate a coefficient for Fe^{2+}/Fe^{3+} but this can be neglected unless the fO_2 is quite high (K. Putirka, pers. comm., 2013).

The mineral-liquid pairs tested for equilibrium are phenocryst/whole rock, phenocryst/melt inclusions, phenocryst/glass and groundmass/glass.

Phenocryst/whole rock pairs in Mbwelesu scoria (AMB6 and AMB2007) satisfy the $K_D^{liq\text{-}cpx}$ test for equilibrium but groundmass/glass pairs do not (Fig. 5.1a). High $K_D^{liq\text{-}cpx}$ values for clinopyroxene groundmass-glass pairs in the Mbwelesu scoria suggest that groundmass crystals represent disequilibrium growth. High Al and Na contents in the groundmass crystals provide evidence of this—rapid disequilibrium growth of clinopyroxene has been shown to entail high Al and Na uptake (Mollo et al., 2013). Clinopyroxene-hosted melt inclusions were paired with the average composition of a large, euhedral clinopyroxene, as only two pairs of analyses of melt inclusions and their adjacent host crystal successfully captured both inclusion and host compositions. Most of the melt inclusions are within the equilibrium $K_D^{liq\text{-}cpx}$ range (Fig. 5.1a). Examination of observed versus predicted values for the DiHd component (Fig. 5.2a) shows almost all groundmass/glass pairs straddling the 1:1 line, with phenocryst/whole rock pairs within 5% of the line. These results indicate that the component test alone is not sufficient to demonstrate equilibrium for the purposes of thermobarometry, as pressure estimates from groundmass-glass pairs are much higher than phenocryst-WR pairs, and are clearly spurious given the late-stage (i.e., low pressure) nature of groundmass crystallisation.

In Niri Mbwelesu Taten lava (AMB2), only two whole rock/(micro)phenocryst pairs satisfy the $K_D^{liq\text{-}cpx}$ test for equilibrium (Fig. 5.1a). No glass was analysed in this sample. The DiHd component diagrams show both phenocrysts and microphenocrysts within 5% of the 1:1 line (Fig. 5.2b).

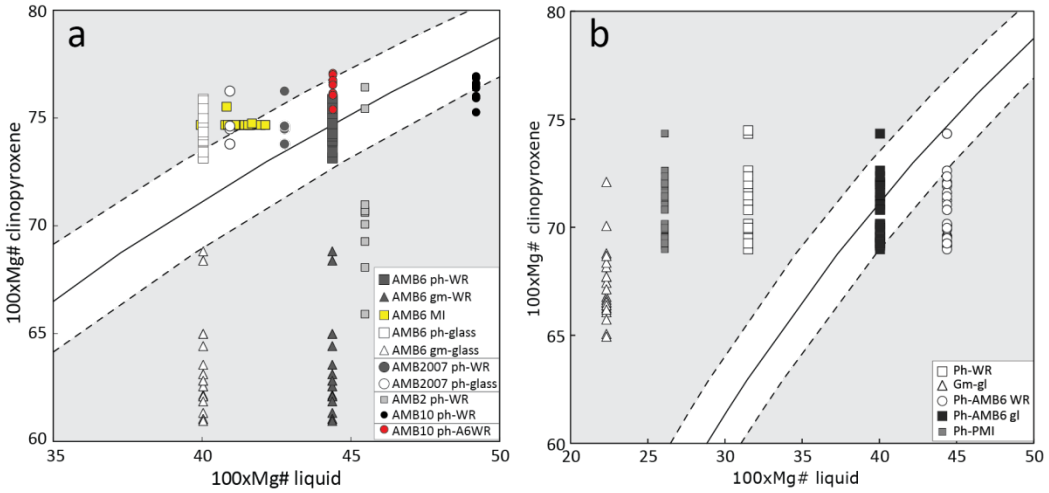

Figure 5.1 Plots showing the equilibrium range for clinopyroxene and melt compositions, with equilibrium line $K_D^{liq\text{-}cpx}$=0.27 (solid line) ±0.3 (dashed lines). **a)** Results for samples AMB6, AMB2007, AMB2 and AMB10. Melt inclusion and phenocryst pairs, as well as AMB10 phenocrysts paired with AMB6 whole rock (as representative of 'standard' central conduit basalt) are also tested for equilibrium. **b)** $K_D^{liq\text{-}cpx}$ results for trachyandesite (AMB86) phenocrysts, which have been tested against the trachyandesite whole rock, the most primitive melt inclusion ('PMI') composition found in the trachyandesite, basaltic scoria AMB6 whole rock, and AMB6 glass. The best match is between trachyandesite phenocrysts and the matrix glass of basaltic scoria AMB6.

In flank lava AMB10, five out of eight clinopyroxenes analysed (glomerocryst crystals) are in equilibrium with the whole rock according to the $K_D^{liq\text{-}cpx}$ test (Fig. 5.1a). No glass was analysed in AMB10. The DiHd component diagram shows glomerocryst crystals displaced more than 5% from the 1:1 line (Fig. 5.2c). As AMB10 appears to be affected by plagioclase accumulation, and therefore is not a true liquid, the central vent basalt composition (AMB6 taken as representative) was tested as a possible alternative parent liquid for the clinopyroxene; all of the analysed clinopyroxene displays equilibrium $K_D^{liq\text{-}cpx}$ values when paired with the AMB6 whole rock composition.

In the trachyandesite, no mineral/melt pairs satisfy the $K_D^{liq\text{-}cpx}$ test for equilibrium, whether phenocrysts, microphenocrysts or groundmass, paired with whole rock or matrix glass. However, almost all of the phenocrysts satisfy the equilibrium condition when paired with the AMB6 (basaltic scoria) matrix glass composition (Fig. 5.1b). The DiHd component diagrams shows phenocrysts within 5% of the 1:1 line (Fig. 5.2d), again displaying a disparity between the $K_D^{liq\text{-}cpx}$ and phase component tests.

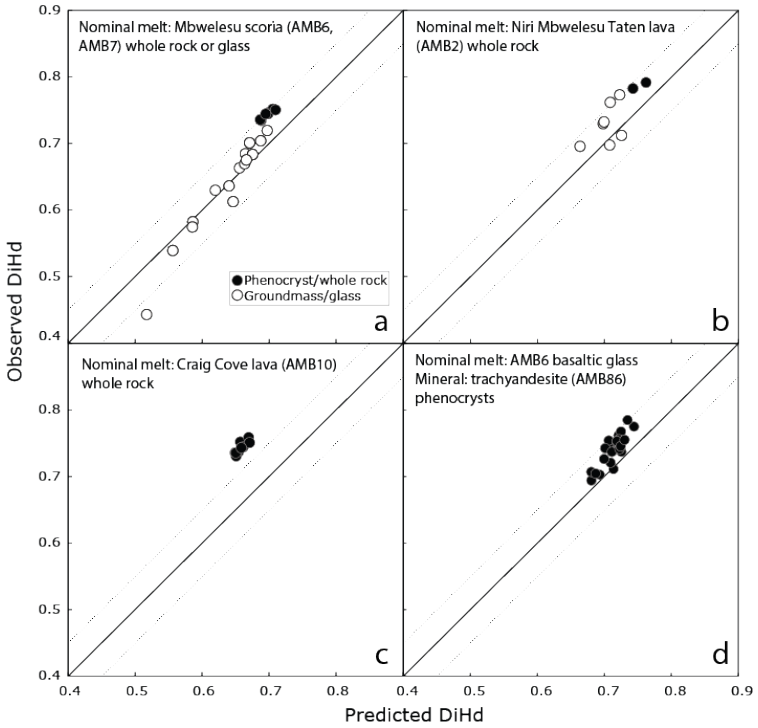

Figure 5.2 Comparison of predicted values with observed values for the dominant pyroxene component, DiHd. Crystal-liquid pairs in **a)** Mbwelesu scoria (AMB6, AMB7), **b)** Niri Mbwelesu Taten lava (AMB2), **c)** Craig Cove lava (AMB10), and **d)** trachyandesite lava (AMB86). Groundmass-glass pairs include microphenocrysts. Dashed lines mark an arbitrary error limit of 5% from the 1:1 line.

Results

Results are summarised in Fig. 5.3 and Table 5.4. Temperature calculations using the Putirka et al. (2003) mineral-melt model all fall below the calculated saturation temperature (Eq. 34), whereas those calculated using Eq. 32d (clinopyroxene-only) tend to be higher. However, all are within error of each other, suggesting that the results from clinopyroxene thermometry are viable. Results cited from this point onward will be from the Putirka et al. (2003) models, which have the highest precision and lowest standard error. Results are quoted as means with one standard deviation as the error; the full range of data are also displayed in Fig. 5.3.

Clinopyroxene-liquid results indicate a mean temperature of 1140±2 °C for Mbwelesu scoria (AMB6, AMB2007) and 1150±4 °C for Niri Mbwelesu Taten lava (AMB2). Calculations for Craig Cove lava (AMB10) return temperatures of 1130±2 °C with AMB10 whole rock as the nominal melt, and 1140±2 °C with AMB6 basalt as the nominal melt. Temperature estimates for trachyandesite (AMB86) phenocrysts are 1130±5 °C; these results represent clinopyroxene crystallisation in a basaltic melt prior to entering the trachyandesite phase assemblage. Pressure estimates are similar across all basaltic samples: 390±20 MPa (AMB6), 410±20 MPa (AMB2007), 330±40 MPa (AMB2), 430–440±20 MPa (AMB10), covering a range of c. 12–17 km depth. The pressure estimate for trachyandesite-hosted

clinopyroxene phenocrysts is 340±70 MPa, corresponding to depths of c. 13±3 km; again, this represents theorised crystallisation from a basaltic parent before incorporation into the trachyandesite.

Clinopyroxene-only results are almost identical to clinopyroxene-melt results for barometry, and higher but within error for thermometry, indicating that these estimates are robust.

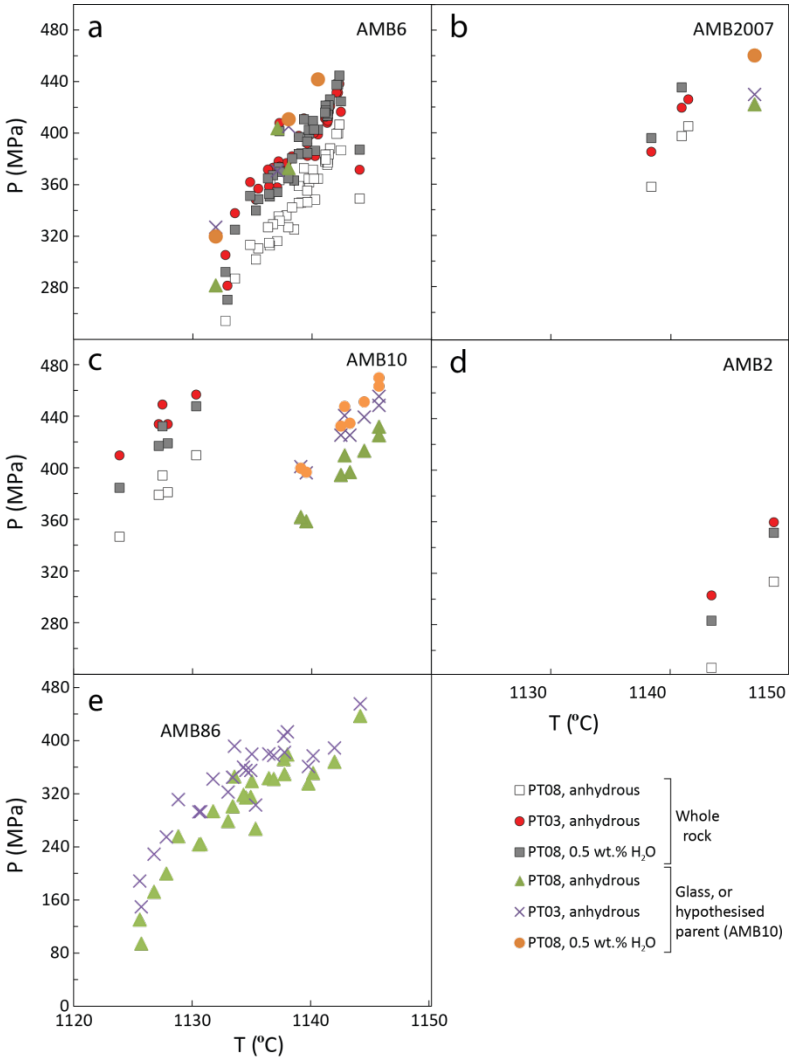

Figure 5.3 Clinopyroxene thermobarometry results for samples (a) AMB6, (b) AMB2007, (c) AMB10, (d) AMB2 and (e) AMB86. PT08=Putirka (2008) model, PT03=Putirka et al. (2003) model. Scales are identical for all panels except panel (e) in which the pressure scale extends to 0 MPa. Note that the nominal melt used for AMB10 is the whole rock composition of AMB6, and the nominal melt used for AMB86 is the matrix glass composition of AMB6; these compositions satisfy the equilibrium test with phenocrysts from the respective samples whereas their host rock bulk and glass compositions do not.

	Clinopyroxene-liquid exchange		T_{sat}	Cpx-only	
	Putirka et al., 2003		*Eq. 34*	*Eq. 32a*	*Eq. 32d*
	T (°C)	P (MPa)	T (°C)	P (MPa)	T (°C)
AMB6 whole rock and phenocrysts, n=27, K_D=0.27±0.01					
Mean	1140 (2)	390 (20)	1150 (3)	420 (30)	1170 (4)
h (km)	-	15 (1)	-	16 (1)	-
AMB6 glass and phenocrysts, n=3, K_D=0.24±0.00					
Mean	1140 (3)	370 (40)	1140 (3)	430 (40)	1160 (6)
h (km)	-	14 (2)	-	16 (2)	-
AMB2007 whole rock and glomerocryst phenocrysts, n=4, K_D=0.25					
Mean	1140 (1)	410 (20)	1150 (2)	400 (30)	1170 (4)
h (km)	-	15 (1)	-	15 (1)	-
AMB2 whole rock and microphenocrysts, n=2, K_D=0.24					
Mean	1150 (4)	330 (40)	1150 (4)	330 (30)	1160 (7)
h (km)	-	12 (2)	-	12 (1)	-
AMB10 whole rock and glomerocryst crystals, n=5, K_D=0.30±0.01					
Mean	1130 (2)	440 (20)	1150 (3)	420 (50)	1180 (3)
h (km)	-	17 (1)	-	16 (2)	-
AMB10 glomerocryst crystals and AMB6 WR as nominal liquid, n=8, K_D=0.25±0.01					
Mean	1140 (2)	430 (20)	1160 (3)	430 (40)	1180 (3)
h (km)	-	16 (1)	-	16 (2)	-
AMB86 trachyandesite phenocrysts, AMB6 glass, n=26, K_D=0.28±0.02					
Mean	1130 (5)	340 (70)	1140 (6)	330 (100)	1160 (6)
h (km)	-	13 (3)	-	12 (4)	-
R^2	0.96	0.97	0.93	0.92	0.82
SEE	33	170	45	310	58

Table 5.4 Results of clinopyroxene-melt thermobarometry for liquid/phenocryst pairs, rounded to two (P) and three (T) significant figures (the errors on T are rounded only to full integers). Results are the mean of n calculations where n=number of phenocryst analyses. All calculations are performed on an anhydrous basis. Eq. 34 calculates clinopyroxene saturation temperature for given pressure (Putirka et al., 2003 model). Values for model precision (R^2) and Standard Error of Estimate (SEE) are given in the lowermost section of the table. Calculated depths (h) are also given, assuming crustal density of 2700 kg m^{-3}.

5.3.2 Olivine-melt thermometry

Results from olivine thermometry provide an independent check on the reliability of results from clinopyroxene, as these phases are believed to have crystallised at or near the same time.

Olivine-melt thermometry calculations were performed using the highest-precision and lowest-error models available; Equations 19 and 22 of Putirka (2008). Eq. 19 is the most

precise model for anhydrous melts, with R^2=0.94. Eq. 22 is the most precise model for hydrous melts, with R^2=0.94 (anhydrous) or 0.95 (hydrous).

$$T(℃) = \frac{13603 + 4.943\times10^{-7}(P(GPa)\times10^9 - 10^{-5}}{6.26 + 2lnD_{Mg}^{ol/liq} + 2ln[1.5(C_{NM}^L)] + 2ln[3(C_{SiO_2}^L)] - NF} - 273.15 \quad \text{(Eq. 19)}$$

$$T(℃) = \frac{15294.6 + 1318.8P(GPa) + 2.4834[P(GPa)]^2}{0.8048 + 2.8352lnD_{Mg}^{ol/liq} + 2.097\ln[1.5C_{NM}^L] + 0.222H_2O^{liq} + 0.5\mathrm{P(GPa)}} + 2.575\ln(3C_{SiO_2}^{liq}) - 1.41NF \quad \text{(Eq. 22)}$$

Where C_{NM}^L is the sum of the cation fractions of Fe, Mn, Mg, and Ca in the liquid, and

$$NF = \frac{7}{2}\ln\left(1 - X_{AlO_{1.5}}^{liq}\right) + 7\ln(1 - X_{TiO_2}^{liq})$$

Assessment of equilibrium

Equilibrium between olivine and liquid is assessed using the Fe-Mg partition coefficient, $K_D^{liq\text{-}ol}$, where

$$K_D^{liq-ol} = \left(\frac{X_{FeO}^{ol}}{X_{FeO}^{liq}}\right)\left(\frac{X_{MgO}^{ol}}{X_{MgO}^{liq}}\right).$$

$K_D^{Fe\text{-}Mg}$ values were calculated at $Fe^{2+}/\Sigma Fe$ corresponding to the oxygen fugacity values estimated for each sample (Section 5.3.5), via the method of Kress & Carmichael (1991).

An equilibrium $K_D^{liq\text{-}ol}$ value of 0.30±0.03 (Roeder & Emslie, 1970) is widely used and remains regularly cited in the literature (*e.g.*, Danyushevsky & Plechov, 2011; Marsh, 2013; Sides et al., 2014). Putirka (2008) tested this value using data from 1504 experiments, which returned a value for $K_D^{liq\text{-}ol}$ of 0.30±0.05, slightly extending the range of the classic Roeder & Emslie (1970) value. $K_D^{liq\text{-}ol}$ has been shown to decrease in low-SiO_2 or high-alkali melts, and to increase at high pressure (Toplis, 2005).

Phenocrystic olivine compositions in the Mbwelesu scoria (AMB6 and AMB2007) are homogeneous ($Fo_{74.9}$), and identical to groundmass olivine compositions, which suggests reequilibration of phenocrystic olivine with the matrix glass. $K_D^{liq\text{-}ol}$ values are high, ranging from 0.37 to 0.44 (Fig. 5.4).

$K_D^{liq\text{-}ol}$ values are similarly high (0.48) for phenocrystic olivine and whole rock in Niri Mbwelesu Taten lava (AMB2). Glass and groundmass olivine were not analysed in this sample (Fig. 5.4).

K_D values are similar again (0.44) for phenocryst and whole rock compositions (Fig. 5.4) in Craig Cove lava (AMB10). Glass in this sample is scarce and occurs in volumes too small to analyse by EPMA; groundmass olivine was not analysed.

Approximately 50% of the phenocrystic olivine in AMB86 is in equilibrium with the whole rock composition (Fig. 5.4). Those below the equilibrium curve indicate that some olivine phenocrysts are too evolved to have crystallised from the whole rock, if the whole rock is assumed to represent a possible liquid. Meanwhile, all olivine phenocrysts are out of equilibrium with the matrix glass. Using the most primitive (lowest-SiO_2, highest MgO) olivine-hosted melt inclusion as nominal liquid doesn't improve results for equilibrium, with the majority of phenocrysts lying outside the equilibrium range.

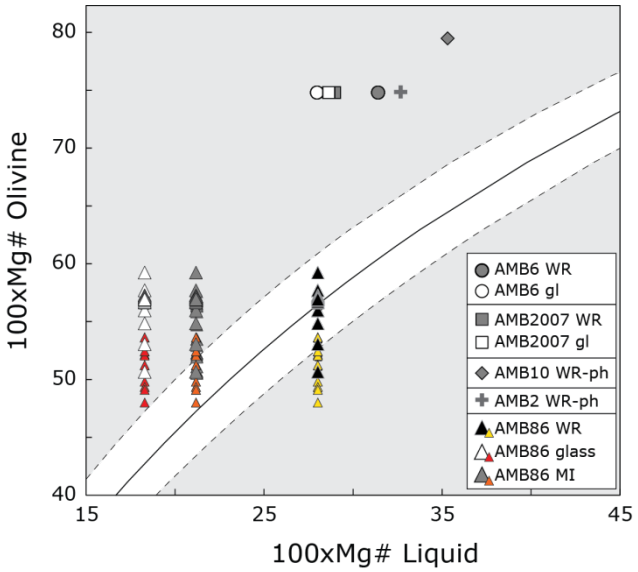

Figure 5.4 Rhodes diagram showing equilibrium $K_D^{liq\text{-}ol}$ curve of 0.30 (solid line) and error limits of ±0.053 (dashed lines) as determined by Putirka (2008). Grey shading shows areas are out of equilibrium. Basaltic samples are represented by a single datapoint each due to homogeneity of olivine composition; while olivine composition in AMB86 covers a range. Smaller, coloured symbols for AMB86 trends represent groundmass crystals.

The observation that groundmass and microphenocrystic olivine, in both the Mbwelesu scoria and the 1986 trachyandesite, returns non-equilibrium values (Roeder & Emslie, 1970; Putirka, 2008) suggests that this method of calculating $K_D^{liq\text{-}ol}$ values does not reflect equilibrium for this melt composition. Groundmass must be in equilibrium with the matrix glass—in particular, the homogeneity of olivine compositions from phenocrysts to groundmass in the Mbwelesu scoria indicates that the groundmass is not a rapid-growth disequilibrium composition. $K_D^{liq\text{-}ol}$ has been shown to decrease in low-SiO_2 or high-alkali melts, and to increase at high pressure (Toplis, 2005). Given the moderately high alkali content of the rocks and matrix glass (total alkalis of 4.9–5.8 wt.% for the basalts, and 7.7–9.3 wt.% for the trachyandesite), an adjustment for alkali content (Toplis, 2005) was applied to investigate whether adjusted $K_D^{liq\text{-}ol}$ values more closely approach equilibrium. The method is detailed in Appendix H.

The Toplis (2005) adjustment shifts $K_D^{liq\text{-}ol}$ values into the range 0.28–0.30 for the basaltic samples, and 0.33–0.35 for the trachyandesite, which are within the equilibrium range of 0.30±0.05 given by Putirka (2008), except for trachyandesite whole rock/phenocryst which remains too high (0.355). The results for equilibrium between groundmass olivine and glass in Mbwelesu scoria, in particular, strongly suggest that this method is justified as these crystals clearly grew from the matrix glass. Results for trachyandesite shift the values so that most olivine phenocrysts are in equilibrium with the trachydacite melt inclusions, and not in equilibrium with the whole rock, while some of the groundmass is in equilibrium with the glass. This suggests that most of the olivine phenocrysts present in the trachyandesite crystallised from the trachydacitic melt sampled by olivine-hosted melt inclusions, with more evolved compositions growing later from the matrix glass.

An alternative evaluation using the method of Kushiro & Walter (1998)—which applies only to mafic to ultramafic melts, so cannot be used for the trachyandesite—in which $K_D^{liq\text{-}ol}$ values are adjusted for melt composition using NBO/T ratios, gives results in the range 0.28–0.30 for the basaltic samples, which agree with those calculated using Toplis (2005) to within ~0.01. Olivine-melt pairs are thus considered to represent equilibrium.

Results from the Toplis (2005) and Kushiro & Walter (1998) methods are compared alongside original unadjusted $K_D^{liq\text{-}ol}$ values in Table 5.5.

	K_D unadjusted	K_D Toplis (2005)	K_D K&W (1998)
AMB6 WR (n=6)	0.46	0.30	0.29
AMB6 glass (n=23)	0.39	0.30	0.30
AMB2007 glass (n=3)	0.40	0.30	0.30
AMB2007 WR	0.41	0.30	0.29
AMB2 WR	0.48	0.33	0.30
AMB10 WR	0.45	0.29	0.28
AMB86 glass (n=11), gm av	0.42	0.33	-
AMB86 WR, pheno av	0.46	0.36	-
AMB86 PMI, phenos	0.36	0.34	

Table 5.5 Comparison of unadjusted $K_D^{liq\text{-}ol}$ values with those adjusted for alkali content using the procedure of Toplis (2005), and those adjusted for NBO/T, using the procedure of Kushiro & Walter (K&W) (1998). 'gm av'=average groundmass olivine composition, 'low-Mg gm'=lowest-forsterite groundmass composition, 'pheno av'=average phenocrystic olivine composition, 'high-Mg pheno'=highest-forsterite phenocryst composition. AMB86 PMI=composition of most primitive melt inclusion in AMB86.

Results

Temperature estimates (Table 5.6) were examined over a range of 0–0.5 wt.% H_2O and 100–500 MPa pressure, based on mid-crustal storage conditions indicated by clinopyroxene barometry (~500 MPa) and 100 MPa to represent crystallisation pressure between mid-crust and the surface, as indicated by melt inclusion entrapment pressures calculated by Allard et al. (2015). Secondary ion mass spectrometry (SIMS) analysis of melt inclusions (Chapter 6) indicates melt H_2O contents of <0.5 wt.% during basalt-hosted olivine crystallisation, so calculations using 0.5 wt.% H_2O have also been made as an upper bound on potential H_2O content.

Results for anhydrous melt at 500 MPa are 1120–1140 °C for Mbwelesu scoria (AMB6 and AMB2007), 1160 °C for Niri Mbwelesu Taten lava (AMB2), and 1120–1130 °C for Craig Cove lava (AMB10). The highest-Fo olivine composition in the trachyandesite (AMB86) indicates a temperature of 1090 °C when paired with the whole rock; groundmass-glass pairs indicate temperatures of 990–1030 °C at 100 MPa.

		Anhydrous		0.5% H_2O
	P (MPa)	Eq. 19	Eq. 22	Eq. 22
AMB6 (Mbwelesu scoria)				
Whole rock	500	1140	1140	1130
Glass (n=23)	100	1140	1120	1110
AMB2007 (Mbwelesu scoria)				
Whole rock	500	1140	1130	1120
Glass (n=3)	100	1140	1120	1110
AMB2 (NMT lava)				
Whole rock	500	1160	1160	1150
AMB10 (Craig Cove lava)				
Whole rock	500	1130	1120	1110
AMB86 (trachyandesite lava)				
Whole rock, Fo_{59}	100	1070	1060	1060
	500	1090	1090	1080
Glass (n=11,) groundmass average (n=17)	100	1030	990	990
	500	1050	1010	1010
PMI, phenocrysts (n=47)	100	1060	1040	1030
	500	1080	1060	1050
SEE		±44	±45	±29
R^2		0.94	0.94	0.95

Table 5.6 Results of olivine-liquid thermometers Eq. 19 and Eq. 22 (Putirka, 2008). The average of 28 phenocryst, microphenocryst and groundmass olivine analyses ($Fo_{74.9\pm0.4}$) was used for glass and whole rock calculations in AMB6 and AMB2007. Temperature results are rounded to three significant figures.

5.3.3 Plagioclase thermobarometry and hygrometry

The plagioclase thermometer Equation 24a of Putirka (2008) is the highest-precision (R^2=0.93) and lowest-error (±36 °C) model available. Putirka (2008) also presents a plagioclase-liquid barometer (Equation 25a), which is recommended only for compositions closely similar to specific datasets for which it works well. The test composition to which recent Ambrym basalts fall closest is the high-K basalt of Meen (1990), for which the model does not perform with great precision, although the results do bracket the real values (e.g., experimental samples equilibrated at 1 GPa give results of 0.5–1.4 GPa; samples equilibrated at 1.5 GPa give results of 0.8–1.6 GPa). Pressure estimates from this barometer are thus regarded with caution, but are included in the absence of more precise methods for estimation of plagioclase crystallisation depths.

$$\frac{10^4}{T(K)} = 6.4706 + 0.3129ln\left(\frac{X_{An}^{pl}}{X_{CaO}^{liq}\left(X_{AlO_{1.5}}^{liq}\right)^2\left(X_{SiO_2}^{liq}\right)^2}\right) - 8.103\left(X_{SiO_2}^{liq}\right) + 4.872\left(X_{KO_{0.5}}^{liq}\right) \quad \text{(Eq. 24a)}$$
$$+ 1.5346\left(X_{Ab}^{pl}\right)^2 + 8.661\left(X_{SiO_2}^{liq}\right)^2 - 3.341\times10^{-2}P(kbar) + 0.18047\left(H_2O^{liq}\right)$$

$$P(kbar) = -42.2 + 4.94\times10^{-2}T(K) + 1.16\times10^{-2}T(K)ln\left[\frac{X_{Ab}^{pl}X_{AlO_{1.5}}^{liq}X_{CaO}^{liq}}{X_{An}^{pl}X_{NaO_{0.5}}^{liq}X_{SiO_2}^{liq}}\right] - 382.3\left(X_{SiO_2}^{liq}\right)^2 \quad \text{(Eq. 25a)}$$
$$+ 514.2\left(X_{SiO_2}^{liq}\right)^3 - 19.6ln\left(X_{Ab}^{pl}\right) - 139.8\left(X_{CaO}^{liq}\right) + 287.2\left(X_{NaO_{0.5}}^{liq}\right)$$
$$+ 163.9\left(X_{KO_{0.5}}^{liq}\right)$$

Results of plagioclase-melt thermobarometry are strongly influenced by estimated water content of the melt, which significantly reduces both temperature and pressure estimates with increasing H_2O content. In addition to low H_2O contents seen in SIMS analyses of olivine-, clinopyroxene- and spinel-hosted melt inclusions, plagioclase-hosted melt inclusions, although not analysed by SIMS, show high EPMA totals which are indistinguishable from totals for matrix glass, which has a consistent measured H_2O content of 0.1 wt.%. No direct evidence of H^+ loss, such as Fe-Ti oxide crystallisation, or molecular H_2O loss, such as daughter crystals or decrepitation (Danyushevsky et al., 2002), is observed in any melt inclusions. Results were thus tested for anhydrous conditions and at 0.5 wt.% H_2O as an upper bound, based on these observations.

In addition, Putirka (2008) introduces a plagioclase hygrometer which performs relatively well, with an R^2 value of 0.87, but can only recover water contents to within ±1.1 wt.% H_2O, provided a reliable temperature constraint is available. Tested against 825 anhydrous compositions not used in the regression, it provided an average value of 0.4 ± 1.0 wt.%. The calculation is very sensitive to temperature input.

Assessment of equilibrium

The exchange coefficient $K_D^{Ab\text{-}An}$ is used as a test for equilibrium, and has been experimentally determined to be 0.27±0.11 for liquids >1050 °C, and 0.10±0.05 for liquids <1050 °C (Putirka, 2008). Comparison of calculated crystallisation temperature with calculated plagioclase saturation temperature (T_{sat}) provides another test for validity of results; Eq. 26 of Putirka (2008) calculates plagioclase saturation temperature for melt compositions at a given pressure, to within ±38 °C:

$$\frac{10^4}{T(K)} = 10.86 - 9.7654\left(X_{SiO_2}^{liq}\right) + 4.241\left(X_{CaO}^{liq}\right) + 4.872\left(X_{KO_{0.5}}^{liq}\right) - 55.56\left(X_{CaO}^{liq}X_{AlO_{1.5}}^{liq}\right) + 37.50\left(X_{KO_{1.5}}^{liq}X_{AlO_{1.5}}^{liq}\right)$$
$$+ 11.206\left(X_{SiO_2}^{liq}\right)^3 - 3.151\times10^{-2}P(kbar) + 0.1709\left(H_2O^{liq}\right)$$

$K_D^{Ab\text{-}An}$ values indicate that plagioclase of $An_{80–62}$ is in equilibrium with AMB6 and AMB7 whole rock, while plagioclase of $An_{72–51}$ is in equilibrium with the matrix glass. Compositions in equilibrium with the whole rock are coarse glomerocryst rims, fine glomerocryst cores and rims, and microphenocrysts. Glomerocryst rims, microphenocrysts and groundmass compositions are in equilibrium with the matrix glass. Coarse glomerocryst cores are not in equilibrium with the whole rock, indicating that these represent an inherited/antecrystic phase which crystallised from a more mafic melt than the host rock.

Niri Mbwelesu Taten lava (AMB2) phenocrysts are in equilibrium with the whole rock. No groundmass or glass were analysed.

In Craig Cove lava (AMB10), coarse glomerocrysts, fine glomerocrysts and ragged plagioclase are all within the equilibrium range for the whole rock, but this is considered spurious as the whole rock composition is clearly skewed by the presence of a large proportion of plagioclase megacrysts, showing markedly elevated Al_2O_3 (Fig. 4.9g) and Sr (Fig. 4.11b). However, coarse glomerocrysts, fine glomerocrysts and skeletal plagioclase are found to satisfy $K_D^{Ab\text{-}An}$ equilibrium with both AMB6 whole rock and AMB6 matrix glass, which are representative of the predominant basaltic composition at Ambrym. The single analysed groundmass crystal is not in equilibrium with AMB6 whole rock or glass, but is in equilibrium with a calculated groundmass composition derived by subtraction from the whole rock of observed modal proportions of megacrystic plagioclase, clinopyroxene and olivine phenocryst compositions[9] (glass areas are not large enough for analysis in this sample).

[9] One possible groundmass composition was calculated by removing modal percentages of all phenocrysts but groundmass plagioclase is not in equilibrium with this composition. Retaining the smaller plagioclase glomerocrysts gives a composition that satisfies equilibrium.

Five possible nominal melts were considered for the 1986 trachyandesite (AMB86): trachyandesite bulk rock, trachyandesite matrix glass, the most primitive trachydacitic melt inclusion, basaltic scoria (AMB6) bulk rock, and basaltic scoria (AMB6) matrix glass. The trachyandesite bulk rock is discarded as a potential melt, as melt inclusions and high-anorthite plagioclase cores show it to be a product of mixing between trachydacitic magma and basalt-derived phenocrysts.

The majority (98%) of plagioclase analyses (phenocrysts as well as groundmass, $An_{39–62}$), display equilibrium with the average AMB86 matrix glass, and 79% ($An_{39–57}$) are in equilibrium with the most primitive trachydacitic melt inclusion composition. Two rare higher-An compositions (An_{74} and An_{65}) satisfy equilibrium with the basaltic scoria (AMB6) bulk composition, while phenocrysts from $An_{53–65}$ satisfy equilibrium with AMB6 glass. Of 14 plagioclase phenocrysts analysed, 12 (86%) have cores or zones which are in equilibrium with the basalt matrix glass or whole rock, indicating that a high proportion of plagioclase phenocrysts originated from a basaltic mixing member.

Results

Thermometry, barometry and hygrometry results and associated K_D^{Ab-An} values are listed in Table 5.7. Thermobarometry results are displayed in Fig. 5.5. All temperature calculations are within error of plagioclase saturation temperature (T_{sat}). Given the poor precision of the plagioclase barometer, these results are only a rough indication. Plagioclase thermometry is much more precise and demonstrates that plagioclase glomerocrysts and microphenocrysts crystallised at temperatures significantly higher than the clinopyroxene and olivine phenocrysts, while groundmass crystallisation temperature correlates with clinopyroxene and olivine crystallisation temperatures.

The results indicate two major P-T regions for Mbwelesu scoria (AMB6, AMB2007). At conditions varying from anhydrous to 0.5 wt.% melt H_2O, these range from 1150–1170 °C and 730–790 MPa for plagioclase in equilibrium with 2005 whole rock ($An_{63–80}$), and 1120–1140 °C and 370–440 MPa for plagioclase in equilibrium with 2005 matrix glass ($An_{56–72}$). Results for AMB2007 suggest crystallisation of plagioclase in a region intermediate between those identified from AMB6 results, covering a range of 1140–1160 °C and 430–650 MPa for anhydrous to 0.5 wt.% H_2O conditions.

Niri Mbwelesu Taten lava (AMB2) phenocryst-whole rock pairs indicate temperature of 1150–1160 °C and pressure of 590–660 MPa (Table 5.7).

Craig Cove lava phenocrysts paired with AMB6 whole rock as a possible parent melt indicate temperatures of 1150–1170 °C and pressures of 790–870 MPa (Table 5.7). Groundmass plagioclase in equilibrium with a calculated groundmass composition indicates a temperature of 1060–1080 °C and pressure of 220–280 MPa.

	Anhydrous				0.5 wt.% H_2O		
	T (ºC)	P (MPa)	T_{sat} (ºC)	H_2O (wt.%)	T (ºC)	P (MPa)	T_{sat} (ºC)
AMB6 whole rock, K_D=0.24±0.05. n=68 (anhydrous) n=56 (hydrous)							
Mean (1σ)	1170 (2)	790 (50)	1160	0.2 (0.1)	1150 (2)	730 (30)	1140
h (km)	-	30 (2)	-	-	-	27 (1)	-
AMB6 glass, K_D=0.21±0.02. n=53 (anhydrous), n=38 (hydrous)							
Mean (1σ)	1140 (2)	440 (30)	1120	neg	1120 (2)	370 (30)	1110
h (km)	-	17 (1)	-	-	-	14 (1)	-
AMB2007 whole rock, n=3, K_D=023.±0.07							
Mean (1σ)	1160 (4)	550 (80)	1150	neg	1140 (4)	480 (70)	1130
h (km)	-	21 (3)	-	-	-	18 (3)	-
AMB2007 glass, n=2, K_D=0.22±0.03							
Mean (1σ)	1140 (2)	410 (40)	1120	neg	1120 (2)	340 (40)	1110
h (km)	-	15 (1)	-	-	-	13 (1)	-
AMB2 WR, n=6, K_D=0.22±0.07							
Mean (1σ)	1160 (4)	660 (80)	1150	0.0 (0.1)	1150 (4)	590 (70)	1140
h (km)	-	25 (3)	-	-	-	22 (3)	-
AMB10 phenocrysts, AMB6WR as liquid, n=80, K_D=0.31±0.03							
Mean (1σ)	1170 (2)	870 (40)	1160	0.1 (0.0)	1150 (2)	790 (40)	1140
h (km)	-	33 (2)	-	-	-	30 (2)	-
AMB10 phenocrysts, AMB6 glass as liquid, n=81, K_D=0.22±0.02							
Mean (1σ)			1120		1120 (2)	400 (40)	1110
h (km)	-		-	-	-	15 (2)	-
AMB10 groundmass, $glass^{calc}$ as liquid, n=1, K_D=0.22							
Mean (1σ)	1080	280	1080	0.3	1060	220	1070
h (km)	-	11	-	-	-	8	-

Table 5.7 Plagioclase thermometry, barometry and hygrometry results for AMB6, AMB2007, AMB2 and AMB10 whole rock and glass compositions. Text in italics indicates the nominal melt composition, number of plagioclase analyses, and mean K_D value between melt and mineral analyses. Figures in parentheses are one standard deviation. $Glass^{calc}$ for AMB10 is the whole rock composition minus large plagioclase, olivine and clinopyroxene phenocrysts. Conversion of calculated pressures to depth h (=P/ρg), assuming a crustal density ρ of 2700 kg m^{-3}. Values given represent the mean of n calculations, with 1σ in parentheses. 'Neg' denotes a negative result from the plagioclase hygrometer.

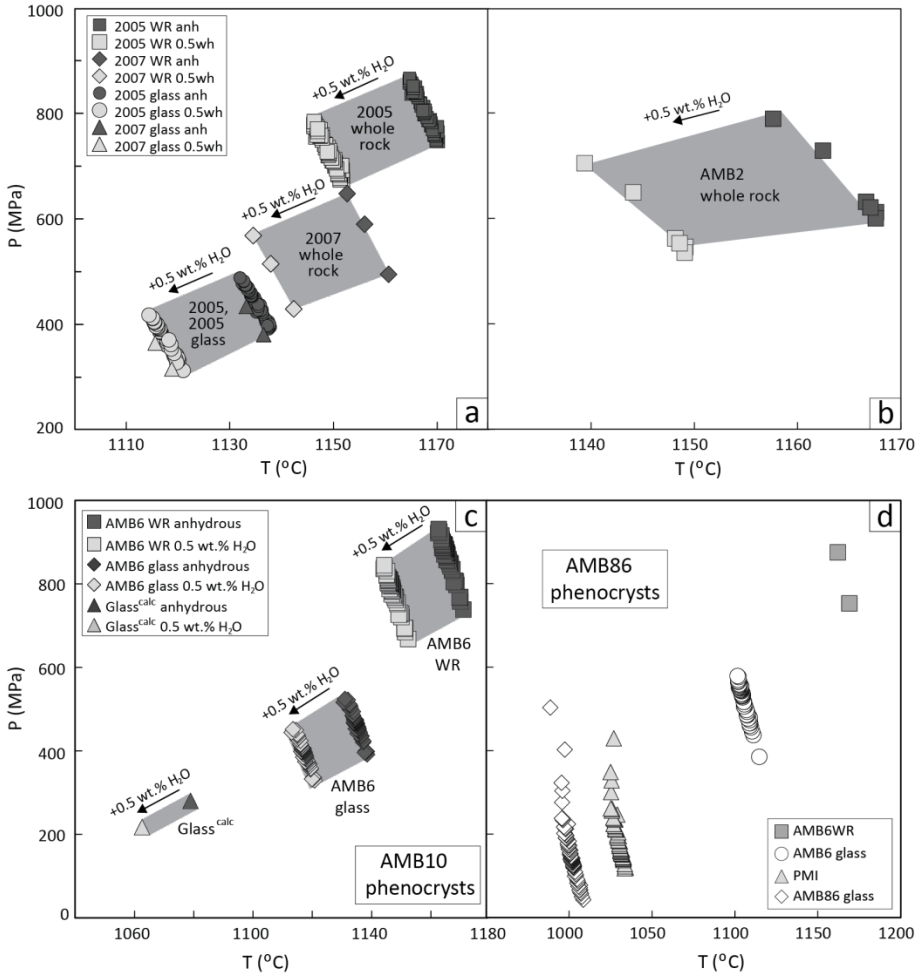

Figure 5.5 Results of plagioclase-melt thermobarometry. (a) Basaltic scoria AMB6 and AMB2007. (b) Niri Mbwelesu Taten lava AMB2. (c) Flank lava AMB10, tested against a number of potential parent melts. (d) Trachyandesite lava AMB86, tested against several potential parent melts. Temperature results are from Eq. 24a of Putirka (2008); pressure results are calculated using the model of Putirka (2005). Standard errors of estimate for these models are ±36 ºC and ±247 MPa (~9 km).

The barometer performs moderately well (to within <300 MPa) for dacite samples from Unzen (Holtz et al., 2005) and Pinatubo (Scaillet & Evans, 1999) of compositions similar to the 1986 trachyandesite glass and melt inclusions.

Trachyandesite results (Table 5.8) indicate that the highest-anorthite plagioclase cores (n=2: An_{74} and An_{65}) crystallised from a basaltic melt such as AMB6 whole rock at 1150–1170 °C and 730–810 MPa. Plagioclase of composition An_{53-65} appears to have crystallised from more slightly more evolved basaltic melt at temperatures of 1110–1120 ºC and pressures of 520–600 MPa. Lower-anorthite plagioclase may have crystallised from melt varying from the composition of the most primitive trachydacitic melt inclusion (An_{39-57}) to that of the matrix glass (An_{39-62}) of the trachyandesite over a range of 1000–1050 °C and 150–230 MPa.

Plagioclase hygrometry results indicate very low water content in all samples, with potentially slightly higher values in AMB10 and AMB86, although this is not resolvable within the error limits (Tables 5.7, 5.8).

	Anhydrous				0.5 wt.% H_2O		
	T (ºC)	P (MPa)	T_{sat} (ºC)	H_2O (wt.%)	T (ºC)	P (MPa)	T_{sat} (ºC)
AMB6WR, n=2, K_D=0.28±0.08							
Mean (1σ)	1170 (5)	810 (90)	1160	0.2 (0.1)	1150 (5)	730 (80)	1140
h (km)	-	31 (3)	-	-	-	28 (3)	-
AMB6 glass, n=54, K_D=0.34±0.03							
Mean (1σ)	1120 (3)	600 (40)	1120	neg	1110 (3)	520 (40)	1110
h (km)	-	23 (2)	-	-	-	20 (2)	-
AMB86 PMI, n=54, K_D=0.34±0.03							
Mean (1σ)	1050 (3)	230 (60)	1050	0.5 (0.1)	1030 (3)	190 (60)	1040
h (km)	-	9 (2)	-	-	-	7 (2)	-
AMB86 glass, n=54, K_D=0.07±0.01							
Mean (1σ)	1020 (4)	190 (80)	1020	0.6 (0.1)	1000 (4)	150 (70)	1010
h (km)	-	7 (3)	-	-	-	6 (3)	-

Table 5.8 Plagioclase thermometry, barometry and hygrometry results for AMB86 (trachyandesite) phenocrysts and four hypothesised equilibrium melts. Text in italics indicates the nominal melt composition, number of plagioclase analyses, and mean K_D value between melt and mineral analyses. Figures in parentheses are one standard deviation. Conversion of calculated pressures to depth h (=P/ρg), assuming a crustal density ρ of 2700 kg m^{-3}. Values given represent the mean of n calculations, with 1σ in parentheses. Note that K_D of 0.10±0.05 for T<1050 °C applies for some of these crystal-melt pairings. 'Neg' denotes a negative result from the plagioclase hygrometer.

5.3.4 Glass thermometry

Finally, to estimate temperature of the matrix glass, Eq. 14 of Putirka (2008) shows the greatest precision (R^2=0.92) and lowest error (51 °C) of available melt thermometers.

$$T(℃) = 754 + 190.6[Mg\#] + 25.52\left[MgO^{liq}\right] + 9.585\left[FeO^{liq}\right] + 14.87\left[(Na_2O + K_2O)^{liq}\right] - 9.83[H_2O^{liq}] \quad \text{(Eq. 14)}$$

Results

Temperature estimates based on matrix glass compositions give temperatures of 1140 °C for the Mbwelesu scoria and ~1010 °C for the trachyandesite (Table 5.9), which corroborates groundmass/glass temperature calculations from plagioclase and olivine thermometry (Tables 5.6 & 5.7).

Sample	n	H_2O (wt.%)	T(°C)
AMB6 glass (Mbwelesu, 2005 basaltic scoria)	23	0	1140
		1	1130
AMB2007 glass (Mbwelesu, 2007 basaltic scoria)	3	0	1150
		1	1140
AMB86 glass (1986 trachyandesitic lava)	11	0	1010
		1	1000

Table 5.9 Results of glass thermometry for all samples in which glass was present. Calculations with H_2O of 1 wt.% are included for comparison.

5.3.5 Oxygen fugacity

A reliable estimate of oxygen fugacity is essential to the understanding of magmatic conditions, as fO_2 exerts a significant influence on the crystallising assemblage (e.g. Toplis & Carroll, 1995), phase compositions (e.g., Cortés et al., 2006) and the sequence of crystallisation (e.g., Berndt et al., 2005). Two different models were used to estimate fO_2: an olivine-spinel-pyroxene oxythermometer based on the thermodynamic models of Sack & Ghiorso (1989, 1991a, b, 1994a, b, c), and a model based on clinopyroxene- and plagioclase-liquid equilibria (France et al., 2010).

The olivine-spinel-pyroxene oxythermometer uses empirical thermodynamic constraints on Fe-Mg exchange between adjacent olivine and spinel crystals (M1 and M2 site ordering, Gibbs energies of reciprocal ordering reactions, and entropies of exchange and reciprocal ordering reactions) to calculate temperature using experimentally-derived $K_D^{(Fe\text{-}Mg)}$ values, and this, combined with a pyroxene composition, returns an fO_2 estimate for a given pressure. The calculator is nominally designed for use with orthopyroxene but using clinopyroxene should have only a minor effect on the results, well within the uncertainty of the calculations (M. Ghiorso, 2010, pers. comm.). The model is available as a web applet on the Computational Thermodynamics Server (CTServer)[10].

Calculations were made using phenocryst or glomerocryst compositions from Mbwelesu scoria (AMB6), Craig Cove lava (AMB10) and trachyandesite (AMB86). AMB2 is excluded as no spinel analyses were obtained in this sample. Glomerocryst and phenocryst compositions were chosen because phenocrystic olivine and spinel are compositionally invariant within each sample, while phenocrystic clinopyroxene shows only minor variance. Close spatial association of these compositional types also indicates a cogenetic relationship and likelihood of equilibrium, with occurrences of all three phases in glomerocrysts are most likely to be in mutual equilibrium. In addition, clinopyroxene-liquid and olivine-liquid

[10] http://ctserver.ofm-research.org/Olv_Spn_Opx/index.php

thermometry show identical temperature results for olivine and clinopyroxene in Mbwelesu scoria (AMB6 and AMB2007), and results well within error of each other in AMB10 and AMB86. Microphenocrystic or groundmass clinopyroxenes are excluded as they appear from Na-Al contents to represent disequilibrium (rapid) growth. The T-fO_2 calculated then represents conditions of crystallisation of phenocrystic olivine, pyroxene, and spinel. Results from the olivine-spinel-pyroxene oxythermometer are listed in Table 5.10. The associated error is ±0.5 log units (Wood, 1991).

	P (MPa)	T (° C)	logfO_2	ΔNNO	Crystals used
AMB6	100	1140	-7.04	1.2	Adjacent olivine and spinel; clinopyroxene adjacent to spinel
	500	1170	-6.55	1.4	
	1000	1200	-5.98	1.5	
AMB10	500	1200	-6.1	1.5	Olivine, spinel, clinopyroxene from single glomerocryst
	1000	1240	-5.5	1.6	
AMB86	100	1040	-10.19	-0.6	Groundmass olivine and clinopyroxene; average spinel
	500	1060	-9.67	-0.3	
	1000	1100	-9.04	-0.2	

Table 5.10 T-fO_2 calculations from the Sack & Ghiorso calculator over a range of pressures. ΔNNO is the value of fO_2 relative to the nickel-nickel oxide (NNO) buffer as defined by Huebner & Sato (1970), NNO=9.36–(24930/T). Temperature results are rounded to three significant figures.

The clinopyroxene-plagioclase-liquid model of France et al. (2010) uses the FeOt content of plagioclase and clinopyroxene, with glass or whole-rock composition as liquid, to estimate fO_2 based on the differential uptake of ferric vs. ferrous iron in the two mineral phases[11]. The model is parameterised for low pressure (<500 MPa) and relatively basic rocks (<60% SiO_2) at ΔFMQ>0, in order to limit the introduction of variability by multiple parameters. The associated error is c. ±1 log unit. Phases most likely to be in equilibrium were selected by the same criteria used for the Ghiorso-Sack calculator; by comparison of thermometry results for phenocrysts of similar size which tend to occur together. Input temperature estimates were chosen based on mineral-melt thermometry results. Results are listed in Table 5.11.

[11] Plagioclase more readily incorporates Fe^{3+} whereas clinopyroxene preferentially incorporates Fe^{2+} (Lundgaard & Tegner, 2004), *i.e.*, more iron will go into plagioclase, and less into clinopyroxene, in an oxidised magma than in a reduced magma, and vice versa.

	P (MPa)	T (° C)	logfO_2	ΔNNO[a]	Phases used
AMB6 glass	100	1140	-6.4	1.8	Plag mp, cpx mp
	500	1140	-6.0	2.3	
AMB2007 glass	100	1140	-6.1	2.2	Plag CCR, cpx ph rim
	500	1140	-5.6	2.7	
AMB2 WR	100	1150	-6.5	1.7	Plag phenos, cpx mp
	500	1150	-6.0	2.2	
AMB10 WR	100	1130	-7.0	1.4	Plag CC, cpx glomerocryst
	500	1130	-6.4	2.0	
AMB6 glass, AMB86 phenos	100	1140	-8.3	0.0	Trachyandesite phenos in eq with AMB6 glass
	500	1140	-7.7	0.5	
AMB86 glass	100	1020	-10.2	0.5	Plag gm, cpx gm
	500	1020	-10.0	0.0	

Table 5.11 Oxygen fugacity calculations using the France et al. (2010) model. 'Crystals used' denotes the phases chosen for calculations. CC=coarse glomerocrysts (undifferentiated), CCR=coarse glomerocryst rims, FCR=fine glomerocryst rims, ph=phenocrysts, mp=microphenocrysts, gm=groundmass.

The two different models used give results within error of each other, indicating relatively oxidising conditions (~NNO+1 to NNO+2) in the scoria and flank basalt storage regions and slightly more reduced conditions (~NNO+0.5 to NNO-0.5) in the trachyandesite storage region. These results concur with Fe^{3+}/Fe^{2+} ratios indicated by clinopyroxene and spinel stoichiometry (Section 4.5), and with the presence of pyrrhotite in the trachyandesite, which indicates fO_2 between QFM and NNO (Luhr, 1990).

The fO_2 estimate from the olivine-spinel-pyroxene calculator is preferred, as equilibrium between clinopyroxene and plagioclase is more difficult to establish, whereas temperature estimates for the olivine and clinopyroxene compositions used are identical, indicating equilibrium. In addition, the olivine, spinel and, to a lesser extent, clinopyroxene compositions are almost invariant within each sample, and these phases frequently occur in physical contact and in inclusion relationships.

5.3.6 Thermobarometry summary

Barometry results are summarised in Fig. 5.6. For Mbwelesu scoria (AMB6, AMB2007) and Niri Mbwelesu Taten lava (AMB2), clinopyroxene thermobarometry indicates mean pressures of 330–410 MPa (12–15 km depth) and mean temperatures of 1140–1150 °C. Plagioclase thermobarometry indicates mean pressures of 730–790 MPa at 1150–1170 °C for plagioclase phenocryst crystallisation from AMB6 whole rock, and 370–440 MPa for plagioclase in equilibrium with 2005 matrix glass ($An_{56–72}$), at mean temperatures of 1120–

1140 °C. Results for AMB2007 are intermediate between conditions for AMB6, at 1140–1160 °C and 430–650 MPa.

Niri Mbwelesu Taten lava (AMB2) shows near-identical pressure, temperature, fO_2 and K_D results to Mbwelesu scoria; clinopyroxene and plagioclase barometry suggest slightly shallower storage. Plagioclase Pphenocryst-whole rock pairs indicate mean temperature of 1150–1160 °C and mean pressure of 590–660 MPa (Table 5.7).

Craig Cove lava phenocrysts paired with AMB6 whole rock as a possible parent melt indicate mean temperatures of 1150–1170 °C and mean pressures of 790–870 MPa (Table 5.7). A groundmass composition was estimated by removing modal percentages of plagioclase megacrysts, and clinopyroxene and olivine phenocrysts. Groundmass plagioclase (although only a single analysis was made) is in equilibrium with this calculated composition and indicates a mean temperature of 1060–1080 °C and mean pressure of 220–280 MPa.

Taking central vent basalt as the parent, AMB10 crystallisation conditions are estimated at means of 430 MPa (16 km depth) and 1140 °C for clinopyroxene, and 1070–1080 MPa (40–41 km depth) and 1240 °C for plagioclase. Groundmass indicates pressure of 300 MPa (11 km depth) and temperature of 1090 °C.

Trachyandesite crystallisation pressures are estimated at means of 340 MPa (13 km depth) for phenocrystic clinopyroxene and 210 MPa (8 km depth) for lower-anorthite plagioclase infill. Although clinopyroxene and plagioclase in the trachyandesite derive from a basaltic melt, the distinct fO_2 signature suggests that crystallisation from the basaltic parent took place in a reservoir distinct from that feeding the basaltic vents.

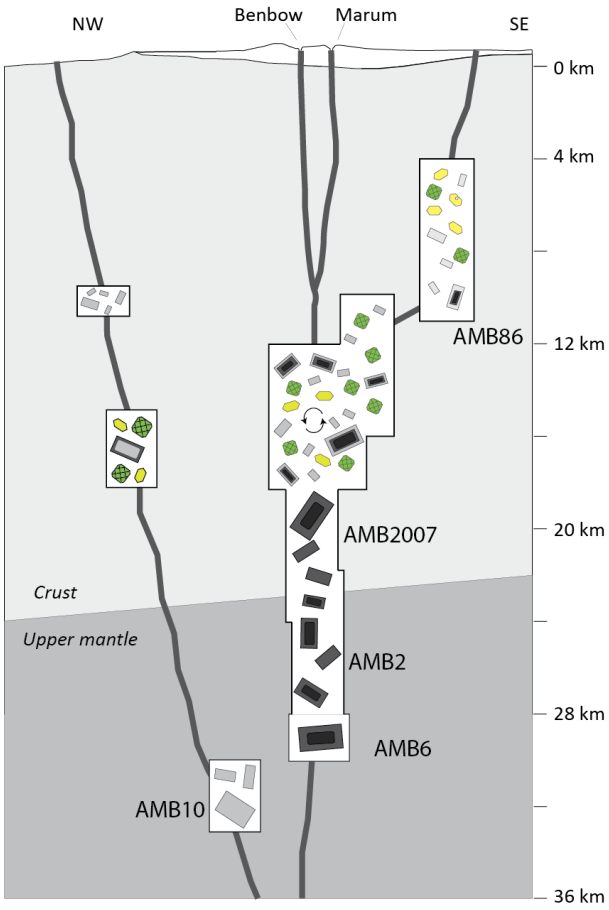

Figure 5.6 Schematic illustration of the magma storage system below Ambrym. Cross-section of emergent part of volcano after Robin et al. (1993). Vertical compression ×0.5. The vertical extent of the 'chambers' corresponds to the depth range calculated from mineral-melt equilibria. Errors of ~±9 km for plagioclase and ~±6 km for clinopyroxene apply. The position of the crust/mantle boundary is based on the estimate of 28 km maximum crustal thickness for the Vanuatu arc (Ibrahim et al., 1980). Lewolembwi is the site of the 1986 trachyandesite eruption. Crystal types in each storage region indicate first appearance; all phases persist to shallow levels but have been omitted from higher storage regions for clarity.

5.4 Discussion

5.4.1 Implications from assessment of equilibrium

In the Mbwelesu scoria, $K_D^{Ab\text{-}An}$ values for plagioclase show a progression from more mafic to more evolved compositions, suggesting continuous evolution with magma ascent and crystallisation. Coarse glomerocryst cores derived from a liquid more mafic than the bulk rock, before crystallising rims in equilibrium with AMB6 bulk rock, concurrently with fine glomerocryst cores and rims, and microphenocrysts, which also grade into equilibrium with the matrix glass. Finally, groundmass plagioclase crystallised from the matrix glass.

Clinopyroxene in the Mbwelesu scoria displays two growth stages: phenocrystic in the mid-crustal level, and rapid disequilibrium groundmass growth. Olivine shows evidence of resorption.

In Craig Cove lava (AMB10), plagioclase megacrysts, clinopyroxene glomerocrysts and olivine all give equilibrium K_D values with the whole-rock composition, but petrographic evidence suggests that this is specious. Firstly, the large proportion of plagioclase megacrysts and attendant elevated Al_2O_3 and Sr in the whole rock indicates plagioclase accumulation; in addition, clinopyroxene glomerocrysts have the appearance of entrained cumulate matter, and olivine has suffered heavy resorption and oxidation, indicating disequilibrium.

Assessment of mineral-melt equilibria in the trachyandesite strongly supports the hypothesis of magma mixing presented in Section 5.2.2, which suggested that basaltic phenocryst compositions should account for 76% of plagioclase, 68% of clinopyroxene , 18% of spinel, and 11% of olivine. Of 14 plagioclase phenocrysts analysed, 12 (86%) have cores or zones which are in equilibrium with the basalt matrix glass or whole rock; many plagioclase phenocrysts are resorbed and infilled with lower-temperature, lower-anorthite plagioclase. Of 26 clinopyroxene phenocrysts analysed, 25 are in equilibrium with AMB6 glass, and one with AMB6 whole rock, but none with AMB86 glass, melt inclusions or whole rock. Olivine phenocrysts host trachydacite melt inclusions which indicates that magma mixing occurred between basalt and trachydacite. A potential source for the trachydacitic liquid may be lenses of silicic liquid separated from crystallising magma stored at shallow levels (cf. Wright & Fiske, 1971).

5.4.2 Crystallisation conditions

These results are the first attempt to model pressures and temperatures of magma crystallisation below Ambrym volcano, and add to the sparse but growing body of data on processes operating below persistently active lava lake volcanoes.

Mineral-melt barometry indicates two major basaltic crystallisation regions, one near the crust-mantle boundary (~24–29 km) characterised by plagioclase crystallisation, and a mid-crustal zone (~11–18 km) where clinopyroxene crystallises. The shallower crystallisation range lies within the likely magma storage region detected at 12–21 km by USGS-NEIC seismic data, while the deeper region corresponds almost exactly to the seismic gap at 25–29 km depth. Temperature calculations demonstrate that olivine crystallises at slightly lower temperatures then clinopyroxene in the basaltic Mbwelesu system, although resorption

textures and homogeneity of composition from phenocrysts to groundmass suggests that reequilibration of earlier-crystallised olivine may have occurred. Spatial association of spinel with olivine and clinopyroxene indicates that spinel also primarily crystallised as part of the mid-crustal assemblage.

Although the accuracy of the plagioclase barometer is poor, the coincidence of pressure estimates for lower-anorthite plagioclase phenocrysts (310–490 MPa) with the mid-crustal storage region indicated by clinopyroxene barometry (350–440 MPa) indicates that these results are a reasonable estimate. Plagioclase thermometry demonstrates that higher-anorthite plagioclase crystallised at temperatures at least 40 ºC higher than phenocrystic clinopyroxene, while lower-anorthite plagioclase crystallised close to clinopyroxene crystallisation temperatures, corroborating the indication from barometry that lower-anorthite plagioclase crystallised alongside clinopyroxene. While it may be considered unusual for plagioclase to precede clinopyroxene and olivine, this sequence has been demonstrated experimentally for a basalt of similar composition to that studied here, under similar conditions; i.e. low H_2O, and low to moderate pressure (Meen, 1990). Previous removal of higher-forsterite olivine is assumed for the samples studied here—post-caldera plagioclase basalts—to bring the magma to this relatively evolved composition, where plagioclase is on the liquidus. In fact, the fractionation models of Picard et al. (1995) postulate generation of the post-caldera plagioclase basalt in a three-stage process, with removal of olivine and augite in the earliest stage, followed by plagioclase-dominated crystallisation at later stages.

5.4.3 Magma supply model

Following identification of the locations and conditions of crystallisation, geochemistry and petrography can illustrate the processes operating in these regions. The persistence of the predominant magma and mineral compositions since the early stages of volcanism suggests a stable and homogeneous magma supply (cf. Harris et al., 1999). Rounded, fritted cores or zones in plagioclase record at least one major dissolution event (e.g., thermal or chemical disequilibrium; Clynne, 1999; Murphy et al., 2000), followed by an uninterrupted period of overgrowth of 200–500 μm of clear plagioclase. Phenocrysts lacking fritted zones perhaps represent the same growth period as the clear rims of the fritted population.

The presence of both euhedral and rounded clinopyroxene and olivine phenocrysts (of similar or identical composition) suggests circulation of phenocrysts into regions where they encounter disequilibrium. Phenocryst convection may be a result of sinking of degassed

magma from the surface (e.g. Kazahaya et al., 1994), a thermal gradient in the magma reservoir (Couch et al., 2001), or a combination of both. Huppert and Sparks (1980) found that recharge results primarily in transfer of heat rather than magma to the existing chamber, which could explain the variable resorption textures of compositionally comparable phases in the basalt; most markedly in olivine which is compositionally invariant but variably resorbed; i.e. the magma has undergone thermal rather than compositional convection. Kazahaya et al. (1994) found that even a small density contrast between degassed and undegassed magma would be sufficient to drive convection. The obvious importance of olivine fractionation to the evolution of the volcanic series, compared to the relative paucity of erupted olivine-rich lava, may reflect olivine settling in the storage region from recharge magma (cf. Huppert & Sparks, 1980). Landi et al. (2004) found that recharge with volatile-rich magma causes dissolution and sieved (rapid) overgrowth of plagioclase at Stromboli (although that is a H_2O-rich case, which will have a stronger impact on plagioclase, as compared to Ambrym which appears H_2O-poor but CO_2-rich). Ambrym is similar to Stromboli in that the shallow magma storage region appears to be recharged by only slightly more primitive magma, resulting in long-lived homogeneity of erupted lavas (Landi et al., 2004). Donaldson (1985) found that plagioclase dissolves faster than it grows with superheating, whereas olivine dissolves at a similar rate to growth, which may explain more pronounced dissolution textures in plagioclase compared to the simple rounding of olivine.

Allard et al. (2015) concluded that convective overturn is required to account for observed degassing patterns, based on comparison between pre-eruptive dissolved volatiles and gas plume composition. In their proposed model, gas-rich magma rises to the top of the conduit, degasses at a very shallow level, and sinks back due to increased density following gas loss. Due to low initial H_2O, the basaltic magma at Ambrym cannot reach the permeability threshold required for degassing until very low pressure (~10 MPa, or ~0.4 km). The prodigious amount of degassing evident in the plume, with extremely minor emission of silicate material, necessarily implies the production of large volumes of degassed magma in the shallow system. Density contrast between degassed magma and fresh gas-rich magma can be accommodated via convective overturn, in order for the system to feed the persistent heavy gas plume. Polacci et al. (2012) found textural evidence of such a process, with two simultaneously-erupted scoria types of low-to-moderate vesicularity and high vesicularity (of identical composition and comparable crystal content), representing degassed and gas-rich magma respectively.

5.4.4 Plumbing model

A first model of the magma storage system beneath Ambrym, based on a combination of new results and previous data, is illustrated in Fig. 5.6. Seismic data and mineral-melt equilibria indicate significant crystallisation at two depths; one near the suggested depth of the Moho for Vanuatu (Coudert et al., 1984; McCall et al., 1970), and one at mid-crustal levels. Possible structural controls on the location of the crustal storage region are not known; it may relate to the base of the volcanic pile and attendant lithological and density contrasts. Melt inclusion entrapment pressures (Allard et al., 2015) and very long period tremor (Legrand et al., 2005) suggest a potential region of ponding and olivine crystallisation at around 3–5 km depth. Petrographic textures seen in phenocrysts from the mid-crustal storage region suggests magma convection at this depth; studies of textural features (Polacci et al., 2012) and degassing processes (Allard et al., 2015) suggest that this is driven by sinking of degassed magma from the shallow conduit.

The model for the central basaltic plumbing system illustrated in Fig. 5.6 is envisaged as follows: relatively primitive magma, bearing plagioclase of $An_{>80}$, stalls near the crust/mantle interface at ~24–29 km depth, where plagioclase rims of $An_{63–80}$ overgrow the more primitive cores. Crystallisation, or heat and volatile input following magma recharge, drives further ascent via density reduction. The magma stalls again around 11–18 km, where clinopyroxene and lower-anorthite ($An_{72–56}$) plagioclase crystallisation occurs; this storage region may correspond to the base of the volcanogenic crust. Crustal thickness for the Western and Eastern belts of Vanuatu is ~20 km, while the South Aoba Basin crust, at the southern end of which Ambrym has developed, has a crustal thickness of 12–13 km (Collot & Fisher, 1988); crustal thickness for Ambrym can be expected to fall between these values. The magma composition at this depth is effectively the same as that of the final erupted scoria, as indicated by clinopyroxene-hosted melt inclusion compositions. Since the residual melt evolves no further, buoyancy imparted by thermal and/or volatile recharge, rather than fractionation-induced density reduction, is the presumed impetus for further ascent. The error margins on mineral-melt barometry, and tendency of late-stage minerals to undergo non-equilibrium growth, precludes distinction of crystallisation pressures at such shallow levels. Melt inclusion entrapment pressures indicate that olivine crystallises at low pressures (70 to 100 MPa, or ~3–5 km depth; Allard et al., 2015), which may indicate a further ponding region at such depths. The slightly lower temperatures indicated by olivine thermometry are congruent with this model. Near-surface tremor at ~3.5–3.7 km depth (Legrand et al., 2005) may represent magma or fluid transport related to this crystallisation region.

Plagioclase and clinopyroxene phenocrysts in the trachyandesite derive from a basaltic melt, but the majority of the plagioclase has undergone resorption and infill with lower-anorthite plagioclase at lower pressures and temperatures, with olivine also crystallising at these lower temperatures. The crustal storage region for the trachyandesite spans shallower depths than the basalts; ~13 km for phenocrystic clinopyroxene and ~8 km for lower-anorthite plagioclase infill. This system is more reduced than the basalt storage region, as demonstrated by fO_2 calculations and by the presence of pyrrhotite in the phase assemblage. The highest-anorthite plagioclase in AMB86 contains notably lower FeOt than the plagioclase erupted from the central vents (Mbwelesu, Niri Mbwelesu Tate) and flank (Craig Cove), which indicates that although they originate from a basaltic parent, fO_2 conditions were different. This suggests a separation between basaltic and trachyandesitic sources at least as far down as the depth of early plagioclase crystallisation. The history of only a single eruption at the trachyandesite vent, despite still-active tremor activity below the eruption area, suggests that the storage region is a closed system which underwent eruption in 1986 following some as yet unidentified trigger, most likely thermal or volatile input from mafic recharge.

5.5 Conclusions

Thermobarometric modelling has for the first time identified distinct levels of magma storage and crystallisation beneath Ambrym volcano, which correlate with depths indicated by earthquake data. Ambrym appears to have a vertically extensive central conduit (the Marum-Benbow complex) characterised by staged crystallisation and magma convection, and nearby, a separate plumbing system at least to the depth of primitive plagioclase crystallisation, extruding magma which stalled in the shallow crust to become geochemically distinct (the trachyandesite vent), via mixing of parent basalt with trachydacite. An analogue system can be found in Kliuchevskoi-Bezymianny (Almeev et al., 2013). Mineral-melt equilibria indicate that the trachyandesite lava of 1986 bears a significant cargo of basaltic phenocrysts, and mass balance calculations suggest that the trachyandesite consists of ~70% central vent type basalt and ~30% trachydacite of composition recorded by melt inclusions in olivine and spinel.

Occurrence of the deep plagioclase crystallisation region near the estimated level of the crust/mantle interface suggests a structural control on magma ascent at this level. Potential structural influences on shallower crystallisation regions are uncertain due to scarcity of data on the structure of the lithosphere below Ambrym.

Petrographic observations provide support for the convective model of magma supply at persistently active lava lake volcanoes, whereby magma rises, degasses, and recirculates downward into the storage region at depth. Textural indications of circulation in phenocrysts associated with the mid-to-shallow-crustal storage region and presence of deeper-derived mineralogy (bytownitic plagioclase) only as a relict/antecrystic phase indicates that the mid-to shallow crust is where magma convection occurs.

These results demonstrate that the combination of petrographic and thermobarometric study can illustrate both the processes and conditions of magma storage beneath a volcanic system.

Chapter 6 Pre-eruptive volatile contents

6.1 Introduction

This chapter presents H_2O-CO_2-S-Cl-F data for melt inclusions and matrix glass from Ambrym basaltic scoria, and S-Cl-F data for melt inclusions and glass in the trachyandesite lava, and compares the results to degassing models to evaluate potential degassing processes. Melt inclusions in basaltic scoria samples ejected during elevated activity from the Mbwelesu vent in 2005 and 2007 provide insights with particular reference to the period of the large SO_2 pulse of early 2005 (Bani et al., 2009).

Comparison of melt inclusions from the basaltic scoria with those from the trachyandesite is hoped to elucidate differences in magma pathways and evolution.

6.1.1 Degassing measurements at Ambrym

Ambrym is one of a number of basaltic volcanoes worldwide—including Stromboli (Burton et al., 2007), Etna (Aiuppa et al., 2008), Miyakejima (Shinohara et al., 2003), Masaya (Stix, 2007), and Nyiragongo (Carn, 2004)—noted as strong passive emitters of gases, releasing high fluxes of CO_2, SO_2 and other volatiles while in an otherwise relatively quiescent state (Bani et al., 2009; Allard et al., 2015). Ambrym has been noted for strong, persistent degassing since its "great columns of smoak" were first described in 1774 by Captain James Cook (Beaglehole, 1961).

More recently, data from the Ozone Mapping Instrument (OMI) showed Ambrym to be the strongest global point source of SO_2 for the first months of 2005. Differential Optical Absorption Spectroscopy (DOAS) measurements made during the same period recorded emissions of up to 270 kg s^{-1} (Bani et al., 2009), comparable to or significantly greater than other strongly degassing volcanic systems (Table 6.1). Spectroscopic measurements during the same period showed fluxes of SO_2, BrO, Cl and F among the highest volcanic rates known (Bani et al., 2009).

Longer-term flux measurements by ultraviolet spectroscopy (Bani et al., 2012) over the period 2004–2009 reveal that the Vanuatu arc releases ~3 Tg yr^{-1} of SO_2, equivalent to ~20% of existing global estimates; Ambrym alone provides nearly two-thirds of the Vanuatu total, with a mean flux of 5 Gg day^{-1} of SO_2. Bani et al. (2012) note that 90% of SO_2 production occurs from the central arc region in which Ambrym is situated.

Volcano	SO_2 flux (kg s^{-1})	Period	Reference
Miyakejima (Japan)	463–625	Late 2000–early 2001	Kazahaya et al. (2004)
Miyakejima (Japan)	46–463	2000–2002	Campion et al. (2010)
Etna (Italy)	6–347	1987–2006	Campion et al. (2010)
Ambrym	270	Early 2005	Bani et al. (2009)
Nyiragongo (DR Congo)	23–38	May/June 2005, January 2006, and June 2007	Sawyer et al. (2008)
Kīlauea (Hawai'i)	20	1998–2001	Elias & Sutton (2013)
Pacaya (Guatemala)	16	1999–2002	Rodriguez et al (2004)
Masaya (Nicaragua)	12	1972–2007	Nadeau & Williams-Jones (2009)
Stromboli (Italy)	2.3	Quiescence	Burton et al. (2007)

Table 6.1 SO_2 fluxes at notable strongly-degassing basaltic/silica-undersaturated volcanoes, ranked from highest to lowest.

The variability of these measurements highlights firstly that gas flux is highly variable, so long-term studies of emissions are essential and long-term degassing rates cannot be extrapolated from 'snapshots'; and secondly, that improvements in instrumentation and monitoring are resulting in increasingly more precise (and generally higher) estimates for volcanoes worldwide. It seems that perhaps Ambrym is not an extreme example but rather that the magnitude of volcanic degassing, worldwide, has been systematically under-estimated until quite recently.

Ambrym also emits CO_2 at a high rate (up to 230 kg s^{-1}, Allard et al., 2009), which is higher, for example, than Etna (190 kg s^{-1}; averaged from several studies; Burton et al, 2013), which is considered a high emitter of CO_2 (Allard et al., 1991). These data show that Ambrym comprises an important component of the global volcanic degassing budget. High SO_2 and CO_2 fluxes (Allard et al., 2009; Bani et al., 2009) indicate that the gas derives from a deep magma source. Similar sulphur, halogen, trace metal and radonuclide patterns for both Marum and Benbow strongly suggest that both craters degas from the same magma body at depth, although CO_2/SO_2 ratios indicate that gas separation occurs at a deeper level at Marum (Allard et al., 2015). Comparison between pre-eruptive dissolved volatiles and gas plume composition indicates that production of large volumes of degassed magma via convective overturn, is required to account for such prodigious degassing accompanied by very minor emission of

silicate material. In this model, gas-rich magma rises to the top of the conduit, degasses at a very shallow level—due to low initial H_2O, the magma cannot reach the permeability threshold required for degassing until ~10 MPa, or ~0.4 km—and sinks back due to increased density following gas loss. Textural evidence of coexisting degassed and gas-rich magma has been demonstrated by two simultaneously-erupted scoria types of low-to-moderate vesicularity and high vesicularity of identical composition and comparable crystal content (Polacci et al., 2012).

6.2 Sample details

Melt inclusions and matrix glasses from basaltic scoria erupted in 2005 (AMB6) and 2007 (AMB2007) and the trachyandesite lava (AMB86) were analysed for major elements and volatile components. The basaltic scoria samples were produced during periods of increased Strombolian activity, and in the case of the 2005 samples, a period of intense degassing (Bani et al., 2009).

Samples were crushed and phenocrysts extracted, mounted in epoxy resin, and ground and polished to expose melt inclusions. Melt inclusions selected for analysis were ovoid, of clear brown glass, and showing no cracks, no connection to the crystal exterior, no shrinkage bubbles, and no evidence of decrepitation, although some petrographic detail may have been lost during polishing. Some inclusions in olivine also contained iron oxide grains which due to their large size are believed to have been trapped along with the silicate melt rather than precipitated after entrapment as a result of oxidation by hydrogen loss. Inclusions larger than ~5–10 μm diameter were targeted for electron probe analysis, and larger than 30 μm diameter for SIMS analysis.

A total of 49 melt inclusions (48 spots on 43 inclusions in AMB6; 8 spots on 6 inclusions in AMB2007) and 14 matrix glass spots (AMB6 only) were analysed for H_2O-CO_2-F-Cl by SIMS on a Cameca ims-4f ion microprobe at the University of Edinburgh, using the analytical methods described in Section 3.5. No melt inclusions from the trachyandesite were analysed by SIMS, due to time constraints. A total of 81 melt inclusions from olivine, clinopyroxene, and spinel were analysed for major elements and S, Cl and F on the electron microprobe at the University of Cambridge. Of the inclusions analysed on SIMS, 19 lack corresponding EPMA data due to localised irregularities in the carbon coating on part of the crystal mount, or failed analyses (i.e., with low totals or interference from the host crystal). This chapter primarily concerns those melt inclusions analysed on SIMS, although some data from melt inclusions

analysed on EPMA only are also included, such as S-Cl trends and trachyandesite-hosted melt inclusion compositions.

	SIMS+ EPMA			SIMS only			Total
	ol	sp	px	ol	sp	px	
AMB6	10	1	16	9	6	1	43
AMB2007	-	3	-	-	3	-	6

Table 6.2 Number of melt inclusions analysed by SIMS in scoriae AMB6 and AMB2007, divided by host phase.

6.3 Results

6.3.1 Mbwelesu scoria

Major elements

Melt inclusion compositions in the basaltic scoria samples (AMB6 and AMB2007) fall mainly in the basaltic andesite to basaltic trachyandesite fields; with a handful (4) of outliers just within the trachybasalt field (Fig. 6.1). Compositions show overlap between olivine-, pyroxene- and spinel-hosted melt inclusions, and also with glass and whole rock compositions (Fig. 6.1; Tables 6.2–6.4). The majority (75%) of the basalt-hosted inclusions fall between whole rock and glass fields, which suggests trapping during fractionation along a liquid line of descent. Significant overlap with matrix glass compositions suggests that trapping occurred at a late stage of the magma evolution.

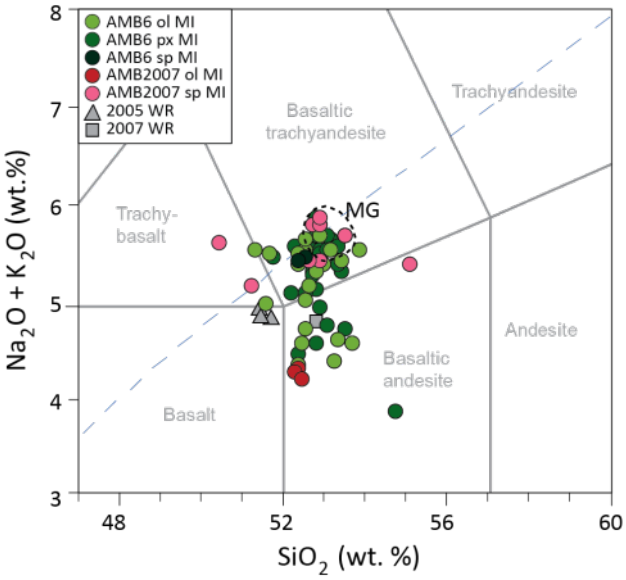

Figure 6.1 Melt inclusion and glass compositions of AMB6 and AMB2007 basalts. The dashed-line field marked MG outlines the compositional field of matrix glass in 2005 and 2007 samples.

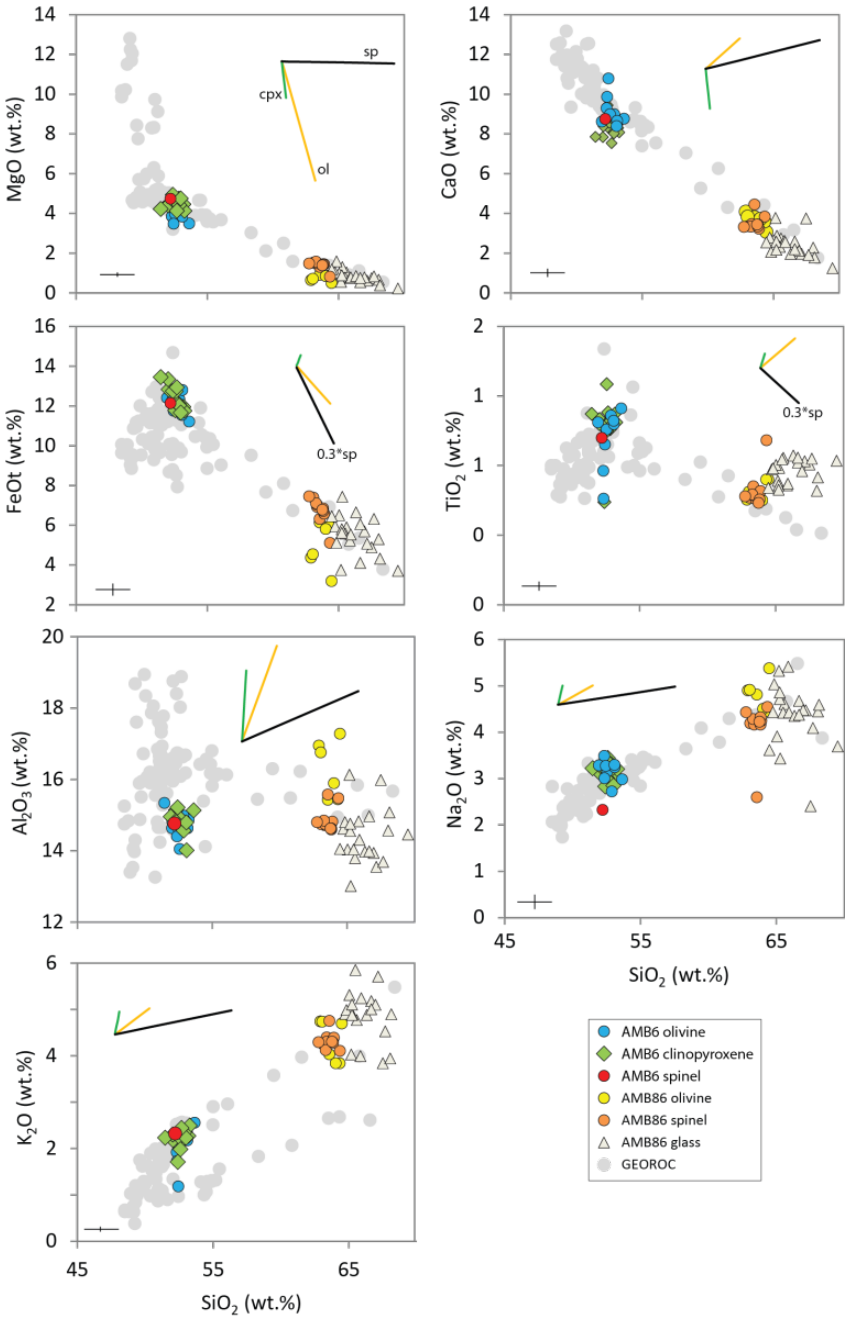

Figure 6.2 Major-element variation diagrams comparing melt inclusion compositions in basaltic scoriae (AMB6, AMB2007) and trachyandesite lava (AMB86) with published data covering the entire volcanic succession (Picard et al., 1995; Robin et al. 1993; Gorton, 1977). Error bars represent the relative error of 5% (10% for Na_2O) associated with EPMA analyses. Coloured bars (yellow=olivine, green=clinopyroxene, black=spinel) indicate the direction and extent of melt evolution which would result from 15% crystallisation of basaltic olivine, clinopyroxene and spinel. The spinel bar has been scaled down by a third (i.e., to 5% crystallisation) on the FeOt-SiO_2 and TiO_2-SiO_2 diagrams in order to fit within the plot area.

On major element variation diagrams (Fig. 6.2), basalt-hosted inclusions fall directly after major inflections in the MgO-SiO_2 and CaO-MgO trends, at a major inflection point in TiO_2-SiO_2, and at the end-point of the steeper first segment of the CaO-SiO_2 trend (which suggests a higher-anorthite trend which shifted to lower-anorthite around 53% SiO_2). This suggests that inclusions were trapped following a significant change in crystallising assemblage, where spinel joined the assemblage, while olivine became less important and plagioclase crystallisation decreased and/or became less anorthitic.

Volatile components

SIMS data (Fig. 6.3a) reveal consistently low (0.19–0.33 wt.%) water contents in melt inclusions, although these are slightly elevated compared to the matrix glass (0.08–0.11 wt.%). Dissolved CO_2 contents cover a range of 60–770 ppm. AMB2007 inclusions display generally lower H_2O than AMB6, and CO_2 contents do not exceed the detection limit. Where multiple (2–3) analyses on a single inclusion were possible, consistent H_2O and CO_2 concentrations were obtained.

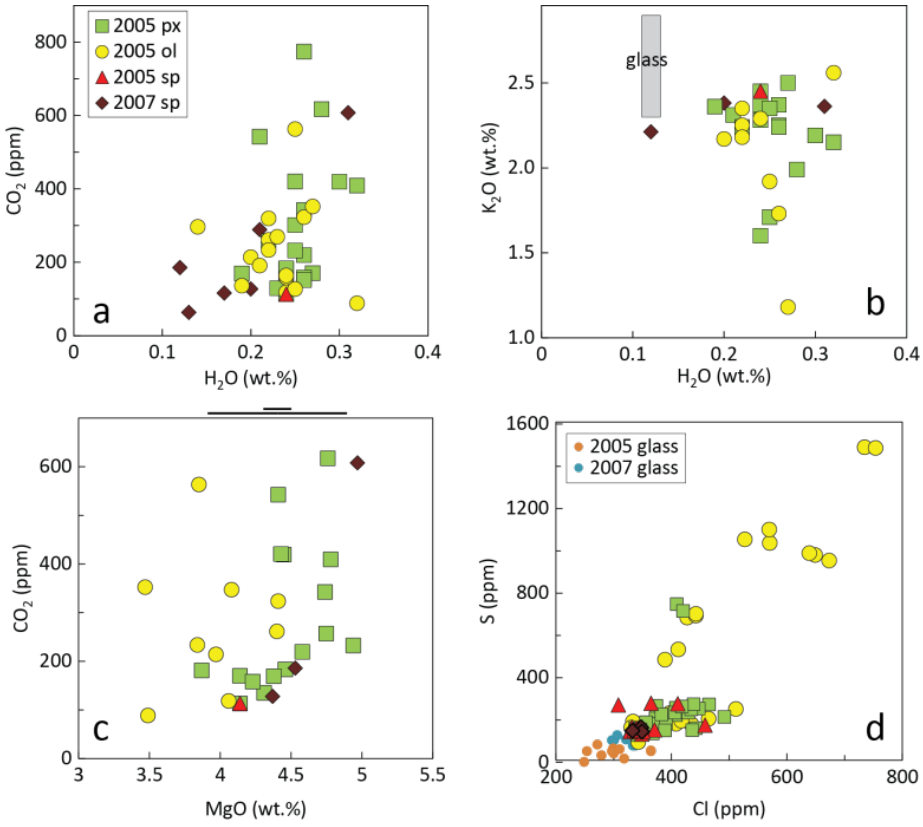

Figure 6.3 Volatile concentrations in melt inclusions from basaltic scoria AMB6 and AMB2007. **a)** CO_2-H_2O contents, showing variation of CO_2 contents over a range of ~800 ppm but very little variation of H_2O (a range of ~0.2 wt.%). **b)** H_2O vs. K_2O shows no correlation, indicating that inclusions are vapour-saturated. **c)** CO_2 vs. MgO shows no correlation, which indicates that CO_2 variation is not a result of variable PEC. The heavy black bar at the top of the graph shows mean ± 1σ of matrix glass MgO content (n=23); the shorter bar above shows mean ± 1σ when a handful of clear outliers are removed from the dataset (n=19), although the outlier analyses seem otherwise valid. **d)** Sulphur vs. chlorine contents, including matrix glass data; most melt inclusion data cluster at relatively low values, forming a continuous trend with matrix glass concentrations, but a subset of inclusions define a positive higher-S-Cl trend. The 2007 glass is slightly enriched in S and Cl compared to 2005.

H_2O contents show no correlation with incompatible elements, indicating that the inclusions are vapour-saturated (Fig. 6.3b). Comparison of CO_2 and MgO contents show no correlation, indicating that volatile contents have not been artificially elevated by PEC,

although olivine-hosted inclusions do display slightly low MgO relative to the matrix glass, indicating that some PEC has occurred (Fig. 6.3c).

Sulphur ranges from 130–1490 ppm and chlorine ranges from 310–830 ppm in melt inclusions, compared to <150 ppm S and 250–340 ppm Cl in the matrix glass (Fig. 6.3d). The F contents of melt inclusions (500–1000 ppm) are effectively indistinguishable from those of the matrix glass (400–800 ppm)[12]. CO_2 concentrations do not correlate with S or Cl concentrations, although one of the highest S concentrations (1080 ppm) coincides with one of the highest CO_2 concentrations (560 ppm).

[12] ppm values are rounded to the nearest 10 in the text, for CO_2-F-Cl-S data.

Analysis	5_mi7	3_mi9	5_mi1	5_mi8	3_mi6	1_mi7	7_eb1	7_eb2	7_eb3	3_eb1	3_mi5 in ox	2_mi11	7_mi5
Host	ol	Ol	ol	ol	ol	ol	ol	ol	ol	ol	sp	px	px
n^{EPMA}	*3*	*3*	*2*	*1*	*1*	*1*	*1*	*1*	*3*	*1*	*2*	*2*	*1*
SiO_2	52.35 (0.05)	52.07 (0.46)	53.03 (0.29)	53.75	52.7	53.27	53.54	52.44	52.46 (0.46)	53.22	52.31 (0.13)	52.85 (0.26)	54.62
Al_2O_3	15.15 (0.38)	14.99 (0.19)	14.60 (0.06)	15.16	14.97	14.05	15.1	14.83	15.22 (0.07)	14.83	14.79 (0.13)	14.7 (0.24)	12.29
TiO_2	0.77 (0.01)	1.05 (0.05)	1.09 (0.03)	1.13	1.01	1.04	0.59	0.61	0.92 (0.05)	1.06	0.96 (0.02)	1.11 (0.02)	1.53
FeO	12.2 (0.42)	12.44 (0.33)	12.35 (0.47)	11.24	12.18	12.84	11.18	12.32	11.76 (0.52)	11.57	12.16 (0.02)	12.98 (0.19)	14.26
MnO	0.26 (0.01)	0.26 (0.02)	0.25 (0.01)	0.26	0.28	0.25	0.28	0.25	0.26 (0.02)	0.25	0.22 (0)	0.26 (0.01)	0.34
MgO	3.85 (0.14)	4.4 (0.15)	4.06 (0.22)	3.49	3.97	3.84	4.08	4.41	3.47 (0.05)	4.44	4.74 (0.1)	4.14 (0.11)	3.87
CaO	9.29 (0.05)	8.64 (0.15)	9.00 (0.07)	8.78	9.01	8.68	10.03	9.87	10.78 (0.18)	8.41	8.76 (0.12)	7.55 (0.07)	8.68
Na_2O	3.49 (0.16)	3.29 (0.01)	2.73 (0.52)	2.99	3.16	3.25	2.93	3.01	3.27 (0.09)	3.30	3.12 (0.01)	3.34 (0.09)	2.31
K_2O	1.92 (0.06)	2.25 (0.01)	2.29 (0.02)	2.56	2.17	2.18	1.67	1.73	1.18 (0.05)	2.35	2.33 (0.02)	2.45 (0.06)	1.6
P_2O_5	0.36 (0)	0.43 (0)	0.44 (0.01)	0.46	0.39	0.43	0.32	0.32	0.32 (0.01)	0.45	0.39 (0)	0.46 (0)	0.33
F ppm	717 (52)	822 (97)	685 (73)	687	847	691	967	587	838 (145)	792.40	698 (66)	749 (49)	480
Cl ppm	571 (9)	403 (11)	427 (21)	525	422	468	420	395	660 (22)	347.88	364 (72)	381 (10)	505
S ppm	1082 (31)	216 (34)	183 (0)	258	198	208	545	494	988 (14)	97	278 (4)	145 (10)	220
Total	98.72 (0.51)	98.51 (0.4)	98.47 (0.65)	97.19	98.61	98.87	97.85	98.14	98.56 (0.87)	98.31	98.54 (0.19)	98.56 (0.47)	97.01
n^{SIMS}	*1*	*2*	*1*	*1*	*1*	*1*	*1*	*1*	*1*	*1*	*1*	*1*	*1*
H_2O wt.%	0.25	0.22 (0.00)	0.24	0.32	0.20	0.22	n.d.	0.26	0.27	0.22	0.25	0.24	0.24
CO_2 ppm	563	261 (83)	118	88	214	233	347	323	352	n.d.	210	113	181
F ppm	457	496 (45)	503	499	394	468	n.d.	522	469	443	341	480	435
Cl ppm	666	558 (86)	543	473	428	548	n.d.	520	521	475	380	511	490
K_D^{Fe-Mg}	0.224	0.232 (0.015)	0.204	0.226	0.187	0.210	0.224	0.220	0.215	0.214	n.a.	0.235	0.226

Table 6.3 EPMA and SIMS data for melt inclusions in olivine (ol), spinel (sp) and pyroxene (px) in 2005 basaltic scoria AMB6. EPMA data in normalised to 100 wt.% anhydrous; 'Total*' is the analytical total before normalisation. Figures in parentheses give values of 1σ where number of analyses (n) is greater than 1; non-averaged data are given in Appendix G. K_D^{Fe-Mg} gives the partition coefficient for Fe-Mg exchange between each melt inclusion and host mineral (average of all olivine, or an average value for large euhedral phenocrystic clinopyroxene), except where marked with * which indicates a matched inclusion/host analysis pair.

Analysis	5_mi9	3_mi3	2_mi12	2_mi14	2_mi9	7_mi10	7_mi11	7_mi4	7_mi3	7_mi6	5_mi3	5_mi5	5_mi6	1_mi1
Host	px	px	Px	Px	px	px	px	px	px	px	px	px	px	px
EPMA (normalised to 100 wt.% anhydrous)														
n	*1*	*2*	*1*	*1*	*1*	*2*	*1*	*3*	*3*	*2*	*1*	*1*	*3*	*2*
SiO_2	53.3	52.98 (0.29)	52.76	52.95	52.67	52.21 (0.16)	52.19	52.65 (0.1)	52.73 (0.3)	52.46 (0.32)	53.4	51.63	53.00 (0.26)	53.11 (0.4)
Al_2O_3	14.66	14.74 (0.21)	14.77	14.92	14.59	14.86 (0.16)	14.68	14.64 (0.06)	14.08 (0.05)	14.42 (0.16)	14.91	15.39	15.02 (0.15)	14.87 (0.02)
TiO_2	1.1	1.08 (0.05)	1.05	1.01	1.27	1.07 (0.02)	1.04	1.04 (0.05)	1.00 (0.01)	0.59 (0.04)	1.05	1.10	1.06 (0.02)	1.04 (0.02)
FeOt	11.98	11.87 (0.35)	12.19	12.13	11.8	12.86 (0.2)	13.38	12.26 (0.38)	12.76 (0.15)	12.76 (0.26)	11.78	13.5	12.05 (0.09)	11.69 (0.1)
MnO	0.25	0.23 (0.01)	0.26	0.27	0.27	0.27 (0.01)	0.26	0.24 (0.01)	0.29 (0.02)	0.27 (0.01)	0.29	0.22	0.25 (0.03)	0.26 (0)
MgO	4.46	4.74 (0.09)	4.38	4.31	4.78	4.45 (0.23)	4.41	4.58 (0.1)	4.76 (0.11)	4.94 (0.04)	4.14	4.23	4.43 (0.07)	4.75 (0.09)
CaO	8.31	8.16 (0.03)	8.21	8.09	8.85	8.4 (0.2)	7.85	8.56 (0.08)	8.85 (0.15)	9.45 (0.13)	8.09	7.87	8.04 (0.12)	8.60 (0.05)
Na_2O	3.04	3.21 (0)	3.45	3.32	3.00	3.11 (0.1)	3.28	3.18 (0.09)	2.97 (0.12)	2.83 (0.07)	3.21	3.23	3.21 (0.09)	2.85 (0.41)
K_2O	2.28	2.37 (0.03)	2.36	2.37	2.15	2.19 (0.14)	2.31	2.25 (0.03)	1.99 (0.05)	1.71 (0.02)	2.5	2.24	2.35 (0.06)	2.24 (0.05)
P_2O_5	0.45	0.47 (0.01)	0.44	0.44	0.43	0.42 (0)	0.43	0.43 (0.01)	0.39 (0.01)	0.3 (0.01)	0.48	0.42	0.44 (0)	0.44 (0)
F ppm	792	685 (18)	753	799	805	620 (20)	723	765 (143)	626 (63)	691 (17)	720	743	731 (61)	642 (78)
Cl ppm	394	345 (1)	355	450	417	456 (24)	446	389 (8)	435 (16)	419 (7)	398	423	350 (8)	377 (1)
S ppm	177	147 (24)	155	163	263	259 (26)	155	230 (41)	258 (19)	740 (25)	153	267	162 (26)	197 (17)
Total	98.57	98.22 (0.46)	98.12	97.96	97.61	97.76 (0.39)	97.57	98.18 (0.59)	97.69 (0.49)	98.79 (0.22)	97.55	98.66	98.88 (0.11)	98.35 (0.87)
$K_D^{Fe\text{-}Mg}$	0.242	0.242	0.237	0.240	0.246	0.238	0.234	0.239	0.237	0.242	0.241	0.237	0.242*	0.247
SIMS														
n	*1*	*2*	*2*	*1*	*2*	*1*	*1*	*2*	*1*	*1*	*1*	*1*	*1*	*1*
H_2O wt.%	0.24	0.26 (0.01)	0.19 (0.00)	0.24	0.32 (0.01)	0.30	0.21	0.26 (0.00)	0.28	0.25	0.27	0.26	0.25	0.22
CO_2 ppm	183	342 (287)	169 (26)	135	409 (106)	419	542	219 (5)	617	232	170	158	420	257
F ppm	421	375 (64)	420(4)	350	465 (20)	391	301	432 (2)	454	401	329	489	457	416
Cl ppm	459	430 (75)	459 (40)	400	556 (21)	524	344	526 (12)	622	456	284	556	444	393

Table 6.3 ctd.: EPMA and SIMS data for melt inclusions in pyroxene (px) in 2005 basaltic scoria AMB6. EPMA data is normalised to 100 wt.% anhydrous; 'Total*' is the analytical total before normalisation. Figures in parentheses give values of 1σ where number of analyses (n) is greater than 1; non-averaged data are given in Appendix G.

Analysis	mt3_mi2	mt2_mi1	mt2_eb1	mt4_eb1	mt4_mi1	mt4_mi4	mt3_olmi1	mt3-mi1	mt2-mi2	mt2-eb1
Host	sp	sp	sp	sp	sp	sp	ol	sp	sp	sp
EPMA (normalised to 100 wt.% anhydrous)										
N	*1*	*1*	*2*	*3*	*1*	*1*	*3*	*1*	*1*	*2*
SiO_2	50.36	52.51	53.6 (1.1)	52.92 (0.41)	51.10	52.80	52.23 (0.09)	n.d.	n.d.	n.d.
Al_2O_3	15.03	14.77	14.13 (0.66)	14.93 (0.01)	14.70	14.85	14.2 (0.19)	n.d.	n.d.	n.d.
TiO_2	1.19	1.10	1.07 (0.08)	1.06 (0.05)	1.11	1.09	0.61 (0.03)	n.d.	n.d.	n.d.
FeOt	13.77	12.64	11.87 (0.18)	11.77 (0.34)	12.83	12.16	12.8 (0.17)	n.d.	n.d.	n.d.
MnO	0.26	0.22	0.24 (0.01)	0.24 (0.02)	0.28	0.22	0.29 (0.03)	n.d.	n.d.	n.d.
MgO	4.97	4.53	4.37 (0.08)	4.46 (0.09)	5.02	4.20	5.11 (0.03)	n.d.	n.d.	n.d.
CaO	8.15	8.14	8.02 (0.44)	8.21 (0.08)	8.84	8.68	9.88 (0.12)	n.d.	n.d.	n.d.
Na_2O	3.28	3.24	3.26 (0.23)	3.34 (0.01)	3.07	3.22	2.82 (0.02)	n.d.	n.d.	n.d.
K_2O	2.36	2.21	2.38 (0.14)	2.45 (0.05)	2.10	2.24	1.47 (0.03)	n.d.	n.d.	n.d.
P_2O_5	0.43	0.40	0.43 (0.01)	0.43 (0.02)	0.74	0.42	0.31 (0.01)	n.d.	n.d.	n.d.
F ppm	635	792	718	678 (97)	844	571	713 (24)	n.d.	n.d.	n.d.
Cl ppm	347	348	332 (6)	344 (10)	453	373	442 (10)	n.d.	n.d.	n.d.
S ppm	164	144	148 (6)	155 (19)	173	154	702 (11)	n.d.	n.d.	n.d.
Total*	97.78	100.50	99.96 (0.16)	99.06 (0.38)	100.85	99.12	98.6 (0.23)	n.d.	n.d.	n.d.
SIMS										
N	*1*	*1*	*2*	*0*	*0*	*0*	*0*	*1*	*1*	*2*
H_2O wt.%	0.31	0.12	0.20 (0.01)	n.d.	n.d.	n.d.	n.d.	0.17	0.13	0.21 (0.01)
CO_2 ppm	607	185	127 (29)	n.d.	n.d.	n.d.	n.d.	116	63	289 (168)
F ppm	488	327	329 (18)	n.d.	n.d.	n.d.	n.d.	501	437	340 (8)
Cl ppm	398	351	335 (19)	n.d.	n.d.	n.d.	n.d.	473	421	307 (14)
Mg wt.%				n.d.	n.d.	n.d.	n.d.	5.19	5.4	5.77 (0.08)

Table 6.4 EPMA and SIMS data for melt inclusions in spinel (sp) and olivine (ol) in basaltic scoria AMB2007. EPMA data is normalised to 100 wt.% anhydrous; Total* is the analytical total before normalisation. Mg wt.% data from SIMS are included for MI not analysed on EPMA to demonstrate that the analysis did sample silicate glass.

Analysis	6_mi1	6_mi2	1_mi10	3_mi8	6_mi6	7_mi9	5_mi4	7_mi1	mi_3_eb2
Host	ol	ol	ol	ol	ol	ol	ol	ol	ol
H_2O wt.%	0.23	0.22	0.25	0.14	0.21	0.19	0.24	0.24	0.24
F ppm	504	425	362	509	449	365	524	491	368
Cl ppm	503	512	335	1752	466	369	499	489	432
CO_2 ppm	269	319	127	296	191	136	158	164	n.d.
MgO wt.%	5.3	5.3	5.62	4.4	5.3	5.21	4.7	5.07	n.d.

Analysis	6_mi3	6_mi4	6_mi5	6_mi9	6_mi9b	3_eb2	mi_3_ox2
Host	px	px	px	px	px	px	ox
H wt.%	0.25	0.26	0.23	0.26	n.d.	n.d.	0.27
F ppm	448	461	447	448	n.d.	n.d.	304
Cl ppm	402	434	464	487	n.d.	n.d.	n.d.
CO_2 ppm	301	151	129	774	257	145	n.d.
Mg wt.%	5.6	5.5	5.7	6.01	6.31	6.35	n.d.

Table 6.5 SIMS data for melt inclusions in basaltic scoria AMB6 not analysed on EPMA. MgO contents are included as verification that the analyses sampled areas of glass.

6.3.2 Trachyandesite

Major elements

Trachyandesite melt inclusions were analysed on EPMA only, in olivine and spinel host crystals (Table 6.6). Melt inclusions in the trachyandesite fall in the trachydacite field. Inclusions from each host crystal type show overlapping compositions, with slightly lower SiO_2 than the matrix glass (Fig. 6.2). Olivine-hosted melt inclusions display slightly higher FeOt and lower Na_2O, but there is otherwise no systematic variation between major element compositions of inclusions from olivine vs. spinel.

K_D values for Fe-Mg exchange between olivine-hosted inclusions and phenocrystic olivine, adjusted for alkali content using the method of Toplis (2005), fall in the range 0.31–0.33, indicating equilibrium.

Major-element variation diagrams (Fig. 6.2) show that melt inclusion compositions lie mainly on the whole-rock trends for the volcanic succession, with a few olivine-hosted outliers perhaps indicating post-entrapment crystallisation or trapping of an exotic melt (e.g., Danyushevsky et al., 2004).

Volatile components

Sulphur ranges from 250–490 ppm, elevated above matrix glass values (60–110 ppm), while chlorine ranges from 990–1490 ppm, indistinguishable from matrix glass values (880–1490 ppm). F contents of melt inclusions (650–920 ppm) are slightly lower than (but largely overlapping with) those of the matrix glass (730–1130 ppm).

S-Cl contents for melt inclusions and matrix glass in the trachyandesite define a separate trend from those in basaltic scoriae AMB6 and AMB2007 (Fig. 6.4a). The highest Cl and lowest SiO_2 contents are found in spinel-hosted melt inclusions, forming a trend via olivine-hosted melt inclusions to the lowest Cl and highest SiO_2 in the matrix glass (Fig. 6.4b).

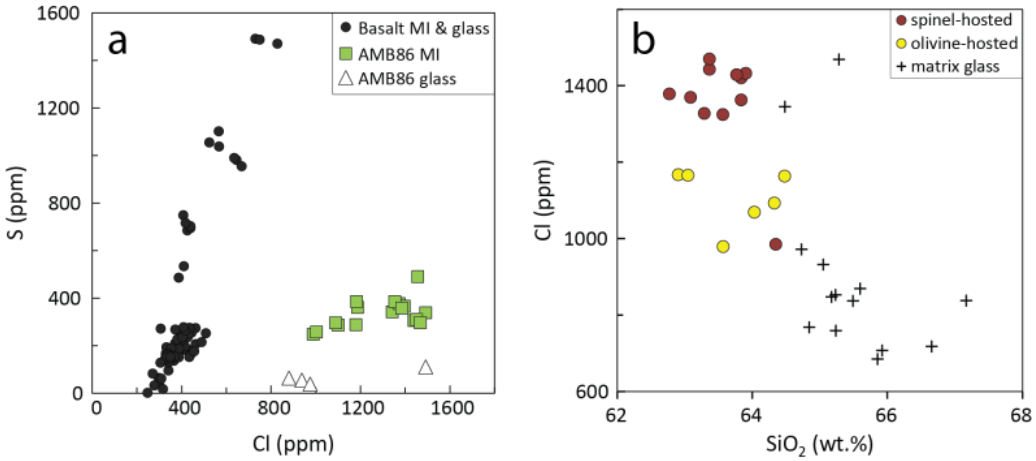

Figure 6.4 a) S and Cl contents in trachyandesite-hosted melt inclusions compared to basalt-hosted inclusions from samples AMB6 and AMB2007. b) Variation of Cl with SiO_2 in AMB86 trachyandesite melt inclusions, showing a progression from higher Cl content at lower SiO_2 values, in spinel-hosted melt inclusions to lower Cl in olivine-hosted inclusions and lowest-Cl, highest-SiO_2 in the matrix glass.

Analysis	pl1_olmi	pl1_olmi1	maf2_olmi1	pl1_oxmi1	pl1_oxmi2	pl1_oxmi3	pl1_oxmi2	maf2_oxmi5	maf2_oxmi8
Host	ol	ol	ol	Sp	sp	sp	Sp	sp	sp
n	*1*	*3*	*2*	*4*	*3*	*1*	*1*	*1*	*1*
SiO_2	64.48	63.97 (0.38)	62.98 (0.1)	63.62 (0.29)	63.30 (0.53)	63.77	63.08	63.57	64.35
Al_2O_3	17.28	15.59 (0.27)	16.85 (0.14)	14.72 (0.09)	14.75 (0.12)	14.63	14.74	15.57	15.47
TiO_2	0.72	0.65 (0.06)	0.63 (0.03)	0.65 (0.02)	0.62 (0.01)	0.59	0.62	0.6	0.94
FeOt	3.18	5.96 (0.16)	4.45 (0.12)	6.84 (0.19)	7.09 (0.37)	6.77	7.38	6.31	5.11
MnO	0.1	0.17 (0.03)	0.13 (0.01)	0.22 (0.02)	0.23 (0.01)	0.24	0.24	0.18	0.14
MgO	0.49	0.87 (0.03)	0.67 (0.04)	1.47 (0.04)	1.49 (0.07)	1.39	1.51	1.3	0.81
CaO	3.06	3.71 (0.11)	3.96 (0.18)	3.39 (0.12)	3.33 (0.01)	3.43	3.35	4.44	3.83
Na_2O	5.38	4.59 (0.19)	4.9 (0.01)	4.19 (0.04)	4.34 (0.08)	4.22	4.19	2.6	4.54
K_2O	4.69	3.9 (0.11)	4.74 (0.01)	4.34 (0.05)	4.23 (0.1)	4.3	4.25	4.75	4.1
P_2O_5	0.35	0.34 (0.06)	0.41 (0)	0.27 (0)	0.32 (0.01)	0.32	0.32	0.35	0.47
F ppm	868	747 (112)	896 (14)	802 (53)	869 (34)	900	871	1146	800
Cl ppm	1163	1047 (60)	1166 (1)	1441 (21)	1356 (26)	1429	1369	1324	985
S ppm	283	273 (25)	367 (17)	307 (18)	357 (18)	480	352	376	252
Total*	101.42	101.26 (0.57)	101.67 (0.18)	101.51 (0.18)	101.09 (0.3)	101.98	101.15	102.24	101.91

Table 6.6 EPMA data for melt inclusions in spinel (sp) and olivine (ol) in trachyandesite lava AMB86. EPMA data is normalised to 100 wt.% anhydrous; Total* is the analytical total before normalisation.

6.3.3 Post-entrapment crystallisation

When compared to whole-rock major element variation trends for the entire volcanic succession, basalt-hosted melt inclusions predominantly lie neatly within the trends which appear to define liquid lines of descent (Fig. 6.2). Only minor displacement from the MgO-SiO_2 trend is seen for olivine-hosted inclusions; and from the CaO-SiO_2 trend for clinopyroxene-hosted inclusions. Those inclusions which are displaced from whole-rock trends have been adjusted for post-entrapment crystallisation (PEC). There is no evidence of Fe loss in olivine-hosted inclusions in the basaltic samples: FeOt values sit towards the higher side of the FeOt-SiO_2 trend, and MgO values, while slightly towards the lower side of the whole-rock trend, are not significantly affected (Fig. 6.2). A lack of fluid bubbles is further evidence against significant post-entrapment crystallisation (PEC). Although it is possible that fluid bubbles were lost during polishing, none were observed in any examined inclusions, including those in unpolished grains examined under stereo microscope.

Trachyandesite-hosted melt inclusions show more displacement from whole-rock trends, with slightly low MgO and FeOt in olivine-hosted inclusions indicating PEC and Fe-loss, and scatter in Al_2O_3, Na_2O, and to a lesser extent, K_2O and TiO_2 believed to mirror the variability seen in the matrix glass: a result of magma mixing (see Section 5.4.1) and late-stage crystallisation.

As discussed in Section 5.3.2, K_D in the scoria samples is lower than expected for mineral-melt pairs clearly in equilibrium (groundmass microlites in glass), with an average of 0.224, which suggests that the classic value of 0.30±0.3–0.5 (Roeder & Emslie, 1970; Putirka, 2008) does not represent equilibrium for this melt composition. The average K_D for melt inclusions is 0.222±0.04, almost indistinguishable from that for groundmass crystals and matrix glass, which indicates that they are in fact in equilibrium. Individual K_D values for melt inclusions are included in Table 6.3.

Inclusions were treated for the effects of PEC using the reverse fractional crystallisation (RFC) mode of crystallisation modelling program Petrolog 2.1 (Danyushevsky, 2001), which adds increments of equilibrium mineral composition back into the inclusion until the melt is in equilibrium with the host crystal. Conditions of melt inclusion entrapment are assumed to coincide with the point when the liquidus composition matches that of the host crystal.

Petrolog 2.1 calculations were performed using the Danyushevsky (2001) mineral-melt models for olivine and clinopyroxene, and the melt oxidation state model of Borisov &

Shapkin (1990). Calculations were performed at NNO+1.2 based on the oxybarometry calculations discussed in Section 5.2.2. The associated error is ±0.5 log units (Wood, 1991).

The stopping condition for the olivine calculations was set as the point at which the inclusion was in equilibrium with the average olivine composition, $Fo_{74.9}$. Olivine displays an essentially homogeneous composition (Section 4.5.1); 41 olivine analyses from cores, rims, and intermediate points, including spots adjacent to melt inclusions, return compositions of $Fo_{74.9\pm0.4}$ (error=1σ). Traverses of host crystals adjacent to inclusions were not performed.

Clinopyroxene compositions also show a narrow range of variation (Mg# of 73.2–76.3).For clinopyroxene calculations, the average Mg# of phenocrysts (74) was used as the stopping condition.

Reverse of fractional crystallisation calculations were performed first at 10 MPa, and then at pressures calculated individually for each melt inclusion composition (55–184 MPa) using the Papale et al. (2006) H_2O-CO_2 solubility model (see Section 6.4 below). Calculations at 10 MPa produce a slightly better fit to the whole-rock trend so results calculated using individual pressures from solubility modelling were discarded.

Results indicate that <6% PEC has occurred for olivine-hosted melt inclusions and <5% PEC for 75% of clinopyroxene-hosted melt inclusions, with the other 25% showing between 5–12% PEC. The corrected compositions and associated trapping temperatures are given in Tables 6.7 and 6.8.

Melt inclusion CO_2, S, Cl and F contents were corrected for PEC using the formula

$$x_0 = \frac{x_i(100 - P_{PEC})}{100}$$

where x_0 = original concentration, x_i = measured concentration, and P_{PEC} = percentage PEC.

Name	5_mi9	3_mi3	2_mi12	2_mi14	2_mi9	7_mi10	7_mi11	7_mi4	7_mi3	7_mi6	5_mi3	5_mi5	5_mi6	1_mi1	7_mi5	2_mi11
SiO_2	53.00	52.72	52.46	52.64	52.41	51.86	51.87	52.36	52.43	52.25	53.03	51.29	52.68	52.88	53.89	52.46
TiO_2	1.09	1.08	1.04	1.00	1.26	1.06	1.03	1.03	0.99	0.59	1.04	1.09	1.05	1.04	1.47	1.10
Al_2O_3	14.32	14.66	14.37	14.43	14.52	14.26	13.98	14.35	13.82	14.24	14.35	14.41	14.61	14.79	11.21	13.89
Fe_2O_3	3.72	3.79	4.03	3.87	3.73	4.12	4.45	3.94	4.04	3.76	3.70	4.39	3.79	3.52	4.47	4.29
FeO	8.52	8.40	8.44	8.51	8.38	8.95	9.15	8.60	9.00	9.29	8.31	9.26	8.52	8.47	9.70	8.89
MnO	0.25	0.23	0.26	0.27	0.27	0.27	0.26	0.24	0.29	0.27	0.29	0.22	0.25	0.26	0.33	0.26
MgO	4.75	4.72	4.72	4.75	4.76	4.98	5.08	4.79	4.95	5.06	4.64	5.17	4.78	4.75	5.12	4.94
CaO	8.53	8.13	8.47	8.43	8.81	8.80	8.34	8.71	8.99	9.54	8.50	8.55	8.30	8.58	9.86	8.15
Na_2O	2.95	3.19	3.34	3.18	2.99	2.95	3.09	3.10	2.90	2.79	3.06	2.97	3.10	2.83	2.06	3.11
K_2O	2.21	2.36	2.28	2.27	2.14	2.07	2.16	2.19	1.94	1.68	2.38	2.05	2.27	2.23	1.40	2.27
P_2O_5	0.44	0.47	0.42	0.42	0.43	0.40	0.40	0.42	0.38	0.30	0.46	0.38	0.42	0.44	0.29	0.43
H_2O	0.23	0.26	0.18	0.23	0.32	0.28	0.20	0.25	0.27	0.24	0.26	0.24	0.24	0.22	0.21	0.22
T (ºC)	1073	1069	1076	1073	1066	1071	1078	1072	1076	1081	1071	1073	1071	1071	1095	1076
Cpx%	2.7	0.1	3.1	4.0	0.0	4.9	5.8	2.1	1.9	1.3	4.5	8.1	3.2	0.2	11.8	6.9
CO_2 (ppm)^{corr}	178	544	164	130	484	398	511	214	605	229	162	145	407	256	160	105
XH_2O (gas)	0.02	0.01	0.02	0.02	0.02	0.02	0.01	0.02	0.01	0.02	0.03	0.02	0.02	0.02	0.02	0.02
XCO_2 (gas)	0.98	0.99	0.98	0.98	0.98	0.98	0.99	0.98	0.99	0.98	0.97	0.98	0.98	0.98	0.98	0.98
P (MPa)	99	188	105	89	167	166	205	116	200	104	96	108	161	110	116	95
XH_2O (gas)	0.02	0.01	0.01	0.02	0.01	0.01	0.01	0.02	0.01	0.01	0.02	0.02	0.01	0.01	0.01	0.02
XCO_2 (gas)	0.98	0.99	0.99	0.98	0.99	0.99	0.99	0.98	0.99	0.99	0.98	0.98	0.99	0.99	0.99	0.98
P (MPa)	39	116	36	29	104	86	109	47	128	50	36	32	89	56	35	23

Table 6.7 Pyroxene-hosted melt inclusion compositions, corrected for post-entrapment crystallisation at 10 MPa and NNO+1.2. Temperature is that calculated in Petrolog 2.1 corresponding to the calculated corrected composition (when clinopyroxene of Mg# 74 is on the liquidus). Cpx% is the percentage of PEC required. The lowermost section of the table shows minimum saturation pressures (P) and coexisting fluid phase compositions (H_2O and CO_2 fractions) calculated using the Papale et al. (2006) and VolatileCalc (Newman & Lowenstern, 2002) models, for corrected CO_2 and H_2O contents.

	Name	5_mi7	3_mi9	5_mi1	5_mi8	3_mi6	1_mi7	7_eb2	7_eb3	3_eb1
	SiO_2	51.66	51.61	52.21	52.87	51.98	52.29	51.83	51.50	52.90
	TiO_2	0.74	1.03	1.04	1.08	0.97	0.99	0.59	0.87	1.05
	Al_2O_3	14.55	14.68	13.99	14.50	14.41	13.32	14.36	14.34	14.70
	Fe_2O_3	4.08	4.25	4.03	3.69	4.07	4.51	3.74	3.71	3.76
	FeO	8.95	8.74	9.12	8.39	8.87	9.29	9.23	9.15	8.18
	MnO	0.27	0.26	0.26	0.27	0.28	0.26	0.25	0.27	0.25
	MgO	5.05	4.91	5.26	4.74	5.03	5.34	5.28	5.24	4.56
	CaO	8.92	8.46	8.63	8.40	8.68	8.24	9.56	10.16	8.33
	Na_2O	3.35	3.22	2.62	2.86	3.04	3.08	2.92	3.08	3.27
	K_2O	1.84	2.20	2.19	2.45	2.09	2.07	1.68	1.11	2.33
	P_2O_5	0.35	0.42	0.42	0.44	0.38	0.41	0.31	0.30	0.45
	H_2O	0.24	0.22	0.23	0.31	0.19	0.21	0.25	0.26	0.22
	T (ºC)	1090	1091	1096	1080	1093	1107	1088	1078	1084
	Olv%	3.7	1.6	3.7	3.8	3.3	4.7	2.7	5.5	0.4
	CO_2 ppm^{corr}	542	314	114	85	207	241	314	333	64
Papale	XH_2O (gas)	0.01	0.01	0.02	0.04	0.02	0.01	0.02	0.02	0.03
Papale	XCO_2 (gas)	0.99	0.99	0.98	0.96	0.98	0.99	0.98	0.98	0.97
Papale	P (MPa)	187	148	84	65	115	147	125	124	55
Volatile Calc	XH_2O (gas)	0.01	0.01	0.02	0.05	0.01	0.01	0.01	0.01	0.04
Volatile Calc	XCO_2 (gas)	0.99	0.99	0.98	0.95	0.99	0.99	0.99	0.99	0.96
Volatile Calc	P (MPa)	115	68	25	20	45	53	68	72	14

Table 6.8 Olivine-hosted melt inclusions corrected for post-entrapment crystallisation at 10 MPa and NNO+1.2. Temperature is that calculated in Petrolog 2.1 corresponding to the calculated corrected composition (when olivine of $Fo_{74.9}$ is on the liquidus). Olv% is the percentage of PEC calculated. The lowermost sections of the table shows saturation pressures (P) and coexisting fluid phase compositions (H_2O and CO_2 fractions) calculated using the Papale et al. (2006) and VolatileCalc (Newman & Lowenstern, 2002) models, for corrected CO_2 and H_2O contents.

6.4 H_2O-CO_2 solubility modelling

Minimum saturation pressures (P_{sat}) and mole fractions of H_2O and CO_2 in the coexisting gas/fluid phase were calculated for each individual melt inclusion using a composition-dependent H_2O-CO_2 solubility model (Papale et al., 2006), and then compared with saturation curves created using the VolatileCalc model (Newman & Lowenstern, 2002).

It must be noted that CO_2 solubility behaviour remains incompletely constrained for alkali-rich basalt compositions and so may not be well-reproduced by these models. New experimental solubility data presented in Chapter 7 will be of some use in evaluating the reliability of melt inclusion modelling.

6.4.1 Model inputs and calculation parameters

Papale et al. (2006) model calculations were performed individually for each melt inclusion composition, using a temperature input of 1140 ºC, based on olivine-melt geothermometry, and Fe speciation calculated using the method of Kress & Carmichael (1991) for an fO_2 of NNO+1.2, as estimated in Section 5.3.5.

Variation of input temperature over the temperature range indicated by geothermometry (Section 5.3) results in negligible variation in model output. Variation in iron speciation is known to have a significant effect on the results from this model (e.g., Iacovino et al., 2013); in this case, varying Fe_2O_3-FeO speciation over the fO_2 error range of ±0.5 log units results in variation of pressure estimates of c. 40 MPa, and variation of XCO_2 (CO_2 in the equilibrium fluid phase coexisting with the melt at that pressure) of c. 0.001 (0.1 mol.%).

6.4.2 Results

The following results are for PEC-corrected melt inclusion compositions. Saturation pressures calculated using VolatileCalc (Newman & Lowenstern, 2002) give pressure estimates of 15–128 MPa, with a coexisting equilibrium fluid phase of ~95–99 mol.% CO_2 (Fig. 6.5a). Minimum saturation pressures calculated from the Papale et al. (2006) calculator range from 55–205 MPa (Tables 6.7 & 6.8), with a coexisting equilibrium fluid phase of ~95–99 mol.% CO_2 (Fig. 6.5b). Calculations made at a temperature of 1140 ºC (from mineral-melt equilibria) were compared with those using individual trapping temperatures calculated for each melt inclusion in Petrolog 2.0; the effect on results is negligible (<0.5 MPa and <0.1 mol% CO_2).

Figure 6.5a illustrates variation of CO_2 in the coexisting vapour phase with changing pressure. Constant dissolved H_2O content over a range of CO_2 concentrations in melt inclusions reflects that, until very low pressures, only CO_2 is exsolving while H_2O is retained in the melt. The calculated fluid phase is thus very CO_2-rich (>97 mol.%) until low pressures (around 70 MPa), after which the fluid becomes increasingly H_2O-rich. The data can then be interpreted as capturing steps along a simple decompression degassing trend controlled by the evolution of H_2O-CO_2 vapour-melt partitioning with magma ascent.

The data have been overlain on a suite of open-system degassing paths constructed using VolatileCalc for 49 wt.% SiO_2 melt, at 1140 ºC, and varying initial dissolved volatile contents, keeping CO_2 constant at 1 wt.% and varying H_2O from 0.5 wt.% to 0.1 wt.%. The data fall between degassing paths for 0.1–0.3 wt.% H_2O^{bulk} at 1 wt.% CO_2^{bulk}, indicating that an initial

dissolved volatile load in which CO_2 is three to ten times greater than H_2O is required to give the observed melt concentrations.

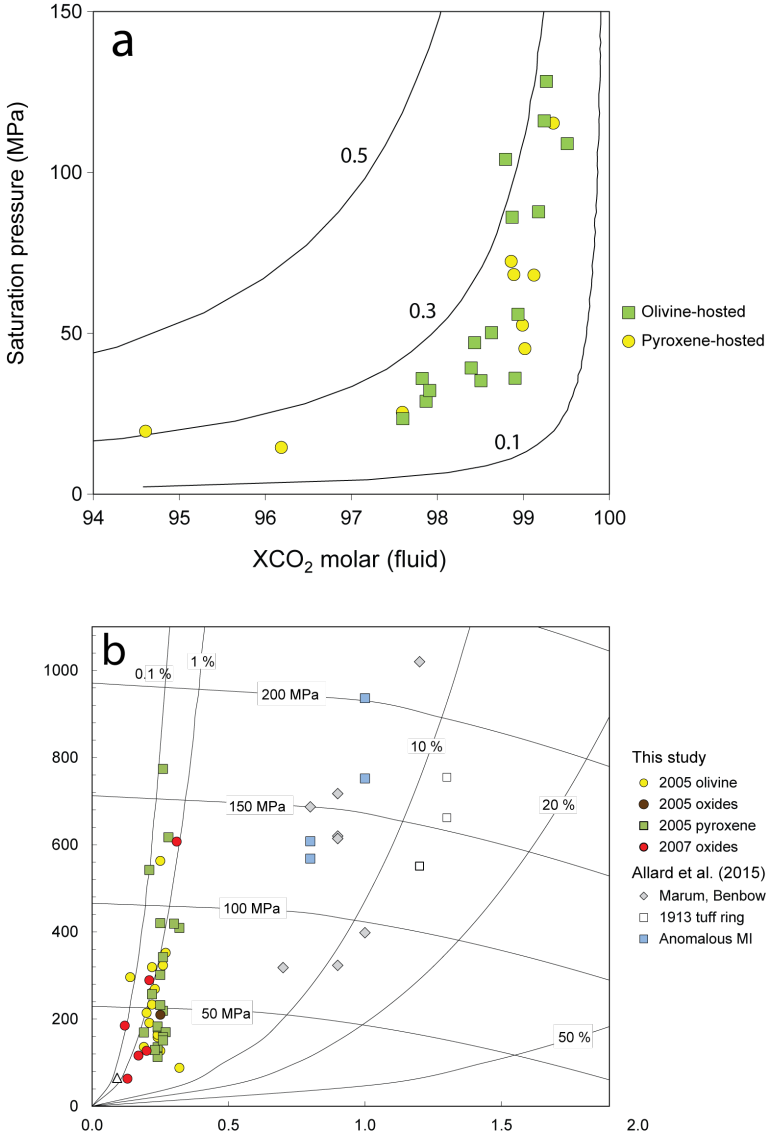

Figure 6.5 a) Open-system degassing pathways calculated in VolatileCalc for 49% SiO_2 magma with variable initial H_2O (labels on curves indicate initial water content in wt.%) and initial CO_2=1 wt.%, at 1140 ºC. **b)** H_2O and CO_2 contents of melt inclusions and groundmass glass of AMB6 basaltic scoria. Vapour isopleths (labelled in mol.% H_2O) and isobars (labelled in MPa) were calculated using VolatileCalc (Newman & Lowenstern, 2002) for a 49 wt.% SiO_2 basalt at 1140 °C. The actual SiO_2 content of the glass and inclusions is ~51–54 wt.%. Data from Allard et al. (2015) are included for comparison.

Plotting the data in comparison with vapour isopleths calculated in VolatileCalc provides an alternative interpretation, that melt inclusion volatile contents are buffered by a coexisting vapour phase of 1 mol.% H_2O and 99 mol.% CO_2 (Fig. 6.5b). This could be interpreted as

fluxing with a CO_2-rich fluid from deeper levels (e.g, Blundy et al., 2010). However, this trend is also well reproduced by a closed-system decompression trend with anywhere from 10–50 mol% initial exsolved vapour (Fig. 6.6). Closed-system degassing is feasible for this magma as the low initial volatile content means that it must reach very low pressures (~10 MPa) before the permeability threshold for degassing is attained (Allard et al., 2015).

The data of Allard et al. (2015) found melt inclusions of similar CO_2 content but up to 1.3 wt.% H_2O. These data are interpreted by Allard et al. (2015) as also representing closed-system degassing. In the context of the new data presented here, it appears that the melt inclusions sampled by both studies represent variably CO_2-enriched magmas. This could provide evidence of fluxing from deeper levels.

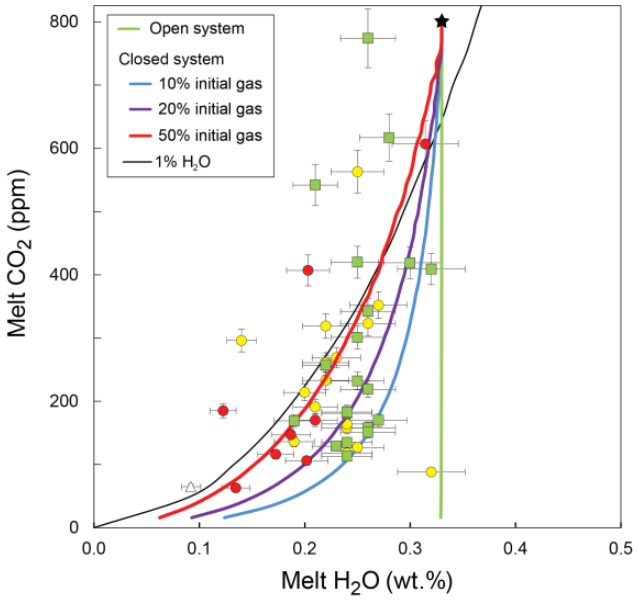

Figure 6.6 Degassing curves modelled in VolatileCalc for a 49 wt.% SiO_2 magma at 1140 ºC, for open-system degassing and closed-system degassing over a range of initial gas contents. The star symbol indicates the point of initiation of the trends, at 0.33 wt.% H_2O and 800 ppm CO_2, i.e. the highest observed volatile contents. Data symbols are as in Fig. 6.5. Also show for comparison is the 1 wt.% vapour isopleth.

The Papale et al. (2006) model was tested to determine whether variation of total volatiles in the system (fluid+melt) would change the calculated proportions of dissolved or coexisting gas phase volatiles (Table 6.9). Varying the bulk volatile amount over a range of ~1–10% does not appreciably change the composition of the equilibrium fluid. The results demonstrate that a very CO_2-rich fluid gives similar dissolved H_2O and CO_2 contents whether fluid-to-melt ratios are low or high (up to 20%).

Bulk volatiles in system (wt.%)	A	B	C	D	E
H_2O	0.25	0.25	0.25	1	10
CO_2	1	5	10	10	10
Total	1.25	5.25	10.25	11	20
CO_2/H_2O	4	20	40	10	1
100 MPa					
Wt.% H_2O (melt)	0.24	0.22	0.20	0.72	3.11
Wt.% CO_2 (melt)	0.02	0.02	0.02	0.02	0.01
Wt.% gas/fluid phase in magma	0.99	5.02	10.06	10.34	17.42
Mole fraction H_2O (gas/fluid)	0.02	0.02	0.02	0.08	0.64
Mole fraction CO_2 (gas/fluid)	0.98	0.98	0.98	0.92	0.36
300 MPa					
Wt.% H_2O (melt)	0.25	0.24	0.24	0.89	5.12
Wt.% CO_2 (melt)	0.15	0.15	0.15	0.14	0.10
Wt.% gas/fluid phase in magma	0.86	4.88	9.91	10.07	15.60
Mole fraction H_2O (gas/fluid)	0.01	0.01	0.01	0.05	0.58
Mole fraction CO_2 (gas/fluid)	0.99	0.99	0.99	0.95	0.42

Table 6.9 Calculations, using the Papale et al. (2006) model, of H_2O and CO_2 partitioning between melt and fluid, given the weight fraction of H_2O and CO_2 in the bulk system; i.e., fluid/(magma+fluid). This allows comparison of partitioning behaviour with variation of total fluid content of the system, and variation of relative proportions of H_2O and CO_2. Five possibilities (A–E) are examined, covering a broad range of potential volatile contents.

Comparison with thermobarometry

Mineral-melt thermobarometry of clinopyroxene-hosted melt inclusions (n=13), using the models of Putirka et al. (2003), gives pressures of 450±40 MPa (mean±1σ; model error is ±170 MPa). The clinopyroxene composition used was the average of a traverse of a large, euhedral clinopyroxene, as only one pair of analyses of melt inclusion and adjacent host crystal successfully captured both inclusion and host compositions for an inclusion also successfully analysed on SIMS. This matched inclusion/host pair gives a pressure result of 470 MPa. The pressure calculated from dissolved CO_2 (420 ppm) gives a result of 161 MPa. These higher-pressure results, compared to those calculated via H_2O-CO_2 solubilities, suggest that existing solubility models may underestimate pressures for this composition, although not greatly when error margins are taken into account.

6.5 Magma flux estimate

Wright & Pilger (2008) estimated mass flux for Ambrym, based on satellite data, of up to 400 kg s^{-1} in 2003, and up to 40 kg s^{-1} in 2005. An alternative method, the petrological method, uses the difference between dissolved volatile contents in melt inclusions and glass to calculate the magma flux required to supply the observed gas flux in the plume. This assumes that all gas released at the surface was originally dissolved in the magma sampled by melt inclusions. In the case of 'gas flushing' or shallow trapping of melt inclusions, this method would significantly overestimate magma flux.

Plume fluxes of SO_2, CO_2, H_2O, Cl and F for Ambrym have been reported by Bani et al. (2009, 2012) and Allard et al. (2009), and are given in Table 6.10. Magma flux is estimated using the difference between pre-eruptive volatile concentrations from melt inclusions and degassed volatile concentrations in the matrix glass, and relating this difference, as a fraction of the entire mass of magma supplied, to the volatile fluxes observed in the plume, using the following equation:

$$\phi_m = \frac{\phi_{\text{plume}}}{X_{\text{mi}} - X_{\text{g}}} \times 100$$

where

ϕ_m = magma flux (kg s^{-1})

ϕ_{plume} = volatile flux in plume (kg s^{-1})

X_{mi} = maximum concentration of given volatile species in melt inclusions (wt.%)

X_g = maximum concentration of given volatile species in glass (wt.%)

The effect of crystallisation is omitted here as the crystal fraction is <25%, of which 16–18% is large phenocrystic plagioclase shown to pre-date crystallisation of the phases in which melt inclusions were analysed, implying a maximum extent of crystallisation of only 7–9% following melt inclusion entrapment.

Results are listed in Table 6.10. Magma flux estimates derived from H_2O calculations are 1–3 orders of magnitude greater than those using other volatile species, and are disregarded due to the likelihood of interference from atmospheric water during plume measurements as well as meteoric water input to the plume. Results from F, whose solubility in silicate melt makes it less suitable for these calculations, and S, which may be buffered by sulphide dissolution, are also excluded. This leaves Cl as the most appropriate volatile species from which to estimate magma flux, and indicates a range of 17,000–30,000 kg s^{-1}.

For comparison, other volcanoes featuring strong summit degassing with low erupted magma volumes include Erebus (30–76 kg s^{-1}), Erta Ale (44–104 kg s^{-1}) and Pu'u 'O'o (1551–2079 kg s^{-1}), where mass flux has been estimated based on heat flux measurements (Harris et al., 1999). Oppenheimer et al. (2004) estimated a magma supply rate of 350–650 kg s^{-1} for Erta Ale based on gas plume measurements.

		SO_2	CO_2	Cl	F	H_2O
ϕ_{plume} (kg s^{-1})		18–382	231	8–14	2–50	2315
X_{MI} (wt.%)		0.30	0.37	0.08	0.10	0.33
X_g (wt.%)		0.03	0.00	0.034	0.08	0.11
ϕ_{magma} (kg s^{-1})	min	1.3×10^4	6.3×10^4	1.7×10^4	9.9×10^3	1.1×10^6
	max	2.8×10^5		3.0×10^4	2.5×10^5	
ϕ_{magma} (m^3 s^{-1})	min	4.8	23.3	6.3	3.7	407.4
	max	103.7		11.1	92.6	

Table 6.10 Results of magma flux calculations using ϕ_{plume} data from Bani et al. (2009), Allard et al. (2009), and Bani et al. (2012). Converted from kg to m^3 assuming magma density of 2700 kg m^{-3}.

This comparison shows that even the lowest estimate for Ambrym is an order of magnitude greater than the highest estimates for similar systems. The enormous magma volume required may be partly explained by the shallow entrapment depth of these inclusions, which means that they sample relatively degassed magma, and therefore underestimate initial dissolved gas content. It may alternatively, or additionally, indicate that the high plume concentrations are a result of gas flushing from a deep magma source (e.g., Barsanti et al., 2009).

6.6 Discussion

6.6.1 Is Ambrym truly water-poor?

The consistently low water contents found in Ambrym melt inclusions seem to indicate that currently erupting magma may be water-poor; a surprising result not only for an arc volcano but for a system known for prodigious outgassing. There is a complete absence of hydrous phases throughout the history of the volcano, although absence of hornblende may be attributed to relatively low Na_2O content (Sisson & Grove, 1993) or replacement by pyroxene, and does not necessarily indicate low H_2O. Early spinel crystallisation and high-anorthite plagioclase (up to a maximum of An_{92}) indicate that water was present early in the crystallisation history (Sisson & Grove, 1993), but the persistent predominance of significant

volumes of plagioclase, from pre-shield lavas to the most recent eruptives (see Section 2.2), suggests low water content, as high water content is known to suppress plagioclase crystallisation (e.g., Sisson & Grove, 1993; Müntener et al., 2001). Recently published melt inclusion data from Ambrym record H_2O contents up to 1.3 wt.% (Allard et al., 2015), not significantly higher than those found in this study.

The lack of variation in H_2O contents between olivine-, pyroxene- and spinel-hosted melt inclusions indicates that the low water contents are not due to diffusive loss of H^+; differing H^+ diffusivities in each mineral phase would be expected to result in variations in the extent of H^+ loss, resulting in a spread of H_2O contents rather than the essentially constant values seen. It is possible, however, that the inclusions may have re-equilibrated during late-stage storage in a host magma of low H_2O content.

Melt inclusions from Yasur volcano (c. 400 km to the SSE of Ambrym) also contain up to 1.3 wt.% H_2O (Métrich et al., 2011), and inclusions in picrite from Aoba (c. 40 km NNW) show H_2O contents up to 3.6 wt.% (Sorbadere et al., 2011) which demonstrates that the subduction system in the vicinity is not generally water-poor. These two studies, along with Allard et al. (2015) contain the only melt inclusion H_2O data published for Vanuatu at present.

Examples of other low-H_2O arc magmas are sparse. H_2O contents of 0.2–0.4 wt.% are reported in olivine-hosted melt inclusions from Galunggung, Indonesia (Sisson & Bronto, 1998), with dissolved CO_2 contents up to 750 ppm. The authors consider diffusive H^+ loss unlikely to have caused such uniform low H_2O contents, and suggest that a hot, dry magma such as this could be generated by decompressional melting due to mantle upwelling. This mechanism would not apply to Ambrym, however, as the Ambrym melt in question is not a primitive, high-MgO magma which could be postulated to derive from mantle upwelling. Low-H_2O, variable-CO_2 melt inclusions have been recorded at Etna (Collins et al., 2009) and Stromboli (Métrich et al., 2010), both of which erupt alkaline basalts of notable compositional similarity to Ambrym basalt; the volatile contents in these cases have been attributed to percolation of and dehydration by CO_2-rich gas during shallow magma storage. H_2O contents of ~1.2 wt.% with variable CO_2 up to 900 ppm have been recorded at Tolbachik volcano, Kamchatka (Plechov et al., 2015), considered to represent a degassing trend.

The high H_2O content measured in the gas plume (~90 mol.%; Allard et al., 2009) does not necessitate a water-rich magma, but rather reflects the shallow portion of the degassing curve where water exsolution becomes more significant, the bulk of the CO_2 having left the magma. Gerlach (1986) estimated that most H_2O does not exsolve until as low a pressure as 2–3 MPa. The open-system degassing pathway calculated in VolatileCalc for a magma with

an initial H_2O content of 0.4 wt.% and CO_2 of 1 wt.% (reflecting best fit observed for melt inclusions; Fig. 6.5a) will exsolve a 60 mol.% H_2O gas phase by the time it reaches 3 MPa. In addition, a significant part of the measured plume H_2O is very likely to derive from remobilised groundwater. Gerlach (1980) considered significant contamination of volcanic gas by meteoric water likely to be the rule at tropical volcanoes; Ambrym is well known for high precipitation and heavy cloud cover around the summit caldera. More recently, Burton et al. (2003) considered this water contamination effect to be insignificant at Etna, but it is worth noting that Ambrym receives approximately three times as much rainfall (~2300–3000 mm yr^{-1}; Németh & Cronin, 2007a) as Etna (~800 mm yr^{-1}; Chester et al., 1985). Lack of isotopic analysis of the emitted gases at Ambrym precludes further comment on this possibility.

6.6.2 Volatile supply

Two main models have been proposed for gas supply at persistently degassing volcanoes with minimal magma output: conduit convection, i.e., ascent of gas-rich magma through sinking degassed magma (Kazahaya et al., 1994), or gas flushing from degassing of deep magma (e.g. Spilliaert et al., 2006).

Sulphur and halogen degassing requires low pressures, implying that magma convection is necessary to supply the high levels of outgassing of these species at Ambrym (cf. Edmonds et al., 2013). Stevenson & Blake (1998) estimated that magma must be brought to depths <5 km (~130 MPa) before significant amounts of sulphur can degas. However, Roberge et al. (2009) showed that degassing of mafic magma from levels of 150–350 MPa (~6–13 km) could produce an SO_2-rich plume, with no need to invoke convective degassing. The plume ratio of CO_2/SO_2 in the Roberge et al. (2009) model (4.6–6) brackets that measured at Ambrym (5.6; Allard et al., 2009).

Petrological observations also support convection (Chapters 4 & 5). Volatile modelling discussed in Section 6.4.2 above, and recent work by Allard et al. (2015) appears on balance to favour degassing over gas flushing. In light of this, convective degassing of deeply-derived volatile-rich magma seems the most viable model.

Aiuppa (2009) invoked the presence of a buffer controlling gas composition to explain long-term, stable gas emission of approximately constant composition at Ambrym and other persistently degassing basaltic systems (Villarrica and Masaya). At Masaya, this has been interpreted as a result of gas flushing from deep magma (Horrocks et al., 1999; Burton et al., 2000), although convective degassing has also been suggested (Rymer et al., 1998).

On balance, the data appear to favour convective degassing, with no particular need to invoke gas flushing. These data represent only a snapshot of the system within the long-term behaviour of the volcano. Further in-depth examination of pre-eruptive volatile contents combined with a more extensive, high time-resolution dataset for gases exsolved at the surface would be extremely valuable to the interpretation of degassing processes.

6.6.3 Volatile cycling in the subduction system

Constraints from melt inclusions indicate a CO_2-rich, H_2O-poor fluid coexisting with the magma at depth below Ambrym. The occurrence of a water-poor arc magma is unusual, as subducted aqueous fluids are widely held to be the catalyst for melting at depth. Regional tectonics may play a role in inhibiting water input into the Vanuatu arc: since Vanuatu is a rapidly subducting system (estimates range from 4.2–9.0 cm yr^{-1} at the DEZ to ~12 cm yr^{-1} in the southern arc; see Sections 2.1.4 and 2.1.6), the downgoing slab may pass too rapidly through the dehydration zone for significant extraction of water to occur (Kerrick & Connolly, 1998). Trace elements indicate that a slab-derived fluid component has fluxed the mantle wedge below the Vanuatu arc, however, which presumably involves an aqueous component. A possible explanation is that the slab fluid may behave as a catalyst for melting with the aqueous component not persisting as far the shallow system, or becoming sequestered in a separate fluid phase.

The composition of the subducting crust may also play a role in observed low water content. The age of the subducting crust strongly influences the composition and the amount of fluids evolved as subduction progresses. In particular, the CO_2 and H_2O cargo is significantly less for young crust compared to mature crust. D'Entrecasteaux ridge material, which enters the subduction zone, will be relatively unhydrated relative to serpentinised ocean crust, as it has not been part of the mid-ocean ridge hydrothermal system.

The lack of CO_2 content in known subduction inputs suggests that the CO_2 is likely to be largely mantle-derived. There is evidence for perturbation of the mantle source below the Vanuatu ridge, whereby an Indian Ocean type MORB source is being drawn into the region where normally Pacific-type MORB would be expected, possibly as a result of DEZ collision (Turner et al., 1999). Recently, Jean-Baptiste et al. (2015) have also uncovered evidence of a ^{3}He-rich hotspot component in the Ambrym source region. These observations introduce the possibility of tapping of an exotic or deep reservoir with a higher than normal carbon content.

6.7 Conclusions

Melt inclusion and gas data suggest two possible models for volatile pathways at Ambrym; CO_2 flushing, or decompressional degassing. A plot of H_2O-CO_2 contents against vapour isopleths appears to demonstrate that dissolved volatile contents are buffered by a constant coexisting vapour composition, which may represent a fluxing fluid phase. However, an alternative interpretation is that this calculated fluid simply records H_2O-CO_2 partitioning with decompression. Results from both the Papale et al. (2006) and Newman & Lowenstern (2002) models indicate a very CO_2-rich system, and minimum saturation pressures of ~15–200 MPa for melt inclusions. It is possible that both flushing and decompression are operating to varying degrees, depending on the dynamics of magma supply, which may vary with time.

Comparison of petrological data with observed gas fluxes suggests that plume concentrations represent an integrated degassing profile comprising shallowly-degassed H_2O, S, Cl and F combined with CO_2-rich vapour from greater depth. This, combined with a very high gas output which indicates extremely large magma fluxes at a system with very low eruption rates, points to convective degassing as the most suitable model for the Ambrym system. Similar volatile compositions from 2005 and 2007 scoria suggest that the samples studied are representative of a persistent degassing state of the system, at least on a timescale of years, although measurements by Allard et al. (2015) record the presence of a slightly more water-rich magma.

Finally, based on available evidence from geochemistry and regional tectonics, this strong CO_2 flux appears likely to have a mantle origin.

Chapter 7 Experimentally determined volatile solubilities

A series of twenty mixed-volatile solubility experiments were carried out on a natural Ambrym basalt composition over a P-T range of 1050–1200 ˚C and 25–190 MPa, at fO_2~QFM. Combinations of H_2O-CO_2-S, and H_2O-Cl±F were added to the experimental charges to generate complex mixed-volatile equilibrium fluids. Experiments were conducted in an internally-heated pressure vessel at the Institut des Sciences de la Terre d'Orléans (ISTO).

This provides the first data on mixed-volatile behaviours at Ambrym, a persistently and heavily degassing basaltic volcano.

7.1 Introduction—the need for experiments

Volatile components strongly affect the properties and behaviour of magma in a host of interconnected ways: most notably melt viscosity and density, liquidus temperature and phase equilibria, which in turn influence rates of ascent, crystallisation and degassing, and eruptive style (e.g., Giordano et al., 2008). Magmatic fluids are also responsible for transport and concentration of economically important metals (e.g., Hedenquist & Lowenstern, 1994). On a larger scale, volatile components of magmas play a significant role in climatic phenomena (Robock, 2000) and the evolution of the Earth's atmosphere (Dasgupta, 2013).

Volatile components can be measured within magma as dissolved volatiles, or in the volcanic plume or fumaroles at the Earth's surface.

Analysing dissolved volatiles, particularly in melt inclusions, gives a very precise measurement of volatile components coexisting in a melt at a given time, but requires models of solubility behaviour for interpretation. Volatile measurements from melt inclusions also have associated uncertainties with regard to trapping pressure, saturation and post-entrapment modification. Experimental studies of volatile solubilities give a less ambiguous control on how the volatile load of a system is distributed at magmatic temperatures and pressures.

Surface measurements provide an indication of the volatile load of a magmatic system at a given time, but do not provide a full understanding of the origins and ascent pathway of the gas phase, and are susceptible to contamination by meteoric fluids. Modelling the behaviour of volatile components in magmas via experimental petrology enables use of gas plume composition data to track magma ascent and forecast eruptive activity.

Large gaps remain in quantitative modelling of the solubilities, behaviour and distribution of volatile components in magmas, particularly with regard to the complex mixed-species fluid phases most likely to be found in nature, and the attendant interactions between volatile species at magmatic temperatures and pressures. The most abundant volatile species in magmas, H_2O and CO_2, are also the most studied, with SO_2 receiving increased attention since its role, both as a precursor to eruption and a climatic agent, was recognised in several important eruptions of recent decades, particularly Pinatubo, 1991 (Bluth et al., 1992), Mount St Helens, 1980 (Gerlach & McGee, 1994), Galeras, 1993 (Fischer et al., 1994) and El Chichon, 1982 (Krueger, 1983). Mixed-volatile studies are rare, particularly where species beyond H-C-S are concerned. Mixed-volatile solubility data are essential to the interpretation of dissolved volatiles in melt inclusions and degassing profiles of magmatic systems. This study examines volatile behaviour of mixed H-C-S fluids and further includes Cl and F to constrain H_2O behaviour in the presence of these less-studied volatile species.

Historically, volatile solubility studies have tended to focus more on silicic magmas due to their higher explosivity and association with economic deposits. However, violent eruptions may also occur in basaltic systems, such as the periodic paroxysms at Ambrym (e.g., in 1913, 1929, 1950, 1988/89; see section 2.2.5), Stromboli (e.g., Aiuppa et al., 2010), and Etna (e.g., Viccaro et al., 2015). In addition, quantification of the scale of volatile emissions from basaltic volcanoes requires improvement, as recent research indicates that the contribution of these volcanoes to the global volcanic degassing budget has been significantly underestimated (e.g., Bani et al., 2012).

Low-pressure CO_2 solubility studies of basaltic compositions are few, partly due to the low solubility of CO_2 at low pressures, and technical difficulties associated with mafic melts.. The early literature on CO_2 solubility was dominated by studies of MORB (e.g., Stolper & Holloway, 1988; Pawley et al., 1992; Dixon et al., 1995; Jendrzejewski et al., 1997); more recently, alkali-rich basalts have received increased attention (e.g., Dixon, 1997; Behrens et al., 2009; Pichavant et al., 2009; Lesne et al., 2011a,b; Pichavant et al., 2013; Iacovino et al., 2013), with increasing recognition that melt composition exerts a strong control on CO_2 solubility. For example, Shishkina et al. (2014) found that dissolved CO_2 increases by ~1 wt.% at 500 MPa with compositional change from tholeiite to nephelinite. The aim of the H_2O-CO_2 experiments in the current study is to add to the body of data on compositional controls on CO_2 solubility in alkali basalts at low pressures, and thus extend the database for constructing compositionally-controlled solubility models.

Existing halogen solubility studies have mainly focused on melts of exotic, high-silica compositions—for example, topaz rhyolite (Webster & Rebbert, 1998), pantellerites (Métrich & Rutherford, 1992), phonolites (Webster et al., 1999), peraluminous rhyolites (Signorelli & Carroll, 2001), and peralkaline rhyolites (Lowenstern, 1994). This study adds to a limited but growing number of investigations of halogen solubilities in basaltic magmas (e.g., Webster et al., 1999; Métrich et al., 2001; Chevychelov et al., 2007, 2008; Alletti et al., 2009).

7.2 Methodology

7.2.1 Choice and preparation of starting material

The sample chosen as a starting material was natural basaltic scoria AMB6 (see Section 4.3 for major element bulk rock composition, and Sections 4.4.1 and 4.5.1 for petrography and phase compositions), with large plagioclase glomerocrysts removed by picking under a binary microscope, as zoning and K_D calculations indicate disequilibrium of the bulk of the large plagioclase crystals with the whole rock composition. The resulting sample was labelled AMB6-SC. This was milled in a TEMA tungsten carbide ring mill and fused for 4 hours at 1400 ˚C in an alumina crucible at atmospheric pressure, then re-milled and fused again at the same temperature and for the same duration, to produce homogeneous, anhydrous, crystal-free glass. This twice-fused glass was then ground by hand under acetone in an agate pestle-and-mortar to obtain a fine, homogeneous glass powder.

This glass, which was used for the H-C-S experiments, was subsequently found to have been contaminated by aluminium from the crucibles used for fusion. Alumina crucibles had previously been used without sample contamination in the laboratory at UEA, after rigorous testing by a previous research student (C. Stannard, pers. comm., 2007). A new batch of crucibles evidently did not behave in the same way as those previously tested, and the contaminated glass was not analysed prior to beginning experiments. 13 out of 20 experiments were performed using this contaminated glass, which means the resulting phase equilibria and solubility data are not applicable to the natural Ambrym system, but provide a useful addition to the experimental database on very high Al basalts (~20–23 wt.% Al_2O_3).

The contaminated starting glass was used up after 13 experiments, and fresh starting glass was then prepared (using a platinum crucible) from the original batch of powdered but unfused starting composition, so 7 out of 20 experimental runs (including all of the Cl-F bearing experiments) used uncontaminated glass. The compositions of both starting glasses

are given in Table 7.1. In the case of the contaminated glass, which was not analysed prior to experiments, the composition given is the normalised anhydrous average of experimental glass compositions from runs #7–13; runs #1–6 were microcrystalline.

	Runs #1–13	Runs #14–20
N	233	20
SiO_2 (wt.%)	50.65 (0.68)	52.02 (0.37)
TiO_2 (wt.%)	1.01 (0.05)	1.02 (0.03)
Al_2O_3 (wt.%)	22.62 (0.65)	15.63 (0.19)
FeO (wt.%)	7.39 (1.06)	11.13 (0.33)
MnO (wt.%)	0.21 (0.02)	0.22 (0.01)
MgO (wt.%)	4.24 (0.25)	4.88 (0.09)
CaO (wt.%)	8.38 (0.48)	9.13 (0.12)
Na_2O (wt.%)	3.00 (0.12)	3.00 (0.07)
K_2O (wt.%)	2.13 (0.17)	2.19 (0.05)
P_2O_5 (wt.%)	0.38 (0.02)	0.40 (0.01)
F (ppm)	256 (142)	464 (144)
Cl (ppm)	81 (12)	203 (20)
Total (wt.%)	100	99.72 (0.46)

Table 7.1 Starting compositions used in experiments. Error (in parentheses) is 1 standard deviation of n analyses. Runs #1–13 used Al-contaminated glass, which was not analysed prior to experiments; the composition given here is the normalised anhydrous average of all experimental glasses from runs #7–#13. Runs #14–20 used uncontaminated glass, fused in a platinum crucible; the composition given here is the average of 20 EPMA analyses of the glass fused at 1 atm and 1400 °C.

7.2.2 Experimental charge preparation

The capsules used were predominantly $Au_{80}Pd_{20}$, which has a sufficiently high melting point for the required temperature range. Pt capsules were used for sulphur-bearing charges as iron loss is intensified in the presence of sulphur, and Pt is somewhat less susceptible to iron loss. Only 6 sulphur-bearing runs were performed due to limited supply of Pt tubing. Gold capsules were used for the lower end of the temperature range (~1050 ˚C), gold being less conducive to iron loss but with a melting point too low for the majority of the experimental runs. Short run durations were used to offset the effects of iron loss.

15–20 mm lengths of 2.5 mm internal diameter and 0.4 mm wall thickness metal tubing were cleaned by boiling for 10 minutes in a mixture of demineralised water and hydrochloric acid, followed by boiling for 5–10 minutes in demineralised water only, and then annealed in a gas flame. Capsules were crimped and welded at one end using an electric arc welder.

For the first series of experiments, variable XH_2O (proportion of H_2O in the bulk volatile phase, pre-experiment) was imposed using mixtures of demineralised water and CO_2 as silver oxalate (Ag_2CO_3). Silver has been shown to have a negligible effect on CO_2 solubility (Pan et al., 1991).

Between 2.5 and 5 wt.% water (as wt.% of bulk capsule contents), sufficient to attain H_2O saturation, was added to each capsule, with one capsule per run containing CO_2 only, to investigate nominally dry conditions. Bulk charge compositions for this experimental series are given in Table 7.2.

For the second series of experiments, the capsules were doped with chlorine ± fluorine, added as aqueous solutions of HCl and HF in varying concentrations. HCl and HF were chosen as halogen sources rather than alkali salts ((Na,K)Cl,F) because the complexing behaviour of Cl with cations such as Na and K strongly affects its behaviour; in addition, melt alkalinity is an important influence on Cl solubility (e.g., Webster et al., 1999; Signorelli & Carroll, 2001) so it is preferable to avoid addition of alkalis to the natural composition. Three HCl solutions of different concentration were used as Cl sources: one of reagent grade 37% HCl, one diluted by half to 18.5% (H_2O: ^{37}HCl = 1:1) and the third diluted by half again to 9.25% (H_2O: ^{37}HCl = 3:1). An aqueous solution of 4% HF was added to one charge per run. The starting fluid compositions for each charge are given in Table 7.3. Bulk charge compositions for this experimental series are given in Table 7.4. One experiment (#19) was designed to test the effect of CO_2 on Cl-F solubility, but the quench failed.

Volatile components were added first to minimise the potential for loss to the atmosphere. Water, HCl and HF (if included) were inserted into the bottom of the capsule using a micrometric syringe, followed by silver oxalate powder (if included). Approximately 30–40 mg of the twice-fused glass powder (with added pyrrhotite (FeS) amounting to 1 wt.% S for sulphur-bearing charges) was then added to the capsule, and the open end of the capsule then crimped, and welded by electric arc. The capsule was weighed after addition of each substance. If sputtering occurred during welding the capsule was discarded. If mass was lost (and no sputter of metal occurred) it was assumed that the loss of mass was due to loss of volatile constituents, and the capsule was discarded.

After welding, the capsules were tested for leaks by immersion in a silicon oil bath for 10 minutes at 250 ˚C. If a leak was present it was revealed by the escape of air bubbles. If the capsules were intact, they were then cleaned in acetone and placed in an oven at 120 ˚C for c. 30 minutes as a second check on capsule integrity, and to encourage homogeneous distribution of the volatile phase, which is particularly important for runs of short duration.

Capsules were then placed in an alumina sample holder for insertion into the experimental vessel (Fig. 7.1a).

Run#	P (MPa)	T (°C)	Duration	Capsule	Charge	S	H_2O	CO_2	XH_2O^0
							wt.% bulk		
1	51	1150	4h 55	$Au_{80}Pd_{20}$	A	-	4.9	0.0	1.0
				$Au_{80}Pd_{20}$	B	-	2.7	0.3	0.9
				$Au_{80}Pd_{20}$	C	-	1.9	1.6	0.6
				$Au_{80}Pd_{20}$	D	-	2.6	2.7	0.5
				Pt	E	0.9	4.9	0.0	1.0
				Pt	F	0.9	2.6	1.8	0.6
2	25	1150	4h 40	$Au_{80}Pd_{20}$	A	-	4.6	0.0	1.0
				$Au_{80}Pd_{20}$	B	-	2.4	1.5	0.6
				$Au_{80}Pd_{20}$	C	-	2.6	2.7	0.5
				Pt	D	0.9	4.8	0.0	1.0
				Pt	E	0.9	2.4	1.3	0.7
				$Au_{80}Pd_{20}$	F	-	4.5	0.0	1.0
				$Au_{80}Pd_{20}$	G	-	0.0	2.7	0.0
3	50	1100	4h 40	$Au_{80}Pd_{20}$	A	-	5.3	0.0	1.0
				$Au_{80}Pd_{20}$	B	-	2.6	1.3	0.7
				$Au_{80}Pd_{20}$	C	-	3.5	2.4	0.6
				$Au_{80}Pd_{20}$	D	-	0.0	3.0	0.0
				Pt	E	0.9	5.8	0.0	1.0
				Pt	F	0.9	2.6	1.3	0.7
4	50	1050	20h 30	Au	A	-	3.6	0.0	1.0
				Au	B	-	2.9	1.5	0.7
				Au	C	-	2.1	2.7	0.4
				Au	D	-	0.0	2.9	0.0
				Au	E	0.9	5.3	0.0	1.0
				Au	F	0.9	2.4	1.4	0.6
5	50	1100	21h 50	$Au_{80}Pd_{20}$	A	-	4.7	0.0	1.0
					All other charges lost significant mass				
6	110	1150	4h 40	$Au_{80}Pd_{20}$	A	-	4.9	0.0	1.0
				$Au_{80}Pd_{20}$	B	-	2.6	1.9	0.6
				$Au_{80}Pd_{20}$	C	-	2.4	2.9	0.5
				$Au_{80}Pd_{20}$	D	-	0.0	2.7	0.0
				Pt	E	0.9	5.2	0.0	1.0
				Pt	F	0.9	2.9	1.3	0.7

Table 7.2 Bulk volatiles loaded in runs 1–6 (H_2O-CO_2-S): 40 mg rock + H_2O, Ag_2CO_3 and FeS. S, H_2O and CO_2 values are wt.% of total charge (powder+volatile sources). Bulk H_2O = H_2O/(rock+H_2O+CO_2), and bulk CO_2= CO_2/(rock+H_2O+CO_2), where mass of CO_2 is calculated by multiplying mass of $AgCO_3$ by molecular fraction of CO_2 (i.e., 0.16). XH_2O^0 is the initial proportion of H_2O in the bulk volatile phase, prior to experiment; XCO_2 is the other component of the volatile phase, where XH_2O+XCO_2 sum to 1. All runs were performed at ~QFM except for run 5, which was performed at ~NNO in order to test the effect of oxidation state on Fe loss. The 'charge' column denotes the different experimental charges, with decreasing H_2O and increasing CO_2 content from A–D, a mixture of S-H_2O in charge E, and S-H_2O-CO_2 in charge F.

Run#	P (MPa)	T (°C)	Duration	Capsule	Charge	wt.% H_2O	wt.% CO_2	XH_2O
7	51	1200	4h 50	$Au_{80}Pd_{20}$	A	5.2	0.0	1.0
				$Au_{80}Pd_{20}$	B	2.4	1.2	0.7
				$Au_{80}Pd_{20}$	C	3.0	2.8	0.5
				$Au_{80}Pd_{20}$	D	2.8	1.6	0.6
				$Au_{80}Pd_{20}$	E	0.0	2.8	0.0
8	92	1200	5h 20	$Au_{80}Pd_{20}$	A	4.7	0.0	1.0
				$Au_{80}Pd_{20}$	B	2.4	1.4	0.6
				$Au_{80}Pd_{20}$	C	2.6	2.6	0.5
				$Au_{80}Pd_{20}$	D	0.0	2.8	0.0
9	106	1175	5h	$Au_{80}Pd_{20}$	A	5.0	0.0	1.0
				$Au_{80}Pd_{20}$	B	2.6	1.4	0.7
				$Au_{80}Pd_{20}$	C	2.8	2.5	0.5
				$Au_{80}Pd_{20}$	D	0.0	2.8	0.0
10	46	1175	4h 50	$Au_{80}Pd_{20}$	A	5.3	0.0	1.0
				$Au_{80}Pd_{20}$	B	2.2	1.2	0.7
				$Au_{80}Pd_{20}$	C	3.0	2.8	0.5
				$Au_{80}Pd_{20}$	D	0.0	2.7	0.0
11	46	1150	18h	$Au_{80}Pd_{20}$	A	5.0	0.0	1.0
				$Au_{80}Pd_{20}$	B	2.4	1.3	0.6
				$Au_{80}Pd_{20}$	C	2.4	2.7	0.5
				$Au_{80}Pd_{20}$	D	0.0	2.8	0.0
12	108	1050	5h 30	$Au_{80}Pd_{20}$	A	4.4	0.0	1.0
				$Au_{80}Pd_{20}$	B	2.8	1.3	0.7
				$Au_{80}Pd_{20}$	C	2.8	2.4	0.5
				$Au_{80}Pd_{20}$	D	0.0	2.6	0.0
13	113	1100	6h	$Au_{80}Pd_{20}$	A	4.9	0.0	1.0
				$Au_{80}Pd_{20}$	B	2.7	1.4	0.7
				$Au_{80}Pd_{20}$	C	2.6	2.6	0.5
				$Au_{80}Pd_{20}$	D	0.0	2.9	0.0
14	59	1100	18h 20	$Au_{80}Pd_{20}$	A	4.7	0.0	1.0
NNO				$Au_{80}Pd_{20}$	B	2.2	1.3	0.6
				$Au_{80}Pd_{20}$	C	2.2	2.5	0.5
				$Au_{80}Pd_{20}$	D	0.0	2.8	0.0

Table 7.2 continued Bulk volatiles loaded in runs 7–14 (H_2O-CO_2)—40 mg rock + H_2O + Ag_2CO_3.

Charge	Fluid	Cl (wt.%)	F (wt.%)
A	3 mg 9.25% HCl	0.8–1.3	0
B	3 mg 18.5% HCl	3.5–4.7	0
C	3 mg 18.5% HCl	7.0–8.9	0
D	3 mg 37% HCl	14.6–16.9	0
E	1 mg 18.5% HCl + 2 mg 4% HF	3.9–5.6	2.5–3.0

Table 7.3 Compositions of bulk starting fluids (pre-experiment) for Cl-F experiments. 5 capsules were included in each run. Approximately 30 mg of glass and 3 mg of fluid (9.25% HCl, 18.5% HCl, or 37% HCl, ± 4% HF) were added to each capsule, to give varying amounts of bulk Cl or F, as listed in the table. For example, 3 mg of 9.25% HCl translates to 0.4 mg pure HCl and 2.6 mg H_2O, giving 1.3 wt.% Cl in the bulk fluid phase prior to experimental conditions. The 'charge' column denotes the different fluid mixtures added to the experimental charges, in order of increasing Cl content from A–D, and with a mixed Cl-F fluid in charge E.

Run#	P (MPa)	T (°C)	fO_2	Duration	Charge	Cl	F	H_2O	CO_2
						(wt.% of bulk capsule contents)			
15	106	1150	QFM	4h 40	A	0.1	0.05	9.6	-
					B	0.4	0.04	8.7	-
					C	0.8	0.04	8.6	-
					D	1.4	0.04	7.4	-
					E	0.4	0.30	9.3	-
16	48	1150	QFM	5h 30	A	0.1	0.05	9.1	-
					B	0.4	0.04	8.6	-
					C	0.7	0.04	8.7	-
					D	0.8	0.04	8.2	-
					E	0.4	0.27	8.7	-
17	24	1150	QFM	5h 10	A	0.1	0.05	9.5	-
					B	0.4	0.04	8.9	-
					C	0.8	0.04	8.2	-
					D	1.5	0.04	7.9	-
					E	0.5	0.25	9.0	-
18	118	1200	QFM	5h	A	0.1	0.04	10.3	-
					B	0.4	0.04	9.1	-
					C	0.8	0.04	8.8	-
					D	1.6	0.04	7.8	-
					E	0.4	0.25	8.3	-
19*	106	1150	QFM	5h 20	A	0.1	0.05	9.2	1.1
					B	0.3	0.05	8.9	1.4
					C	0.8	0.04	8.7	1.2
					D	1.5	0.04	7.4	1.3
					E	0.4	0.26	8.5	1.3
20	191	1150	QFM	5h 25	A	0.1	0.05	9.1	-
					B	0.4	0.04	10.3	-
					C	0.7	0.04	8.7	-
					D	1.5	0.04	8.5	-
					E	0.4	0.26	8.3	-

Table 7.4 Bulk volatiles loaded in runs 15–20 (H_2O-Cl-F, one with CO_2). Wt.% values are wt.% of the bulk sample including fluids; i.e., 30 mg rock + H_2O, HCl ± HF ± Ag_2CO_3 (run 19). Cl and F present in the natural sample are also included, All capsules are $Au_{80}Pd_{20}$. *Run 19 was designed to test the effect of CO_2 on Cl-F solubility, but the quench failed.

7.2.3 Experimental conditions and set-up

Experimental temperatures and pressures are included in Tables 7.2 and 7.4. Runs 1–14 were performed at temperatures of 1050–1200 °C, and runs 15–20 at either 1150 °C or 1200 °C. Experiments were performed in a vertically-mounted internally-heated pressure vessel (Fig. 7.1b), with a rapid-quench capability to avoid quench crystallisation (Holloway et al., 1992; Roux & Lefèvre, 1992; Berndt et al., 2002). The temperature was measured with two S-

type thermocouples, with a gradient across the sample of less than 5° C. Argon gas was used as a pressure medium, with the addition of H_2 gas to alter the fO_2 of the assemblage to QFM at the final experimental pressure; usually on the order of 5–7 bars in these experiments. Oxygen fugacity was not monitored by Shaw membrane or sensor due to short experimental durations. Run durations were short, typically 5–6 hours, to reduce the likelihood of iron loss. This duration is considered sufficient for the attainment of equilibrium between the basaltic liquid and the fluid phase (e.g., Dixon et al, 1995; Lesne et al., 2011b). Two longer runs (#11, 18h, and #14, 18h 20m) were performed to evaluate the effect of longer duration on iron loss.

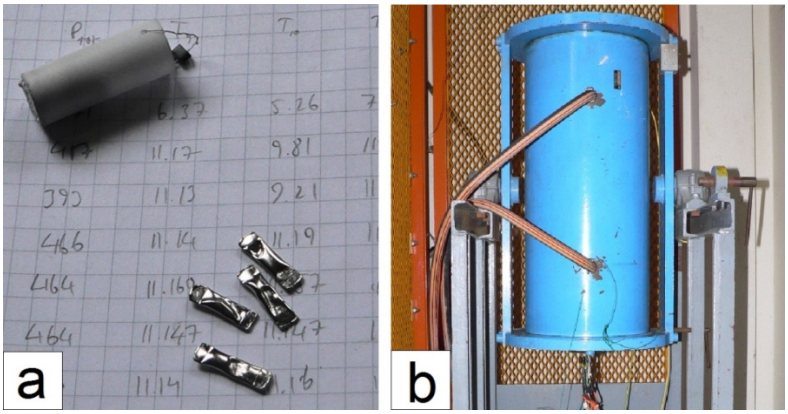

Figure 7.1 a) Alumina sample holder (upper left) with Pt wire hook for rapid quench (to quench, a current melts the wire, causing the sample holder to drop out of the furnace), and experimental capsules (after experiment); grid square=1 cm. **b)** IHPV in working position; height of autoclave is c. 1 m.

7.2.4 Experimental products

After each experiment, the capsules were weighed, and then pierced, noting whether a hiss or smell of sulphur occurred on piercing, to confirm the presence of a fluid phase at the end of the run. The pierced samples were placed in a drying oven for ~20 minutes, and weighed again. The release of fluid or gas as well as a weight difference after piercing and heating demonstrates fluid saturation in the capsule. All capsules lost mass upon piercing, and all except 17A and D produced a hiss, H_2S odour and/or fluid bubble.

On extraction from the capsules, the experimental products were first examined visually to ascertain whether they were glassy or crystallised. Crystallised samples were darker with a dull, matte lustre on broken surfaces, in contrast to the transparent light brown of glassy samples. Chips from each sample were mounted in Epofix™ epoxy resin and polished using SiC paper followed by diamond paste down to 3- or 1-μm grade. These were first examined under an optical microscope (reflected light) to identify any equilibrium phases or quench crystals present. The samples were also examined on a scanning electron microscope for identification of very small crystals, or crystals not easily identified by morphology.

7.3 Results

7.3.1 Crystalline phases and Fe loss

All crystal-bearing samples were generated from the contaminated Al-rich starting composition; inferences cannot be made from these with regard to natural phase equilibria. For this reason, crystal phases were not systematically analysed, although they may provide insights into the phase equilibria of very high aluminium (~22 wt.% Al_2O_3) compositions. All crystallised samples contained abundant plagioclase, which is partly attributed to the high Al_2O_3 content. Fe-Ti oxides occurred in just under a third (16) of crystallised charges as sub-micron rounded grains. Olivine occurred in 10 charges. No clinopyroxene was observed, perhaps due to high Ca uptake by plagioclase enhanced by the high availability of Al. Crystallised samples (42 out of 65 in the H_2O-CO_2 series) were not studied in detail, except for analysis of glass where present in sufficient volume. Analyses of plagioclase in run #2 (25 MPa, 1150 °C), which is present as interlocking lattice of elongate microlites (~10–20 μm) with glass being the only other phase, show anorthite contents of An_{72-84} , and display an apparent influence of volatile content, with reduced An content in the presence of sulphur, and in the nominally anhydrous CO_2-only charge (Table 7.5).

Charge	S	H_2O	CO_2	XH_2O^0	An%	n
A	-	4.6	0.0	1.0	79–84	3
B	-	2.4	1.5	0.6	78	1
C	-	2.6	2.7	0.5	81	1
D	0.9	4.8	0.0	1.0	-	-
E	0.9	2.4	1.3	0.7	73	1
F	-	4.5	0.0	1.0	78	1
G	-	0.0	2.7	0.0	72	1

Table 7.5 Plagioclase analyses in run #2 (25 MPa, 1150 °C) with An content and number of plagioclase analyses (n).

Iron loss of 14–28% relative (calculated on an anhydrous basis) is evident in runs 15–20, all of which were produced in $Au_{80}Pd_{20}$ capsules, precluding comparison of iron loss between different capsule types. A longer run (#14; 18h 20m) shows lower iron loss (4–16% relative) but was more oxidising (~NNO) and lower-temperature (1100 °C), both of which will reduce the amount of iron loss. In the Al-contaminated experiments, Fe loss is estimated[13] at <15% relative in those glasses analysed.

[13] The contaminated starting composition was not analysed prior to experiment, so was estimated from the average value for the post-experiment glasses.

The effect of sulphur on H_2O-CO_2 solubilities was not clarified as nearly all sulphur-added charges were microcrystalline with insufficient glass for analysis.

7.3.2 Volatile constituents

Experimental glasses were analysed for major elements and S, Cl and F on the electron microprobe at the University of Cambridge, and for H_2O, CO_2, Cl and F on the secondary ion microprobe at the NERC Ion Microprobe Facility in Edinburgh (Tables 7.6 and 7.7)[14].

C-O-H-S experiments

The amount of water dissolved in the melt is dependent on pressure and the proportion of H_2O in the fluid (Fig. 7.2a,b; Tables 7.6 and 7.7). The pressure relationship is linear with very little scatter (R^2=0.99) for halogen-bearing experiments, but shows greater scatter for CO_2-bearing experiments (R^2=0.63), with the most pronounced dispersal of datapoints occurring at higher pressures (Fig. 7.2b). Both sets of experiments (CO_2-bearing and halogen-bearing) fall along essentially the same trendline despite the significant aluminium contamination of glass used in the H_2O-CO_2 experiments.

CO_2 data from the SIMS sessions have an effective background of ~220 ppm, as the machine was shown to be reporting CO_2 contents up to 221 ppm in glasses known to be CO_2-free. Only in charges 8C (1200 °C, 92 MPa), 9C, and 9D (1175 °C, 106 MPa) do CO_2 contents exceed this limit (Table 7.6). These data show a linear correlation with pressure (Fig. 7.2c). Data from Dixon (1995) and Lesne et al. (2011a, b) are plotted alongside these data for comparison.

The highest value is 387 ppm at 106 MPa; the closest comparable CO_2 solubility in the literature is 504±101 ppm at 106 MPa, for Etna basalt with 3.5 wt.% Na_2O and 2.0 wt.% K_2O (Lesne et al., 2011b). Ambrym CO_2 solubilities are lower than those found by Lesne et al.

[14] Run 17 lost mass from all capsules (0.7–4.3 mg, i.e., 2–13 wt.% of bulk charge contents) but contains dissolved H_2O appropriate to the run pressure (1.4–1.5 wt.%), as estimated by solubility model of Moore (2008). In addition, the mass lost from some capsules in one case exceeds the total mass of volatiles added, so this does not appear to be due to volatile loss. Nothing unusual was noted during the experiment or upon extraction of the capsules from the sample holder. Two possibilities are leakage of melt without escape of volatile components, which is physically highly unlikely, and is also extremely unlikely to happen to all five capsules (and presumably would have been very noticeable on inspection of the capsules), or a fault in the laboratory balance. Results are included with the proviso that they may not be reliable for volatile species other than H_2O (which was apparently fully retained) if volatile loss did occur.

(2011b) for Vesuvius, Etna and Stromboli, but higher than those found by Lesne et al. (2011a) for Stromboli and Masaya (Fig. 7.2c).

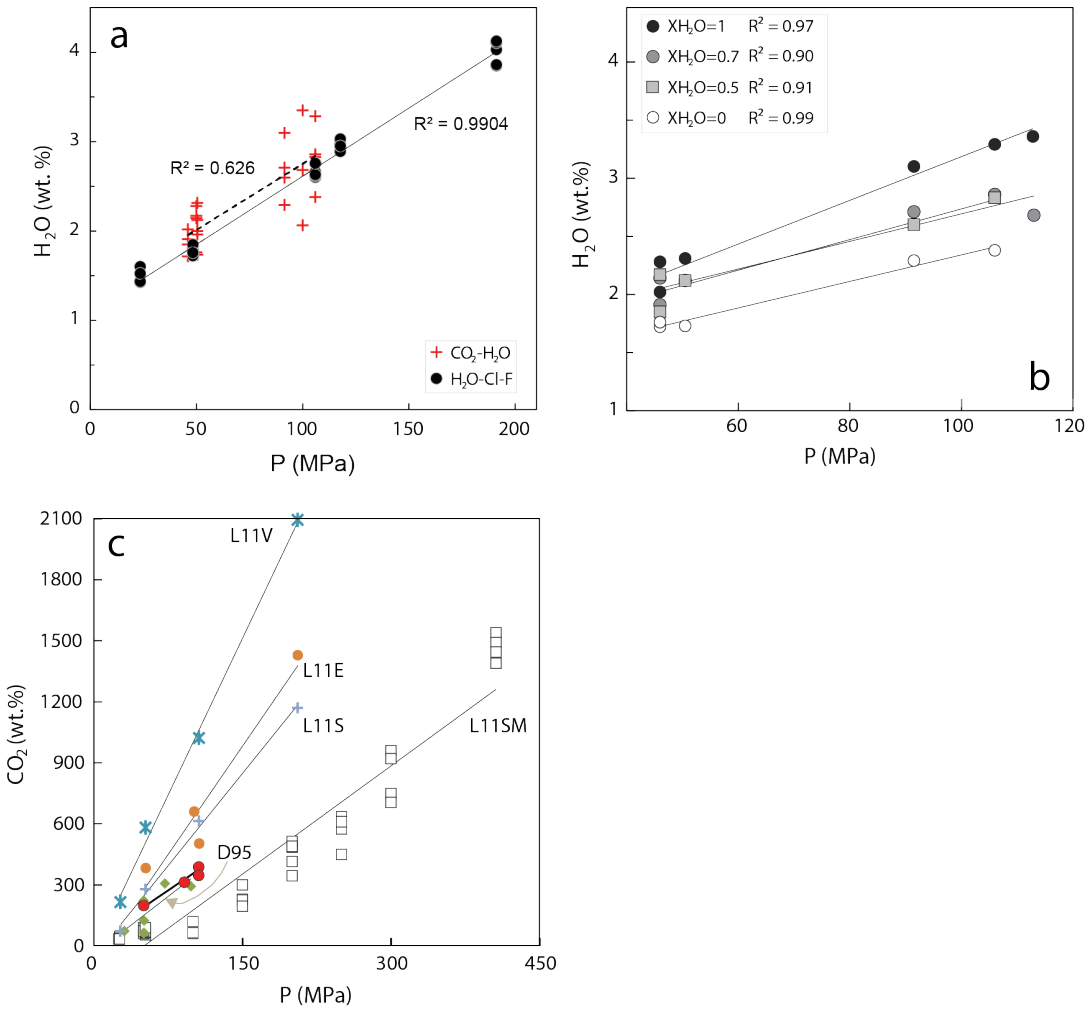

Figure 7.2 a) Variation of melt water content with pressure for H_2O-CO_2 and H_2O-Cl-F experiments. **b)** Variation of melt water content with pressure for H_2O-CO_2 experiments, showing variation with proportion of H_2O in the **initial** fluid (XH_2O). **c)** Variation of melt CO_2 with pressure (red filled circles=Ambrym data). Data from Dixon, 1995 (labelled D95, MORB), Lesne et al., 2011b (L11V, L11E and L11S, for Vesuvius, Etna and Stromboli respectively) and Lesne et al., 2011a (L11SM, alkali basalts from Stromboli and Masaya) for comparison.

Despite no addition of H_2O fluid, nominally CO_2-only charges show H_2O contents of 1.7–2.4 wt.%, strongly correlated with pressure, such that

$$H_2O=0.0114 \times P(MPa) + 1.2;\ R^2=0.99.$$

This H_2O most likely derives from reduction of iron via the reaction $Fe_2O_3 + H_2 \Leftrightarrow FeO + H_2O$ (e.g., Holloway et al., 1992). Further reduction of ferrous iron due to alloying with the capsule may also produce H_2O (Lesne et al., 2011b). Lesne et al. (2011b) reported H_2O contents of 0.6–1.7 wt.% for nominally anhydrous glasses of similar composition over a similar pressure range, but at more oxidising conditions (~NNO+1).

Glass	n	P (MPa)	T (°C)	XH_2O^{bulk}	XH_2O^{fl}	SiO_2	TiO_2	Al_2O_3	FeO	MgO	MnO	CaO	Na_2O	K_2O	P_2O_5	F	Cl	Total	CO_2	H_2O
7A	10	51	1200	1.0	1	48.77	0.94	22.55	7.70	3.98	0.19	8.50	2.81	1.97	0.34	530	80	97.84	-	2.31
						0.25	*0.06*	*0.13*	*0.33*	*0.12*	*0.03*	*0.09*	*0.05*	*0.05*	*0.01*	*266*	*29*	*0.50*		
7B	10	51	1200	0.7	0.4	49.85	0.96	22.90	7.06	3.99	0.20	8.50	2.91	2.00	0.35	467	93	98.80	b.d	2.12
						0.31	*0.04*	*0.19*	*0.18*	*0.08*	*0.01*	*0.10*	*0.05*	*0.03*	*0.01*	*166*	*27*	*0.46*		
7C	10	51	1200	0.5	0.5	49.35	0.96	22.71	7.59	4.00	0.20	8.57	2.85	1.95	0.35	395	61	98.60	b.d.	2.12
						0.36	*0.03*	*0.15*	*0.30*	*0.11*	*0.01*	*0.09*	*0.04*	*0.06*	*0.01*	*115*	*35*	*0.38*		
7D	10	51	1200	0.6	0.6	49.66	0.97	22.76	7.55	3.98	0.20	8.45	2.90	1.99	0.38	402	78	98.90	b.d.	2.00
						0.37	*0.03*	*0.21*	*0.25*	*0.07*	*0.03*	*0.09*	*0.06*	*0.05*	*0.03*	*72*	*39*	*0.75*		
7E	10	51	1200	0.0	0	50.35	1.03	22.48	6.83	4.43	0.21	8.19	2.97	2.12	0.37	303	104	99.05	b.d.	1.73
						0.35	*0.09*	*1.13*	*0.79*	*0.52*	*0.04*	*1.01*	*0.16*	*0.32*	*0.03*	*97*	*34*	*0.54*		
8A	10	92	1200	1.0	1	48.42	0.94	22.08	7.43	3.97	0.19	8.51	2.81	1.98	0.35	218	71	96.72	-	3.10
						0.25	*0.03*	*0.21*	*0.29*	*0.07*	*0.01*	*0.08*	*0.05*	*0.05*	*0.01*	*78*	*33*	*0.42*		
8B	10	92	1200	0.6		49.30	0.95	22.74	6.32	3.97	0.18	8.58	2.89	1.97	0.35	205	95	97.30	b.d	2.71
						0.24	*0.04*	*0.32*	*0.67*	*0.05*	*0.03*	*0.14*	*0.07*	*0.07*	*0.01*	*67*	*18*	*0.29*		
8C	10	92	1200	0.5	0.1	49.42	0.94	22.59	6.63	4.04	0.19	8.54	2.87	1.97	0.35	165	75	97.58	b.d.	2.60
						0.39	*0.03*	*0.23*	*0.20*	*0.11*	*0.01*	*0.11*	*0.05*	*0.03*	*0.01*	*66*	*34*	*0.50*		
8D	10	92	1200	0.0	0	50.56	1.01	22.55	6.45	4.12	0.20	8.10	2.88	2.25	0.36	224	100	98.53	313	2.29
						0.40	*0.04*	*0.26*	*0.22*	*0.13*	*0.02*	*0.34*	*0.07*	*0.20*	*0.01*	*85*	*32*	*0.59*	*69*	
9A	10	106	1175	1.0	1	47.70	0.90	22.06	7.57	3.93	0.19	8.47	2.61	1.93	0.36	414	80	95.77	-	3.29
						0.63	*0.03*	*0.25*	*0.35*	*0.10*	*0.02*	*0.10*	*0.46*	*0.05*	*0.01*	*94*	*24*	*0.83*		
9B	10	106	1175	0.7	0.4	47.97	0.93	22.10	7.52	4.00	0.19	8.52	2.79	1.95	0.36	341	86	96.40	b.d.	2.86
						0.30	*0.03*	*0.15*	*0.40*	*0.08*	*0.02*	*0.06*	*0.06*	*0.02*	*0.01*	*84*	*24*	*0.51*		
9C	10	106	1175	0.5	0.5	48.49	0.95	22.49	6.73	3.88	0.19	8.48	2.88	2.03	0.35	459	62	96.55	346	2.83
						0.45	*0.03*	*0.14*	*0.22*	*0.09*	*0.02*	*0.08*	*0.03*	*0.04*	*0.01*	*154*	*23*	*0.44*	*98*	
9D	10	106	1175	0.0	0	49.50	0.99	22.01	6.26	4.20	0.20	8.12	3.03	2.17	0.38	286	73	96.93	387	2.38
						0.48	*0.03*	*0.16*	*0.18*	*0.12*	*0.03*	*0.15*	*0.05*	*0.06*	*0.01*	*98*	*26*	*0.44*	*53*	

Table 7.6 Run conditions and EPMA and SIMS data for C-O-H-S crystal-free experimental glasses. Means of n analyses, with standard deviation in italics. XH_2O is the mole fraction of water in the bulk volatile phase. Major elements and water in wt.%; F, Cl and CO_2 in ppm. 'b.d.'=below detection limit.

Glass	n[1]	P (MPa)	T (°C)	XH_2O	XH_2O^{fl}	SiO_2	TiO_2	Al_2O_3	FeO	MgO	MnO	CaO	Na_2O	K_2O	P_2O_5	F	Cl	Total	CO_2	H_2O	n[2]
10A	10	46	1175	1	1	50.02	0.95	22.12	8.08	4.00	0.21	8.50	2.93	1.87	0.35	219	75	99.08	b.d.	2.02	3
						0.64	*0.04*	*0.62*	*0.42*	*0.23*	*0.03*	*0.51*	*0.09*	*0.23*	*0.02*	*69*	*32*	*0.86*	-	0.20	
10B	10	46	1175	0.65	0.4	49.94	0.98	22.55	7.41	3.95	0.18	8.74	2.94	1.91	0.38	332	70	99.04	b.d.	1.91	3
						0.50	*0.11*	*1.56*	*1.07*	*0.57*	*0.03*	*1.38*	*0.13*	*0.45*	*0.03*	*134*	*25*	*1.07*	-	*0.20*	
10C	10	46	1175	0.52	0.5	50.05	1.02	21.71	7.85	4.19	0.20	7.87	3.06	2.17	0.37	171	78	98.54	b.d.	1.85	3
						0.48	*0.07*	*0.68*	*0.78*	*0.33*	*0.03*	*0.74*	*0.13*	*0.27*	*0.02*	*75*	*19*	*0.66*	-	*0.13*	
10D	10	46	1175	0	0	50.95	1.02	22.16	7.40	4.15	0.20	8.22	3.02	2.10	0.37	211	79	99.64	b.d.	1.72	3
						0.57	*0.15*	*1.85*	*1.26*	*0.78*	*0.04*	*1.79*	*0.20*	*0.44*	*0.05*	*65*	*22*	*0.97*	-	*0.12*	
11A	10	46	1150	1	1	50.62	1.01	22.76	5.75	4.13	0.17	8.41	2.95	2.07	0.36	99	83	98.26	b.d.	2.28	2
						0.37	*0.11*	*1.42*	*0.99*	*0.74*	*0.04*	*1.29*	*0.21*	*0.59*	*0.04*	*97*	*22*	*1.74*	-	*0.00*	
11B	10	46	1150	0.65	0.4	50.85	1.05	22.41	5.93	4.19	0.20	8.30	3.16	2.09	0.39	84	95	98.61	b.d.	2.14	3
						0.42	*0.17*	*1.75*	*1.08*	*0.73*	*0.04*	*1.64*	*0.16*	*0.69*	*0.04*	*71*	*33*	*0.96*	-	*0.21*	
11C	10	46	1150	0.47	0.2	50.52	1.09	21.45	6.31	4.97	0.24	7.15	3.04	2.59	0.40	96	76	97.80	b.d.	2.17	2
						0.67	*0.10*	*1.03*	*0.75*	*0.46*	*0.02*	*1.07*	*0.12*	*0.36*	*0.01*	*71*	*21*	*0.57*	-	*0.08*	
11D	10	46	1150	0	0	51.90	1.07	22.09	5.69	4.50	0.21	7.90	3.15	2.27	0.41	137	81	99.23	b.d.	1.76	2
						0.50	*0.14*	*1.73*	*1.12*	*0.80*	*0.03*	*1.49*	*0.13*	*0.45*	*0.07*	*81*	*28*	*0.63*	-	*0.04*	
13A	9	113	1100	1.00	1	47.38	0.96	20.66	9.02	4.12	0.21	7.58	2.79	2.09	0.37	55	68	95.20	b.d.	3.35	2
						0.54	*0.15*	*2.57*	*1.73*	*0.85*	*0.06*	*2.05*	*0.12*	*0.51*	*0.08*	*42*	*20*	*1.56*	-	*0.28*	
13B	9	113	1100	0.70	0.1	48.72	1.05	20.61	8.78	4.33	0.23	7.56	3.07	2.03	0.40	84	91	96.81	b.d.	2.68	2
						0.53	*0.07*	*0.59*	*0.43*	*0.28*	*0.03*	*0.81*	*0.10*	*0.39*	*0.02*	*44*	*25*	*1.17*	-	*0.09*	
13C	5	113	1100	0.00	0.4	48.12	1.09	20.06	9.41	4.39	0.24	6.80	3.00	2.41	0.41	121	58	95.96	b.d.	2.06	3
						0.53	*0.04*	*0.73*	*0.41*	*0.24*	*0.02*	*0.43*	*0.08*	*0.21*	*0.03*	*41*	*15*	*0.71*	-	*0.39*	
14A	6	59	1100	1.00	1	52.22	0.93	15.37	9.10	4.62	0.23	9.14	2.93	2.10	0.39	178	161	97.08	b.d.	2.92*	-
						0.30	0.04	0.17	0.21	0.04	0.03	0.12	0.07	0.03	0.01	16	24	0.60	-	*0.60*	
14B	6	59	1100	0.60	0.2	52.42	0.98	15.27	9.13	4.67	0.22	9.04	2.95	2.07	0.38	180	146	97.19	b.d.	2.05	3
						0.40	*0.04*	*0.15*	*0.18*	*0.10*	*0.01*	*0.06*	*0.06*	*0.04*	*0.01*	*42*	*10*	*0.58*	-	*0.37*	
14C	6	59	1100	0.50	?	52.13	0.95	15.38	9.61	4.75	0.21	8.99	2.97	2.08	0.39	146	147	97.51	b.d.	2.49*	-
						0.58	*0.03*	*0.11*	*0.28*	*0.09*	*0.01*	*0.19*	*0.08*	*0.07*	*0.01*	*50*	*31*	*0.55*	-	*0.55*	
14D	6	59	1100	0.00	0	51.87	0.98	15.24	10.52	4.78	0.23	8.98	2.98	2.11	0.38	161	165	98.12	b.d.	1.88*	-
						0.19	*0.05*	*0.16*	*0.26*	*0.08*	*0.03*	*0.12*	*0.07*	*0.06*	*0.00*	*59*	*11*	*0.41*	-	*0.41*	

Table 7.6 continued EPMA and SIMS data for C-O-H-S experimental glasses. Means of n analyses ([1]=EPMA, [2]=SIMS), with standard deviation in italics. F, Cl, CO_2 in ppm. 'b.d.'=below detection limit. XH_2O is the mole fraction of water in the bulk volatile phase. H_2O contents marked * are estimated by difference.

H_2O and CO_2 solubilities were evaluated by comparison with published data and solubility models (Dixon et al., 1995; Papale et al., 2006; Moore, 2008). Composition-dependent solubility diagrams for the Al-rich starting composition were created (Fig. 7.3) using the models of Moore (2008) and Papale et al. (2006). For the Dixon et al. (1995) model, pressure and dissolved H_2O were the only input parameters.

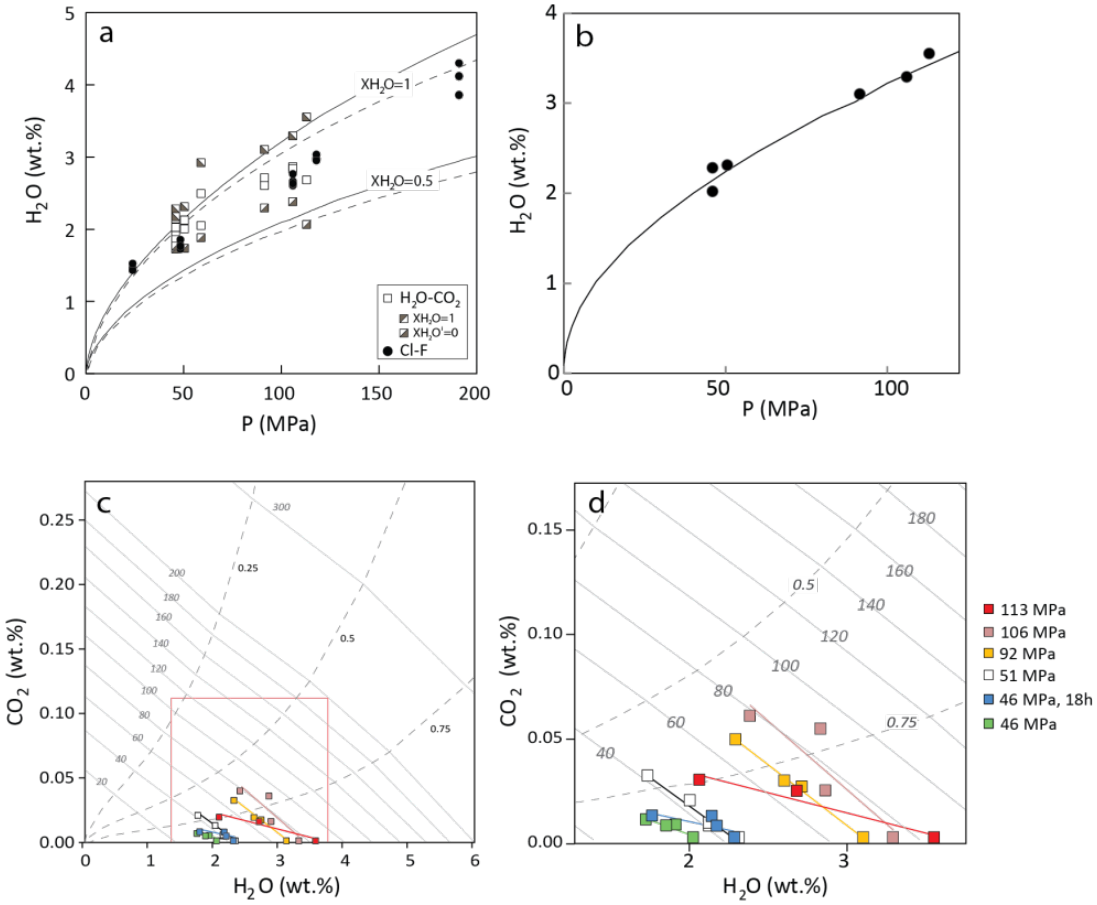

Figure 7.3 Water and CO_2 contents compared to published models. a) Comparison of Ambrym data with curves calculated using Moore (2008) solubility model for Al-enriched (dashed line) and natural (solid line) starting glasses, for XH_2O^{vapour} of 1 and 0.5, at T=1150 °C. b) Comparison of pure H_2O charges for with Dixon et al. (1995) model for H_2O solubility. c) Papale (2006) solubility model for Al-enriched starting composition at QFM and 1150 °C, with experimental data in red box. 1150 °C is the median temperature value in these experiments; temperature-related variation in solubility curves is minor over the applicable range (1150±50 °C). d) Area bounded by red line in panel c, enlarged to show detail of experimental data. Data mainly show almost identical slopes to the model isolines except for the 113 MPa run (#13). It is unclear why data for this experiment shows a different trend.

Dissolved water contents in H_2O-only charges follow the trends predicted by the Moore (2008) solubility model; by comparison, nominally anhydrous (CO_2-only) charges appear to actually fall somewhere near XH_2O^{vapour}=0.5 (Fig. 7.3a). H_2O-only charges also follow the Dixon et al. (1995) model for MORB (Fig. 7.3b), and the handful of reliable data for CO_2-

bearing charges fall on a similar trendline to MORB data from Dixon et al. (1995), rather than in line with data for alkali basalts (e.g., Lesne et al., 2011a, 2011b) as might be expected. The model of Papale et al. (2006) underestimates pressure for the Al-rich contaminated composition (Fig. 7.3c,d). It can be seen, however, that despite the high background for CO_2 measurements, the majority of data form trends parallel to those predicted by the model, indicating that the data below the effective background are in fact valid. The exception is the trend for run #13 (113 MPa), which cuts across the model isolines, and to a lesser extent for run #11 (46 MPa, 18 hours), in which one datapoint skews the trend.

H_2O-Cl-F experiments

Results of the H_2O-Cl-F experiments are displayed in Table 7.7 and Figure 7.4. Water contents of the glasses in the Cl-F experiments show a linear correlation with pressure, ranging from 1.4 wt.% at 24 MPa, to 4.1 wt.% at 191 MPa (Fig. 7.2a). Cl ranges from 130–250 ppm and remains effectively constant with increased bulk Cl in the charge. There is no correlation with major elements or H_2O (Fig. 7.4a). Cl displays a weak positive correlation (R^2=0.39) with pressure (Fig. 7.4b), expressed as

$$Cl(ppm) = 0.24*P(MPa) + 132$$

Any correlation with T cannot be ascertained as Cl-bearing experiments were only performed at two different temperatures.

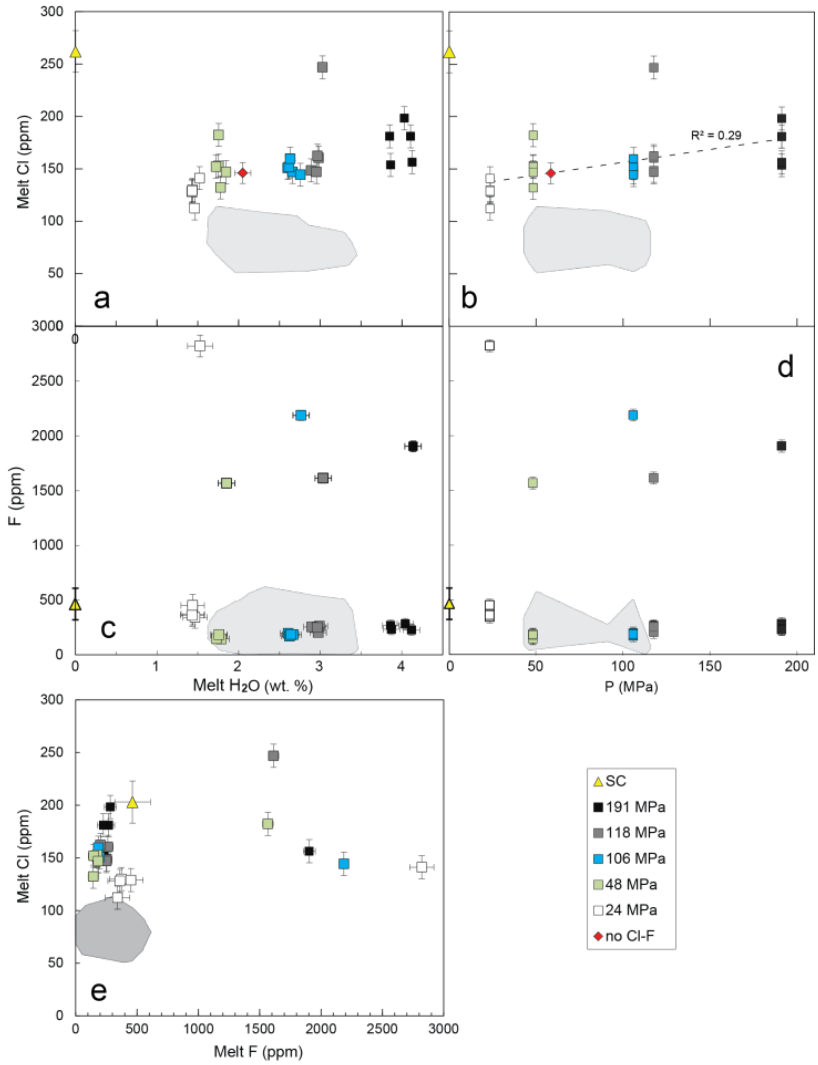

Figure 7.4 Variation of chlorine and fluorine contents in experimental glasses. Grey fields show Cl-F contents in non-halogen doped experimental glasses. SC=starting composition (cf. Table 7.1). Note that the 24 MPa run lost mass during the experiment and can be seen to display higher F in both non-F-added and F-added melts. The five high–F datapoints are the Cl-F-doped experiments; the others are Cl-doped only. Error bars show averaged standard deviations for each series. a) Melt Cl vs. melt H_2O. b) Melt Cl variation with pressure.c) Melt F vs. melt H_2O. d) Melt F vs. pressure. e) Melt Cl vs. melt F. There appears to be a positive correlation between the two for non-F saturated conditions but a negative correlation at F-saturated conditions.

F contents are up to ~2200 ppm in F-doped experimental glasses, considerably higher than natural sample concentrations (529 ± 292 ppm in matrix glass and 584 ± 221 ppm in melt inclusions). There is no significant correlation between F and H_2O (Fig. 7.4c). F solubility shows a potential correlation with pressure but data are too few to properly assess this effect (Fig. 7.4d).

At low F contents (<500 ppm) and P>24 MPa for Cl-bearing experiments there is a weak to moderate positive correlation (R^2=0.41) between F and Cl content, expressed as

$$Cl = 1.73 \times F - 62.7$$

At F contents >1500 ppm there appears to be a negative correlation between F and Cl (Fig. 7.4e).

Fluid-melt partitioning

Cl, F and H_2O concentrations in the fluid phase at experimental temperature and pressure were calculated by mass balance from bulk concentrations in the starting components, and analysed melt concentrations (Fig. 7.5a,b). Fluid/melt partition coefficients were then calculated using analysed melt and calculated fluid concentrations[15].

Values for D_{Cl}, the partition coefficient of Cl between fluid and melt (Cl_{fluid}/Cl_{melt},) are extremely high: 49–1600 calculated on a weight % basis (wt.% in fluid ÷ wt.% in melt), and 18–446 on a molar basis, indicating an extreme preference for the fluid phase (Fig. 7.5c). D_{Cl} does not vary with any intensive parameters. There is no correlation between pressure and D_{Cl}.

Values for D_F, the partition coefficient of F between fluid and melt (F_{fluid}/F_{melt}) are ~7–36 when calculated on a weight % basis, and 2–10 on a molar basis, indicating quite a high preference for the fluid phase (Fig. 7.5d). Indeed, F naturally present in the starting glass (464±144 ppm) appears to have been lost to the fluid phase during experiments; dissolved F decreased to 145–283 ppm following experiments in non-F-loaded glasses (Table 7.7). D_F demonstrates a negative correlation with F^{melt}.

There is a positive correlation between Cl/F ratio in the fluid and Cl/F ratio in the melt for F-added charges (Fig. 7.5d).

There was no extraction of cations (Na, K) by the Cl-bearing fluid. Wyllie & Tuttle (1964) noted that the main action of HCl in the system Ab-H_2O-HCl was to transport alkalis, and sodium in particular, into the vapour phase—but variations in major elements in the final glass do not exceed the limits of analytical error (except Fe, which is attributed to Fe loss).

[15] The weight fraction of pure Cl in the starting contents of the capsule was calculated from the weight fraction of aqueous HCl solution added to the charge, times the weight fraction of HCl in the aqueous solution (volume % divided by density of HCl). Subtraction of the calculated mass of dissolved Cl from mass of bulk Cl then gives the mass of Cl in the fluid phase at experimental temperature and pressure.

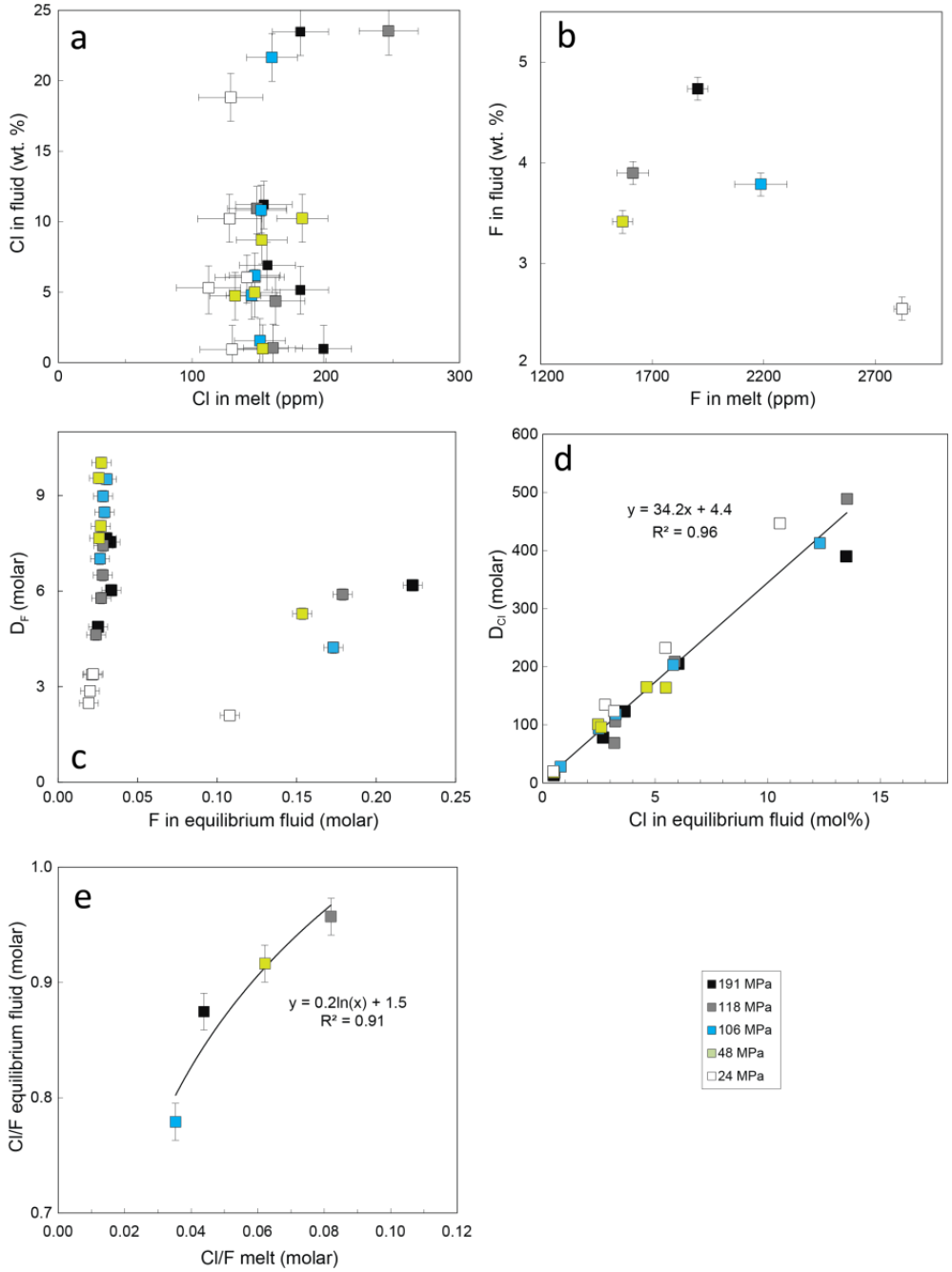

Figure 7.5 Fluid/melt relationships of Cl and F in halogen-doped experiments. **a)** Cl in equilibrium fluid vs. Cl in melt. **b)** F in equilibrium fluid vs. F in melt. **c)** D_F vs. F in fluid. **d)** Fluid-melt partition coefficient D_{Cl} vs. Cl in equilibrium fluid. These data also demonstrate that there is no correlation between D_{Cl} and pressure. Error bars smaller than symbols. **e)** Cl/F ratio in equilibrium fluid vs. Cl/F in melt, for F-added charges only. Errors have been propagated from measurement errors and averaged across all data series.

Glass	P (MPa)	T (°C)	SiO_2	TiO_2	Al_2O_3	FeO	MgO	MnO	CaO	Na_2O	K_2O	P_2O_5	F ppm	Cl ppm	Total	H_2O wt%
15A	106	1150	51.95	1.01	15.72	8.01	0.21	4.85	9.24	2.86	2.09	0.38	195	151	96.37	2.60
			0.41	*0.04*	*0.12*	*0.31*	*0.01*	*0.09*	*0.09*	*0.05*	*0.04*	*0.01*	*66*	*29*	*0.51*	*0.04*
15B	106	1150	51.81	1.01	15.57	9.12	0.22	4.84	9.05	2.82	2.06	0.38	184	147	96.93	2.66
			0.39	*0.02*	*0.12*	*0.14*	*0.02*	*0.05*	*0.1*	*0.04*	*0.06*	*0.01*	*53*	*28*	*0.39*	*0.03*
15C	106	1150	51.84	0.99	15.4	8.52	0.23	4.73	9.04	2.89	2.1	0.39	171	152	96.16	2.62
			0.32	*0.03*	*0.1*	*0.38*	*0.02*	*0.08*	*0.11*	*0.09*	*0.04*	*0.01*	*46*	*8*	*0.57*	*0.06*
15D	106	1150	52.34	1.03	15.57	8.44	0.22	4.85	9.11	2.82	2.11	0.39	187	160	96.92	2.63
			0.21	*0.04*	*0.11*	*0.33*	*0.02*	*0.15*	*0.08*	*0.11*	*0.04*	*0.01*	*25*	*11*	*0.4*	*0.05*
15E	106	1150	52.4	1.02	15.71	8.05	0.21	4.82	9.18	2.88	2.09	0.39	2187	144	97.01	2.76
			0.16	*0.04*	*0.18*	*0.23*	*0.02*	*0.11*	*0.13*	*0.05*	*0.04*	*0.01*	*36*	*21*	*0.27*	*0.04*
16A	48	1150	52.34	1.01	15.89	8.65	0.23	4.96	9.25	2.97	2.12	0.39	177	153	97.86	1.75
			0.48	*0.02*	*0.13*	*0.2*	*0.02*	*0.14*	*0.1*	*0.07*	*0.05*	*0.01*	*27*	*30*	*0.56*	*0.03*
16B	48	1150	52.43	0.98	15.63	8.81	0.22	4.95	9.11	2.97	2.09	0.38	145	132	97.62	1.78
			0.33	*0.03*	*0.2*	*0.43*	*0.02*	*0.09*	*0.08*	*0.09*	*0.04*	*0.01*	*45*	*17*	*0.45*	*0.04*
16C	48	1150	52.63	1	15.49	9.08	0.22	4.91	9.11	3.03	2.08	0.38	147	152	97.96	1.72
			0.22	*0.03*	*0.16*	*0.19*	*0.02*	*0.1*	*0.08*	*0.05*	*0.07*	*0.01*	*50*	*14*	*0.23*	*0.01*
16D	48	1150	52.77	1.05	15.77	8.51	0.22	4.92	9.21	2.95	2.13	0.39	1567	182	98.11	1.85
			0.48	*0.03*	*0.16*	*0.16*	*0.03*	*0.17*	*0.1*	*0.04*	*0.03*	*0*	*46*	*15*	*0.44*	*0.03*
16E	48	1150	52.63	1.02	15.63	8.79	0.23	4.87	9.17	2.93	2.06	0.39	184	147	97.78	1.76
			0.56	*0.02*	*0.13*	*0.24*	*0.02*	*0.11*	*0.14*	*0.1*	*0.04*	*0.02*	*42*	*17*	*0.68*	*0.02*

Table 7.7: EPMA and SIMS data for H_2O-Cl-F experiments. N=3 for H_2O data.

Glass	P (MPa)	T (°C)	SiO_2	TiO_2	Al_2O_3	FeO	MnO	MgO	CaO	Na_2O	K_2O	P_2O_5	F ppm	Cl ppm	Total	H_2O wt.%
17A	24	1150	53.79	1.05	15.94	7.98	0.20	4.97	9.26	3.16	2.26	0.40	373	130	99.07	1.44
			0.24	*0.03*	*0.13*	*0.26*	*0.01*	*0.12*	*0.09*	*0.08*	*0.05*	*0.01*	*95*	*17*	*0.44*	*0.03*
17B	24	1150	53.15	1.04	15.59	8.36	0.21	4.92	9.19	3.08	2.25	0.40	342	112	98.21	1.46
			0.27	*0.03*	*0.19*	*0.3*	*0.02*	*0.14*	*0.17*	*0.18*	*0.05*	*0.01*	*130*	*42*	*0.81*	*0.05*
17C	24	1150	52.87	1.05	15.66	8.18	0.20	5.10	9.41	3.1	2.17	0.41	361	128	98.21	1.43
			0.35	*0.03*	*0.17*	*0.36*	*0.02*	*0.10*	*0.12*	*0.04*	*0.06*	*0.01*	*74*	*21*	*0.59*	*0.05*
17D	24	1150	53.11	1.06	15.67	8.43	0.21	5.03	9.34	3.09	2.17	0.40	452	129	98.6	1.43
			0.24	*0.04*	*0.19*	*0.26*	*0.01*	*0.12*	*0.1*	*0.07*	*0.05*	*0.01*	*76*	*19*	*0.50*	*0.04*
17E	24	1150	53.18	1.03	15.62	7.92	0.21	5.03	9.4	3.14	2.20	0.41	2821	141	98.46	1.52
			0.69	*0.03*	*0.26*	*0.43*	*0.02*	*0.17*	*0.18*	*0.07*	*0.08*	*0.01*	*119*	*19*	*0.80*	*0.06*
18A	118	1200	50.37	1.00	15.7	8.78	0.23	4.83	9.01	2.76	2.07	0.39	263	161	95.19	2.98
			0.05	*0.02*	*0.08*	*0.14*	*0.02*	*0.10*	*0.14*	*0.1*	*0.03*	*0.01*	*29*	*25*	*0.62*	*0.00*
18B	118	1200	52.21	1.03	15.55	8.06	0.21	4.82	9.11	3.00	2.08	0.39	203	162	96.51	2.97
			0.28	*0.03*	*0.16*	*0.29*	*0.01*	*0.11*	*0.06*	*0.06*	*0.04*	*0.01*	*87*	*26*	*0.57*	*0.06*
18C	118	1200	51.48	1.04	15.81	8.13	0.22	4.89	9.04	2.74	2.10	0.38	254	149	95.88	2.97
			0.50	*0.04*	*0.08*	*0.24*	*0.02*	*0.10*	*0.08*	*0.16*	*0.05*	*0.01*	*24*	*8*	*0.50*	*0.05*
18D	118	1200	51.62	1.01	15.74	7.93	0.22	4.89	9.22	2.77	2.08	0.39	1614	247	96.06	3.03
			0.27	*0.03*	*0.11*	*0.33*	*0.03*	*0.11*	*0.08*	*0.08*	*0.04*	*0.01*	*72*	*28*	*0.57*	*0.04*
18E	118	1200	51.32	1.01	15.56	8.63	0.24	4.86	9.21	2.75	2.10	0.38	251	147	96.11	2.95
			0.48	*0.03*	*0.21*	*0.32*	*0.02*	*0.12*	*0.1*	*0.05*	*0.04*	*0.01*	*42*	*27*	*0.85*	*0.06*
20A	191	1150	51.03	1.02	15.03	8.9	0.22	4.65	8.94	2.69	2.02	0.38	283	198	94.92	4.03
			0.45	*0.03*	*0.13*	*0.18*	*0.02*	*0.08*	*0.08*	*0.09*	*0.05*	*0.01*	*56*	*41*	*0.57*	*0.03*
20B	191	1150	51.03	1.00	15.14	9.11	0.23	4.74	8.98	2.55	2.07	0.38	269	181	95.29	3.85
			0.45	*0.02*	*0.11*	*0.33*	*0.01*	*0.12*	*0.17*	*0.16*	*0.09*	*0.01*	*50*	*10*	*0.34*	*0.05*
20C	191	1150	51.00	1.00	15.53	8.02	0.22	4.74	9.08	2.68	2.04	0.39	234	154	94.77	3.86
			0.42	*0.02*	*0.24*	*0.32*	*0.01*	*0.09*	*0.13*	*0.11*	*0.04*	*0.01*	*56*	*9*	*0.45*	0.04
20D	191	1150	50.75	0.99	15.33	8.57	0.22	4.67	8.98	2.63	2.06	0.38	227	181	94.61	4.11
			0.51	*0.03*	*0.23*	*0.25*	*0.02*	*0.14*	*0.13*	*0.09*	*0.06*	*0.01*	*38*	*24*	*0.36*	*0.13*
20E	191	1150	50.87	0.99	15.16	9.04	0.23	4.62	8.86	2.66	2.01	0.38	1905	156	95.03	4.12
			0.19	*0.03*	*0.14*	*0.26*	*0.01*	*0.11*	*0.07*	*0.05*	*0.06*	*0.01*	*46*	*19*	*0.43*	*0.08*

Table 7.6 continued: EPMA and SIMS data for H_2O-Cl-F experiments. Italics give standard deviation for n analyses, where n=10 for EPMA data n=and 3 for SIMS data (H_2O) except 17B, 18A–E, and 20C where n=2.

7.4 Discussion

7.4.1 H_2O-CO_2 solubilities

Solubility behaviour of H_2O and CO_2 is not strongly altered by the artificially elevated Al content. Al is a network former (Mysen et al., 1981) which contributes to polymerisation of the melt and so might be expected to reduce CO_2 solubility, but aluminium in excess over metal cations (i.e., a peraluminous melt) will behave as a network modifier and decrease polymerisation. Results show no correlation between Al (which varies by ~3 wt.% in post-experiment glasses) and CO_2^{melt}.

Compositional controls on CO_2 solubility in basaltic melts remain only partially understood, and these results from Ambrym do not fit neatly into existing models. For example, Lesne et al. (2011b) derived a new CO_2 solubility model for volatile-rich alkali basalts, giving saturation pressures up to 50% lower than existing models for CO_2 in basalt. Although a relatively alkali-rich composition (i.e., the Ambrym starting composition) would be expected to display high CO_2 solubility (e.g., Behrens et al., 2009; Botcharnikov et al., 2005; Dixon, 1997; Lesne et al., 2011b; Vetere et al., 2014), dissolved CO_2 contents in Ambrym experimental samples are found to be most closely comparable to the results of Dixon et al. (1995) for mid-ocean ridge basalt (Fig. 7.2c), and not to more similar alkali basalt compositions such as Etna, Stromboli or Masaya (Lesne et al., 2011a, 2011b).

This mismatch between experimental data and existing solubility models suggests that calculations of minimum saturation pressures of melt inclusions based on melt composition and dissolved CO_2 are likely to be underestimates.

7.4.2 Halogen solubilities

The presence of halogens does not appreciably affect water solubility in these experiments (Fig. 7.2a); variations in Cl and F are correlated with pressure rather than water content (Fig. 7.4a–d), although previous studies indicate that water solubility increases with increasing melt Cl (e.g., Stelling et al., 2008). Cl and F behave similarly to each other in the Ambrym experiments in relation to their respective concentrations in the fluid phase, which is unusual given existing knowledge of the solubility behaviours of fluorine and chlorine. Chlorine is volatile and escapes from magma very readily, whereas fluorine is very soluble in silicate liquids and is retained in the melt to a much greater degree (Wyllie, 1979). Mathez &

Webster (2005) demonstrated that Cl is 3–30 times more enriched in reduced basaltic melt compared to F.

Chlorine

$D_{Cl}^{aq\text{-}m}$ values in these experiments are extremely high (49–1600, weight basis), compared to previous studies of basaltic compositions; e.g., 0.9–6 (Webster et al., 1999), ~10 for Stromboli basalt (Métrich et al., 2001), and 11–17 for hawaiitic melt from Etna (Alletti et al., 2009) which is compositionally very close to the studied Ambrym basalt. Higher values of 7–240 are reported for rhyolitic melt by Webster & Rebbert (1998).

Previous studies have demonstrated that solubility of chlorine in basalts is generally high, with melt Cl contents of up to 1.8–5.9 wt.%, and that as chlorine activity increases in the bulk system, melt Cl concentration increases (e.g., Webster et al., 1999; Stelling et al., 2008). Here, melt chlorine never increases above 0.02 wt.%, and instead partitions more and more strongly into the vapour phase as the concentration in the bulk fluid increases.

Anomalous Cl results

The experimental composition used here apparently reached Cl saturation at ~0.02 wt.% across the range of experimental conditions. This is far lower than previously measured Cl solubilities in basalt, and the natural glass and melt inclusions in the sample used to create the starting composition also display higher Cl contents than experimental glasses, which suggests that some feature of the experiments prevented Cl from partitioning into the melt phase.

For comparison, Chevychelov et al. (2008) conducted mixed H-Cl-F experiments at similar conditions to the range investigated for Ambrym. Using a very similar starting composition (subalkaline basalt from Etna; Table 7.8), and the same experimental method, those authors found enhanced melt Cl (as high as 2.67 wt.%, showing an almost linear positive correlation with Cl_{fluid}) and enhanced aqueous fluid F concentrations. In their experiments, D_{Cl} was almost always <1. The experimental method was almost identical to this (Ambrym) study, including addition of Cl and F as aqueous solutions, which suggests that adding Cl in fluid rather than salt form is not the cause of the high D_{Cl} values in the Ambrym experiments (e.g., by inducing a preference for the fluid phase). Similar fluid/melt proportions were used, with a fluid:glass ratio of 0.09–0.14; for the Ambrym experiments the ratio was 0.10–0.12. Chevychelov et al. (2008) also used $Au_{20}Pd_{80}$ capsules, as in the Ambrym experiments; theirs, however, were pre-saturated in Fe at fO_2=NNO. Both the Chevychelov et

al. (2008) etnaite glasses and the Ambrym glasses were run in a rapid-quench internally-heated pressure vessel. The etnaite was run at 1200 ºC, 200 MPa and fO_2=NNO; the Ambrym glass was run over a range of 1100–1200 ºC and 24–191 MPa at ~QFM; a very similar set of conditions. In both experimental series, fH_2 was controlled using a mixture of argon and hydrogen gas. The Chevychelov et al. (2008) experiments ran for 3–3.6 days compared to ~4.5–5.5 hours for AMB6SC. The only major differences appear to be the pre-saturation of capsules and the length of the experimental run, which might indicate that oxidation state is involved in the anomalous behaviour of either or both of these experimental series.

	Etnaite	Ambrym
SiO_2	48.0	52.0
TiO_2	1.9	1.0
Al_2O_3	16.6	15.6
FeOt	9.3	11.1
MnO	0.2	0.2
MgO	6.1	4.9
CaO	11.5	9.1
Na_2O	3.5	3.0
K_2O	2.1	2.2
P_2O_5	0.6	0.4
Cl	0.1	0.02
F	0.05	0.05
H_2O*	0.12	0.28
A/CNK	0.57	0.65
N/NK	0.72	0.67
ANCM/S	1.00	0.79

Table 7.8 Comparison of etnaite composition studied by Chevychelov et al. (2008) with Ambrym starting composition used in this study. *H_2O by difference.

No explanation has been arrived at for the results of the Cl solubility experiments. The lack of variation with any intensive parameters provides no clues as to the mechanism at work. Similar studies have often used significantly higher bulk Cl contents (e.g., Stelling et al., 2008), but in runs with similar amounts to the maximum bulk Cl used here (~2 wt.%), melt Cl values of ~2 wt.% were obtained.

One possible explanation is the presence of an immiscible saline fluid phase ('brine', cf. Shinohara et al., 1989). Presence of a two-phase fluid (brine) is known to cause dissolved Cl to remain constant (e.g., Shinohara et al., 1989; Webster, 1997), but brine saturation is not associated with these P-T conditions, or with relatively low bulk Cl (less than 7 mol% of the fluid phase in 80% of experimental charges).

A number of possible experimental/analytical sources for the anomalously low Cl contents were considered, namely: 1) the Cl source for the experiments did not actually contain Cl, 2) the runs leaked, or 3) the analytical method for Cl did not work. Each of these possibilities has been examined and found not to apply. Cl was added to the charges as aqueous HCl solution freshly made up from analytical grade 37% HCl, and for one charge in

every run the analytical grade 37% solution was used without dilution, so the Cl source must be reliable for those charges at least. The same low dissolved Cl content is seen even in those charges which contained undiluted analytical grade HCl. The Cl-doped glasses contain higher Cl than in non-doped glasses, and show appropriate water contents for the various run pressures (as calculated using Moore, 2008), which demonstrates that elevated Cl was indeed present, and that there was no leakage (Fig. 7.6a). The glasses were analysed on both SIMS and EPMA with good agreement between the two methods, indicating that analytical methods are not the source of the anomalous data (Fig. 7.6b).

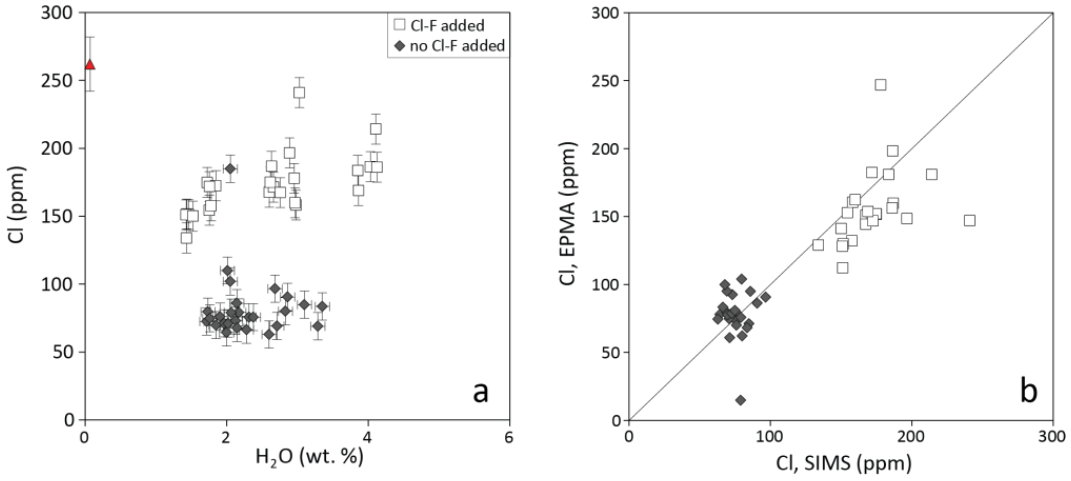

Figure 7.6 a) Cl vs. H_2O in experimental glasses. The error bars show the average standard deviation for each group. These results demonstrate that added Cl was present during the halogen-doped experiments. **b)** Comparison of EPMA and SIMS data showing ~1:1 relationship, demonstrating that anomalous Cl results are not an analytical artefact.

Small volumes of water and HCl or HF were used to make the Cl-bearing mixtures, and this is a probable source of inaccuracy. Ideally larger volumes should be mixed for greater accuracy; this was done due to inexperience. Regardless of this, the undiluted reagent grade 37% HCl solution would have been the correct concentration, and the charges using that solution show the same low concentrations as the others. The solution was also noted to have the distinctive strong, acrid odour of HCl during capsule preparation, confirming that the reagent was the correct substance.

The mixtures loaded into the capsule (silicate powder plus fluids) contained 0.1–2.3 wt.% bulk Cl. Experimental methods were comparable to Stelling et al. (2008), where most capsules had ~0.1–3.9 wt.% bulk Cl, and Cl was also mainly added as HCl, except for a few capsules loaded with $PtCl_4$. Despite the similarities in methods and composition, the Stelling et al. (2008) study resulted in melt Cl contents of 0.15–4 wt.%, in contrast to the uniformly low melt Cl in the Ambrym experiments.

The experimental glasses in fact have lower Cl than the starting composition (Fig. 7.6a). The natural matrix glass has higher Cl again, up to ~500 ppm. This indicates that not only is the added Cl not going into the melt, some condition of the experiments is actually driving off the resident natural chlorine.

The single non-Cl-added data point with high Cl derives from a more oxidised run, at approximately NNO (with no H_2 loaded into the vessel), in contrast to all other runs which were performed at QFM. Oxidation state is known to affect Cl solubility, although not to such an apparent extent (J. Webster, pers. comm. 2009). Higher Cl solubility in the starting glass, which was twice fused at 1400 °C at atmospheric conditions (c. 5 log units more oxidising than NNO at 1400 °C), also suggests an oxidation effect on Cl solubility. The Cl in the starting material is lower than in the natural glass (fO_2 estimated at NNO+1.2) however, possibly due to Cl loss during the high-temperature fusion of the starting glass.

Fluorine

Fluorine solubility does not show any clear correlation with pressure. Chevychelov et al. (2007) found that the presence of F enhanced Cl solubility in a basaltic melt very similar to the Ambrym starting composition, which contradicts other studies. Chevychelov et al. (2007) found that F solubility was approximately linearly dependent on the F content of the fluid, which agrees with findings in this study.

Fluorine is known to have a strong preference for the melt phase, even at extremely low pressures: HF is more soluble in melt than H_2O, as the F^- ion is smaller, and SiF_4 is more stable than $Si(OH)_4$ (Burnham, 1979). Fluorine solubility generally does not show a strong dependence on melt composition, with the exception of Ca content (Mathez & Webster, 2005), K content (Martini, 1984), which increases F solubility, and Si content, which decreases F solubility, as less fluorine can be accommodated with increasing polymerisation of the magma structure. Accordingly, a high-K basalt such as the Ambrym composition used here should display high F solubility; however, the highest-F melt content attained was ~0.2 wt.%. Chevychelov et al. (2007) produced experimental melts with fluorine content of up to 0.79 wt.% using basalt of very similar composition.

Fluorine has been shown to enhance water solubility in magmas (Martini, 1984); according to experimental data of Wyllie (1979), increased HF content increases the overall content of dissolved volatiles with a corresponding decrease in liquidus temperature. Ambrym data do not show enhanced solubilities of other volatiles with increased fluorine (Fig. 7.4c,e).

It is possible that the negative correlation between F^{melt} and Cl^{melt} in the F-doped glasses (Fig. 7.4e) is due to uptake by F of melt ions needed by Cl to enter the melt via complexing. It has also been suggested, however, that F enhances Cl solubility by increasing availability of Al, Na, Ca and Mg ions (Webster, 1997). The extent of this effect varies with F abundance and A/CNK (Webster, 1997); for example, on the order of ~1 to several wt.% F is needed to significantly influence Cl solubility in peralkaline and metaluminous liquids.

7.5 Conclusions

Results from H_2O-CO_2 experiments demonstrate H_2O solubility in line with the Moore (2008) solubility model, and higher CO_2 solubility than predicted by existing models for alkali basalts. Additionally, the aluminium-contaminated glasses in the H_2O-CO_2 experiments fall on the same trendline as the uncontaminated glasses, demonstrating that the elevated aluminium content does not affect H_2O solubility. Analytical limitations led to attainment of only a handful of datapoints for CO_2-loaded experiments, limiting the scope of interpretation.

A compromised starting composition prevented constraints on the natural crystal phase equilibria of Ambrym basalt. A very limited investigation of plagioclase compositions in contaminated glass suggest a possible effect of sulphur and of CO_2 respectively on plagioclase composition at low pressure, namely a 7–12% reduction in anorthite content at 24 MPa and 1150 °C.

The most striking result from halogen-bearing experiments is the anomalously low uptake of Cl (and to a lesser extent, fluorine) in the melt, with both partitioning strongly into the fluid phase at experimental conditions. The anomalous behaviour of Cl requires further experiments to ascertain whether experimental error is behind the results. Although all obvious potential sources of error have been ruled out, the solubility behaviours are so at odds with existing studies that it seems quite likely that these results may not be trustworthy.

Results also indicate interaction between Cl and F, but no influence of halogens on H_2O solubility. Finally, there is a suggestion that oxidation state plays a role in Cl solubility behaviour.

Chapter 8 Conclusions and further work

8.1 Conclusions

The intent of this work was to elucidate the source of enormous passive outgassing at Ambrym volcano, and to investigate magma storage conditions, via a combination of petrological study and experimental petrology. Ambrym is one of a handful of basaltic systems emitting volumes of magmatic vapour much larger than previously realised, and requiring closer study to understand the source and transport mechanisms of such prodigious volatile outputs.

This study first utilised petrography, mineral chemistry and major element modelling to characterise crystallisation conditions and magmatic processes operating in the magma storage system. Within this framework, measurement of dissolved volatile contents and modelling of the magmatic fluid phase, numerically and experimentally, was then applied to examine the nature of fluid transport from depth.

8.1.1 Petrography, major element modelling, and mineral chemistry

Petrological investigations and modelling primarily focused on samples of lava lake scoria and reticulite ejected in 2005 and 2007. A secondary focus investigated the compositional bimodality evidenced by the 1986 trachyandesite lava flow. Two flank lava flows and two basaltic intracaldera lava flows were briefly described, to broadly evaluate petrological variations between all major modes of post-caldera activity.

Recharge- and degassing-driven magma convection in the mid-crust

Variable resorption of phenocrysts and effectively constant mafic mineral compositions suggest phenocryst convection in a storage region of consistent magma composition. Excess degassing, recently well-documented at Ambrym, is a further indicator of magma convection (e.g. Kazahaya et al., 1994). Kazahaya et al. (1994) found that even a small density contrast between degassed and undegassed magma would be sufficient to drive convection. Although more primitive and more evolved compositions are also present, Ambrym has maintained a recurring predominant basaltic composition throughout the volcanic succession (Picard et al., 1995); the persistence of this composition since the early stages of volcanism suggests a stable and homogeneous magma supply (cf. Harris et al., 1999). This, coupled with recurrent periods

of elevated central vent activity on the scale of months to years, suggest frequent magmatic recharge via steady-state melt generation at Ambrym. The idea of magma recharge is an important development in volcanology and has been recognised as such for some decades now (e.g. Brown, 1956; Huppert & Sparks, 1980). Indications of recharge at Ambrym—suspected olivine settling, thermal resorption textures, episodic heavy degassing—suggest that it is the main driving force behind magma convection in the mid-crustal storage region.

This study has resulted in a model of the magma storage system with major crystallisation occurring at two depths; near-Moho (~27–30 km) and mid-crustal (~13–17 km), coincident with aseismic zones picked out by earthquake location data. The model envisages evolution of a relatively primitive magma to the near-basaltic-andesite composition of scoria matrix glass via staged crystallisation during ascent from the crust/mantle boundary. Ascent is likely driven by thermal and volatile input associated with magma recharge, and density reduction via crystal settling. Textural indications of convection in phenocrysts associated with the mid-crustal storage region indicate that this is where magma convection occurs. Less-frequent eruptions, from flank fissures or short-lived vents, feature lavas which have traversed less direct paths through the crust, picking up cumulates (AMB10) or interacting with silicic melt en route to the surface (AMB86).

Trachyandesite petrogenesis

At Ambrym, mineral and melt inclusion compositions reveal that the 1986 trachyandesite was generated by mixing of basalt with trachydacite. The lava contains a disequilibrium assemblage in which plagioclase and clinopyroxene compositions correspond to those seen in the Mbwelesu basalts, while olivine and spinel display a more evolved mineralogy and host trachydacitic melt inclusions. This can be modelled as combination of Mbwelesu basalt with melt inclusion trachydacite in the ratio ~70:30.

The explanation of andesite petrogenesis is a long-standing challenge in igneous petrology, with processes suggested including fractional crystallisation, magma mixing, assimilation, and partial melting of the crust or volcanic pile (e.g. Eichelberger, 1974; Grove & Kinzler, 1986; Stimac & Pearce, 1992; Reubi & Blundy, 2008). A paucity of melt inclusions sampling a true andesite melt is one of the strongest lines of evidence against andesite being a ‘true melt’ formed via fractional crystallisation (e.g. Reubi & Blundy, 2009), and certainly in the case of Ambrym, melt inclusions have demonstrated that this particular trachyandesite is a hybrid rather than a true andesitic liquid.

The mode of formation of the trachydacite melt has not been constrained. Possibilities include segregation of silicic melt from crystallising basaltic bodies in the crust (e.g., Gunnarsson et al., 1998; Marsh et al., 2008), or partial melt of crustal material by mafic injection (e.g. Annen & Sparks, 2002; Lange & Carmichael, 1996; Smith et al., 2006).

8.1.2 Pre-eruptive volatile contents

When this study was first undertaken, no studies on pre-eruptive volatile contents had yet been published. Following the recent publication of the first melt inclusion data for Ambrym by Allard et al. (2015), this study provides further constraints on melt inclusion entrapment depths and evolution of volatile components during ascent. This study also adds to a developing framework of interpretation of very high gas fluxes from basaltic volcanoes (e.g., Allard, 1997; Allard, 2010; Blundy et al., 2010; Burton et al., 2007; Burton, 2013; Kazahaya et al., 1994; Mather et al., 2006; Stix, 2007).

Dissolved volatile contents in melt inclusions indicate that during quiescent degassing phases, Ambrym is characterised by closed-system decompression degassing of CO_2–rich magma. The data show a classic degassing profile for exsolution with decompression of a very CO_2-rich fluid, and require an original dissolved volatile component at depth of perhaps 1 wt.% CO_2 and 0.3–0.4 wt.% H_2O.

Pressures calculated from melt inclusions (<200 MPa) are consistent with petrographic indications that olivine and clinopyroxene are relatively shallowly-crystallising phases in this magma, and also with thermobarometry which estimates low crystallisation temperatures (1120–1140 ºC), and pressures of ~310–490 MPa; higher than those from solubility modelling but within error, particularly given the indication from experimental data that the Ambrym alkalic basalt composition is not well-reproduced by existing CO_2 solubility models, which underestimate pressure based on CO_2 content by up to ~30 MPa over the range investigated.

Melt inclusion data suggest two possible models for volatile patterns at Ambrym: CO_2 flushing, or decompressional degassing. A plot of H_2O-CO_2 contents against vapour isopleths appears to demonstrate that dissolved volatile contents are buffered by a constant coexisting vapour composition, lying along an isopleth of 1 wt.% H_2O—although this trend could also be viewed as decompressional degassing of a very H_2O-poor magma. The presence of higher-H_2O melt inclusions (Allard et al., 2015) may provide support for the CO_2 fluxing model, but the amount of water involved is still low (<1.3 wt.%), and may reflect variability of the source magma.

Comparison of petrological data with observed gas fluxes suggests that plume concentrations represent an integrated degassing profile comprising shallowly-degassed H_2O, S, Cl and F combined with CO_2-rich vapour from greater depth. This, combined with a very high gas output which indicates extremely large magma fluxes at a system with very low eruption rates, points to convective degassing as the most suitable model for the Ambrym system. Similar volatile compositions from 2005 and 2007 scoria suggest that the samples studied are representative of a persistent degassing state of the system, at least on a timescale of years.

Finally, based on available evidence from geochemistry and regional tectonics—lack of any apparent carbonate source, high $^3He/^4He$ ratios, and evidence of exotic mantle influx—this strong CO_2 signal appears likely to have a mantle origin.

8.1.3 Experimentally-determined volatile solubilities

Results from H_2O-CO_2 experiments demonstrate H_2O solubility in line with the Moore (2008) solubility model, and lower CO_2 solubility than predicted by the Papale et al. (2006) model. The aluminium-contaminated glasses in the H_2O-CO_2 experiments fall on the same P-H_2O trendline as the uncontaminated glasses, demonstrating that the elevated aluminium content does not affect H_2O solubility. Analytical limitations led to attainment of only a handful of datapoints for CO_2-loaded experiments, limiting the scope of interpretation.

A compromised starting composition prevented constraints on the natural crystal phase equilibria of Ambrym basalt. A very limited investigation of plagioclase compositions in contaminated glass suggest a possible effect of sulphur and of CO_2 respectively on plagioclase composition at low pressure, namely a 7–12% reduction in anorthite content at 24 MPa and 1150 °C.

The most striking result from halogen-bearing experiments is the anomalously low uptake of Cl (and to a lesser extent, fluorine) in the melt, with both partitioning strongly into the fluid phase at experimental conditions. The anomalous behaviour of Cl requires further experiments to ascertain whether experimental error is behind the results. Although all obvious potential sources of error have been ruled out, the solubility behaviours are so at odds with existing studies that it seems quite likely that these results may not be trustworthy.

Results also indicate interaction between Cl and F, but no influence of halogens on H_2O solubility. Finally, there is a suggestion that oxidation state plays a role in Cl solubility behaviour.

Although the dataset is somewhat limited, it nonetheless adds some useful data to the historically under-represented field of volatile solubilities in alkali basalts, particularly for Cl and F.

8.2 Further work

This study has raised many possibilities for further work and has demonstrated that there are several intriguing aspects of magmatism at Ambrym volcano yet to be fully investigated.

8.2.1 Petrological work

This study has characterised the petrology of magma associated with the quiescent lava lake behaviour and occasional lava flows. An important next step will be petrological evaluation of products of paroxysmal events, to investigate controls on changes to a more explosive eruptive regime. Examination of pyroclasts associated with larger eruptions is necessary to understand the impetus for more explosive or larger-volume eruptive events.

Another sample type of interest is the post-caldera olivine basalt previously reported from the south-east part of the caldera (Picard et al., 1995), which may represent a more primitive recharge magma. Samples from a wider range of flank eruptions would give further insights into magma pathways through the crust and edifice, outside of the central conduit. The two flank lavas sampled are notably distinct from each other and from intracaldera samples, which suggests that an interesting variation of magma evolution pathways might be found.

Trace element analysis of melt inclusions and mineral phases would improve constraints on magma pathways through the system and could further clarify the origin of the trachyandesitic melt. Analysis of melt inclusions in high-anorthite relict plagioclase in the trachyandesite may reveal the composition of the basaltic mixing member. It would be worthwhile conducting a field examination of the trachyandesite lava flow to search for macroscopic evidence of mixing, such as enclaves or mingling textures.

8.2.2 Pre-eruptive volatile contents

Melt inclusion analysis has returned striking results for Mbwelesu scoria; sampling melt inclusions from other phases of activity at Ambrym would add greatly to understanding how

volatiles are moving through the system. In particular, inclusions from the most primitive rocks, to evaluate dissolved volatiles at greater depth, and samples from the pyroclastic series, to evaluate volatiles associated with tuff cone/caldera formation would provide significant stepping-stones to modelling the whole system.

Volatiles analysis of trachyandesite-hosted melt inclusions is also needed to elucidate the relationship to the basaltic conduit and storage history in the crust.

Another area which requires investigation is the source of the high CO_2 content, which could be partly resolved by investigation of oxygen and carbon isotope compositions in the magma.

8.2.3 Experimental series

The most important aspect to be investigated experimentally is a rigorous exploration of CO_2 ($\pm H_2O$) solubility in this composition. This would enable far more accurate evaluation of melt inclusion saturation pressures as well as adding significantly to the literature on CO_2 solubility in alkali basalts.

Another aspect to be revisited experimentally is the behaviour of chlorine, which has remained unexplained in the experiments performed. It seems that the anomalous behaviour of Cl in these experiments must be an artefact of the experimental method, although the source of the behaviour could not be identified; repeat experiments are needed to test this possibility.

Further potential experimental series include investigation of phase equilibria, including the influence of volatile components on phase stability. Sulphur in particular appears to play a strong role at Ambrym, which has not yet been investigated. Sulphur was included in this study but data were too few to make meaningful inferences.

Sub-liquidus experimental products (all of which were aluminium-contaminated) were not fully characterised by electron microprobe due to time constraints. Determination of phase compositions would be valuable for calibration of mineral-melt equilibrium models for high-Al_2O_3 compositions.

References

Aiuppa, A. (2009). Degassing of halogens from basaltic volcanism: Insights from volcanic gas observations. *Chemical Geology* **263**, 99–109.

Aiuppa, A., Burton, M., Caltabiano, T., Giudice, G.. Guerrieri, S., Liuzzo, M., Murè F. & Salerno, G. (2010). Unusually large magmatic CO_2 gas emissions prior to a basaltic paroxysm, Geophysical Research Letters **37**, L17303, doi:10.1029/2010GL043837.

Aiuppa, A., Federico, C., Giudice, G., Gurrieri, S., Liuzzo, M., Shinohara, H., Favara, R. & Valenza M. (2006). Rates of carbon dioxide plume degassing from Mount Etna volcano. *Journal of Geophysical Research* **111**, B09207.

Aiuppa, A., Giudice, G., Gurrieri, S., Liuzzo, M., Burton, M.R., Caltabiano, T., McGonigle, A.J.S., Salerno, G., Shinohara, H. & Valenza, M. (2008). Total volatile flux from Mount Etna. *Geophysical Research Letters* **35**.

Allard, P. (1997). Endogenous magma degassing and storage at Mount Etna. *Geophysical Research Letters* **24 (17)**, 2219–2222.

Allard, P. (2010). A CO_2-rich gas trigger of explosive paroxysms at Stromboli basaltic volcano, Italy. *Journal of Volcanology and Geothermal Research* **189**, 363–374.

Allard, P., Aiuppa, A., Bani, P., Métrich, N., Bertagnini, A., Gauthier, P. G., Parello, F., Sawyer, G. M., Shinohara, H., Bagnato, E., Mariet, C., Garaebiti, E. & Pelletier, B. (2009). Ambrym Basaltic Volcano (Vanuatu Arc): Volatile Fluxes, Magma Degassing Rate and Chamber Depth. *AGU Fall Meeting 2009 Abstracts* **4**.

Allard, P., Aiuppa, A., Bani, P., Métrich, N., Bertagnini, A., Gauthier, P.J., Shinohara, H., Sawyer, G., Parello, F., Bagnato, E., Pelletier, B. & Garaebiti, E. (2015). Prodigious emission rates and magma degassing budget of major, trace and radioactive volatile species from Ambrym basaltic volcano, Vanuatu island Arc. *Journal of Volcanology and Geothermal Research*. (Available online 3 September 2015).

Allard, P., Behncke, B., D'Amico, S., Neri, M., & Gambino, S. (2006). Mount Etna 1993–2005: anatomy of an evolving eruptive cycle. Earth-Science Reviews, 78(1), 85-114.

Allard, P., Carbonelle, J., Métrich, N. & Zettwoog, P. (1991). Eruptive and diffuse emissions of carbon dioxide from Etna volcano. *Nature* **351**, 387-391.

Alletti, M. Baker, D.R., Scaillet, B., Aiuppa, A., Moretti, R. and Ottolini, L. (2009). Chlorine partitioning between a basaltic melt and H_2O-CO_2 fluids at Mount Etna. *Chemical Geology* **263**, 37–50.

Almeev, R., Holtz, F., Koepke, J. & Parat, F. (2012). Experimental calibration of the effect of H_2O on plagioclase crystallization in basaltic melt at 200 MPa. *American Mineralogist* **97**, 1234-1240.

Almeev, R. R., Kimura, J. I., Ariskin, A. A., & Ozerov, A. Y. (2013). Decoding crystal fractionation in calc-alkaline magmas from the Bezymianny Volcano (Kamchatka, Russia) using mineral and bulk rock compositions. *Journal of Volcanology and Geothermal Research* **263**, 141–171.

Alt, J.C. & Teagle, D.A.H. (1999). The uptake of carbon during alteration of ocean crust. G*eochimica et Cosmochimica Acta* **63**, 1527–1535.

Andres, R.J. & Kasgnoc, A. D. (1998) A time-averaged inventory of sulphur emissions. *Journal of Geophysical Research* **103**, 25251–25261.

Andrews, J.E., Packham, G., Eade, J.V., Holdsworth, B.K., Jones, D.L., deVries Klein, G., Kroenke, L.W., Saito, T., Shafik, S., Stoeser, D.B. & van der Lingen, G.J. (1973). Site 286. The shipboard Scientific Party. In *Initial Reports of the Deep Sea Drilling Project* **30**, 69–89. U.S. Government Printing Office.

Annen, C., & Sparks, R. S. J. (2002). Effects of repetitive emplacement of basaltic intrusions on thermal evolution and melt generation in the crust. *Earth and Planetary Science Letters* **203**, 937-955.

Arai, S. & Takahashi, N. (1988). Relic plagioclase-bearing harzburgite from the Mineoka Belt, Boso Peninsula, Central Japan. *Journal of the Japanese Association of Mineralogy, Petrology and Economic Geology* (Ganseki Kobutsu Kosho Gakkai-Shi) **83**, 210–214.

Arculus, R.J. & Wills, K.J. (1980). The petrology of plutonic blocks and inclusions from the Lesser Antilles Arc. *Journal of Petrology* **21**, 743–799.

Atkin, J. (1868). On volcanoes in the New Hebrides and Banks's Islands. *Proceedings of the Geological Society of London* **24**, 305–307.

Baker, D.R. (2008). The fidelity of melt inclusions as records of melt composition *Contributions to Mineralogy and Petrology* **156**, 377–395.

Baker, P. E., Coltorti, M., Briqueu, L., Hasenaka, T., & Condliffe, E. (1994). Volcanic ash layers from sites 828, 830, 831, 832 and 833, New Hebrides Island Arc. In *Proceedings of the Ocean Drilling Program. Scientific results* 134, 403–412.

Baker, P.E. & Condliffe, E. (1996). Compositional variations in submarine volcanic ashes from the vicinity of the Vanuatu Island Arc: a response to ridge—arc collision? *Journal of Volcanology and Geothermal Research* **72**, 225–238.

Bani, P., Oppenheimer, C., Tsanev, V.I., Crimp, R., Cronin, S., Calkins, J., Charley, D., Lardy, M. (2009). Surge in sulphur and halogen degassing from Ambrym volcano, Vanuatu. *Bulletin of Volcanology* **10**, 1159–1168.

Bani, P., Oppenheimer, C., Allard, P., Shinohara, H., Tsanev, V., Carn, S. & Garaebiti, E. (2012). First estimate of volcanic SO_2 budget for Vanuatu island arc. *Journal of Volcanology and Geothermal Research* **211**, 36-46.

Bani, P., Vergniolle, S., Zielinski, C., Lardy, M., Le Pichon, A., Ponceau, D., Gallois, F., Herry, P., Todman, S., & Garaebiti, E. (2010). Probing the magma plumbing of Ambrym volcano, by a triangular acoustic network. *Geophysical Research Abstracts* **12**, EGU2010-6781, EGU General Assembly 2010.

Barclay, J. & Carmichael, I. S. E. (2004). A hornblende basalt from western Mexico: water-saturated phase relations constrain a pressure–temperature window of eruptibility. *Journal of Petrology* **45,** 485–506.

Bardintzeff, J.-M. (1984). Pyroxenes and their inclusions, good markers of nuee ardente eruptions, Saint Vincent, West Indies. *Bulletin of Mineralogy* **107**, 41–54.

Barsanti, M., Papale, P., Barbato, D., Moretti, R., Boschi, E., Hauri, E., & Longo, A. (2009). Heterogeneous large total CO_2 abundance in the shallow magmatic system of Kilauea volcano, Hawaii. *Journal of Geophysical Research: Solid Earth (1978–2012)*, **114(B12)**.

Beaglehole, J. C. (Ed.). (1961). The voyage of the Resolution and Adventure 1772–1775. Cambridge: Cambridge University Press.

Beccaluva, L., Macciotta, G., Savelli, C., Serri, G. & Zeda, O. (1980). Geochemistry and K/Ar ages of volcanics dredges in the Philippine Sea (Mariana, Yap, and Palau Trenches and Parece Vela Basin). The Tectonic and Geologic Evolution of Southeast Asian Seas and Islands (Hayes, D. E.), Agu, Washington DC. 247–268.

Behrens, H., Misiti, V., Freda, C., & Vetere, F. (2009). Solubility of H2O and CO2 in ultrapotassic melts at 1200 and 1250 C and pressure from 50 to 500 MPa. *American Mineralogist* **94**, 105–120.

Bellon, H., Marcelot, C., Lefèvre. C. & Maillet. P. (1984). Le volcanisme de l'île d'Erromango (Republique de Vanuatu): Calendrier de l'activité (données ^{40}K-^{40}Ar). *Comptes Rendus de l'Académie des Sciences Paris* **299** (II), 257–262.

Berndt, J., Koepke, J. & Holtz, F. (2005). An experimental investigation of the influence of water and oxygen fugacity on differentiation of MORB at 200 MPa. *Journal of Petrology* **46**, 135–167.

Berndt, J., Liebske, C., Holtz, F., Freise, M., Nowak, M., Ziegenbein, D., Hurkuck, W. & Koepke, J. (2002) A combined rapid-quench and H-2-membrane setup for internally heated pressure vessels: Description and application for water solubility in basaltic melts. *American Mineralogist* **87**, 1717–1726.

Bertagnini, A., Di Roberto, A., & Pompilio, M. (2011). Paroxysmal activity at Stromboli: lessons from the past. *Bulletin of Volcanology* **73**, 1229–1243.

Blot, C. (1981). Deep root of andesitic volcanoes: new evidence of magma generation at depth in the Benioff zone. *Journal of Volcanology and Geothermal Research* **10**, 339–364.

Blundy, J.D., Cashman, K., Rust, A. & Witham, F. (2010). A case for CO_2-rich arc magmas. *Earth and Planetary Science Letters* **290**, 289–301.

Bluth, G.J.S., Doiron, S.D., Schnetzler, C.C., Krueger, A.J. & Louis S. Walter, L.S. (1992). Global tracking of the SO_2 clouds from the June, 1991 Mount Pinatubo eruptions. *Geophysical Research Letters* **19**, 151–154.

Borisov, A.A. & Shapkin, A.I. (1990). A new empirical equation rating Fe^{3+}/Fe^{2+} in magmas to their composition, oxygen fugacity, and temperature. *Geochemistry International* **27**, 111–116.

Botcharnikov, R., Freise, M., Holtz, F. & Behrens, H. (2005). Solubility of C-O-H mixtures in natural melts: new experimental data and application range of recent models. *Annals of Geophysics* **48**, 633–646.

Briqueu, L., Laporte, C., Crawford, A.J., Hasenaka, T., Baker, P.E. & Coltorti, M. (1994). Temporal magmatic evolution of the Aoba Basin, central New Hebrides island arc; Pb, Sr, and Nd isotopic evidence for the coexistence of two mantle components beneath the arc. In: Greene, H.G., Collot, J.Y., Stokking, L.B. et al. (Eds.), Proceedings of the Ocean Drilling Program, Scientific Results, 134, College Station, TX, United States (USA), pp. 393–401.

Brooker, R. A., Kohn, S. C., Holloway, J. R., McMillan, P. F., & Carroll, M. R. (1999). Solubility, speciation and dissolution mechanisms for CO_2 in melts on the $NaAlO_2$–SiO_2 join. *Geochimica et Cosmochimica Acta* **63**, 3549–3565.

Brophy, J.G., Whittington, C.S. & Park, Y.-R. (1999). Sector-zoned augite megacrysts in Aleutian high alumina basalts: implications for the conditions of basalt crystallization

and the generation of calc-alkaline series magmas. *Contributions to Mineralogy and Petrology* **135**, 277–290.

Brown, G. M. (1956). The layered ultrabasic rocks of Rhum, Inner Hebrides. *Philosophical Transactions of the Royal Society B: Biological Sciences* **240**, 1–54.

Bryan, W.B. & Ewart, A. (1971). Petrology and geochemistry of volcanic rocks from Tonga. *Year Book of the Carnegie Institute of Washington* **69**, 249–258.

Burnham CW (1979). The importance of volatile constituents. In: Yoder HS (ed) The Evolution of Igneous Rocks. Princeton University Press, pp. 439–482.

Burton M., P. Allard, F. Murè & C. Oppenheimer (2003). FTIR remote sensing of fractional magma degassing at Mount Etna Sicily, pp. 281–294. In: Volcanic degassing, Geological Society of London Special Publications 213, eds., Oppenheimer, C., Pyle, D. and Barclay, J.

Burton, M.R., Mader, H.M. & Polacci, M. (2007). The role of gas percolation in quiescent degassing of persistently active basaltic volcanoes. *Earth and Planetary Science Letters* **264**, 46–60.

Burton, M. R., Oppenheimer, C., Horrocks, L. A., & Francis, P. W. (2000). Remote sensing of CO_2 and H_2O emission rates from Masaya volcano, Nicaragua. *Geology* **28**, 915-918.

Burton, M. R., Sawyer, G. M., & Granieri, D. (2013). Deep carbon emissions from volcanoes. *Reviews in Mineralogy and Geochemistry* **75**, 323–354.

Campion, R., Salerno, G. G., Coheur, P. F., Hurtmans, D., Clarisse, L., Kazahaya, K. & Bernard, A. (2010). Measuring volcanic degassing of SO_2 in the lower troposphere with ASTER band ratios. *Journal of Volcanology and Geothermal Research* **194**, 42-54.

Carmichael, I.S.E. (1967). The iron-titanium oxides of salic volcanic rocks and their associated ferromagnesian silicates. *Contributions to Mineralogy and Petrology* **14**, 36–64.

Carn, S.A. (2004). Eruptive and passive degassing of sulfur dioxide at Nyiragongo volcano (D.R. Congo): the 17 January 2002 eruption and its aftermath. *Acta Vulcanologica* **14–15**, 75–86.

Castle, N. & Herd, C.D.K. (2014). Observational and experimental results for Tissint magma formation; the story thus far. Abstract, 45th Lunar and Planetary Science Conference (2014).

Cawood, P.A. (1985). Petrography, phase chemistry and provenance of volcanogenic debris from the southern Tonga ridge: implications for arc history and magmatism. Geology and Offshore Resources of Pacific Island Arcs - Tonga Region (Scholl, D. W., Vallier, T. L.), Circum-Pacific Council For Energy And Mineral Resources, Houston, Texas, pp.149–169.

Cawthorne, R.G. & Collerson, K.D. (1974). The recalculation of pyroxene end-member parameters and the estimation of ferrous and ferric iron content from electron microprobe analyses. *American Mineralogist* **59**, 1203–1208.

Charley, D. (1988). Rapport de Mission à Ambrym en Aout 1988: Document ORSTOM, Port Vila, 5 pp.

Cheney, C.S. (1986). New volcanic eruption near Endu, SE Ambrym. *Geology Department Memo*, 24 November 1986, 1 p.

Cheney, C.S., (1988), Volcanic activity report, Ambrym and Epi. *Geology Department Memo*, 17 August 1988, 1 p.

Chester, D.K., Duncan, A.M., Guest, J.E. & Kilburn, C.R.J. (1985) Mount Etna: The anatomy of a volcano. California: Stanford University Press.

Chevychelov V. Yu, Botcharnikov, R.E. & Holtz, F. (2007). Solubility of Cl and F in basaltic melt and partitioning of Cl and F between the fluid and melt at T = 1200 ºC, P = 200 MPa and fO_2—NiNiO. *Herald of the Department of Earth Sciences RAS*, **1** (25).

Chevychelov, V. Y., Botcharnikov, R.E., & Holtz, F. (2008). Experimental study of chlorine and fluorine partitioning between fluid and subalkaline basaltic melt. *Doklady Earth Sciences* **422**, 1089–1092.

Clynne, M. (1999). A complex magma mixing origin for rocks erupted in 1915, Lassen Peak, California. *Journal of Petrology* **40**, 105–132.

Colley, H. & Hindle, W.H. (1984). Volcano-tectonic evolution of Fiji and adjoining marginal basins. *In* Kokelaar, B.P. & Howell, M.F. (eds) Marginal Basin Geology. *Geological Society of London, Special Publication* **16**, 151–162.

Collins, S. J., Pyle, D.M. & Maclennan, J. (2009). Melt inclusions track pre-eruption storage and dehydration of magmas at Etna. *Geology* **37.6**, 571-574.

Collot, J.-Y., Daniel, J. & Burne, R.V. (1985). Recent tectonics associated with the subduction/collision of the D'Entrecasteaux zone in the central New Hebrides. *Tectonophysics* **112**, 325–356.

Collot, J. Y., & Fisher, M. A. (1988). Crustal structure, from gravity data, of a collision zone in the central New Hebrides island arc. In: Greene H. G., Wong F. L., editors. Geology and Offshore Resources of Pacific Island Arcs-Vanuatu Region. Circum-Pacific Council for Energy and Mineral Resources Earth Science Series. Vol. 8. Houston, TX: Circum-Pacific Council for Energy and Mineral Resources; p125–139.

Collot, J.-Y. & Fisher, M.A. (1992). The D'Entrecasteaux Zone–New Hebrides island arc collision zone: an overview. In: Greene, H. G., Collot, J.-Y., Stokking, L. B. *et al* (eds) *Proceedings of the Ocean Drilling Program, Scientific Results* 134. College Station, TX: Ocean Drilling Program, pp. 19–31.

Cortés, J.A., Wilson, M., Condliffe, E. & Lorella Francalanci, L. (2006) The occurrence of forsterite and highly oxidizing conditions in basaltic lavas from Stromboli volcano, Italy. *Journal of Petrology* **47**, 1345–1373.

Costa, F., Scaillet, B. & Pichavant, M. (2004). Petrological and experimental constraints on the pre-eruption conditions of Holocene dacite from Volcán San Pedro (36° S, Chilean Andes) and the importance of sulfur in silicic subduction-related magmas". *Journal of Petrology* **45**, 855–881.

Couch, S., Harford, C. L., Sparks, R. S. J. & Carroll, M. R. (2001). Mineral disequilibrium in lavas explained by convective self-mixing in open magma chambers. *Nature* **411**, 1037–1039.

Couch, S., Sparks, R. S. J., & Carroll, M. R. (2003). The kinetics of degassing-induced crystallization at Soufriere Hills Volcano, Montserrat. *Journal of Petrology* **44**, 1477–1502.

Coudert, E., Cardwell, R. K., Isacks, B. L., & Chatelain, J. L. (1984). P-wave velocity of the uppermost mantle and crustal thickness in the central Vanuatu Islands (New Hebrides Island arc). *Bulletin of the Seismological Society of America* **74**, 913–924.

Coulon, C., Clocchiatti, R., Maury, R.C. & Westercamp, D. (1984). Petrology of basaltic xenoliths in andesitic to dacitic host lavas from Martinique (Lesser Antilles): evidence for magma mixing. *Bulletin of Volcanology* **47**, 705–734.

Coulon, C., Maillet, P. & Maury, R.C. (1979). Volcanism of the New Hebrides arc: petrology of Efate island lavas. *Bulletin of the Geological Society of France* **21**, 619–629.

Coulon, C. & Maury, R.C. (1981). Petrology of tholeiitic lavas from Tanna Island (New Hebrides): importance of cumulative processes in island arc magmatism. *Bulletin of Volcanology* **44**, 661–680.

Crawford A. J., Briqueu L., Laporte C. & Hasenaka T. (1995). Coexistence of Indian and Pacific oceanic upper mantle reservoirs beneath the central New Hebrides island arc. *In:* Taylor B. & Natland J. *(editors)*: Active Margins and Marginal Basins of the Western Pacific. *Geophysical Monograph, American Geophysical Union* **88**, 199–217.

Crimp, R., Cronin, S., Charley, D., Oppenheimer, C., & Bani, P. (2006). Dental fluorosis attributed to volcanic degassing on Ambrym, Vanuatu. Abstract: Cities on Volcanoes 4.

Cronin, S.J.S., & Sharp, D.S. (2002). Environmental impacts on health from continuous volcanic activity at Yasur (Tanna) and Ambrym, Vanuatu. *International Journal of Environmental Health Research* **12**, 109–123.

Danyushevsky, L.V. (2001). The effect of small amounts of H_2O on crystallization of mid-ocean ridge and backarc basin magmas. *Journal of Volcanology and Geothermal Research* **110**, 265–280

Danyushevsky, L. V., Carroll, M.R. & Falloon, T.J. (1997). Origin of high-An plagioclase in Tongan high-Ca boninites: implications for plagioclase-melt equilibria at low P(H_2O). *The Canadian Mineralogist* **35**, 313–326.

Danyushevsky, L.V., Leslie, R., Crawford, A.J. & Durance, P. (2004). Melt inclusions in primitive olivine phenocrysts: The role of localized reaction processes in the origin of anomalous compositions. *Journal of Petrology* **45**, 2531-2553.

Danyushevsky, L.V., McNeill, A.W. & Sobolev, A.V. (2002) Experimental and petrological studies of melt inclusions in phenocrysts from mantle-derived magmas: an overview of techniques, advantages and complications. *Chemical Geology* **183**, 5–24.

Danyushevsky, L. V. & Plechov, P. (2011). Petrolog3: Integrated software for modeling crystallization processes. *Geochemistry, Geophysics, Geosystems* **12(7)**.

Dasgupta, R. (2013). Ingassing, storage, and outgassing of terrestrial carbon through geologic time. *Reviews in Mineralogy and Geochemistry* **75**, 183-229.

Deegan, F., Troll, V.R., Freda, C., Misiti, V., Chadwick, J.P., McLeod, C. L. & Davidson, J.P. (2010). Magma-carbonate interaction processes and associated CO2 release at Merapi Volcano, Indonesia, insights from experimental petrology. *Journal of Petrology* **51**, 1027–1051.

Defant, M. J., & Nielsen, R. L. (1990). Interpretation of open system petrogenetic processes: phase equilibria constraints on magma evolution. *Geochimica et Cosmochimica Acta* **54**, 87–102.

Di Carlo, I., Pichavant, M., Rotolo, S.G. & Scaillet, B. (2006). Experimental crystallization of a high-K arc basalt: The golden pumice, Stromboli volcano (Italy). *Journal of Petrology* **47**, 1317–1343.

Dixon, T.H. & Batiza, R. (1979). Petrology And geochemistry of recent lavas in the Northern Marianas. *Contributions to Mineralogy and Petrology* **70**, 167–181.

Dixon, J.E., Stolper, E.M. & Holloway, J.R. (1995). An experimental study of water and carbon dioxide solubilities in mid ocean ridge basaltic liquids .1. Calibration and solubility models. *Journal of Petrology* **36**, 1607–1631.

Dixon, J.E. (1997). Degassing of alkalic basalts. *American Mineralogist* **82**, 368–378.

Donaldson, C.H. & Henderson, C.M.B. (1988). A new interpretation of round embayments in quartz crystals. *Mineralogical Magazine* **52**, 27-33.

Donaldson, C. H. (1985). The rates of dissolution of olivine, plagioclase, and quartz in a basalt melt. *Mineralogical Magazine*, *49*(354), 683-693.

Dubois, J., Deplus, C., Diament, M., Daniel, J., & Collot, J.Y. (1988). Subduction of the Bougainville seamount (Vanuatu): mechanical and geodynamic implications. *Tectonophysics* **149**, 111–119.

Edmonds, M., Sides, I. R., Swanson, D. A., Werner, C., Martin, R. S., Mather, T. A., Herd, R. A., Jones, R. L., Mead, M. I., Sawyer, G., Roberts, T. J., Sutton, A.J. & Elias, T. (2013). Magma storage, transport and degassing during the 2008-10 summit eruption at Kilauea Volcano, Hawaii. *Geochimica et Cosmochimica Acta* **123**, 284–301.

Eichelberger, J.C. (1974). Magma Contamination within the Volcanic Pile: Origin of Andesite and Dacite. *Geology* **2**, 29–33.

Eiler, J.M., Crawford, A.J., Elliott, T., Farley, K.A., Valley, J.W. & Stolper, E.M. (2000). Oxygen isotope geochemistry of oceanic-arc lavas. *Journal of Petrology* **41 (2)**, 229–256.

Eissen, J.P, Lardy, M., Monzier, M., Mollard, L. & Charley, D. (1989). ORSTOM (Nouméa and Port Vila) report. GVN report 10/1989 (SEAN 14:10).

Eissen, J. P., Lefevre, C., Maillet, P., Morvan, G., & Nohara, M. (1991). Petrology and geochemistry of the central North Fiji Basin spreading centre (Southwest Pacific) between 16º S and 22º S. *Marine Geology*, **98**, 201–239.

Elias, T. & Sutton, A. J. (2013). Sulfur dioxide emission rates from Kilauea Volcano, Hawaii, an Update: 1998-2001. BiblioGov.

Falloon, T.J., Danyushevsky, L.V., Crawford, T.J., Maas, R., Woodhead, J.D., Eggins, S.M., Bloomer, S.H., Wright, D.J., Zlobin, S.K. & Stacey, A.R. (2007). Multiple mantle plume components involved in the petrogenesis of subduction-related lavas from the northern termination of the Tonga arc and northern Lau Basin: evidence from the geochemistry of arc and backarc submarine volcanics. *Geochemistry Geophysics Geosystems* **8** (2007gc001619).

Falloon, T.J. & Green, D.H. (1988). Anhydrous partial melting of peridotite from 8 to 35 Kb and the petrogenesis of MORB. *Journal of Petrology, Special Lithosphere Issue*, 379–414.

Falloon, T.J., Hatton, C.J. & Harris, L. (1988). Anhydrous partial melting of a fertile and depleted peridotite from 2 to 30Kb and application to basalt petrogenesis. *Journal of Petrology* **29**, 1257–1282.

Falloon, T.J. & Danyushevsky, L.V. (2000). Melting of refractory mantle at 1.5, 2.0 and 2.5 GPa under H_2O-undersaturated conditions: implications for the petrogenesis of high-Ca

boninites and the influence of subduction components on mantle melting. *Journal of Petrology* **41**, 257–283.

Fichaut, M., Marcelot, G. & Clocchiatti, R. (1989). Magmatology of Mt. Pelée (Martinique, F.W.I.). II: Petrology of gabbroic and dioritic cumulates. *Journal of Volcanology and Geothermal Research* **38**, 171–187.

Fischer, T.P., Morrissey, M.M., Calvache, M.L., Gòmez, M.D., Torres, C.R., Stix, J. & Williams, S.N. (1994). Correlations between SO_2 flux and long-period seismicity at Galeras volcano. *Nature* **368**, 135–137.

France, L., Ildefonse, B., Koepke, J., & Bech, F. (2010). A new method to estimate the oxidation state of basaltic series from microprobe analyses. *Journal of Volcanology and Geothermal Research* **189**, 340–346.

Francis, P., Oppenheimer, C. & Stevenson, D. (1993). Endogenous growth of persistently active volcanoes. *Nature* **366**, 554–557.

Frenzel, G., Mühe, R.K. & Stoffers, P. (1990). Petrology of the volcanic rocks from the Lau Basin, Southwest Pacific. *Geol. Jb.* **D92**, 395–479.

Fretzdorff, S., Livermore, R.A., Devey, C.W., Leat, P.T. & Stoffers, P. (2002). Petrogenesis of the back-Arc East Scotia Ridge, South Atlantic Ocean ; *Journal of Petrology* **43**, 1435–1467.

Gerlach, T.M. (1980). Evaluation of volcanic gas analyses from Kilauea Volcano. *Journal of Volcanology and Geothermal Research* **7**, 295–317.

Gerlach, T.M. (1986). Exsolution of H_2O, CO_2 and S during eruptive episodes at Kilauea volcano, Hawaii. *Journal of Geophysical Research* **91 (B12)**, 12177–12185.

Gerlach, T.M. & McGee, K.A. (1994). Total sulfur dioxide emissions and pre-eruption vapor-saturated magma at Mount St. Helens, 1980-88. *Geophysical Research Letters* **21**, 2833-2836.

Gerlach, T.M., Westrich, H.R. & Symonds, R.B. (1996). Preeruption vapor in magma of the climactic Mount Pinatubo eruption: Source of the giant stratospheric sulfur dioxide cloud, in Newhall, C.G., and Punongbayan, R.S., eds., Fire and mud: Eruptions and lahars of Mount Pinatubo, Philippines: Seattle, University of Washington Press, p. 425–434.

Geshi, N., Shimano, T., Nagai, M. & Nakada, S. (2002). Magma Plumbing System Of The 2000 Eruption On Miyakejima Volcano, Japan ; *Bulletin of the Volcanological Society of Japan* **247**, 419–434.

Gill, J.B., Seales, C., Thompson, P., Hochstaedter, A.G. & Dunlap, C. (1992). Petrology and geochemistry of Pliocene-Pleistocene volcanic rocks from the Izu Arc, Leg 126. *Proceedings of the Ocean Drilling Program Scientific Results* **126**, 383–404.

Giordano, D., Russell, J.K., Dingwell, D.B. (2008). Viscosity of magmatic liquids: A model. *Earth and Planetary Science Letters* **271**, 123–134.

Global Volcanism Program, (2013). in: E. Venzke (Ed.), Volcanoes of the World v. 4.4.1, Smithsonian Institution (2013). http://dx.doi.org/10.5479/si.GVP.VOTW4-2013 (Downloaded 14 Nov 2015).

Goff, F., Love, S.P., Warren, R.G., Counce, D., Obenholzer, J., Siebe, C. & Schmidt, S.C. (2001). Passive infrared remote sensing evidence for large intermittent CO_2 emissions at Popocatepetl volcano, Mexico. *Chemical Geology* **177**, 133–156.

Gorton, M.P.(1977). The geochemistry and origin of Quaternary volcanism in the New Hebrides. *Geochimica et Cosmochimica Acta* **41**, 1257–1270.

Gourgaud, A., Fichaut, M. & Joron J.-L. (1989). Magmatology of Mt. Pelée, (Martinique, F.W.I.). I: Magma mixing and triggering of the 1902 and 1929 pelean nuées ardentes. *Journal of Volcanology and Geothermal Research* **38**, 143–169.

Greene, H.G., Macfarlane, A., Johnson, D.P. & Crawford, A.J. (1988). Structure and tectonics of the central New Hebrides arc. In: Greene, H.G. & Wong, F.L. (eds) Geology and offshore resources of Pacific island arcs—Vanuatu region. *Circum-Pacific Council for Energy and Mineral Resources Earth Science Series* **8**, 377–412.

Greene, H.G., Collot, J.-Y., Fisher, M.A. & Crawford, A.J. (1994). Neogene tectonic evolution of the New Hebrides island arc: a review incorporating ODP drilling results. In: Greene, H. G., Collot, J.-Y., Stokking, L. B. *et al* (eds) *Proceedings of the Ocean Drilling Program, Scientific Results* 134. College Station, TX: Ocean Drilling Program, pp. 19–46.

Gregory, J.W. (1917). The Ambrym eruptions of 1913–14. *Geological Magazine* **4**, 529–540.

Grove, T.L. & Kinzler, R.J. (1986). The petrogenesis of andesites. *Annual Review of Earth and Planetary Sciences* **14**, 417–454.

Gunnarsson, B., Marsh, B.D. & Taylor, H.P.J. (1998). Generation of Icelandic rhyolites: silicic lavas from the Torfajökull central volcano. *Journal of Volcanology and Geothermal Research* **83**, 1–45.

Hamuro, K. (1985). Petrology of the Higashi-Izu monogenetic volcano group. *Bulletin of the Earthquake Research Institute* **60**, 335–400.

Handley, H.K., Macpherson, C.G., Davidson, J.P., Berlo, K. & Lowry, D. (2007). Constraining fluid and sediment contributions to subduction-related magmatism in Indonesia: Ijen volcanic complex. *Journal of Petrology* **48**, 1155–1183.

Harris, A.J.L., Flynn, L.P., Rothery, D.A., Oppenheimer, C. & Sherman, S.B. (1999). Mass flux measurements at active lava lakes: implications for magma recycling, *Journal of Geophysical Research—Solid Earth* **104**, 7117–7136.

Hawkesworth, C.J., Turner, S.P., McDermott, F., Peate, D.W. & van Calsteren, P.W. (1997). U-Th isotopes in arc magmas: implications for element transfer from the subducted crust. *Science* **276**, 551–555.

Hawkins, J.W. Jr. & Allan, J.F. (1994). Petrologic evolution of Lau Basin Sites 834 through 839. *Proceedings of the Ocean Drilling Program, Scientific Results* **135**, 427–470.

Hawkins, J.W. Jr. & Melchior, J.T. (1985). Petrology of Mariana Trough and Lau Basin basalts. *Journal of Geophysical Research* **B90**, 11431–11468.

Hedenquist, J.W., & Lowenstern, J.B. (1994). The role of magmas in the formation of hydrothermal ore deposits. *Nature* **370**, 519–527.

Helz, R. T. (1973). Phase relations of basalts in their melting range at PH_2O=5 kb as a function of oxygen fugacity. Part I. Mafic phases. *Journal of Petrology* **14**, 249–302.

Herrmann, W. & Berry, R.F. (2002). MINSQ—a least squares spreadsheet method for calculating mineral proportions from whole rock major element analyses. *Geochemistry: Exploration, Environment, Analysis* **2**, 361–368.

Hirschmann, M. M., Ghiorso, M. S. Davis, F. A. Gordon, S. M. Mukherjee, S., T. L. Grove Krawczynski, M. Medard, E. & Till, C. B. (2008). Library of Experimental Phase

Relations (LEPR): A database and Web portal for experimental magmatic phase equilibria data. *Geochemistry, Geophysics, Geosystems Technical Brief* **9 (3)**, pp 15.

Holloway, J. R. & Burnham, C. W. (1972). Melting relations of basalt with equilibrium water pressure less than total pressure. *Journal of Petrology* **13**, 1–29.

Holloway, J. R., Pan, V., & Gudmundsson, G. (1992). High-pressure fluid-absent melting experiments in the presence of graphite: oxygen fugacity, ferric/ferrous ratio and dissolved CO_2. *European Journal of Mineralogy* **4**, 105–114.

Holtz, F., Sato, H., Lewis, J., Behrens, H. & Nakada, S. (2005), Unzen dacite; Experimental Petrology of the 1991–1995 Unzen Dacite, Japan. Part I: Phase Relations, Phase Composition and Pre-eruptive Conditions. *Journal of Petrology* **46**, 319–337.

Honma, H. (1997). Petrological characteristics of Opirarukaomappu plutonic complex in the southern Hidaka metamorphic belt, Hokkaido, Japan. *Memoirs of the Geological Society of Japan* **47**, 43–55.

Horrocks, L., Burton, M., Francis, P., & Oppenheimer, C. (1999). Stable gas plume composition measured by OP-FTIR spectroscopy at Masaya Volcano, Nicaragua, 1998–1999. *Geophysical Research Letters* **26**, 3497–3500.

Huebner, J. S. & Sato, M. (1970). The oxygen fugacity–temperature relationships of manganese oxide and nickel oxide buffers. *American Mineralogist* **55**, 934–952.

Humphreys, M.C.S., Kearns, S.L. & Blundy, J.D. (2006). SIMS investigation of electron-beam damage to hydrous, rhyolitic glasses: Implications for melt inclusion analysis. *American Mineralogist* **91**, 667–679.

Huppert H.E. & Sparks, R.S.J. (1980). The fluid dynamics of a basaltic magma chamber replenished by influx of hot, dense ultrabasic magma. *Contributions to Mineralogy and Petrology* **75**, 279–289.

Iacovino, K., Moore, G., Roggensack, K., Oppenheimer, C., & Kyle, P. (2013). H2O–CO2 solubility in mafic alkaline magma: applications to volatile sources and degassing behavior at Erebus volcano, Antarctica. *Contributions to Mineralogy and Petrology* **166**, 845–860.

Ibrahim, A.K., Pontoise, B., Latham, G., Larue, M., Chen, T., Isacks, B., Recy, J. & Louat R. (1980). Structure of the New Hebrides Arc-Trench System. *Journal of Geophysical Research: Solid Earth* **85**, 253–266.

Ikeda, Y., Katsui, Y., Nakagawa, M., Kawachi, S., Watanabe, T., Fujibayashi, N., Shibata, T. & Kagami, H. (1990). Petrology of the 1988-89 essential ejecta and associated glassy rocks of Tokachi-Dake volcano in central Hokkaido, Japan. *Bulletin of the Volcanological Society of Japan* **235**, 147–162.

Ikeda, Y. & Yuasa, M. (1989). Volcanism in nascent back-arc basins behind the Shichito Ridge and adjacent area in the Izu-Ogasawara arc, Northwest Pacific: evidence for mixing between E-type MORB and island arc magmas at the initiation of back-arc rifting. *Contributions to Mineralogy and Petrology* **101**, 377–393.

Irvine, T., & Baragar, W. (1971). A guide to the chemical classification of the common volcanic rocks. *Canadian Journal of Earth Sciences* **8**, 523–548.

Ishizuka, O., Geshi, N., Ito, J., Kawanabe, Y. & Tuzino, T. (2008). The magmatic plumbing of the submarine Hachijo NW volcanic chain, Hachijojima, Japan: long-distance magma transport? *Journal of Geophysical Research* **B113** (2007jb005325).

Jaques, A.L. & Green, D.H. (1980). Anhydrous melting of peridotite at 0–15 Kb pressure and the genesis of tholeiitic basalts. *Contributions to Mineralogy and Petrology* **73**, 287–310.

Jean-Baptiste, P., Allard, P., Bani, P. (2009). Highly variable helium isotope ratios in the Vanuatu volcanic arc. (Abs) *AGU Fall Meeting 2009 Abstracts.*

Jean-Baptiste, P., Allard, P., Fourré, E., Bani, P., Calabrese, S., Aiuppa, A., Gauthier, P.J., Parello, F., Pelletier, B. & Garaebiti, E. (2015). Spatial distribution of helium isotopes in volcanic gases and thermal waters along the Vanuatu (New Hebrides) volcanic arc. *Journal of Volcanology and Geothermal Research*. Advance online publication doi:10.1016/j.jvolgeores.2015.09.026.

Jendrzejewski, N., Trull, T. W., Pineau, F., & Javoy, M. (1997). Carbon solubility in Mid-Ocean Ridge basaltic melt at low pressures (250–1950 bar). *Chemical Geology* **138**, 81–92.

Jochum, K.P., Weis, U., Stoll, B., Kuzmin, D., Yang, Q., Raczek, I., Jacob, D.E., Stracke, A., Birbaum, K., Frick, D.A. & Günther, D. (2011). Determination of reference values for NIST SRM 610–617 glasses following ISO guidelines. *Geostandards and Geoanalytical Research* **35**, 397–429.

Johnston, F. K., Turchyn, A. V., & Edmonds, M. (2011). Decarbonation efficiency in subduction zones: Implications for warm Cretaceous climates. *Earth and Planetary Science Letters* **303**, 143–152.

Kazahaya, K., Shinohara, H. & Saito, G. (1994). Excessive degassing of Izu-Oshima volcano: Magma convection in a conduit. *Bulletin of Volcanology* **56**, 207–216.

Kazahaya, K., Shinohara, H., Uto, K., Odai, M., Nakahori, Y., Mori, H., Iino, H., Miyashita, M. & Hirabayashi, J. (2004). Gigantic SO_2 emission from Miyakejima volcano, Japan, caused by caldera collapse. *Geology* **32**, 425–428.

Kerrick, D.M. & Connolly, J.A.D (1998). Subduction of ophicarbonates and recycling of CO_2 and H_2O. *Geology* **26**, 375–378.

Komatsu, M. (1975). Recrystallization of the high alumina pyroxene peridotite of the Uenzaru area in Hidaka Province, Hokkaido, Japan. *Journal of the Geological Society of Japan* **81**, 11–28.

Kovalenko, V.I., Naumov, V.B., Tolstykh, M.L., Tsareva, G.M. & Kononkova, N.N. (2004). Composition and sources of magmas in Medvezhya Caldera (Itirup Island, Southern Kuriles) from a study of melt inclusions. *Geochemistry International* **42**, 393–413.

Koyaguchi, T. (1986). Evidence for two-stage mixing in magmatic inclusions and rhyolitic lava domes on Niijima Island, Japan. *Journal of Volcanology and Geothermal Research* **29**, 71–98.

Kress, V. C. & Carmichael, I. S. E. (1991). The compressibility of silicate liquids containing $Fe_2O_3$and the effect of composition, temperature, oxygen fugacity and pressure on their redox states. *Contributions to Mineralogy and Petrology***108**, 82–92.

Kroenke, L.W. (1984). Vanuatu and the Eastern Outer Solomon Islands: Formation of the New Hebrides and Vitiaz Arcs and Development of the North Fiji Basin. *In:* Cenozoic Tectonic Development of the southwest Pacific: UN ESCAP, CCOP/SOPAC Technical Bulletin **6**, 63–75.

Krueger, A.J. (1983). Sighting of El Chichón Sulfur Dioxide Clouds with the Nimbus 7 Total Ozone Mapping Spectrometer. *Science* **220**, 1377-1379.

Kushiro, L. & Walter, M.J. (1998). Mg-Fe partitioning between olivine and mafic-ultramafic melts. *Geophysical Research Letters* **25**, 2337-2340.

Landi, P., Métrich, N., Bertagnini, A., & Rosi, M. (2004). Dynamics of magma mixing and degassing recorded in plagioclase at Stromboli (Aeolian Archipelago, Italy). *Contributions to Mineralogy and Petrology* **147**, 213-227.

Lange, R. A., & Carmichael, I. S. (1996). The Aurora volcanic field, California-Nevada: oxygen fugacity constraints on the development of andesitic magma. *Contributions to Mineralogy and Petrology* **125**, 167–185.

Lardy, M. & Marty, B. (1990). Ambrym. Bulletin of the Global Volcanism Network 15 (11).

Lazko, E.E. & Gladkov, N.G. (1991) Ultramafic and gabbroid rocks of the Ipod Basin (Yap Fracture Zone, Philippine Sea). *International Geology Review* **33**, 704–725.

Le Bas, M.J., le Maitre, R.W., Streckeisen, A. & Zanettin, B. (1986). A chemical classification of volcanic rocks based on the total alkali-silica diagram. *Journal of Petrology* **27**, 745–750.

Legrand, D., Rouland, D., Frogneux, M., Carniel, R., Charley, D., Roult, G. & Robin, C. (2005). Interpretation of very long period tremors at Ambrym volcano, Vanuatu, as quasi-static displacement field related to two distinct magmatic sources. *Geophysical Research Letters* **32**, L06314.

Lesne, P., Kohn, S. C., Blundy, J., Witham, F., Botcharnikov, R. E., & Behrens, H. (2011a). Experimental simulation of closed-system degassing in the system basalt–H2O–CO2–S–Cl. *Journal of Petrology* **52**, 1737–1762.

Lesne, P., Scaillet, B., & Pichavant, M. (2015). The solubility of sulfur in hydrous basaltic melts. *Chemical Geology* **418**, 104–116.

Lesne, P., Scaillet, B., Pichavant, M., & Beny, J. M. (2011b). The carbon dioxide solubility in alkali basalts: an experimental study. *Contributions to Mineralogy and Petrology* **162**, 153–168.

Le Roux, P.J., Shirey, S.B., Hauri, E.H., Perfit, M.R. & Bender, J.F. (2006). The effects of variable sources, processes and contaminants on the composition of northern EPR MORB (8–10°N and 12–14°N): Evidence from volatiles (H_2O, CO_2, S) and halogens (F, Cl). *Earth and Planetary Science Letters* **251**, 209–231.

Lindsay, J. M. (Ed.). (2005). *Volcanic hazard atlas of the Lesser Antilles*. Seismic Research.

Lipman, P. W., & Mullineaux, D.R., eds. (1981). *The 1980 eruptions of Mount St. Helens, Washington*. No. 1250. US Dept. of the Interior, US Geological Survey,

Longhi, J., Fram, M.S., Auwera, J.V. & Montieth, J.N. (1993). Pressure effects, kinetics, and rheology of anorthositic and related magmas. *American Mineralogist* **78**, 1016-1030.

Louat, R., Pelletier, B. (1989). Seismotectonics and present-day relative plate motion in the New Hebrides arc-North Fiji basin region. *Tectonophysics* **167**, 41–55.

Lowenstern, J.B. (1994). Chlorine, fluid immiscibility, and degassing in peralkaline magmas from Pantelleria, Italy. *American Mineralogist* **79**, 353–369.

Luhr, J. F. (1990). Experimental phase relations of water- and sulfur-saturated arc magmas and the 1982 eruptions of El Chichón volcano. *Journal of Petrology* **31**, 1071–1114.

Lundgaard, K.L. & Tegner, C. (2004). Partitioning of ferric and ferrous iron between plagioclase and silicate melt. *Contributions to Mineralogy and Petrology* **147**, 470–483.

Luyendyk, B. P., Bryan, W. B. & Jezek, P. A. (1974). Shallow structure of the New Hebrides island arc. *Geological Society of America Bulletin* **85**, 1287–1300.

Macfarlane, A., Carney, J.N., Crawford, A.J. & Greene, H.G. (1988). Vanuatu—A review of the onshore geology. *In:* Greene, H.G. & Wong, F.L. (Eds) *Geology and offshore resources of Pacific island arcs—Vanuatu region*. Circum-Pacific Council for Energy and Mineral Resources Earth Science Series, Houston, Texas, 8, 45–91.

Maillet, P., Monzier, M., Eissen, J.-Ph., Louat, R. (1989). Geodynamics of an arc-ridge junction: the case of the New Hebrides Arc/North Fiji Basin. *Tectonophysics* **165**, 251–268.

Maillet, P., Monzier, M. & Lefevre, C. (1986). Petrology of Matthew and Hunter volcanoes, south New Hebrides island arc (Southwest Pacific). *Journal of Volcanology and Geothermal Research* **30**, 1–27.

Maillet, P., Ruellan, E., Gérard, M., Person, A., Bellon, H., Cotten, J., Joron, J.-L., Nakada, S. & Price, R.C. (1995). Tectonics, Magmatism, and Evolution of the New Hebrides Backarc Troughs (Southwest Pacific). *In:* Taylor, B. (Ed). *Backarc Basins: Tectonics and Magmatism*. Plenum Press, New York, 177–235.

Marcelot, G., Lefevre, C., Maillet, P. & Maury, R.C. (1979). Volcanism of the New Hebrides arc: characterization of the two magmatic series on Erromango island. *Bulletin of the Geological Society of France* **21**, 631–641.

Marcelot, G., Maury, R.C. & Lefevre, C. (1983). Mineralogy of Erromango lavas (New Hebrides): evidence of an early stage of fractionation in island arc basalts. *Lithos* **16**, 135–151.

Marlow, M.S., Johnson, L.E., Pearce, J.A., Fryer, P.B., Pickthorn, L.-B.G. & Murton, B.J. (1992). Pleistocene volcanic rocks in the Mariana forearc revealed by drilling at Site 781. *Proceedings of the Ocean Drilling Program, Scientific Results* **125**, 293–310.

Marsh, B. D. (2013). On some fundamentals of igneous petrology. *Contributions to Mineralogy and Petrology* **166**, 665-690.

Marsh, B., Teplow, W., Reagan, M. & Sims, K. (2008). Puna Dacite: Likely Temperature, Viscosity, Origin, Size, and Parent Body Nature. *American Geophysical Union, Fall Meeting 2008*, abstract #V23A-2130.

Marshall, P. (1914). The Recent Volcanic Eruptions on Ambrym Island. *Transactions and Proceedings of the Royal Society of New Zealand* **47**, 387–391.

Martini, M. (1984). On the behaviour of fluorine in volcanic processes. *Bulletin of Volcanology* **47**, 483–489.

Marziano G.I., Gaillard, F., Pichavant, M. (2008). Limestone assimilation by basaltic magmas: an experimental re-assessment and application to Italian volcanoes. *Contributions to Mineralogy and Petrology* **155**, 719–738.

Mason, D.R. (1987). Least-squares mixing program for Maclntosh. Glenside, Australia.

Mather, T.A., Pyle, D.M., Tsanev, V.I., McGonigle, A.J.S., Oppenheimer, C., Allen, A.G. (2006). A reassessment of current volcanic emissions from the Central American arc with specific examples from Nicaragua. *Journal of Volcanology and Geothermal Research* **149 (3–4)**, 297–311.

Mathez, E.A. & Webster, J.D. (2005). Partitioning behavior of chlorine and fluorine in the system apatite-silicate melt-fluid. *Geochimica et Cosmochimica Acta* **69**, 1275–1286.

McCall, G.J.H., LeMaitre, R.W., Malahoff, A., Robinson, G.P. & Stephenson, P.J. (1970). The Geology and Geophysics of the Ambrym Caldera, New Hebrides. *Bulletin of Volcanology* **34**, 681–696.

Meen. J.K. (1990). Elevation of potassium content of basaltic magma by fractional crystallization: the effect of pressure. *Contributions to Mineralogy and Petrology* **104**, 309–331.

Melchior, A.H. (1988). Rapport de mission de reconnaissance volcanologique a Ambrym (25–28 May 1988) et a Tanna (14 May 1988), Document ORSTOM, Nouméa, 10 pp.

Métrich, N., Allard, P., Aiuppa, A., Bani, P., Bertagnini, A., Shinohara, H. & Massare, D. (2011). Magma and volatile supply to post-collapse volcanism and block resurgence in Siwi Caldera (Tanna Island, Vanuatu Arc). *Journal of Petrology*, egr019.

Métrich, N. & Rutherford, M.J. (1992). Experimental study of chlorine in hydrous silicic melts. *Geochimica et Cosmochimica* Acta **56**, 607–616.

Métrich, N., Bertagnini, A., Landi, P.& Rosi, M. (2001). Crystallization driven by decompression and water loss at Stromboli volcano (Aeolian Islands, Italy). *Journal of Petrology* **42,** 1471–1490.

Métrich, N., Bertagnini, A., & Di Muro, A. (2010). Conditions of magma storage, degassing and ascent at Stromboli: new insights into the volcano plumbing system with inferences on the eruptive dynamics. *Journal of Petrology* **51(3)**, 603-626.

Michibayashi, K., Ohara, Y., Stern, R.J., Fryer, P.B., Kimura, J.-I., Tasaka, M., Harigane, Y. & Ishii, T. (2009). Peridotites from a ductile shear zone within back-arc lithospheric mantle, southern Mariana Trench: results of a Shinkai 6500 dive. *Geochemistry Geophysics Geosystems* **10** (2008gc002197).

Minster, J.B. & Jordan, T.H. (1978). Present-day plate motions. Journal of Geophysical Research 83, 5331–5354.

Mitchell, A.H.C., Warden, A.J., 1971. Geological evolution of the New Hebrides island arc. *Journal of the Geological Society of London* **127**, 50–529.

Mollard (1989). Telex no. 3193 NM, from ORSTOM Vila to ORSTOM Nouméa.

Mollo, S., Blundy, J.D., Iezzi, G., Scarlato, P. & Langone, A. (2013). The partitioning of trace elements between clinopyroxene and trachybasaltic melt during rapid cooling and crystal growth. *Contributions to Mineralogy and Petrology* **166**, 1633–1654.

Mollo, S., Del Gaudio, P., Ventura, G., Iezzi, G., & Scarlato, P. (2010). Dependence of clinopyroxene composition on cooling rate in basaltic magmas: implications for thermobarometry. *Lithos*, **118**, 302–312.

Monzier, M. & Douglas, C. (1989). Rapport de mission à Ambrym (Vanuatu) du 26 au 30 septembre 1989. *Rapports de missions, Sciences de la Terre, Geologie-Geophysique* **10**. ORSTOM, Nouméa, 26 pp.

Monzier, M. & Robin, C. (1996). Volcanic Hazard Map for Ambrym Island. ORSTOM, Port Vila, Vanuatu.

Monzier, M., Robin, C., Eissen, J.-P. & Picard, C. (1991). Découverte d'un large anneau de tufs basaltiques associé à la formation de la caldera d'Ambrym (Vanuatu, SW Pacifique). *Comptes Rendus de l'Académie des Sciences Paris* **313,** 1319–1326.

Moore, G. (2008). Interpreting H_2O and CO_2 contents in melt inclusions: constraints from solubility experiments and modeling. *Reviews in Mineralogy and Geochemistry* **69**, 333–361.

Morgan, G.B. & London, D. (2005). Effect of current density on the electron microprobe analysis of alkali aluminosilicate glasses. *American Mineralogist* **90**, 1131–1138.

Morishita, T. & Arai, S. (2001). Petrogenesis of corundum-bearing mafic rock in the Horoman peridotite complex, Japan. *Journal of Petrology* **42**, 1279–299.

Morishita, T. & Kodera, T. (1998). Finding of corundum-bearing gabbro boulder possibly derived from the Horoman peridotite complex, Hokkaido, Japan. *Journal of the Japanese Association of Mineralogy, Petrology and Economic Geology (Ganseki Kobutsu Kosho Gakkai-Shi)* **93**, 52–63.

Müntener, O., Kelemen, P.B. & Grove, T.L. (2001). The role of H2O during crystallization of primitive arc magmas under uppermost mantle conditions and genesis of igneous pyroxenites: an experimental study. *Contributions to Mineralogy and Petrology* 1**41**, 643–658.

Murphy, M.D., Sparks, R.S.J., Barclay, J., Carroll, M.R. & Brewer, T.S. (2000). Remobilisation of andesite magma by intrusion of mafic magma at the Soufrière Hills volcano, Montserrat, West Indies. *Journal of Petrology* **11**, 21–42.

Mysen, B.O., Virgo, D. & Kushiro, I. (1981). The structural role of aluminum in silicate melts—a Raman spectroscopic study at 1 atmosphere. *American Mineralogist* **66**, 678–701.

Nadeau, P.A. & Williams-Jones, G. (2009). Apparent downwind depletion of volcanic SO_2 flux—lessons from Masaya Volcano, Nicaragua. *Bulletin of Volcanology* **71**, 389–400.

Nelson, S.A. & Carmichael, I.S.E. (1979). Partial molar volumes of oxides component in silicate liquids. *Contributions to Mineralogy and Petrology* **71**, 117–124.

Nelson, S.T., & Montana, A. (1992). Sieve-textured plagioclase in volcanic rocks produced by rapid decompression. *American Mineralogist* **77**, 1242–1249.

Németh, K. & Cronin, S.J. (2007a). The enigmatic giant tuff cone and ignimbrites of Ambrym, Vanuatu: a more conventional story of mafic caldera formation. *Abstract Volume IUGG* **XXIV**, Perugia, Italy: #4653.

Németh, K. & Cronin, S.J. (2007b). Syn- and post-eruptive erosion, gully formation, and morphological evolution of a tephra ring in tropical climate erupted in 1913 in West Ambrym, Vanuatu. *Geomorphology* **86**, 115–130.

Newman, S. & Lowenstern, J.B. (2002). VolatileCalc: a silicate melt-H_2O-CO_2 solution model written in Visual Basic for Excel. *Computational Geoscience* **28**, 597–604.

Niida, K. (1984). Petrology of the Horoman ultramafic rocks in the Hidaka metamorphic belt, Hokkaido. *Journal of the Faculty of Science, Hokkaido University, Series 4, Geology and Mineralogy* **21**, 197–250.

O'Driscoll, B., Emeleus, C. H., Donaldson, C. H., & Daly, J. S. (2010). Cr-spinel seam petrogenesis in the Rum Layered Suite, NW Scotland: cumulate assimilation and in situ crystallization in a deforming crystal mush. *Journal of Petrology* **51**, 1171–1201.

Oppenheimer, C. & Francis, P. (1998). Implications of longeval lava lakes for geomorphological and plutonic processes at Erta 'Ale volcano, Afar. *Journal of Volcanology and Geothermal Research* **80**, 101–111.

Oppenheimer, C., McGonigle, A.J.S., Allard, P., Wooster, M.J. & Tsanev, V.I. (2004). Sulfur, heat and magma budget of Erta 'Ale lava lake, Ethiopia. *Geology* **32**, 509–512.

Pan, V., Holloway, J.R. & Hervig, R.L. (1991). The pressure and temperature dependence of carbon dioxide solubility in tholeiitic basalt melts. *Geochimica et Cosmochimica Acta* **55(6)**, 1587–1595.

Papale, P., Moretti, R. & Barbato, D. (2006). The compositional dependence of the saturation surface of H_2O+CO_2 fluids in silicate melts. *Chemical Geology* **229**, 78–95.

Parkinson, I.J., Arculus, R.J. & Eggins, S.M. (2003). Peridotite xenoliths from Grenada, Lesser Antilles island arc. *Contributions to Mineralogy and Petrology* **146**, 241–262.

Paterson, B.A. & Stephens, W.E. (1992). Kinetically-induced compositional zoning in titanite: implications for accessory-phase/melt partitioning of trace elements. *Contributions to Mineralogy and Petrology* **109**, 373–385.

Pawley, A. R., Holloway, J. R., & McMillan, P. F. (1992). The effect of oxygen fugacity on the solubility of carbon-oxygen fluids in basaltic melt. *Earth and Planetary Science Letters* **110**, 213-225.

Payne, C. E., & Peters, K. J. (2015). Geochemistry in prospectivity modelling: investigating gold mineralization in the Taupo Volcanic Zone, New Zealand. *Geochemistry: Exploration, Environment, Analysis* **15**, 193–204.

Pearce, J.A., Baker, P.E., Harvey, P.K. & Luff, I.W. (1995). Geochemical evidence for subduction fluxes, mantle melting and fractional crystallization beneath the South Sandwich island arc. *Journal of Petrology* **36**, 1073–1109.

Pearce, J.A., Kempton, P.D. & Gill, J.B. (2007). Hf-Nd evidence for the origin and distribution of mantle domains in the SW Pacific. *Earth and Planetary Science Letters* **260**, 98–114.

Peate, D. W., Pearce, J. A., Hawkesworth, C. J., Colley, H., Edwards, C. M. H. & Hirose, K. (1997). Geochemical variation in Vanuatu Arc lavas: the role of subducted material and a variable mantle wedge composition. *Journal of Petrology* **38**, 1331–1358.

Petterson, M.G., Neal, C.R., Mahoney, J.J., Kroenke, L.W., Saunders, A.D., Babbs, T.L., Duncan, R.A., Tolia, D. & McGrail, B. (1997). Structure and deformation of north and central Malaita, Solomon Islands: tectonic implications for the Ontong Java Plateau-Solomon arc collision, and for the fate of oceanic plateaus. *Tectonophysics* **283**, 1–33.

Picard, C., Monzier, M., Eissen, J.-P. & Robin, C. (1995). Concomitant evolution of tectonic environment and magma geochemistry, Ambrym volcano (Vanuatu, New Hebrides arc). *In* Smellie, J.L. (Ed): Volcanism Associated with Extension at Consuming Plate Margins, *Geological Society of London Special Publication* **81**, 135–154.

Pichavant, M., Di Carlo, I., Le Gac, Y., Rotolo, S.G. & Scaillet, B. (2009). Experimental constraints on the deep magma feeding system at Stromboli volcano, Italy. *Journal of Petrology* **50**, 601–624.

Pichavant, M., Di Carlo, I., Rotolo, S. G., Scaillet, B., Burgisser, A., Le Gall, N., & Martel, C. (2013). Generation of CO_2-rich melts during basalt magma ascent and degassing. *Contributions to Mineralogy and Petrology* **166**, 545–561.

Pichavant, M. & Macdonald, R. (2007). Crystallization of primitive basaltic magmas at crustal pressures and genesis of the calc-alkaline igneous suite: experimental evidence from St Vincent, Lesser Antilles arc. *Contributions to Mineralogy and Petrology* **154**, 535–558.

Pichavant, M., Martel, C., Bourdier, J. L. & Scaillet, B. (2002). Physical conditions, structure, and dynamics of a zoned magma chamber: Mount Pelée (Martinique, Lesser Antilles Arc). *Journal of Geophysical Research: Solid Earth (1978–2012)* **107(B5)**, ECV-1.

Pichavant, M., Mysen, B.O. & Macdonald, R. (2002). Source and H_2O content of high-MgO magmas in island arc setting: an experimental study of a primitive calc-alkaline basalt from St Vincent, Lesser Antilles arc. *Geochimica et Cosmochimica Acta* **66**, 2193–2209.

Pino, N.A., Moretti, R., Allard, P. & Boschi, E. (2011). Seismic precursors of a basaltic paroxysmal explosion track deep gas accumulation and slug upraise. *Journal of Geophysical Research Atmospheres* 116. DOI: 10.1029/2009JB000826.

Plechov, P., Blundy, J., Nekrylov, N., Melekhova, E., Shcherbakov, V., & Tikhonova, M. S. (2015). Petrology and volatile content of magmas erupted from Tolbachik Volcano, Kamchatka, 2012–13. *Journal of Volcanology and Geothermal Research* **307**, 182–199.

Polacci, M., Baker, D. R., La Rue, A., Mancini, L., & Allard, P. (2012). Degassing behaviour of vesiculated basaltic magmas: an example from Ambrym volcano, Vanuatu Arc. *Journal of Volcanology and Geothermal Research*, **233**, 55–64.

Purey-Cust, H.E. (1896). The Eruption of Ambrym Island, New Hebrides, S.W. Pacific, 1894. *Geographical Journal* **8**, 585–602.

Putirka, K. D. (2008) Thermometers and barometers for volcanic systems. *In*: Putirka, K. D. & Tepley, F. (Eds.), Minerals, Inclusions and Volcanic Processes, *Reviews in Mineralogy and Geochemistry* **69**, 61–120.

Putirka, K., Ryerson, F.J. & Mikaelian, H. (2003). New igneous thermobarometers for mafic and evolved lava compositions, based on clinopyroxene + liquid equilibria. *American Mineralogist* **88**, 1542–1554.

Reubi, O. & Blundy, J.D. (2008). Assimilation of plutonic roots, formation of high-K 'exotic' melt inclusions and genesis of andesitic magmas at Volcán de Colima, Mexico. *Journal of Petrology* **49**, 2221–2243.

Reubi, O. & Blundy, J.D. (2009) A dearth of intermediate melts at subduction zone volcanoes and the petrogenesis of arc andesites. *Nature* **461**, 1269–1273.

Roberge, J., Delgado-Granados, H. & Wallace, P.J. (2009). Mafic magma recharge supplies high CO_2 and SO_2 gas fluxes from Popocatépetl volcano, Mexico. *Geology* **37**, 107–110.

Robin, C., Eissen, J.-P. & Monzier, M. (1993). Giant tuff cone and 12-km-wide associated caldera at Ambrym Volcano (Vanuatu, New Hebrides Arc). *Journal of Volcanology and Geothermal Research* **55**, 225–238.

Robock, A. (2000). Volcanic eruptions and climate. *Reviews of Geophysics* **38(2)**, 191–219.

Rodrıguez, L.A., Watson, I.M., Rose, W.I., Branan, Y.K., Bluth, G.J.S., Chigna, G., Matı, O., Escobar, D., Carn, S.A., Fischer, T.P. (2004). SO_2 emissions to the atmosphere from active volcanoes in Guatemala and El Salvador, 1999–2002. *Journal of Volcanology and Geothermal Research* **138**, 325–344.

Roeder, P.L. & Emslie, R.F. (1970). Olivine-liquid equilibrium. *Contributions to Mineralogy and Petrology* **29**, 275–289.

Rose, W.I., & Durant, A.J. (2009). Fine ash content of explosive eruptions. *Journal of Volcanology and Geothermal Research* **186**, 32–39.

Rosi, M., Bertagnini A. & Landi, P. (2000). Onset of the persistent activity at Stromboli Volcano (Italy). *Bulletin of Volcanology* **62**, 294–300.

Roux, J., & Lefèvre, A. (1992). A fast-quench device for internally heated pressure vessels. *European Journal of Mineralogy* **4**, 279–281.

Rymer, H., de Vries, B. V. W., Stix, J., & Williams-Jones, G. (1998). Pit crater structure and processes governing persistent activity at Masaya Volcano, Nicaragua. *Bulletin of Volcanology* **59**, 345–355.

Sack R.O. & Ghiorso, M.S. (1989) Importance of considerations of mixing properties in establishing an internally consistent database: Thermochemistry of minerals in the system Mg_2SiO_4-Fe_2SiO_4-SiO_2. *Contributions to Mineralogy and Petrology* **102**, 41–68.

Sack R.O. & Ghiorso, M.S. (1991a) An internally consistent model for the thermodynamic properties of Fe-Mg-titanomagnetite-aluminate spinels. *Contributions to Mineralogy and Petrology* **106**, 474–505.

Sack R.O. & Ghiorso, M.S. (1991b) Chromian spinels as petrogenetic indicators: thermodynamics and petrological applications. *American Mineralogist* **76**, 827–847.

Sack R.O. & Ghiorso, M.S. (1994a) Thermodynamics of multicomponent pyroxenes: I. Formulation of a general model. *Contributions to Mineralogy and Petrology* **116**, 277–286.

Sack R.O. & Ghiorso, M.S. (1994b) Thermodynamics of multicomponent pyroxenes: II. Phase relations in the quadrilateral. *Contributions to Mineralogy and Petrology* **116**, 287–300.

Sack R.O. & Ghiorso, M.S. (1994c). Thermodynamics of multicomponent pyroxenes: III. Calibration of $Fe^{2+}(Mg)^{-1}$, $TiAl(MgSi)^{-1}$, $TiFe^{3+}(MgSi)^{-1}$, $AlFe^{3+}(MgSi)^{-1}$, $NaAl(CaMg)^{-1}$, $Al_2(MgSi)^{-1}$ and $Ca(Mg)^{-1}$ exchange reactions between pyroxenes and silicate melts. *Contributions to Mineralogy and Petrology* **118**, 271–296.

Sakuyama, M. (1981). Petrological study of the Myoko and Kurohime volcanoes, Japan: crystallization sequence and evidence for magma mixing. *Journal of Petrology* **22**, 553–583.

Saunders, A.D. & Tarney, J. (1979). The geochemistry of basalts from a back-arc spreading centre in the East Scotia Sea. *Geochimica et Cosmochimica Acta* **43**, 555–572.

Sawyer, G. M., Carn, S. A., Tsanev, V. I., Oppenheimer, C., & Burton, M. (2008). Investigation into magma degassing at Nyiragongo volcano, Democratic Republic of the Congo. *Geochemistry, Geophysics, Geosystems* **9(2)**.

Scaillet, B., & Evans, B. W. (1999). The 15 June 1991 eruption of Mount Pinatubo. I. Phase equilibria and pre-eruption P–T–fO_2–fH_2O conditions of the dacite magma. *Journal of Petrology* **40**, 381–411.

Scaillet, B. & Pichavant, M. (2005). A model of sulphur solubility for hydrous mafic melts: application to the determination of magmatic fluid compositions of Italian volcanoes. *Annals of Geophysics* **48**, 671–698.

Scordilis, E.M. (2006). Empirical global relations converting M_S and m_b to moment magnitude. *Journal of Seismology* **10**, 225–236.

Sen, G., Hickey-Vargas, R., Waggoner, D.G. & Maurrasse, F. (1988). Geochemistry of basalts from the Dumisseau Formation, Southern Haiti: implications for the origin of the Caribbean Sea crust. *Earth and Planetary Science Letters* **87**, 423–437.

Shinohara, H., Iiyama, J. T., & Matsuo, S. (1989). Partition of chlorine compounds between silicate melt and hydrothermal solutions: I. Partition of NaCl-KCl. *Geochimica et Cosmochimica Acta* **53**, 2617–2630.

Shinohara, H., Keiichi Fukui, K., Kazahaya, K. & Saito, G. (2003). Degassing process of Miyakejima volcano: implications of gas emission rate and melt inclusion data. Developments in Volcanology 5: Melt Inclusions in Volcanic Systems—Methods, Applications and Problems, 147–161.

Shiotani, Y. & Niida, K. (1997). Origin of mafic layers in the Horoman peridotite complex. *Memoirs of the Geological Society of Japan* **47**, 123–137.

Shiraki, K., Ito, J., Nitta A., Miyamoto, M., Kono, M. & Urano, H. (2000). Basalts, high-Mg andesites and diorites in the Palau Islands, Micronesia. *Journal of Geography* **109**, 774–783.

Shishkina, T. A., Botcharnikov, R. E., Holtz, F., Almeev, R. R., Jazwa, A. M., & Jakubiak, A. A. (2014). Compositional and pressure effects on the solubility of H_2O and CO_2 in mafic melts. *Chemical Geology* **388**, 112–129.

Shishkina, T. A., Botcharnikov, R. E., Holtz, F., Almeev, R. R., & Portnyagin, M. V. (2010). Solubility of H_2O-and CO_2-bearing fluids in tholeiitic basalts at pressures up to 500MPa. *Chemical Geology* **277**, 115–125.

Shore, M. & Fowler, A.D. (1996). Oscillatory zoning in minerals: a common phenomenon. *The Canadian Mineralogist* **34**, 1111–l126.

Sides, I., Edmonds, M., Maclennan, J., Houghton, B. F., Swanson, D. A. & Steele-MacInnis, M. J. (2014). Magma mixing and high fountaining during the 1959 Kīlauea Iki eruption, Hawai‘i. *Earth and Planetary Science Letters* **400**, 102-112.

Sims, K.W.W., Goldstein, S.J., Blichert-Toft, J., Perfit, M.R., Kelemen, P., Fornari, D.J., Michael, P., Murrell, M.T., Hart, S.R., DePaolo, D.J., Layne, G., Ball, L., Jull, M. & Bender, J. (2002). Chemical and isotopic constraints on the generation and transport of magma beneath the East Pacific Rise. *Geochimica et Cosmochimica Acta* **66**, 3481–3504.

Signorelli, S. & Carroll, M. (2001). Chlorine solubility in peraluminous rhyolites from Soufrière hills volcano, Montserrat: implications for magmatic degassing. *Bulletin of Volcanology* **62**, 431–440.

Sigurdsson, H. & Shepherd, J. B. (1974). Amphibole-bearing basalts from the submarine volcano Kick 'em Jenny in the Lesser Antilles Island Arc. *Bulletin of Volcanology* **38**, 891–910.

Sisson, T.W. & Grove, T.L. (1993). Experimental investigations of the role of water in calc-alkaline differentiation and subduction zone magmatism. *Contributions to Mineralogy and Petrology* **113**, 143–166.

Sisson, T. W., & Bronto, S. (1998). Evidence for pressure-release melting beneath magmatic arcs from basalt at Galunggung, Indonesia. *Nature* **391**, 883–886.

Smith, A.L. & Roobol, M.J. (1990). Mt. Pelée, Martinique: a study of an active island-arc volcano. Memoirs of the Geological Society of America **175**, 1–105.

Smith, I. E., Worthington, T. J., Price, R. C., Stewart, R. B. & Maas, R. (2006). Petrogenesis of dacite in an oceanic subduction environment: Raoul Island, Kermadec arc. *Journal of Volcanology and Geothermal Research* **156**, 252–265.

Sorbadere, F., Schiano, P., Métrich, N. & Garaebiti, E. (2011). Insights into the origin of primitive silica-undersaturated arc magmas of Aoba volcano (Vanuatu Arc). *Contributions to Mineralogy and Petrology* **162**, 995-1009.

Spilliaert, N., Allard, P., Métrich, N. & Sobolev, A. V. (2006). Melt inclusion record of the conditions of ascent, degassing, and extrusion of volatile-rich alkali basalt during the powerful 2002 flank eruption of Mount Etna (Italy). *Journal of Geophysical Research* **111**, B04203, doi:10.1029/2005JB003934.

Stelling, J., Botcharnikov, R. E., Beermann O. & Nowak, M. (2008). Solubility of H_2O-and chlorine-bearing fluids in basaltic melt of Mount Etna at T=1050–1250 °C and P=200 MPa. *Chemical Geology* **256**, 102–110.

Stephenson, P.J., McCall, G.J.H., Le Maitre, R.W. & Robinson G.P. (1966) The Ambrym Island Research Project. New Hebrides Geological Survey Annual Report, 1966 (ed. Warden).

Stern, R.J. (1979). On the origin of andesite in the Northern Mariana Island Arc: implications from Agrigan. *Contributions to Mineralogy and Petrology* **68**, 207–219.

Stevenson, D.S. & Blake, S. (1998). Modelling the dynamics and thermodynamics of volcanic degassing. *Bulletin of Volcanology* **60**, 307–317.

Stimac, J. A., & Pearce, T. H. (1992). Textural evidence of mafic-felsic magma interaction in dacite lavas, Clear Lake, California. *American Mineralogist* **77**, 795–809.

Stix, J. (2007). Stability and instability of quiescently active volcanoes: The case of Masaya, Nicaragua. *Geology* **35**, 535–538.

Stoeser, D.B. (1975). Igneous rocks from Leg 30 of the Deep Sea Drilling Project. In Andrews, J.E., Packham, G., et al., *Initial Reports of the Deep Sea Drilling Project* **30**. Washington (U.S. Government Printing Office), 401–414.

Stolper, E., & Holloway, J. R. (1988). Experimental determination of the solubility of carbon dioxide in molten basalt at low pressure. *Earth and Planetary Science Letters* **87**, 397–408.

Stormer, J. C., & Nicholls, J. (1978). XLFRAC: a program for the interactive testing of magmatic differentiation models. *Computers & Geosciences* **4**, 143–159.

Sugawara M., Yamahana I., Okamura S., Nishido H. (1995). Miocene volcanism and primitive basalt from the Shimokawa district, North Hokkaido, Japan: constraints on Miocene tectonics from petrogenesis of primary magma. *Memoirs of the Geological Society of Japan* **44**, 23–37.

Sun, S.-S. & McDonough, W.F. (1989). Chemical and isotopic systematics of oceanic basalts: implications for mantle composition and processes. *Geological Society, London, Special Publications* **42**, 313–345.

Syracuse, E.M, van Keken, P.E. & Abers, G.A. (2010). The global range of subduction zone thermal models. *Physics of the Earth and Planetary Interiors* **183**, 73–90.

Takahashi, N. (1991). Evolutional history of the uppermost mantle of an arc system: petrology of the Horoman peridotite massif, Japan. In *Ophiolite genesis and evolution of the oceanic lithosphere: proceedings of the Ophiolite Conference, held in Muscat, Oman, 7-18 January 1990* (Vol. 5, p. 195). Kluwer Academic Print on Demand.

Takahashi, N. (2001). Origin of plagioclase lherzolite from the Nikanbetsu Peridotite Complex, Hokkaido, Northern Japan: implications for incipient melt migration and segregation in the partially molten upper mantle. *Journal of Petrology* **42**, 39–54.

Takahashi, N. & Arai S. (1989). Textural and chemical features of chromian spinel-pyroxene symplectites in the Horoman Peridotites, Hokkaido, Japan. *Scientific Reports of the Institute of Geosciences, University of Tsukuba* **B10**, 45–55.

Takazawa, E., Frey, F.A., Shimizu, N. & Obata, M. (1996). Evolution of the Horoman peridotite (Hokkaido, Japan): implications from pyroxene compositions. *Chemical Geology* **134**, 3–26.

Tamura Y. (1994). Genesis of island arc magmas by mantle-derived bimodal magmatism: evidence from the Shirahama Group, Japan. *Journal of Petrology* **35**, 619–645.

Tamura, Y., Tani, K., Chang, Q., Shukuno, H., Kawabata, H., Ishizuka, O. & Fiske, R.S. (2007). Wet and dry basalt magma evolution at Torishima volcano, Izu-Bonin Arc, Japan: the possible role of phengite in the downgoing slab. *Journal of Petrology* **48**, 1999–2031.

Taylor, F.W., Bevis, M.G., Schultz, B.E., Kuang, D., Recy, J., Calmant, S., Charley, D., Regnier, M., Perin, B., Jackson, M. & Reichenfeld, C. (1995). Geodetic measurements of convergence at the New Hebrides island arc indicate arc fragmentation caused by an impinging aseismic ridge. *Geology* **23**, 1011–1014.

Taylor, F.W., Jouannic, C. & Bloom, L. (1985). Quaternary uplift of the Torres Islands, northern New Hebrides frontal arc: comparison with Santo and Malekula islands, central New Hebrides frontal arc. *Journal of Geology* **93**, 419–438.

Tazieff, H. (1977). An exceptional eruption: Mt. Nyiragongo, January 10th, 1977. *Bulletin of Volcanology* **40**, 189–200.

Thornber, C.R. & Huebner, J.S. (1985). Dissolution of olivine in basaltic liquids: experimental observations and applications. *American Mineralogist* **70**, 934–945.

Toplis, M.J. (2005). The thermodynamics of iron and magnesium partitioning between olivine and liquid: criteria for assessing and predicting equilibrium in natural and experimental systems. *Contributions to Mineralogy and Petrology* **149**, 22–39.

Toplis, M. J., & Carroll, M. R. (1995). An experimental study of the influence of oxygen fugacity on Fe-Ti oxide stability, phase relations, and mineral—melt equilibria in ferro-basaltic systems. *Journal of Petrology* **36**, 1137-1170.

Tsuya, H. (1955). Geological and petrological studies of volcano, Fuji, V. 5. On the 1707 eruption of volcano Fuji. *Bulletin of the Earthquake Research Institute* **33**, 341–383.

Turner, S.P., Peate, D.W., Hawkesworth, C.J., Eggins, S.M., & Crawford, A.J. (1999). Two mantle domains and the time scales of fluid transfer beneath the Vanuatu arc. *Geology*, **27**, 963–966.

Vance, J.A. (1965) Zoning in igneous plagioclase: patchy zoning. *Journal of Geology* **73**, 636–651.

Van Der Laan, S.R., Arculus, R.J., Pearce, J.A., Murton, B.J. (1992). Petrography, mineral chemistry and phase relations of the basement boninite series of site 786, izu-bonin forearc. *Proceedings of the Ocean Drilling Program, Scientific Results* **125**, 171–201.

Vergniolle, S., Zielinski, C., Bani, P., Lardy, M., Le Pichon, A., Ponceau, D., Millier, P., Gallois, F., Herry, P., Todman, S. & Garaebiti, E. (2013). Listening to Ambrym volcano

(Vanuatu), by a triangular acoustic network: a precursor to a Strombolian episode [abstract]. In: *Proceedings of the International Association of Volcanology and Chemistry of the Earth's Interior (IAVCEI) General Assembly*, Kagoshima, Japan, abstract 3A1_2A-O7, p. 246.

Verhoogen, J. (1948). Les eruptions 1938–1940 du Volcan Nyamuragira. *Exploration du Parc National Albert: Inst. Parcs Nat. du Congo Belge*, Fasc. 1, 186 pp.

Vetch, P. & Haefali, S. (1997). August visit reveals lava fountains, Strombolian explosions 11/1997 (BGVN 22:11).

Vetere, F., Holtz, F., Behrens, H., Botcharnikov, R. E., & Fanara, S. (2014). The effect of alkalis and polymerization on the solubility of H_2O and CO_2 in alkali-rich silicate melts. *Contributions to Mineralogy and Petrology* **167**, 1–17.

Viccaro, M., Calcagno, R., Garozzo, I., M. & Nicotra, E. (2015). Continuous magma recharge at Mt. Etna during the 2011–2013 period controls the style of volcanic activity and compositions of erupted lavas. *Mineralogy and Petrology* **109**, 67–83.

Volynets, O.N., Avdeiko, G. P., Tsvetkov, A.A., Ananev, V.V., Antonov, A.Yu., Gladkov, N.G. & Markov, I.A. (1990). Ultrabasic inclusions in Quaternary lavas of the Kurile island arc. *Transactions of the Academy of Sciences of the USSR, Geological Series* **3**, 43–57.

Wallace, P. J. (2005). Volatiles in subduction zone magmas: concentrations and fluxes based on melt inclusion and volcanic gas data. *Journal of Volcanology and Geothermal Research* **140**, 217–240.

Wallace, L.M., McCaffrey, R., Beavan, J. & Ellis, S. (2005) Rapid microplate rotations and backarc rifting at the transition between collision and subduction. *Geology* 33 (11), 857–860.

Watson, E.B. & Liang, Y. (1995). A simple model for sector zoning in slowly grown crystals: implications for growth rate and lattice diffusion, with emphasis on accessory minerals in crustal rocks. *American Mineralogist* **80**, 1179–1187.

Webster, J.D. (1997). Chloride solubility in felsic melts and the role of chloride in magmatic degassing. *Journal of Petrology* **38**, 1793–1807.

Webster, J.D., Kinzler, R.J., and Mathez, E.A. (1999). Chloride and water solubility in basalt and andesite liquids and implications for magmatic degassing. *Geochimica et Cosmochimica Acta* **63**, 729–738.

Webster, J.D. & Rebbert, C.R. (1998). Experimental investigation of H_2O and Cl^- solubilities in F-enriched silicate liquids; implications for volatile saturation of topaz rhyolite magmas. *Contributions to Mineralogy and Petrology* **132**, 198–207.

Wiart, P., 1995. Impact et gestion des risques volcaniques au Vanuatu. *Notes Techniques, Sciences de la Terre, Géologie-géophysique* **13**. ORSTOM, Vanuatu, 80 pp.

Wilson, M. (1989). Igneous Petrogenesis: A Global Tectonic Approach. 466 pp. London: Unwin Hyman.

Witham, C.S. (2005). Volcanic disasters and incidents: a new database. *Journal of Volcanology and Geothermal Research* **148**, 191–233.

Wood, B. J. (1991). Oxygen barometry of spinel peridotites. In: Oxide minerals: Petrologic and magnetic significance, edited by Lindsley D. H. Washington D.C.: Mineralogical Society of America. pp. 417–431.

Woodhead, J. D. (1988). The origin of geochemical variation in Mariana lavas: a general model for petrogenesis in intra-oceanic arcs. *Journal of Petrology* **29**, 805–830.

Wright, T.L. & Fiske, R.S. (1971). Origin of the differentiated and hybrid lavas of Kilauea volcano, Hawaii. *Journal of Petrology* **12**, 1–65.

Wright, R. & Pilger, E. (2008). Radiant flux from Earth's subaerially erupting volcanoes. *International Journal of Remote Sensing* **29**, 6443–6466.

Wyllie, P. J. & Tuttle, O. F. (1964). Experimental investigation of silicate systems containing two volatile components, Part III. The effects of SO_3, P_2O_5, HCl, and Li_2O, in addition to H_2O, on the melting temperatures of albite and granite. *American Journal of Science* **262**, 930–939.

Wyllie, P.J. (1979). Magmas and volatile components. *American Mineralogist* **64**, 469–500.

Young, S.R., Sparks, R.S.J., Aspinall, W.P., Lynch, L.L. & Miller, A.D. (1998). Overview of the eruption of Soufriere Hills volcano, Montserrat, 18 July 1995 to December 1997. *Geophysical Research Letters* **25**, 3389–3392.

Appendices

Index of appendices

APPENDIX A: Major characteristics and eruptive history of the volcanoes of Vanuatu

APPENDIX B: Descriptions of activity associated with eruption of samples

APPENDIX C: Basaltic scoria Mineral analyses:

APPENDIX D: Basaltic lava flow (AMB2) mineral analyses

APPENDIX E: Trachybasaltic flank lava flow (AMB10) mineral analyses

APPENDIX F: Trachyandesite mineral analyses

APPENDIX G: Melt inclusion and matrix glass analyses

APPENDIX H: alkali adjustment of $K_D^{Fe\text{-}Mg}$ for olivine

Appendix A: Summary of the major characteristics and eruptive history of the volcanoes of Vanuatu

	Volcano type	Most recent activity	Notable features
HISTORICAL			
Yasur	Stratovolcano	2010 (ongoing)	Quasi-continuous Strombolian and Vulcanian activity since first observed (ash eruptions) in 1774. A 361 m high pyroclastic cone with a subcircular, 400-m-wide summit crater containing several vents from which jets of ash and lava issue at intervals. Yasur sits mainly inside a small caldera (Yenkahe) and is the most recent of a series of volcanic centres built atop the down-faulted remains of a Pleistocene volcano. The small caldera sits within a larger (4-km diameter) caldera associated with eruption of andesitic pyroclastics. Active tectonism along the Yenkahe caldera margin has raised the adjacent coastal area by >20 m over the past 100 years.
Ambrym	Pyroclastic shield	2010 (ongoing)	Large basaltic volcano, 12-km-wide caldera. Thick, almost exclusively pyroclastic sequence, initially dacitic, then basaltic, overlies lava flows of a pre-caldera shield volcano. The caldera was formed either during a major Plinian eruption with dacitic pyroclastic flows, or by quiet subsidence with drainage via flank fissures and eruption of mafic lapilli, c. 1900 years ago. A series of scoria cones and maars occur along a fissure system oriented ESE-WNW. Eruptions have apparently occurred almost yearly during historical time from cones within the caldera or from flank vents. However, from 1850 to 1950, reporting was mostly limited to extra-caldera eruptions that would have affected local populations.
Gaua	Stratovolcano	2010	Basaltic-to-andesitic, 6 × 9 km summit caldera. Small parasitic vents near the caldera rim fed Pleistocene lava flows reaching the coast; littoral cones formed where reached the sea. Quiet collapse that formed the roughly 700-m-deep caldera was followed by extensive ash eruptions. Historically active cone Garat within crescent-shaped intracaldera crater lake, other small cinder cones in SW part of the caldera. Garat cone is topped by three pit craters. Activity at Garat in 1962 ended long period of dormancy.
Lopevi	Stratovolcano	2007	Basaltic to andesitic. A 7-km diameter conical island, 1413-m high, one of Vanuatu's most active volcanoes. A small summit crater containing a cinder cone, breached to the NW, atop an older cone rimmed by the remnant of a larger crater. Active during historical time at both summit and flank vents, primarily along a NW-SE-trending fissure that cuts across the island, producing moderate explosive eruptions and lava flows that reached the coast. Historical eruptions date back to the mid-19th century. The island was evacuated following major eruptions in 1939 and 1960. The 1960eruption, from a NW-flank fissure vent, produced a pyroclastic flow that swept to the sea and a lava flow that formed a new peninsula on the western coast.
Aoba	Shield volcano	2006	2500 km^3 basaltic shield, the biggest volcano in chain, elongate along a NE-SW rift zone dotted with scoria cones. Topped by a broad pyroclastic cone containing three crater lakes within the youngest of at least two nested calderas, the largest of which is 6 km in diameter. Post-caldera explosive eruptions formed the summit craters of Lake Voui and Lake Manaro Ngoru c. 360 years ago. A tuff cone was constructed within lake Voui c. 60 years later. The latest known flank eruption, c. 300 years ago, destroyed the population of the Nduindui area near the western coast.
Epi	Stratovolcanos	2004	A large caldera, with submarine post-caldera cones active in historical time, lies off the eastern coast of Epi Island. Epi Island largely consists of two Quaternary volcanoes, one related to the submarine Kuwae caldera to the east. This volcano has three well-preserved subsidiary cones to the east with youthful summit craters. Pomare volcano is truncated on its eastern side by the largely submarine East Epi caldera, which has been the source of all historical eruptions. Three small submarine basaltic and dacitic cones, known as Epi A, Epi B, and Epi C, are located along the northern rim of the breached caldera. Ephemeral islands were formed during eruptions in 1920 and 1953, and the summit of the shallowest cone, Epi B, was at 34 m below sea level at the time of a 2001 survey.

Table A.1 Characteristics and eruptive history of Vanuatu volcanoes, in order of most recent activity. Abridged from Global Volcanism Program summaries.

Kuwae	Caldera	1974	The largely submarine Kuwae caldera lies between Epi and Tongoa islands. The 6 x 12 km caldera contains two basins that cut the NW end of Tongoa Island and the flank of the late-Pleistocene or Holocene Tavani Ruru volcano on the SE tip of Epi Island. Native legends and radiocarbon dates from pyroclastic-flow deposits have been correlated with a 1452 AD ice-core peak thought to be associated with collapse of Kuwae caldera; but there is some controversy on these points. The submarine volcano Karua lies near the northern rim of Kuwae caldera and is one of the most active volcanoes of Vanuatu. It has formed several ephemeral islands since it was first observed in eruption during 1897.
Suretamatai	Complex volcano	1966	Dominantly basaltic-to-andesitic, younger lavas overlying a number of small, older stratovolcanoes. No summit caldera. Chain of NNE-SSW small stratovolcanoes. Youngest and largest near the northern end, contains a crater lake. Historically moderate explosive eruptions.
Traitor's Head	Stratovolcano	1881	Three Holocene volcanic cones on Erromango, the youngest on that island. Small, well-preserved basaltic-to-andesitic stratovolcanoes. The largest rises to 837 m, and the most youthful looking has an unbreached crater. A low plateau to the NW is underlain by ash deposits distributed by southeasterly trade winds. The volcanoes initially formed an offshore island that was joined to the mainland by uplift after volcanism ceased. A submarine vent offshore between the tip of the peninsula and Goat Island, 5 km to the NE, erupted in 1881, the only historical activity of the Erromango volcanoes.
HOLOCENE			
Motlav	Stratovolcano	Unknown	At least five Pleistocene basaltic stratovolcanoes capped by two well-preserved late-Pleistocene to Holocene pyroclastic cones. One is a largely pyroclastic composite cone with a 500-m-wide summit crater; the other is a pyroclastic cone truncated by a summit crater that is breached on the southern side.
Mere Lava	Stratovolcano		The small 4-km-wide symmetrical island of basaltic Mera Lava contains a well-preserved summit crater and an east-west line of young cinder cones cutting across the NE flank. Several small cinder cones occupy the triangular summit crater of 1028-m-high Star Peak, the high point of the island. The low degree of dissection indicates that Mera Lava was in eruption during the Holocene. Mere Lava was reported to have been smoking when it was first seen by the explorer Queiros in 1606.
North Vate	Stratovolcanos	Unknown	Late-Pleistocene to Holocene composite basaltic cones with well-preserved craters. Largely submarine calderas north of Vate Island of varying sizes have been inferred, ranging from a large caldera whose southern rim is defined by the islands of Nguna, Pele, and Emao to a smaller caldera, but their submarine morphology is difficult to define. Pumiceous deposits of the Efaté Pumice Formation cover much of Vate (Efaté) Island and record a major trachydacitic explosive eruption c. 1 million years ago that originated from a submarine vent somewhere north of the island.
Possible Holocene			
Unnamed	Stratovolcanos	Unknown	Ewose, Buninga, and Tongariki islands lie on the rim of a proposed caldera thought to be one of several formed in the central volcanic chain of Vanuatu c. 2 ka. Pyroclastic rocks intruded by dikes are exposed on Ewose, whereas Buninga and Makura are largely composed of tilted lava flows. Tongariki consists of remnants of a basaltic stratovolcano with dacitic pumiceous tuffs in low-lying areas.
Aneityum	Stratovolcanos	Unknown	Two coalescing, dominantly basaltic Pleistocene volcanoes. NW side of Inrerow Atamwan volcano and the SE side of Nanawarez volcano are truncated by large erosional cirques.

Table A.1 continued Characteristics and eruptive history of Vanuatu volcanoes, in order of most recent activity. Abridged from Global Volcanism Program summaries.

Appendix B: Activity associated with samples studied

Descriptions of 1988, 1989, 2005 and 2007 activity in this section are from Bulletin of the Global Volcanism Network/Scientific Event Alert Network activity reports. Description of the 1929 eruption is based on Monzier & Douglas (1989) and a contemporary newspaper report in the Auckland Evening Post. Description of the 1986 activity is from Cheney (1986), cited in Cheney (1988).

2005 activity

Activity in early 2005 was dominated by prodigious degassing. The volcano had emitted ash and gas for several months until June 1st, and SO_2 haze was observed on June 17th. The MODIS (Moderate Resolution Imaging Spectroradiometer) satellite detected thermal anomalies indicating the presence of lava lakes in both Marum and Benbow until June 19th, after which thermal anomalies did not reappear until January 2007, with two minor exceptions in April and November 2006 (Fig. A2.1).

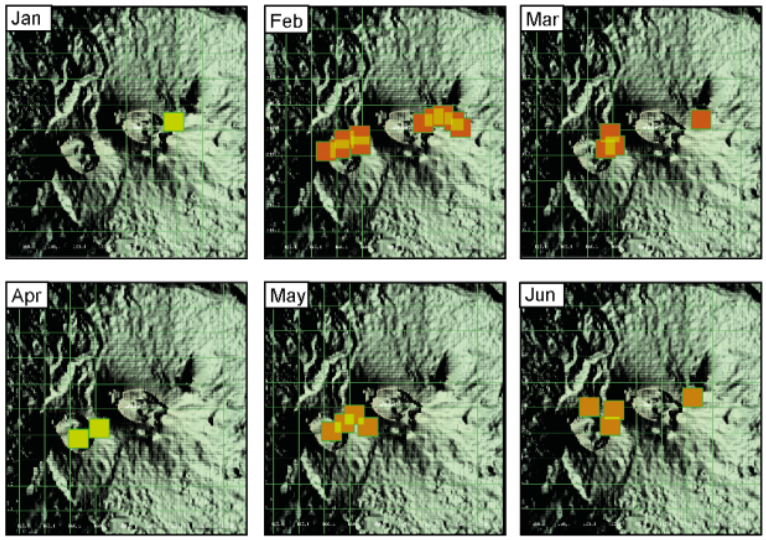

Figure B.1 MODIS thermal alerts by month for 2005. No further hotspots were observed until early 2007, with the exception of brief, weak (green to pale orange) hotspots in April and November 2006.

In 2007, thermal anomalies were recorded in Marum crater on January 11th and 15th, from February 3rd–19th, and almost every day from March 9th to end-May (Fig. A2.2). Lava and ash emissions were reported by pilots and recorded by satellite imagery in April and May, with ash plumes rising to heights of 1.8–4 km on the 3rd of April and 1st–3rd of May. Strong degassing was reported from both Marum and Benbow from the 26th of May to the 12th of June, with the appearance of a lava lake and "intermittent ash eruptions and light tephra emissions…[including] Pele's Hair, reticulite, spatter, and scoria-sized ejecta" at Mbwelesu crater (BGVN 32:05). Reporting from this period is constrained to the dates during which a

group of scientists were present in the caldera, and does not necessarily indicate start and end dates of observed activity, with the exception of the appearance of the lava lake in Mbwelesu during May, which was recorded by thermal imaging.

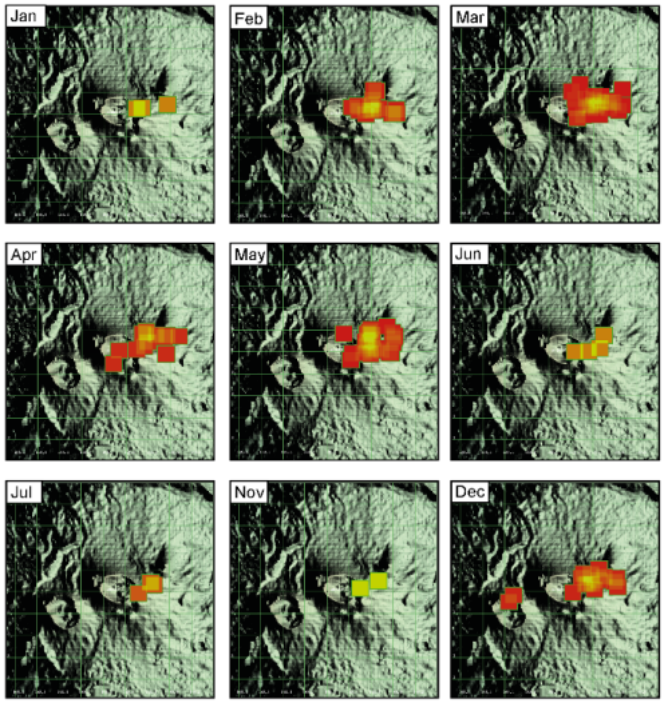

Figure B.2 MODIS thermal alerts summarised by month for 2007. No alerts were recorded from August to October.

1988/89 lava flow

An eruption with ash clouds below 12 km altitude was reported on February 13th 1988 from Benbow crater. This phase of activity ended on February 19th. In May, an approximately 50 m wide lava lake was present in Mbwelesu. White clouds were observed issuing from Benbow, and dark grey clouds from Marum (Melchior, 1988). The lava flow occurred on August 10th, flowing south for c. 5 km from a new adventitious cone (Niri Mbwelesu Taten) on the south flank of Marum (Cheney, 1988; Charley, 1988). The eruption was finished by August 31st and no further activity was observed until April 1989.

Pilots observed plumes over the volcano on the 24th and 31st of April 1989, rising ~3.5 km and ~6 km respectively. On April 31st, ash clouds were detected by satellite, estimated at ~6 km altitude by a passing pilot. A lava flow issued from Niri Mbwelesu Taten, following the same path as the previous flow but extending further by several kilometres. Burned vegetation (suspected to have been burned by acid rain) and a "strong taste" to the rainwater indicated strong outgassing associated with this event. The eruption was "normal" behaviour for the volcano, according to islanders, although slightly more violent than the 1986 and 1988 events. The eruption ended at some point between the 10th and 14th of May. A 6-km-high gas

plume and 3-km-high ash plume were seen on 25 May. No notable seismic activity was recorded at stations on the islands of Malekula (Lamap) or Epi at this time (Mollard, 1989).

During September 26th–30th 1989, a "gently bubbling" lava lake occupied Benbow, with slight degassing from Marum. A "strongly bubbling" lava lake was present in Mbwelesu but no explosive activity occurred. Niri Mbwelesu and the source cones of the lava flows displayed fumarole activity at this time. By early September the lava lake in Mbwelesu had disappeared, and blocks, fragments, ash and gas were being violently emitted from a vent within the crater, with projectiles often passing over the crater rim. From the 5th–18th September ash and blocks 10–100 cm were being ejected from a vent just below the rim of Niri Mbwelesu, with a block 2 m across found near the new Niri Taten crater (adjacent to the 1988 lava sources). An area of intense degassing, with temperatures of >625 ºC—presumably this refers to fumarole temperature since no lava was present in Niri Taten—was measured in Niri Taten. A blue-tinted plume from Benbow suggested high SO_2 output (Lardy & Marty, 1990; BGVN 15:11).

1929 event

The 1929 eruption was a violent event of a month's duration, and included a central eruption of Benbow, eruptions from flank fissures and vents, and submarine eruptions. Fatalities, destruction of homes, crops, and mission stations, and the evacuation of ~500 people occurred as a result (see contemporary newspaper report, Fig. 4.3).

On the evening of June 28th, a Presbyterian mission worker who was travelling to the island by boat saw "a flare-up in the darkness, and then a river of lava swept towards the sea, wiping up trees and gardens and isolated native huts." (The Evening Post, Auckland, 31-08-1929; Fig. 4.5). Three lava flows descended from the flank near Benbow to coastal villages towards the west and northwest at Baulap, Malvert and Craig Cove. Around 500 people were evacuated in the darkness by boat to the nearby island of Malekula. The following day, June 29th, "terrors were increased by the opening of another volcano a few miles from Craig Cove, while an eruption occurred on the beach, and less than three-quarters of a mile offshore a further upheaval occurred in the 100-fathom line. So great was the disturbance at this depth that a column of water and debris was seen in the daylight to be reaching nearly 600 feet. The Presbyterian church and the residence was carried away, and 7 feet of rock has been deposited where the buildings stood."

On the evening of the 29th, three new craters opened on the western flank, and a fourth opened the following afternoon. On the morning of the 30th of June, three submarine craters

began to erupt between Craig Cove and Dip Point, at a distance of 2–6 km offshore. The eruption of the crater near Craig Cove (which had opened the previous day) remained intense, developing into a state of quasi-continuous eruption by the end of the day. By the 1st of July the submarine eruptions were happening further and further apart and finally tailed off.

The principal centres of activity during this eruption were 1) Benbow; 2) the crater (tentatively identified as 'Feluk') ~10.6 km N80W of Benbow, which was also active in 1894; and 3) the submarine craters. Marum did not show any particular activity during this sequence of events.

AMBRYM ERUPTION

STORY OF EVACUATION

MISSION STATIONS DESTROYED

(By Telegraph.)
(Special to "The Evening Post.")
AUCKLAND, This Day.

A spectator at the disastrous eruption on Ambrym Island, New Hebrides, on 28th June, Mr. C. R. Stringer, of the Presbyterian Mission, is now in Auckland.

Mr. Stringer was returning to the island from a meeting of the Mission Synod when, from an anchorage 25 miles away, he saw the disturbance commence. It began with a flare-up in the darkness, and then a river of lava swept towards the sea, wiping up trees and gardens and isolated native huts, forcing the hurried evacuation of this portion of the coast, and finally demolishing two mission stations and sending up clouds of steam as the hot rock met the sea. Several infirm natives who lived in the bush lost their lives, but the population round the mission stations received warning and took to boats.

Ambrym Island is roughly triangular in shape, a circuit of coastline being about 70 miles. The centre of the island is an ash plain, and the habitation is generally concentrated on the three corners of the island. An eruption in 1913 caused considerable loss of life among the native communities and the mission station and hospital were destroyed. Mr. Stringer had charge of the Presbyterian Mission at Craig Cove. A French priest also was stationed near this spot, and about five miles away at Baiap a New Zealander, Mr. Taylor, conducted a Seventh Day Adventist mission.

"Mount Benbow was the chief offender this time," said Mr. Stringer. "The extraordinary thing is that the mountain is about 11 miles from Craig Cove, and a crater about 3000 feet deep, a mile long, and three-quarters of a mile wide had to be filled up before the lava stream overflowed and made for the coast. The lava found the valleys, and in places the molten stream was half a mile wide. It reached Baiap that night, and Mr. Taylor, his wife, and child had abandoned their station only half an hour when it was engulfed. They spent the night in a native village." Mr. Stringer said the lava did not reach Craig Cove until the day broke.

Immediately the security of the settlement was threatened the natives launched the mission motor-boat. In Mr. Stringer's absence, James Kum, a native teacher, took charge, and 74 people were taken on the launch without undue panic. Mr. Harvey, a European trader, took 63 natives on his launch, and the refugees were taken 13 miles to Malekula, on another island. The inhabitants of this island had seen the eruption in its early stages, and a number of boats were sent to help with the evacuation. It was pitch dark and a fair sea was running, but the population of 400 or 500 was safely transferred, a few bush natives hurrying from inland to join in the exodus. Terrors were increased by the opening of another volcano a few miles from Craig Cove, while an eruption occurred on the beach, and less than three-quarters of a mile off shore a further upheaval occurred in the 100-fathom line. So great was the disturbance at this depth that a column of water and debris was seen in the daylight to be reaching nearly 600 feet. The Presbyterian church and the residence was carried away, and 7 feet of rock has been deposited where the buildings stood. The Roman Catholic building escaped, and the lava stream played some strange tricks, sweeping up almost to the walls of the trader's house and the copra store without causing further damage. Yam plots and coconut palms went down before the lava, but the native village was only lightly touched. Glowing ashes had set alight to seven or eight huts. The eruption near the water smothered a sandy stretch with a hill 50 feet in height. In the hasty departure nothing could be done to save the contents of the Presbyterian Mission.

Figure B.3 Account of the 1929 eruption published in The Evening Post, Auckland, 31st August 1929.

1986 trachyandesite lava flow

Available descriptions of the 1986 eruption are brief, reported only in departmental memos of ORSTOM Nouméa (New Caledonia) or the Geology Department in Port Vila, Vanuatu. Increased activity was reported by a pilot on November 13, 1986, followed by ash emission on November 17, and a decrease in activity around the 19th–20th. A new cone was formed in the eastern part of the caldera (Cheney, 1986) from which a lava flow of ~4 km in length extended (Melchior, 1988).

Appendix C: Basaltic scoria mineral analyses

Datapoint	1 / 1	2 / 1	3 / 1	6 / 1	7 / 1	9 / 1	10/1	11/1	14/1	15/1	16/1	17/1	18/1	19/1	20 /1	18 /1	19 /1	19 /2	19 /3	19 /5	19 /6
SiO_2	50.52	48.13	46.99	46.33	46.71	47.02	47.39	48.14	46.99	47.94	46.80	48.79	50.35	50.97	50.02	50.05	50.90	51.19	49.08	47.76	47.92
Al_2O_3	29.16	31.28	31.40	31.99	31.72	31.64	31.09	30.70	31.39	31.12	31.79	30.13	29.52	28.89	29.33	29.26	28.76	28.91	30.15	31.21	31.14
Fe_2O_3	1.23	1.21	1.25	1.28	1.31	1.28	1.20	1.26	1.26	1.21	1.23	1.26	1.23	1.32	1.36	1.22	1.30	1.23	1.23	1.32	1.30
MgO	0.15	0.12	0.12	0.11	0.11	0.12	0.12	0.13	0.11	0.13	0.11	0.13	0.16	0.17	0.15	0.15	0.16	0.16	0.14	0.14	0.14
CaO	13.37	15.73	16.44	16.70	16.61	16.53	15.99	15.36	16.29	15.59	16.52	14.85	13.77	13.34	14.06	13.94	13.33	13.42	14.82	15.94	15.61
Na_2O	3.41	2.19	1.80	1.65	1.73	1.80	2.04	2.40	1.81	2.18	1.71	2.60	3.12	3.32	3.02	3.11	3.36	3.32	2.60	2.05	2.15
K_2O	0.36	0.19	0.15	0.13	0.15	0.16	0.19	0.22	0.15	0.21	0.15	0.23	0.33	0.37	0.32	0.31	0.38	0.37	0.28	0.22	0.21
SrO	0.17	0.14	0.14	0.16	0.15	0.15	0.16	0.19	0.14	0.15	0.17	0.16	0.16	0.17	0.15	0.17	0.20	0.17	0.14	0.18	0.17
Total	98.29	98.92	98.20	98.23	98.39	98.60	98.11	98.32	98.05	98.43	98.40	98.05	98.57	98.48	98.31	98.13	98.30	98.71	98.36	98.70	98.53
Cations on the basis of 8 oxygens																					
Si	2.35	2.24	2.20	2.17	2.19	2.20	2.22	2.25	2.21	2.24	2.19	2.28	2.33	2.36	2.33	2.33	2.37	2.37	2.29	2.23	2.23
Al	1.60	1.71	1.74	1.77	1.75	1.74	1.72	1.69	1.74	1.71	1.75	1.66	1.61	1.58	1.61	1.61	1.57	1.58	1.66	1.71	1.71
Fe^{3+}	0.04	0.04	0.04	0.05	0.05	0.05	0.04	0.04	0.04	0.04	0.04	0.04	0.04	0.05	0.05	0.04	0.05	0.04	0.04	0.05	0.05
Mg	0.01	0.01	0.01	0.01	0.01	0.01	0.01	0.01	0.01	0.01	0.01	0.01	0.01	0.01	0.01	0.01	0.01	0.01	0.01	0.01	0.01
Ca	0.67	0.78	0.83	0.84	0.83	0.83	0.80	0.77	0.82	0.78	0.83	0.74	0.68	0.66	0.70	0.70	0.66	0.66	0.74	0.80	0.78
Na	0.31	0.20	0.16	0.15	0.16	0.16	0.19	0.22	0.17	0.20	0.16	0.24	0.28	0.30	0.27	0.28	0.30	0.30	0.24	0.19	0.19
K	0.02	0.01	0.01	0.01	0.01	0.01	0.01	0.01	0.01	0.01	0.01	0.01	0.02	0.02	0.02	0.02	0.02	0.02	0.02	0.01	0.01
Total	4.99	4.99	4.99	5.00	4.99	4.99	4.99	5.00	4.99	4.99	4.99	4.99	4.99	4.98	4.99	4.99	4.99	4.98	4.99	4.99	4.99
An	66.96	79.01	82.74	84.20	83.43	82.78	80.34	76.91	82.48	78.82	83.44	74.92	69.50	67.39	70.64	69.90	67.09	67.54	74.61	80.06	79.02
Ab	30.91	19.88	16.35	15.03	15.69	16.29	18.54	21.77	16.62	19.94	15.67	23.72	28.51	30.37	27.44	28.22	30.61	30.25	23.71	18.64	19.73
Or	2.13	1.11	0.91	0.77	0.88	0.93	1.12	1.33	0.90	1.25	0.89	1.37	1.99	2.24	1.92	1.88	2.29	2.22	1.68	1.30	1.25

Table C1: Coarse glomerocryst plagioclase compositions in 2005bbasaltic scoria AMB6.

	19/7	19/8	19/9	19/11	19/12	19/13	19/14	19/15	27/1	27/2	27/3	27/4	27/7	27/8	27/9	28/1	28/2	28/5	28/6	28/7
SiO_2	47.83	47.13	47.17	47.62	45.42	45.38	45.21	46.05	48.55	48.98	50.09	46.79	47.16	46.90	47.03	46.61	46.29	46.99	47.97	48.38
Al_2O_3	31.04	31.34	31.46	31.16	32.82	32.89	32.86	32.29	30.22	30.17	29.23	31.80	31.59	31.84	31.67	31.91	31.99	31.65	30.82	30.69
Fe_2O_3	1.26	1.26	1.21	1.17	1.17	1.16	1.13	1.17	1.28	1.22	1.26	1.23	1.20	1.25	1.31	1.24	1.26	1.26	1.27	1.30
MgO	0.13	0.11	0.12	0.12	0.08	0.09	0.08	0.09	0.14	0.14	0.16	0.12	0.12	0.11	0.12	0.12	0.10	0.12	0.12	0.13
CaO	15.82	16.42	15.99	16.02	17.54	17.56	17.66	17.22	14.96	14.90	14.22	16.46	16.40	16.43	16.43	16.62	16.86	16.24	15.71	15.39
Na_2O	2.10	1.83	1.98	2.04	1.14	1.19	1.12	1.38	2.56	2.66	3.01	1.76	1.89	1.77	1.88	1.73	1.52	1.88	2.17	2.39
K_2O	0.20	0.15	0.17	0.18	0.09	0.09	0.09	0.11	0.26	0.28	0.33	0.15	0.16	0.15	0.16	0.15	0.13	0.17	0.17	0.21
SrO	0.16	0.17	0.15	0.16	0.15	0.15	0.13	0.16	0.16	0.15	0.15	0.12	0.16	0.17	0.17	0.13	0.17	0.15	0.17	0.16
Total	98.43	98.31	98.16	98.37	98.29	98.39	98.17	98.37	98.05	98.42	98.35	98.32	98.57	98.53	98.65	98.40	98.21	98.38	98.32	98.56
Cations on the basis of 8 oxygens																				
Si	2.23	2.21	2.21	2.23	2.13	2.13	2.13	2.16	2.27	2.28	2.33	2.19	2.20	2.19	2.20	2.18	2.17	2.20	2.24	2.25
Al	1.71	1.73	1.74	1.72	1.82	1.82	1.82	1.79	1.67	1.66	1.60	1.76	1.74	1.75	1.74	1.76	1.77	1.75	1.70	1.69
Fe^{3+}	0.04	0.04	0.04	0.04	0.04	0.04	0.04	0.04	0.04	0.04	0.04	0.04	0.04	0.04	0.05	0.04	0.04	0.04	0.04	0.05
Mg	0.01	0.01	0.01	0.01	0.01	0.01	0.01	0.01	0.01	0.01	0.01	0.01	0.01	0.01	0.01	0.01	0.01	0.01	0.01	0.01
Ca	0.79	0.82	0.80	0.80	0.88	0.88	0.89	0.87	0.75	0.74	0.71	0.83	0.82	0.82	0.82	0.83	0.85	0.81	0.79	0.77
Na	0.19	0.17	0.18	0.19	0.10	0.11	0.10	0.13	0.23	0.24	0.27	0.16	0.17	0.16	0.17	0.16	0.14	0.17	0.20	0.22
K	0.01	0.01	0.01	0.01	0.01	0.01	0.01	0.01	0.02	0.02	0.02	0.01	0.01	0.01	0.01	0.01	0.01	0.01	0.01	0.01
Total	4.99	4.99	4.99	4.99	4.99	4.99	4.99	4.99	4.99	4.99	4.99	4.99	5.00	4.99	5.00	5.00	4.99	4.99	4.99	4.99
An	79.67	82.45	80.84	80.35	89.04	88.66	89.26	86.74	75.17	74.31	70.93	83.02	82.00	82.97	82.06	83.44	85.30	81.79	79.13	77.13
Ab	19.14	16.63	18.12	18.56	10.44	10.83	10.22	12.60	23.28	24.04	27.13	16.06	17.06	16.14	16.99	15.68	13.92	17.17	19.82	21.63
Or	1.19	0.92	1.04	1.09	0.52	0.52	0.52	0.65	1.55	1.65	1.93	0.92	0.94	0.89	0.95	0.87	0.79	1.05	1.05	1.24

Table C1 ctd: Coarse glomerocryst plagioclase compositions in 2005 basaltic scoria AMB6.

	43 /1	44 /1	45 /1	46 /1	47 /1	48 /1	49 /1	50 /1	51 /1	52 /1	53 /1	54 /1	55 /1	56 /1	57 /1	17 /1	20 /1	21 /1	24 /1	28 /1	29 / 1
SiO_2	48.74	49.61	46.78	48.26	49.36	49.43	48.20	48.37	47.68	48.96	50.40	49.99	48.42	47.93	50.62	47.40	49.97	50.45	47.64	47.35	50.91
Al_2O_3	30.72	30.18	31.24	31.17	30.31	30.28	30.67	31.14	31.33	30.42	29.49	29.60	30.77	30.93	29.22	31.31	29.68	29.36	31.01	32.42	30.23
Fe_2O_3	1.24	1.29	1.29	1.28	1.34	1.31	1.25	1.22	1.27	1.28	1.35	1.25	1.24	1.28	1.25	1.25	1.28	1.29	1.19	1.38	1.50
MgO	0.13	0.14	0.13	0.13	0.14	0.14	0.13	0.14	0.13	0.14	0.16	0.16	0.14	0.13	0.16	0.12	0.15	0.15	0.13	0.12	0.17
CaO	14.77	14.13	15.73	15.30	14.36	14.42	15.23	15.41	15.69	14.71	13.52	13.73	15.07	15.47	13.35	16.31	14.23	13.78	15.84	16.20	13.85
Na_2O	2.64	2.87	2.00	2.25	2.73	2.81	2.41	2.31	2.12	2.69	3.21	3.09	2.39	2.31	3.26	2.01	3.03	3.21	2.16	2.12	3.39
K_2O	0.27	0.28	0.20	0.25	0.30	0.29	0.23	0.23	0.20	0.25	0.38	0.34	0.25	0.22	0.40	0.17	0.29	0.35	0.20	0.18	0.30
SrO	0.14	0.19	0.14	0.17	0.17	0.17	0.17	0.20	0.15	0.17	0.15	0.19	0.15	0.19	0.15	0.16	0.16	0.16	0.16	0.15	0.17
Total	98.57	98.59	97.45	98.73	98.62	98.75	98.22	98.94	98.49	98.51	98.57	98.26	98.34	98.37	98.33	98.65	98.69	98.67	98.25	99.85	100.42
Cations on the basis of 8 oxygens																					
Si	2.27	2.30	2.21	2.24	2.29	2.29	2.25	2.25	2.23	2.28	2.34	2.33	2.26	2.24	2.35	2.21	2.32	2.34	2.23	2.19	2.32
Al	1.68	1.65	1.74	1.71	1.66	1.66	1.69	1.70	1.72	1.67	1.61	1.62	1.69	1.70	1.60	1.72	1.62	1.60	1.71	1.76	1.62
Fe^{3+}	0.04	0.04	0.05	0.04	0.05	0.05	0.04	0.04	0.04	0.04	0.05	0.04	0.04	0.05	0.04	0.04	0.04	0.04	0.04	0.05	0.05
Mg	0.01	0.01	0.01	0.01	0.01	0.01	0.01	0.01	0.01	0.01	0.01	0.01	0.01	0.01	0.01	0.01	0.01	0.01	0.01	0.01	0.01
Ca	0.74	0.70	0.80	0.76	0.71	0.72	0.76	0.77	0.78	0.73	0.67	0.68	0.75	0.77	0.66	0.82	0.71	0.68	0.79	0.80	0.68
Na	0.24	0.26	0.18	0.20	0.25	0.25	0.22	0.21	0.19	0.24	0.29	0.28	0.22	0.21	0.29	0.18	0.27	0.29	0.20	0.19	0.30
K	0.02	0.02	0.01	0.01	0.02	0.02	0.01	0.01	0.01	0.01	0.02	0.02	0.01	0.01	0.02	0.01	0.02	0.02	0.01	0.01	0.02
Total	5.00	4.99	5.00	4.99	4.99	4.99	4.99	4.99	4.99	4.99	4.99	4.99	4.99	5.00	4.99	5.00	4.99	4.99	5.00	5.01	5.00
An	74.36	71.89	80.29	77.79	73.06	72.63	76.67	77.60	79.39	74.03	68.36	69.62	76.55	77.68	67.71	80.93	70.96	68.88	79.27	79.98	68.08
Ab	24.02	26.39	18.49	20.72	25.14	25.60	21.96	21.01	19.39	24.50	29.38	28.35	21.96	21.02	29.90	18.06	27.34	29.06	19.53	18.95	30.16
Or	1.62	1.72	1.23	1.49	1.80	1.76	1.37	1.39	1.22	1.47	2.26	2.03	1.49	1.31	2.39	1.01	1.70	2.06	1.20	1.07	1.76

Table C2: Fine glomerocryst plagioclase compositions in 2005 basaltic scoria AMB6.

	1 / 1	2 / 1	3 / 1	4 / 1	5 / 1	5 / 1	6 / 1	8 / 1	10 / 1	12 /1	13 /1	14 /1	15 /1	16 /1	19 /1	20 /1	21 /1	22 /1	6 / 1
SiO_2	47.32	50.00	50.06	51.26	51.76	48.38	46.63	49.73	47.79	47.70	47.25	46.80	46.91	48.59	46.50	47.11	46.63	50.44	47.85
Al_2O_3	31.42	30.47	30.86	29.98	29.37	31.18	32.31	30.09	32.18	31.18	31.94	32.31	31.98	30.32	32.21	31.67	31.90	29.60	31.37
Fe_2O_3	1.25	1.36	1.36	1.47	1.38	1.23	1.27	1.23	1.57	1.27	1.25	1.27	1.23	1.71	1.15	1.27	1.24	1.26	1.29
MgO	0.15	0.16	0.16	0.17	0.17	0.13	0.11	0.15	0.14	0.12	0.11	0.12	0.12	0.28	0.11	0.12	0.13	0.15	0.13
CaO	15.62	14.35	14.52	13.74	12.84	15.61	16.64	14.10	16.58	16.04	16.31	16.54	16.34	15.39	16.56	16.21	16.66	13.85	15.83
Na_2O	2.26	3.06	2.92	3.38	3.68	2.30	1.51	2.93	1.98	2.04	1.86	1.71	1.82	2.43	1.78	1.97	1.75	3.13	2.08
K_2O	0.21	0.31	0.30	0.37	0.41	0.20	0.11	0.32	0.15	0.17	0.16	0.14	0.14	0.30	0.14	0.17	0.15	0.35	0.18
SrO	0.17	0.17	0.14	0.16	0.16	0.16	0.14	0.16	-	0.14	0.16	0.15	0.14	-	0.15	0.15	0.17	0.15	0.16
Total	98.31	99.80	100.21	100.45	99.70	99.10	98.63	98.61	100.32	98.57	98.95	98.94	98.58	99.05	98.51	98.55	98.53	98.85	98.78
Cations on the basis of 8 oxygens																			
Si	2.21	2.30	2.29	2.33	2.37	2.24	2.18	2.31	2.19	2.23	2.20	2.18	2.19	2.26	2.18	2.20	2.18	2.33	2.23
Al	1.73	1.65	1.66	1.61	1.58	1.70	1.78	1.64	1.74	1.71	1.75	1.77	1.76	1.66	1.78	1.74	1.76	1.61	1.72
Fe^{3+}	0.04	0.05	0.05	0.05	0.05	0.04	0.04	0.04	0.05	0.04	0.04	0.04	0.04	0.06	0.04	0.04	0.04	0.04	0.05
Mg	0.01	0.01	0.01	0.01	0.01	0.01	0.01	0.01	0.01	0.01	0.01	0.01	0.01	0.02	0.01	0.01	0.01	0.01	0.01
Ca	0.78	0.71	0.71	0.67	0.63	0.78	0.83	0.70	0.82	0.80	0.81	0.83	0.82	0.77	0.83	0.81	0.84	0.69	0.79
Na	0.21	0.27	0.26	0.30	0.33	0.21	0.14	0.26	0.18	0.18	0.17	0.15	0.16	0.22	0.16	0.18	0.16	0.28	0.19
K	0.01	0.02	0.02	0.02	0.02	0.01	0.01	0.02	0.01	0.01	0.01	0.01	0.01	0.02	0.01	0.01	0.01	0.02	0.01
Total	5.00	5.00	4.99	5.00	4.99	4.99	4.98	4.99	5.00	4.99	4.99	4.99	4.99	5.00	5.00	5.00	5.00	4.99	4.99
An	78.26	70.84	72.03	67.73	64.24	78.00	85.32	71.26	81.53	80.49	82.14	83.51	82.54	76.43	82.98	81.16	83.29	69.46	79.96
Ab	20.49	27.31	26.17	30.11	33.29	20.83	13.98	26.80	17.59	18.49	16.92	15.66	16.60	21.82	16.18	17.85	15.80	28.42	18.98
Or	1.25	1.85	1.80	2.16	2.47	1.17	0.70	1.94	0.88	1.03	0.94	0.83	0.86	1.75	0.84	0.99	0.91	2.12	1.06

Table C3: Non-glomerocrystic plagioclase in 2005 basaltic scoria AMB6.

	2 / 1	13 /1	14 /1	4 / 1	5 / 1	6 / 1	7 / 1	24 / 1	25 / 1	26 / 1	27 /1	47 /1	7 / 1	8 / 1	21 /1	22 / 1	23 / 1	24 / 1	25 /1
SiO_2	52.77	50.12	50.45	49.65	51.61	51.07	51.78	54.30	53.69	52.95	53.52	50.63	51.26	49.57	47.15	49.72	49.07	49.56	49.98
Al_2O_3	27.24	30.55	30.09	30.87	29.85	29.89	29.73	27.89	28.15	28.96	27.76	29.92	29.61	31.13	32.12	31.17	31.12	31.14	30.61
Fe_2O_3	2.38	1.37	1.32	1.59	1.48	1.29	1.31	1.46	1.48	1.54	1.57	1.39	1.41	1.28	1.45	1.59	1.70	1.50	1.43
MgO	0.54	0.15	0.16	0.20	0.22	0.17	0.16	0.17	0.17	0.24	0.20	0.16	0.16	0.14	0.12	0.17	0.27	0.15	0.14
CaO	11.83	13.97	13.68	14.49	13.23	13.53	13.23	11.45	11.73	12.25	11.53	13.79	13.47	14.76	15.98	15.02	14.97	14.96	14.34
Na_2O	4.00	3.06	3.27	2.92	3.71	3.58	3.70	4.62	4.36	4.10	4.44	3.36	3.58	2.88	2.08	2.76	2.68	2.79	3.06
K_2O	0.61	0.35	0.36	0.30	0.41	0.38	0.41	0.62	0.59	0.52	0.58	0.33	0.38	0.29	0.18	0.38	0.34	0.28	0.29
SrO	0.17	0.16	0.17	0.18	0.17	0.16	0.19	0.17	0.17	0.18	0.18	0.19	0.17	0.15	0.16	0.17	0.15	0.16	0.13
Total	99.47	99.63	99.40	100.10	100.62	99.99	100.46	100.60	100.27	100.65	99.71	99.69	99.95	100.10	99.13	100.88	100.18	100.44	99.89
Cations on the basis of 8 oxygens																			
Si	2.42	2.30	2.32	2.27	2.34	2.34	2.35	2.45	2.44	2.40	2.44	2.32	2.34	2.27	2.19	2.26	2.25	2.26	2.29
Al	1.47	1.65	1.63	1.67	1.60	1.61	1.59	1.49	1.50	1.55	1.49	1.62	1.60	1.68	1.76	1.67	1.68	1.68	1.65
Fe^{3+}	0.08	0.05	0.05	0.05	0.05	0.04	0.04	0.05	0.05	0.05	0.05	0.05	0.05	0.04	0.05	0.05	0.06	0.05	0.05
Mg	0.04	0.01	0.01	0.01	0.01	0.01	0.01	0.01	0.01	0.02	0.01	0.01	0.01	0.01	0.01	0.01	0.02	0.01	0.01
Ca	0.58	0.69	0.67	0.71	0.64	0.66	0.64	0.55	0.57	0.59	0.56	0.68	0.66	0.72	0.80	0.73	0.74	0.73	0.70
Na	0.36	0.27	0.29	0.26	0.33	0.32	0.33	0.40	0.38	0.36	0.39	0.30	0.32	0.26	0.19	0.24	0.24	0.25	0.27
K	0.04	0.02	0.02	0.02	0.02	0.02	0.02	0.04	0.03	0.03	0.03	0.02	0.02	0.02	0.01	0.02	0.02	0.02	0.02
Total	4.99	4.99	5.00	5.00	5.00	5.01	5.00	5.00	4.99	5.00	5.00	5.00	5.00	5.00	5.00	5.00	5.01	5.00	5.00
An	59.79	70.14	68.30	71.97	64.73	66.11	64.81	55.71	57.73	60.39	56.93	68.02	66.07	72.68	80.05	73.41	74.03	73.55	70.90
Ab	36.55	27.78	29.56	26.23	32.88	31.67	32.79	40.69	38.78	36.56	39.70	30.03	31.73	25.65	18.85	24.40	23.96	24.81	27.38
Or	3.66	2.09	2.14	1.80	2.39	2.23	2.40	3.59	3.48	3.05	3.38	1.96	2.21	1.67	1.10	2.19	2.00	1.64	1.72

Table C4: Plagioclase microphenocrysts in 2005 basaltic scoria AMB6.

	3/1	5/1	6/1	7/1	9/1	10/1	4/1	7/1	9/1	10/1	11/1	14/1	19/1	20/1
SiO_2	47.39	50.48	53.81	54.39	53.39	55.02	50.89	48.65	54.65	51.01	54.27	54.06	53.06	53.67
Al_2O_3	32.12	30.27	27.01	26.98	27.66	26.23	29.80	31.03	25.94	29.94	26.86	26.70	27.90	27.40
Fe_2O_3	1.64	1.88	2.37	2.16	2.07	1.99	1.64	1.48	2.69	1.63	2.28	2.03	2.00	2.12
MgO	0.15	0.19	0.25	0.36	0.22	0.21	0.18	0.15	0.57	0.16	0.24	0.24	0.23	0.28
CaO	16.01	13.70	11.15	10.69	11.63	10.25	13.45	15.14	10.61	13.93	10.96	11.01	11.77	11.35
Na_2O	2.15	3.38	4.84	5.03	4.60	5.16	3.57	2.79	4.94	3.44	4.99	4.84	4.49	4.68
K_2O	0.33	0.53	0.70	0.77	0.68	0.74	0.38	0.26	0.89	0.38	0.86	0.78	0.61	0.66
SrO	0.15	0.17	0.18	0.21	0.16	0.16	0.17	0.14	0.18	0.12	0.18	0.19	0.18	0.19
Total	99.85	100.52	100.19	100.53	100.34	99.66	100.00	99.53	100.37	100.49	100.54	99.77	100.12	100.23
Cations on the basis of 8 oxygens														
Si	2.19	2.30	2.45	2.47	2.43	2.51	2.33	2.25	2.48	2.32	2.46	2.47	2.42	2.44
Al	1.75	1.63	1.45	1.44	1.48	1.41	1.61	1.69	1.39	1.61	1.44	1.44	1.50	1.47
Fe^{3+}	0.06	0.06	0.08	0.07	0.07	0.07	0.06	0.05	0.09	0.06	0.08	0.07	0.07	0.07
Mn	0.00	0.00	0.00	0.00	0.00	0.00	0.00	0.00	0.00	0.00	0.00	0.00	0.00	0.00
Mg	0.01	0.01	0.02	0.02	0.01	0.01	0.01	0.01	0.04	0.01	0.02	0.02	0.02	0.02
Ca	0.79	0.67	0.54	0.52	0.57	0.50	0.66	0.75	0.52	0.68	0.53	0.54	0.57	0.55
Na	0.19	0.30	0.43	0.44	0.41	0.46	0.32	0.25	0.44	0.30	0.44	0.43	0.40	0.41
K	0.02	0.03	0.04	0.04	0.04	0.04	0.02	0.02	0.05	0.02	0.05	0.05	0.04	0.04
Total	5.01	5.01	5.01	5.02	5.01	5.00	5.01	5.01	5.01	5.01	5.02	5.01	5.01	5.01
An	78.87	66.97	53.73	51.63	55.99	50.09	66.06	73.87	51.50	67.63	52.16	53.22	57.09	55.05
Ab	19.21	29.94	42.23	43.92	40.10	45.62	31.69	24.63	43.37	30.21	42.96	42.28	39.39	41.11
Or	1.92	3.09	4.04	4.45	3.91	4.29	2.25	1.50	5.13	2.17	4.88	4.50	3.52	3.84

Table C5: Plagioclase groundmass in 2005 basaltic scoria AMB7.

	21 / 1 .	22 / 1 .	23 / 1 .	24 / 1 .	28 / 1 .	29 / 1 .	30 / 1 .	32 / 1 .	33 / 1 .	36 / 1 .	37 / 1 .	10 / 1 .	11 / 1 .	2 / 1 .
SiO_2	53.84	54.54	53.08	55.08	55.24	51.40	57.37	53.87	48.66	55.67	54.28	53.14	54.43	54.65
Al_2O_3	27.14	27.12	28.13	26.69	26.41	29.52	23.95	26.72	31.03	26.39	26.26	27.65	27.30	26.80
Fe_2O_3	1.92	1.91	1.95	1.85	2.06	1.57	2.20	2.05	1.57	1.71	2.41	1.86	1.91	2.25
MgO	0.22	0.18	0.27	0.28	0.21	0.18	0.24	0.39	0.15	0.23	0.26	0.21	0.18	0.23
CaO	11.30	10.58	11.80	10.37	9.91	13.04	9.00	10.92	14.95	9.64	10.81	11.98	11.04	10.86
Na_2O	4.77	4.90	4.49	5.10	5.31	4.01	5.74	4.88	2.77	5.62	4.91	4.48	4.92	4.80
K_2O	0.61	0.82	0.60	0.97	0.99	0.45	1.21	0.69	0.29	1.03	1.02	0.58	0.81	0.77
SrO	0.18	0.18	0.17	0.17	0.19	0.18	0.15	0.18	0.14	0.20	0.18	0.18	0.19	0.20
Total	99.86	100.15	100.38	100.49	100.29	100.24	99.93	99.61	99.48	100.46	100.13	99.98	100.68	100.44
Cations on the basis of 8 oxygens														
Si	2.46	2.48	2.41	2.49	2.50	2.35	2.60	2.46	2.25	2.52	2.48	2.43	2.46	2.48
Al	1.46	1.45	1.51	1.42	1.41	1.59	1.28	1.44	1.69	1.41	1.41	1.49	1.46	1.43
Fe^{3+}	0.07	0.07	0.07	0.06	0.07	0.05	0.08	0.07	0.05	0.06	0.08	0.06	0.06	0.08
Mn	0.00	0.00	0.00	0.00	0.00	0.00	0.00	0.00	0.00	0.00	0.00	0.00	0.00	0.00
Mg	0.01	0.01	0.02	0.02	0.01	0.01	0.02	0.03	0.01	0.02	0.02	0.01	0.01	0.02
Ca	0.55	0.51	0.57	0.50	0.48	0.64	0.44	0.54	0.74	0.47	0.53	0.59	0.54	0.53
Na	0.42	0.43	0.40	0.45	0.47	0.35	0.50	0.43	0.25	0.49	0.43	0.40	0.43	0.42
K	0.04	0.05	0.04	0.06	0.06	0.03	0.07	0.04	0.02	0.06	0.06	0.03	0.05	0.04
Total	5.01	5.00	5.01	5.01	5.01	5.02	5.00	5.01	5.01	5.02	5.02	5.01	5.01	5.00
An	54.68	51.80	57.16	49.99	47.87	62.62	43.21	53.06	73.59	45.83	51.66	57.68	52.81	53.05
Ab	41.81	43.40	39.36	44.46	46.42	34.83	49.86	42.96	24.70	48.36	42.51	39.00	42.58	42.48
Or	3.51	4.79	3.48	5.54	5.71	2.55	6.93	3.98	1.70	5.81	5.83	3.32	4.61	4.47

Table C5 ctd: Plagioclase groundmass in 2005 basaltic scoria AMB7.

	21 / 1	22 / 1	23 / 1	24 / 1	25 / 1	26 / 1	27 / 1	28 / 1	29 / 1	30 / 1	31 / 1	32 / 1	33 / 1	34 / 1	35 / 1	38 / 1	39 / 1	40 / 1	41 / 1	42 / 1
SiO_2	49.86	50.60	50.63	50.75	50.42	50.63	50.00	50.75	50.65	50.34	49.84	49.79	49.57	49.52	49.44	49.92	49.85	49.62	50.74	50.49
TiO_2	0.46	0.44	0.43	0.44	0.47	0.47	0.47	0.47	0.48	0.53	0.57	0.58	0.59	0.57	0.57	0.53	0.51	0.52	0.43	0.42
Al_2O_3	3.20	2.98	2.93	3.07	3.32	3.32	3.58	3.38	3.45	3.80	4.13	4.08	4.17	4.10	4.14	3.72	3.73	3.66	2.96	3.05
Cr_2O_3	0.01	0.03	0.02	0.02	0.02	0.02	0.03	0.03	0.03	0.03	0.02	0.00	0.02	0.01	0.00	0.00	0.01	0.02	0.01	0.01
FeO	8.54	9.12	8.59	8.74	9.01	8.49	8.93	8.86	8.89	9.03	8.90	9.10	9.25	9.21	9.02	9.32	8.96	8.98	8.56	8.72
MnO	0.24	0.24	0.25	0.22	0.24	0.25	0.23	0.25	0.25	0.23	0.23	0.24	0.25	0.22	0.22	0.22	0.22	0.23	0.26	0.24
MgO	14.96	15.34	15.16	15.01	14.82	14.89	14.82	14.99	14.98	14.57	14.25	14.46	14.15	14.08	14.38	14.44	14.47	14.61	15.06	15.03
CaO	19.72	19.90	19.77	20.20	20.06	19.93	20.11	19.97	20.28	20.21	20.03	20.30	20.25	20.41	20.30	20.16	20.16	19.99	19.86	20.02
Na_2O	0.36	0.34	0.36	0.33	0.36	0.33	0.36	0.35	0.32	0.34	0.33	0.35	0.35	0.29	0.35	0.33	0.35	0.35	0.34	0.31
Total	97.38	99.00	98.19	98.81	98.76	98.37	98.54	99.06	99.34	99.11	98.31	98.92	98.63	98.43	98.43	98.65	98.29	98.01	98.25	98.32
Cations on the basis of 6 oxygens																				
Si	1.90	1.90	1.91	1.91	1.90	1.91	1.89	1.90	1.90	1.89	1.89	1.88	1.88	1.88	1.87	1.89	1.89	1.89	1.92	1.91
Ti	0.01	0.01	0.01	0.01	0.01	0.01	0.01	0.01	0.01	0.02	0.02	0.02	0.02	0.02	0.02	0.02	0.01	0.01	0.01	0.01
Al	0.14	0.13	0.13	0.14	0.15	0.15	0.16	0.15	0.15	0.17	0.18	0.18	0.19	0.18	0.18	0.17	0.17	0.16	0.13	0.14
Fe^{2+}	0.27	0.29	0.27	0.27	0.28	0.27	0.28	0.28	0.28	0.28	0.28	0.29	0.29	0.29	0.29	0.29	0.28	0.29	0.27	0.28
Mn	0.01	0.01	0.01	0.01	0.01	0.01	0.01	0.01	0.01	0.01	0.01	0.01	0.01	0.01	0.01	0.01	0.01	0.01	0.01	0.01
Mg	0.85	0.86	0.85	0.84	0.83	0.84	0.84	0.84	0.84	0.82	0.80	0.81	0.80	0.80	0.81	0.81	0.82	0.83	0.85	0.85
Ca	0.81	0.80	0.80	0.81	0.81	0.81	0.81	0.80	0.81	0.81	0.81	0.82	0.82	0.83	0.82	0.82	0.82	0.81	0.80	0.81
Na	0.03	0.02	0.03	0.02	0.03	0.02	0.03	0.03	0.02	0.02	0.02	0.03	0.03	0.02	0.03	0.02	0.03	0.03	0.03	0.02
Total	4.03	4.03	4.02	4.02	4.03	4.02	4.03	4.02	4.02	4.02	4.02	4.03	4.03	4.02	4.03	4.03	4.03	4.03	4.02	4.02
En	44.10	44.14	44.35	43.60	43.21	43.81	43.23	43.69	43.36	42.66	42.36	42.33	41.74	41.52	42.26	42.29	42.59	42.96	44.12	43.80
Wo	41.77	41.14	41.56	42.17	42.05	42.17	42.16	41.83	42.20	42.52	42.80	42.72	42.95	43.24	42.87	42.41	42.63	42.24	41.82	41.94
Fs	14.12	14.71	14.09	14.24	14.74	14.02	14.61	14.49	14.44	14.83	14.84	14.95	15.31	15.24	14.87	15.30	14.78	14.81	14.07	14.26
Mg#	76	75	76	75	75	76	75	75	75	74	74	74	73	73	74	73	74	74	76	75

Table C6: Large euhedral clinopyroxene traverse in basaltic scoria AMB6. The traversed phenocryst is shown in Fig. 4.28.

	Rim to rim traverse of glomerocrystic clinopyroxene phenocryst																		MI host analyses				
	2/1	2/2	2/3	2/4	2/6	2/7	2/8	2/9	2/10	2/11	2/12	2/13	2/14	2/15	2/17	2/18	2/19	2/20	28/1	1/1	8/1	9/1	13/1
SiO2	49.84	49.98	49.99	49.96	49.59	50.41	49.59	50.27	50.19	50.10	49.93	50.30	49.12	51.07	51.43	50.79	51.21	51.14	49.56	49.85	50.12	50.30	50.17
TiO2	0.53	0.56	0.57	0.58	0.52	0.53	0.53	0.53	0.51	0.52	0.53	0.49	0.44	0.43	0.43	0.44	0.45	0.48	0.49	0.54	0.47	0.46	0.51
Al2O3	3.97	4.42	4.06	4.23	4.38	3.93	4.24	3.88	3.83	4.04	4.77	3.66	5.68	3.16	3.00	3.01	3.14	3.28	3.74	4.03	3.46	3.41	3.54
FeO	9.04	9.12	9.25	9.28	8.75	8.88	9.47	9.07	8.52	8.66	8.73	9.13	8.34	8.30	8.43	8.84	8.71	8.74	9.34	8.86	8.63	8.48	8.65
MnO	0.22	0.22	0.21	0.22	0.23	0.22	0.24	0.23	0.24	0.24	0.21	0.23	0.24	0.22	0.23	0.25	0.24	0.24	0.23	0.25	0.23	0.22	0.24
MgO	14.51	14.40	14.47	14.67	14.27	14.68	15.05	14.62	14.68	14.49	14.06	14.82	14.60	15.00	15.19	14.94	14.88	15.20	14.86	14.70	14.63	14.95	14.59
CaO	20.61	20.72	20.64	20.56	20.52	20.58	20.44	20.64	20.45	20.82	20.51	20.63	20.00	20.43	20.65	20.73	20.54	20.60	20.13	20.13	20.29	20.21	20.16
Na2O	0.34	0.35	0.32	0.32	0.34	0.34	0.33	0.33	0.37	0.32	0.28	0.33	0.32	0.33	0.33	0.35	0.31	0.36	0.36	0.34	0.31	0.30	0.35
Total	99.11	99.81	99.56	99.86	98.63	99.63	99.95	99.60	98.85	99.27	99.03	99.64	98.82	99.00	99.71	99.37	99.50	100.05	98.82	98.72	98.16	98.35	98.21
Cations on the basis of 6 oxygens																							
Si	1.88	1.87	1.88	1.87	1.87	1.88	1.86	1.88	1.89	1.88	1.87	1.88	1.85	1.91	1.91	1.90	1.91	1.90	1.87	1.88	1.90	1.90	1.90
Ti	0.01	0.02	0.02	0.02	0.01	0.01	0.02	0.01	0.01	0.01	0.01	0.01	0.01	0.01	0.01	0.01	0.01	0.01	0.01	0.02	0.01	0.01	0.01
Al	0.18	0.19	0.18	0.19	0.20	0.17	0.19	0.17	0.17	0.18	0.21	0.16	0.25	0.14	0.13	0.13	0.14	0.14	0.17	0.18	0.15	0.15	0.16
Fe2+	0.28	0.29	0.29	0.29	0.28	0.28	0.30	0.28	0.27	0.27	0.27	0.29	0.26	0.26	0.26	0.28	0.27	0.27	0.30	0.28	0.27	0.27	0.27
Mn	0.01	0.01	0.01	0.01	0.01	0.01	0.01	0.01	0.01	0.01	0.01	0.01	0.01	0.01	0.01	0.01	0.01	0.01	0.01	0.01	0.01	0.01	0.01
Mg	0.81	0.80	0.81	0.82	0.80	0.82	0.84	0.82	0.82	0.81	0.79	0.83	0.82	0.84	0.84	0.83	0.83	0.84	0.84	0.83	0.83	0.84	0.82
Ca	0.83	0.83	0.83	0.82	0.83	0.82	0.82	0.83	0.82	0.84	0.83	0.83	0.81	0.82	0.82	0.83	0.82	0.82	0.82	0.81	0.82	0.82	0.82
Na	0.03	0.03	0.02	0.02	0.02	0.02	0.02	0.02	0.03	0.02	0.02	0.02	0.02	0.02	0.02	0.03	0.02	0.03	0.03	0.02	0.02	0.02	0.03
Total	4.03	4.03	4.03	4.03	4.03	4.03	4.05	4.03	4.03	4.03	4.01	4.03	4.03	4.02	4.02	4.03	4.02	4.03	4.04	4.03	4.02	4.02	4.02
En	42.18	41.85	41.94	42.34	42.06	42.61	42.94	42.33	42.97	42.23	41.73	42.63	43.38	43.68	43.71	42.93	43.09	43.54	42.99	43.06	42.96	43.67	42.99
Wo	43.08	43.28	43.02	42.65	43.47	42.93	41.90	42.95	43.04	43.62	43.74	42.64	42.72	42.76	42.69	42.83	42.76	42.41	41.86	42.38	42.82	42.44	42.71
Fs	14.74	14.87	15.05	15.02	14.47	14.46	15.16	14.73	13.99	14.16	14.53	14.74	13.91	13.56	13.60	14.25	14.15	14.05	15.15	14.56	14.21	13.90	14.31
Mg#	74	74	74	74	74	75	74	74	75	75	74	74	76	76	76	75	75	76	74	75	75	76	75

Table C6 ctd Clinopyroxene in basaltic scoria AMB6: glomerocrystic phenocryst traverse and MI host phenocrysts.

	AMB6								AMB7													
	Phenocryst		Glomerocrystic					gm	Groundmass and microphenos													
	70 /1	71 / 1	48 /1	49 /1	19 /1	26 /1	5 / 1	12 / 1	4 / 1	5 / 1	12 / 1	17 / 1	18 / 1	26 /1	31 /1	12 / 1	26 /1	37 /1	12 /1	17 /1	18 / 1	26 /1	31 /1
SiO_2	50.07	50.85	51.44	50.85	50.35	49.91	47.36	47.42	45.63	46.77	46.91	46.47	46.94	47.21	48.28	47.42	49.54	44.20	46.91	46.47	46.94	47.21	48.28
TiO_2	0.58	0.55	0.45	0.50	0.54	0.52	1.22	1.30	1.55	1.30	1.56	1.36	1.27	1.25	0.96	1.30	0.94	1.51	1.56	1.36	1.27	1.25	0.96
Al_2O_3	2.56	2.49	3.09	3.43	3.76	3.65	8.23	6.51	6.93	5.99	5.65	7.36	8.39	6.89	5.78	6.51	4.75	10.15	5.65	7.36	8.39	6.89	5.78
FeO	10.58	10.09	8.97	9.17	9.14	9.21	13.00	12.51	12.65	11.64	12.61	12.66	12.45	12.08	11.03	12.51	11.30	14.80	12.61	12.66	12.45	12.08	11.03
MnO	0.55	0.55	0.25	0.28	0.27	0.23	0.25	0.24	0.28	0.26	0.28	0.27	0.27	0.32	0.28	0.24	0.35	0.32	0.28	0.27	0.27	0.32	0.28
MgO	13.41	13.88	15.47	14.95	14.81	14.84	11.37	12.22	11.64	11.81	11.81	12.14	11.42	11.44	13.36	12.22	13.97	10.76	11.81	12.14	11.42	11.44	13.36
CaO	19.94	19.79	19.86	19.93	20.30	20.13	18.13	19.75	19.43	20.34	19.86	17.74	19.43	18.80	19.77	19.75	17.86	15.93	19.86	17.74	19.43	18.80	19.77
Na_2O	0.31	0.35	0.32	0.35	0.35	0.32	0.74	0.42	0.45	0.44	0.40	0.54	0.47	0.56	0.37	0.42	0.39	0.39	0.40	0.54	0.47	0.56	0.37
K_2O	0.01	0.01	0.00	0.00	0.01	0.01	0.79	0.12	0.06	0.08	0.07	0.31	0.62	0.33	0.03	0.12	0.39	0.83	0.07	0.31	0.62	0.33	0.03
Total	98.03	98.57	99.90	99.49	99.55	98.83	101.09	100.55	98.64	98.63	99.17	98.85	101.28	98.90	99.88	100.55	99.51	98.91	99.17	98.85	101.28	98.90	99.88
Cations on the basis of 6 oxygens																							
Si	1.92	1.93	1.91	1.90	1.89	1.88	1.78	1.79	1.76	1.80	1.80	1.78	1.76	1.81	1.82	1.79	1.87	1.71	1.80	1.78	1.76	1.81	1.82
Ti	0.02	0.02	0.01	0.01	0.02	0.01	0.03	0.04	0.04	0.04	0.04	0.04	0.04	0.04	0.03	0.04	0.03	0.04	0.04	0.04	0.04	0.04	0.03
Al	0.12	0.11	0.14	0.15	0.17	0.16	0.36	0.29	0.32	0.27	0.26	0.33	0.37	0.31	0.26	0.29	0.21	0.46	0.26	0.33	0.37	0.31	0.26
Fe^{2+}	0.34	0.32	0.28	0.29	0.29	0.29	0.41	0.40	0.41	0.37	0.40	0.41	0.39	0.39	0.35	0.40	0.36	0.48	0.40	0.41	0.39	0.39	0.35
Mn	0.02	0.02	0.01	0.01	0.01	0.01	0.01	0.01	0.01	0.01	0.01	0.01	0.01	0.01	0.01	0.01	0.01	0.01	0.01	0.01	0.01	0.01	0.01
Mg	0.77	0.79	0.86	0.83	0.83	0.84	0.64	0.69	0.67	0.68	0.68	0.69	0.64	0.65	0.75	0.69	0.78	0.62	0.68	0.69	0.64	0.65	0.75
Ca	0.82	0.80	0.79	0.80	0.81	0.81	0.73	0.80	0.80	0.84	0.82	0.73	0.78	0.77	0.80	0.80	0.72	0.66	0.82	0.73	0.78	0.77	0.80
Na	0.02	0.03	0.02	0.03	0.03	0.02	0.05	0.03	0.03	0.03	0.03	0.04	0.03	0.04	0.03	0.03	0.03	0.03	0.03	0.04	0.03	0.04	0.03
K	0.00	0.00	0.00	0.00	0.00	0.00	0.04	0.01	0.00	0.00	0.00	0.01	0.03	0.02	0.00	0.01	0.02	0.04	0.00	0.01	0.03	0.02	0.00
Total	4.02	4.01	4.02	4.02	4.03	4.03	4.05	4.05	4.05	4.04	4.04	4.04	4.05	4.03	4.04	4.05	4.02	4.05	4.04	4.04	4.05	4.03	4.04
En	39.81	41.12	44.48	43.45	42.90	43.06	35.87	36.55	35.59	35.83	35.61	37.94	35.29	36.05	39.58	36.55	42.15	35.27	35.61	37.94	35.29	36.05	39.58
Wo	42.56	42.12	41.05	41.61	42.25	41.96	41.12	42.46	42.72	44.36	43.05	39.86	43.14	42.59	42.10	42.46	38.73	37.52	43.05	39.86	43.14	42.59	42.10
Fs	17.63	16.76	14.47	14.95	14.85	14.98	23.01	20.99	21.70	19.81	21.34	22.20	21.57	21.36	18.32	20.99	19.12	27.21	21.34	22.20	21.57	21.36	18.32
Mg#	69	71	75	74	74	74	61	64	62	64	63	63	62	63	68	64	69	56	63	63	62	63	68

Table C7: Phenocryst, glomerocryst crystals, and groundmass clinopyroxene analyses for glassy basaltic scoria AMB6, and groundmass/microphenocryst analyses for microcrystalline basaltic scoria AMB7.

	122/1	106/1	102/1	123/1	129/1	130/1	107/1	100/1	117/1	101/1	124/1	108/1
SiO_2	46.90	47.37	48.17	47.07	48.11	48.89	48.69	47.48	48.22	50.32	50.61	51.68
TiO_2	0.02	0.02	0.05	0.02	0.05	0.02	0.03	0.03	0.06	0.31	0.03	0.09
Al_2O_3	32.23	32.25	31.67	31.97	31.51	31.61	30.95	31.10	30.88	25.96	29.37	29.34
FeO	1.08	1.03	1.19	1.08	0.97	1.08	1.08	1.10	1.50	3.75	1.08	1.30
MgO	0.11	0.12	0.15	0.12	0.13	0.12	0.14	0.13	0.23	1.20	0.16	0.14
CaO	16.91	16.83	16.63	16.63	16.46	16.00	15.41	16.65	15.82	13.52	13.95	13.25
Na_2O	1.80	1.93	2.06	1.87	2.26	2.41	2.56	2.25	2.44	3.15	3.36	3.81
K_2O	0.15	0.16	0.19	0.16	0.18	0.20	0.23	0.17	0.25	0.51	0.36	0.41
SrO	0.12	0.12	-	0.08	-	0.16	0.13	-	-	-	0.15	-
Total	99.32	99.84	100.17	98.99	99.69	100.50	99.23	98.94	99.46	98.85	99.06	100.06
Cations on the basis of 8 oxygens												
Si	2.18	2.19	2.22	2.20	2.23	2.24	2.26	2.22	2.24	2.37	2.34	2.37
Ti	0.00	0.00	0.00	0.00	0.00	0.00	0.00	0.00	0.00	0.01	0.00	0.00
Al	1.77	1.76	1.72	1.76	1.72	1.71	1.69	1.71	1.69	1.44	1.60	1.58
Fe^{2+}	0.04	0.04	0.05	0.04	0.04	0.04	0.04	0.04	0.06	0.15	0.04	0.05
Mg	0.01	0.01	0.01	0.01	0.01	0.01	0.01	0.01	0.02	0.08	0.01	0.01
Ca	0.84	0.83	0.82	0.83	0.82	0.79	0.77	0.83	0.79	0.68	0.69	0.65
Na	0.16	0.17	0.18	0.17	0.20	0.21	0.23	0.20	0.22	0.29	0.30	0.34
K	0.01	0.01	0.01	0.01	0.01	0.01	0.01	0.01	0.01	0.03	0.02	0.02
Total	5.02	5.02	5.02	5.01	5.02	5.02	5.02	5.03	5.03	5.06	5.02	5.02
An	83.11	82.00	80.78	82.33	79.29	77.70	75.88	79.56	77.02	68.16	68.17	64.23
Ab	16.03	17.06	18.14	16.74	19.70	21.13	22.78	19.47	21.52	28.77	29.73	33.39
Or	0.85	0.95	1.08	0.93	1.01	1.16	1.35	0.97	1.46	3.06	2.10	2.38

	112/1	113/1	97/1	109/1	
SiO_2	50.83	51.02	50.50	50.54	51.83
TiO_2	0.51	0.48	0.57	0.56	0.10
Al_2O_3	3.50	3.34	3.83	3.92	2.02
Cr_2O_3	0.01	0.01	0.03	0.04	-
FeO	9.14	8.46	9.25	8.95	23.58
MnO	0.22	0.25	0.27	0.21	0.25
MgO	14.95	15.20	14.59	14.74	21.75
CaO	20.51	20.52	20.64	20.74	0.63
Na_2O	0.34	0.36	0.36	0.36	0.01
Total	100.02	99.66	100.06	100.07	100.17
Cations on the basis of 6 oxygens					
Si	1.89	1.90	1.88	1.88	1.94
Ti	0.01	0.01	0.02	0.02	0.00
Al	0.15	0.15	0.17	0.17	0.09
Fe^{2+}	0.28	0.26	0.29	0.28	0.74
Mn	0.01	0.01	0.01	0.01	0.01
Mg	0.83	0.84	0.81	0.82	1.21
Ca	0.82	0.82	0.82	0.83	0.03
Na	0.02	0.03	0.03	0.03	0.00
Total	4.03	4.02	4.03	4.03	4.01
En	42.94	43.82	42.14	42.52	61.39
Wo	42.34	42.51	42.86	42.99	1.28
Fs	14.73	13.67	14.99	14.49	37.34
Mg#	74	76	74	75	62

Table C8: Plagioclase and clinopyroxene phenocrysts in 2007 basaltic scoria AMB2007.

Appendix D: Basaltic lava flow (AMB2) mineral analyses

	Plagioclase					
	Phenocrysts					Microlite
Sample	1/1 (c)	2/1 (r)	3/1 (r)	6/1 (c)	8/1	4/1
SiO_2	48.10	48.80	47.96	51.59	47.95	50.14
Al_2O_3	31.27	30.58	30.55	29.35	31.19	28.75
Fe_2O_3	1.21	1.27	1.30	0.88	1.09	1.68
CaO	15.82	15.27	15.64	12.97	15.45	13.85
Na_2O	2.22	2.43	2.12	3.71	2.32	3.20
K_2O	0.18	0.20	0.13	0.31	0.18	0.34
SrO	0.17	0.14	0.14	0.19	0.15	0.19
Total	99.01	98.74	97.89	99.04	98.40	98.27
Cations on the basis of six oxygens						
Si	2.23	2.27	2.25	2.37	2.24	2.34
Al	1.71	1.67	1.69	1.59	1.72	1.58
Fe^{3+}	0.04	0.04	0.05	0.03	0.04	0.06
Ca	0.79	0.76	0.79	0.64	0.77	0.69
Na	0.20	0.22	0.19	0.33	0.21	0.29
K	0.01	0.01	0.01	0.02	0.01	0.02
Total	4.99	4.99	4.98	4.99	5.00	5.00
An	78.9	76.7	79.7	64.7	77.8	69.1

	Clinopyroxene								
	Phenocrysts			Microphenocrysts				Groundmass	
	10 /1	11/1	12/1	4/1	5/1	70/1	71/1	1/1	9/1
SiO_2	50.02	49.66	49.32	50.26	51.89	50.07	50.85	45.69	47.75
TiO_2	0.52	0.70	0.51	0.76	0.37	0.58	0.55	1.29	1.06
Al_2O_3	3.83	3.99	4.38	3.30	1.55	2.56	2.49	7.24	6.48
Fe_2O_3	8.30	10.13	7.82	11.06	11.06	10.58	10.09	11.00	9.82
MnO	0.19	0.26	0.17	0.59	0.70	0.55	0.55	0.22	0.20
MgO	14.38	13.74	14.32	13.24	14.95	13.41	13.88	11.93	12.92
CaO	21.21	19.92	21.76	19.47	17.80	19.94	19.79	20.60	20.92
Na_2O	0.31	0.34	0.28	0.33	0.23	0.31	0.35	0.32	0.29
Total	98.79	98.75	98.67	99.03	98.58	98.03	98.57	98.33	99.50
Cations on the basis of 4 oxygens									
Si	1.89	1.88	1.86	1.91	1.96	1.92	1.93	1.76	1.80
Ti	0.01	0.02	0.01	0.02	0.01	0.02	0.02	0.04	0.03
Al	0.17	0.18	0.19	0.15	0.07	0.12	0.11	0.33	0.29
Fe^{2+}	0.26	0.32	0.25	0.35	0.35	0.34	0.32	0.35	0.31
Mn	0.01	0.01	0.01	0.02	0.02	0.02	0.02	0.01	0.01
Ca	0.86	0.81	0.88	0.79	0.72	0.82	0.80	0.85	0.85
Na	0.02	0.02	0.02	0.02	0.02	0.02	0.03	0.02	0.02
Mg	0.81	0.78	0.81	0.75	0.84	0.77	0.79	0.69	0.73
Total	4.03	4.02	4.03	4.01	4.00	4.02	4.01	4.05	4.03
Mg#	76	71	77	68	71	69	71	66	70

Table D1: Plagioclase and clinopyroxene analyses in intracaldera basalt lava AMB2. (c) and (r) denote core and rim analyses.

Appendix E: Trachybasaltic flank lava (AMB10) mineral analyses

	Megacrysts											Skeletal phenocryst		GM
	3 / 1	4 / 1	5 / 1	6 / 1	7 / 1	8 / 1	11 / 1	12 / 1	13 / 1	1 / 1	2 / 1	62 / 1	63 / 1	9 / 1
SiO_2	52.16	51.08	50.98	51.18	51.28	51.03	51.52	51.94	50.50	51.13	49.07	48.83	48.66	54.67
TiO_2	0.04	0.05	0.05	0.04	0.04	0.05	0.04	0.05	0.04	0.04	0.03	0.04	0.03	0.06
Al_2O_3	29.35	29.77	29.83	29.64	29.66	29.69	29.51	29.02	30.17	29.73	31.05	30.42	30.47	27.62
Fe_2O_3	1.22	1.24	1.21	1.17	1.25	1.21	1.26	1.14	1.21	1.26	1.25	1.16	1.26	1.45
MgO	0.17	0.16	0.17	0.16	0.16	0.16	0.17	0.16	0.16	0.17	0.15	0.14	0.15	0.17
CaO	12.61	13.57	13.41	13.34	13.46	13.50	13.51	12.73	13.59	13.43	15.17	14.59	15.08	11.28
Na_2O	3.97	3.53	3.59	3.61	3.59	3.56	3.62	4.01	3.40	3.60	2.71	2.69	2.44	4.96
K_2O	0.46	0.41	0.47	0.43	0.46	0.44	0.46	0.52	0.39	0.44	0.28	0.31	0.27	0.81
SrO	0.17	0.17	0.16	0.17	0.17	0.15	0.14	0.17	0.16	0.17	0.14	0.14	0.17	-
Total	100.02	99.87	99.75	99.64	99.96	99.68	100.10	99.63	99.53	99.84	99.76	98.21	98.40	100.99
Cations on the basis of 8 oxygens														
Si	2.38	2.34	2.34	2.35	2.35	2.34	2.35	2.38	2.32	2.34	2.26	2.28	2.27	2.46
Ti	0.00	0.00	0.00	0.00	0.00	0.00	0.00	0.00	0.00	0.00	0.00	0.00	0.00	0.00
Al	1.58	1.61	1.61	1.60	1.60	1.61	1.59	1.57	1.63	1.60	1.68	1.67	1.67	1.47
Fe^{3+}	0.04	0.04	0.04	0.04	0.04	0.04	0.04	0.04	0.04	0.04	0.04	0.04	0.04	0.05
Mg	0.01	0.01	0.01	0.01	0.01	0.01	0.01	0.01	0.01	0.01	0.01	0.01	0.01	0.01
Ca	0.62	0.67	0.66	0.66	0.66	0.66	0.66	0.63	0.67	0.66	0.75	0.73	0.75	0.54
Na	0.35	0.31	0.32	0.32	0.32	0.32	0.32	0.36	0.30	0.32	0.24	0.24	0.22	0.43
K	0.03	0.02	0.03	0.03	0.03	0.03	0.03	0.03	0.02	0.03	0.02	0.02	0.02	0.05
Total	5.00	5.00	5.01	5.00	5.00	5.01	5.00	5.01	5.00	5.01	5.01	4.99	4.99	5.02
An	62.01	66.38	65.54	65.41	65.67	65.94	65.55	61.81	67.24	65.62	74.32	73.65	76.14	53.18
Ab	35.33	31.26	31.74	32.06	31.68	31.48	31.82	35.21	30.46	31.84	24.04	24.52	22.25	42.29
Or	2.67	2.37	2.72	2.52	2.65	2.58	2.63	2.98	2.30	2.54	1.64	1.83	1.61	4.53

Table E.1: Plagioclase megacrysts, single skeletal phenocryst, and single groundmass analyses from flank trachybasalt AMB10.

	Glomerocryst1 traverse 1							Glomerocryst1 traverse 2												
	1/1	2/1	3/1	4/1	5/1	6/1	7/1	8/1	9 /1	10/1	11/1	12/1	13/1	14/1	15/1	16/1	17/1	18/1	19/1	20/1	21/1
SiO_2	50.07	50.87	50.96	51.92	51.37	51.53	51.97	51.61	51.15	51.08	51.69	51.39	52.11	51.29	51.45	51.89	51.19	51.87	51.35	51.55	50.85
TiO_2	0.03	0.04	0.04	0.05	0.04	0.05	0.05	0.05	0.04	0.04	0.04	0.04	0.05	0.05	0.04	0.05	0.05	0.04	0.04	0.05	0.05
Al_2O_3	29.59	29.20	29.20	28.61	29.03	29.00	28.34	28.69	28.89	29.06	28.92	28.84	28.29	28.63	29.16	28.34	28.85	28.64	28.62	28.88	28.80
Fe_2O_3	1.26	1.21	1.17	1.14	1.18	1.18	1.21	1.21	1.18	1.18	1.22	1.20	1.18	1.22	1.17	1.23	1.23	1.20	1.20	1.19	1.23
MgO	0.15	0.16	0.16	0.17	0.16	0.16	0.17	0.18	0.17	0.16	0.17	0.16	0.17	0.17	0.16	0.17	0.17	0.17	0.17	0.17	0.16
CaO	13.99	13.50	13.50	12.52	13.31	13.04	12.57	13.09	13.02	13.51	12.93	13.36	12.68	13.06	13.09	12.52	12.99	12.62	13.05	13.06	13.37
Na_2O	2.98	3.17	3.22	3.84	3.38	3.42	3.68	3.48	3.41	3.28	3.47	3.41	3.60	3.45	3.48	3.73	3.50	3.77	3.55	3.54	3.43
K_2O	0.32	0.40	0.41	0.55	0.45	0.47	0.48	0.46	0.46	0.42	0.49	0.46	0.51	0.46	0.47	0.52	0.47	0.53	0.47	0.48	0.45
SrO	0.20	0.15	0.19	0.20	0.18	0.16	0.16	0.16	0.16	0.16	0.20	0.18	0.18	0.17	0.18	0.19	0.17	0.16	0.17	0.16	0.16
Total	98.49	98.58	98.75	98.89	98.97	98.90	98.50	98.79	98.37	98.78	99.02	98.94	98.65	98.37	99.10	98.54	98.51	98.88	98.50	98.94	98.38
Cations on the basis of 8 oxygens																					
Si	2.33	2.35	2.36	2.39	2.37	2.38	2.40	2.38	2.37	2.36	2.38	2.37	2.41	2.38	2.37	2.40	2.37	2.39	2.38	2.38	2.36
Ti	0.00	0.00	0.00	0.00	0.00	0.00	0.00	0.00	0.00	0.00	0.00	0.00	0.00	0.00	0.00	0.00	0.00	0.00	0.00	0.00	0.00
Al	1.62	1.59	1.59	1.55	1.58	1.58	1.54	1.56	1.58	1.58	1.57	1.57	1.54	1.56	1.58	1.54	1.58	1.56	1.56	1.57	1.58
Fe^{3+}	0.04	0.04	0.04	0.04	0.04	0.04	0.04	0.04	0.04	0.04	0.04	0.04	0.04	0.04	0.04	0.04	0.04	0.04	0.04	0.04	0.04
Mg	0.01	0.01	0.01	0.01	0.01	0.01	0.01	0.01	0.01	0.01	0.01	0.01	0.01	0.01	0.01	0.01	0.01	0.01	0.01	0.01	0.01
Ca	0.70	0.67	0.67	0.62	0.66	0.64	0.62	0.65	0.65	0.67	0.64	0.66	0.63	0.65	0.65	0.62	0.64	0.62	0.65	0.65	0.67
Na	0.27	0.28	0.29	0.34	0.30	0.31	0.33	0.31	0.31	0.29	0.31	0.31	0.32	0.31	0.31	0.33	0.31	0.34	0.32	0.32	0.31
K	0.02	0.02	0.02	0.03	0.03	0.03	0.03	0.03	0.03	0.02	0.03	0.03	0.03	0.03	0.03	0.03	0.03	0.03	0.03	0.03	0.03
Total	4.99	4.98	4.98	5.00	4.99	4.98	4.98	4.98	4.98	4.98	4.98	4.99	4.98	4.99	4.99	4.99	4.99	4.99	4.99	4.99	5.00
An	70.76	68.47	68.10	62.21	66.67	65.88	63.47	65.70	65.93	67.77	65.35	66.50	64.04	65.79	65.61	62.93	65.36	62.89	65.15	65.19	66.46
Ab	27.31	29.09	29.41	34.55	30.62	31.28	33.65	31.57	31.28	29.73	31.70	30.75	32.87	31.44	31.57	33.96	31.84	33.97	32.03	31.94	30.85
Or	1.93	2.44	2.49	3.24	2.71	2.84	2.87	2.72	2.79	2.50	2.95	2.75	3.09	2.77	2.82	3.11	2.81	3.15	2.82	2.86	2.69

Table E.1 ctd.: Traverse of fine glomerocryst plagioclase crystal in flank lava AMB10.

	Cl1tr2 ctd		Plag traverse glomerocryst2															
	22/1	23/1	34/1	35/1	36/1	38/1	39/1	42/1	43/1	44/1	45/1	46/1	47/1	48/1	49/1	50/1	51/1	52/1
SiO_2	51.06	51.60	49.98	49.94	50.34	51.51	51.16	51.24	51.34	51.01	50.66	51.73	51.18	51.37	51.40	50.52	51.31	49.57
TiO_2	0.04	0.04	0.04	0.04	0.04	0.04	0.05	0.05	0.04	0.04	0.04	0.05	0.04	0.04	0.04	0.04	0.04	0.04
Al_2O_3	28.66	28.67	29.85	29.38	29.50	28.69	28.75	28.58	28.51	28.77	29.03	28.64	28.77	28.82	28.82	28.93	28.67	30.08
Fe_2O_3	1.22	1.21	1.26	1.23	1.20	1.22	1.21	1.17	1.19	1.19	1.20	1.20	1.21	1.20	1.21	1.19	1.19	1.27
MgO	0.17	0.16	0.15	0.16	0.16	0.17	0.17	0.17	0.17	0.16	0.16	0.16	0.17	0.17	0.16	0.17	0.17	0.15
CaO	13.18	13.09	14.11	14.10	13.81	13.23	13.10	12.95	13.07	13.11	13.43	12.99	13.03	13.15	13.22	13.42	13.03	14.76
Na_2O	3.38	3.57	2.99	2.98	3.14	3.55	3.45	3.55	3.53	3.55	3.36	3.63	3.52	3.46	3.52	3.36	3.55	2.70
K_2O	0.45	0.47	0.33	0.37	0.40	0.46	0.46	0.48	0.48	0.46	0.43	0.49	0.48	0.47	0.46	0.44	0.46	0.32
SrO	0.18	0.19	0.14	0.17	0.16	0.15	0.15	0.17	0.16	0.16	0.17	0.19	0.17	0.18	0.18	0.18	0.18	0.16
Total	98.24	98.88	98.74	98.23	98.65	98.91	98.38	98.24	98.38	98.37	98.37	98.96	98.44	98.74	98.91	98.13	98.49	98.94
Cations on the basis of 8 oxygens																		
Si	2.37	2.38	2.32	2.33	2.33	2.38	2.37	2.38	2.38	2.37	2.35	2.39	2.37	2.37	2.37	2.35	2.38	2.30
Ti	0.00	0.00	0.00	0.00	0.00	0.00	0.00	0.00	0.00	0.00	0.00	0.00	0.00	0.00	0.00	0.00	0.00	0.00
Al	1.57	1.56	1.63	1.61	1.61	1.56	1.57	1.56	1.56	1.57	1.59	1.56	1.57	1.57	1.57	1.59	1.57	1.64
Fe^{3+}	0.04	0.04	0.04	0.04	0.04	0.04	0.04	0.04	0.04	0.04	0.04	0.04	0.04	0.04	0.04	0.04	0.04	0.04
Mg	0.01	0.01	0.01	0.01	0.01	0.01	0.01	0.01	0.01	0.01	0.01	0.01	0.01	0.01	0.01	0.01	0.01	0.01
Ca	0.66	0.65	0.70	0.70	0.69	0.65	0.65	0.64	0.65	0.65	0.67	0.64	0.65	0.65	0.65	0.67	0.65	0.73
Na	0.30	0.32	0.27	0.27	0.28	0.32	0.31	0.32	0.32	0.32	0.30	0.32	0.32	0.31	0.32	0.30	0.32	0.24
K	0.03	0.03	0.02	0.02	0.02	0.03	0.03	0.03	0.03	0.03	0.03	0.03	0.03	0.03	0.03	0.03	0.03	0.02
Total	4.99	4.99	4.99	4.99	4.99	4.99	4.99	4.99	4.99	5.00	4.99	4.99	4.99	4.99	4.99	5.00	4.99	4.99
An	66.45	65.08	70.85	70.77	69.17	65.47	65.86	64.90	65.22	65.23	67.05	64.49	65.20	65.82	65.63	67.03	65.15	73.72
Ab	30.83	32.11	27.16	27.04	28.43	31.80	31.38	32.23	31.91	32.02	30.40	32.63	31.91	31.38	31.64	30.35	32.12	24.37
Or	2.72	2.81	1.99	2.18	2.40	2.72	2.75	2.87	2.86	2.75	2.56	2.88	2.89	2.80	2.73	2.62	2.73	1.91

Table E.1 ctd.: Fine glomerocryst traverse in flank trachybasalt AMB10.

	Small plag glomerocryst EW traverse														
	60 / 1	60 / 2	60 / 3	60 / 4	60 / 5	60 / 6	60 / 7	60 / 8	60/9	60/10	60/11	60/12	60/13	60/14	60/15
SiO_2	49.30	50.12	51.21	51.46	51.26	51.53	52.09	51.17	51.36	51.19	51.58	51.58	51.37	51.37	49.50
TiO_2	0.03	0.05	0.04	0.05	0.04	0.05	0.05	0.05	0.04	0.04	0.05	0.05	0.04	0.04	0.04
Al_2O_3	30.03	29.15	28.81	28.61	28.69	28.74	28.16	28.88	28.58	28.74	28.43	28.99	28.96	28.73	29.77
Fe_2O_3	1.29	1.20	1.23	1.14	1.20	1.18	1.24	1.24	1.19	1.21	1.19	1.17	1.21	1.20	1.29
MgO	0.15	0.17	0.16	0.17	0.16	0.17	0.18	0.16	0.17	0.17	0.17	0.17	0.17	0.17	0.18
CaO	14.67	13.83	13.12	12.94	13.14	13.03	12.63	13.21	12.85	13.34	13.06	13.10	13.37	13.22	14.21
Na_2O	2.69	3.15	3.54	3.61	3.49	3.47	3.73	3.49	3.60	3.47	3.53	3.42	3.38	3.51	2.90
K_2O	0.30	0.42	0.48	0.48	0.46	0.49	0.53	0.47	0.48	0.46	0.45	0.47	0.44	0.47	0.35
SrO	0.17	0.16	0.16	0.16	0.18	0.16	0.18	0.15	0.16	0.17	0.15	0.17	0.17	0.20	0.16
Total	98.54	98.13	98.63	98.51	98.50	98.70	98.66	98.70	98.33	98.68	98.52	99.01	99.00	98.80	98.27
Cations on the basis of 8 oxygens															
Si	2.29	2.34	2.37	2.38	2.38	2.38	2.41	2.37	2.38	2.37	2.39	2.38	2.37	2.37	2.31
Ti	0.00	0.00	0.00	0.00	0.00	0.00	0.00	0.00	0.00	0.00	0.00	0.00	0.00	0.00	0.00
Al	1.65	1.60	1.57	1.56	1.57	1.56	1.53	1.57	1.56	1.57	1.55	1.57	1.57	1.57	1.64
Fe^{3+}	0.05	0.04	0.04	0.04	0.04	0.04	0.04	0.04	0.04	0.04	0.04	0.04	0.04	0.04	0.05
Mg	0.01	0.01	0.01	0.01	0.01	0.01	0.01	0.01	0.01	0.01	0.01	0.01	0.01	0.01	0.01
Ca	0.73	0.69	0.65	0.64	0.65	0.65	0.63	0.65	0.64	0.66	0.65	0.65	0.66	0.65	0.71
Na	0.24	0.29	0.32	0.32	0.31	0.31	0.33	0.31	0.32	0.31	0.32	0.31	0.30	0.31	0.26
K	0.02	0.02	0.03	0.03	0.03	0.03	0.03	0.03	0.03	0.03	0.03	0.03	0.03	0.03	0.02
Total	4.99	4.99	4.99	4.99	4.99	4.98	4.99	4.99	4.99	4.99	4.99	4.98	4.99	4.99	4.99
An	73.77	69.03	65.28	64.56	65.69	65.52	63.13	65.80	64.42	66.13	65.37	66.00	66.82	65.67	71.51
Ab	24.44	28.48	31.88	32.61	31.59	31.58	33.74	31.44	32.70	31.14	31.94	31.17	30.56	31.57	26.38
Or	1.80	2.49	2.83	2.83	2.72	2.91	3.13	2.76	2.88	2.73	2.69	2.83	2.62	2.76	2.11

Table E.1 ctd.: Fine glomerocryst traverse in flank trachybasalt AMB10.

Small plag glomerocryst NS traverse																		
	61 / 1	61 / 2	61 / 3	61 / 4	61 / 5	61 / 7	61 / 8	61/10	61/11	61/12	61/13	61/14	61/15	61/16	61/17	61/18	61/19	61/20
SiO_2	49.57	50.99	50.39	50.74	50.66	50.81	51.66	51.24	51.04	51.08	51.19	50.98	51.99	51.38	52.07	51.30	51.01	50.88
TiO_2	0.04	0.04	0.04	0.04	0.04	0.04	0.04	0.04	0.04	0.04	0.04	0.04	0.05	0.05	0.05	0.04	0.04	0.04
Al_2O_3	29.89	29.06	29.10	28.97	28.90	29.10	28.47	28.87	29.04	28.67	28.88	28.97	28.46	28.44	28.50	28.69	28.91	28.71
Fe_2O_3	1.22	1.16	1.21	1.21	1.19	1.20	1.22	1.14	1.19	1.22	1.20	1.24	1.22	1.17	1.18	1.19	1.19	1.16
MgO	0.15	0.16	0.16	0.17	0.16	0.15	0.17	0.17	0.17	0.17	0.17	0.17	0.17	0.16	0.17	0.17	0.17	0.16
CaO	14.28	13.45	13.57	13.30	13.56	13.65	13.07	13.25	13.22	13.15	13.21	13.28	13.09	12.96	12.76	13.07	13.53	13.28
Na_2O	2.97	3.30	3.22	3.36	3.32	3.26	3.60	3.39	3.42	3.44	3.45	3.36	3.42	3.50	3.73	3.48	3.43	3.38
K_2O	0.38	0.44	0.44	0.44	0.42	0.42	0.48	0.47	0.45	0.46	0.45	0.45	0.48	0.48	0.51	0.47	0.44	0.43
SrO	0.18	0.17	0.16	0.17	0.18	0.15	0.19	0.17	0.16	0.17	0.16	0.17	0.16	0.16	0.21	0.19	0.17	0.15
Total	98.57	98.66	98.18	98.28	98.32	98.69	98.79	98.65	98.62	98.29	98.64	98.55	98.95	98.18	99.07	98.49	98.78	98.07
Cations on the basis of 8 oxygens																		
Si	2.30	2.36	2.35	2.36	2.36	2.35	2.39	2.37	2.36	2.37	2.37	2.36	2.40	2.39	2.40	2.38	2.36	2.37
Ti	0.00	0.00	0.00	0.00	0.00	0.00	0.00	0.00	0.00	0.00	0.00	0.00	0.00	0.00	0.00	0.00	0.00	0.00
Al	1.64	1.59	1.60	1.59	1.58	1.59	1.55	1.57	1.58	1.57	1.57	1.58	1.55	1.56	1.55	1.57	1.58	1.57
Fe^{3+}	0.04	0.04	0.04	0.04	0.04	0.04	0.04	0.04	0.04	0.04	0.04	0.04	0.04	0.04	0.04	0.04	0.04	0.04
Mg	0.01	0.01	0.01	0.01	0.01	0.01	0.01	0.01	0.01	0.01	0.01	0.01	0.01	0.01	0.01	0.01	0.01	0.01
Ca	0.71	0.67	0.68	0.66	0.68	0.68	0.65	0.66	0.66	0.65	0.65	0.66	0.65	0.65	0.63	0.65	0.67	0.66
Na	0.27	0.30	0.29	0.30	0.30	0.29	0.32	0.30	0.31	0.31	0.31	0.30	0.31	0.32	0.33	0.31	0.31	0.30
K	0.02	0.03	0.03	0.03	0.03	0.02	0.03	0.03	0.03	0.03	0.03	0.03	0.03	0.03	0.03	0.03	0.03	0.03
Total	5.00	4.99	4.99	4.99	4.99	4.99	4.99	4.99	4.99	4.99	4.99	4.99	4.98	4.99	4.99	4.99	5.00	4.99
An	71.00	67.43	68.11	66.81	67.53	68.06	64.80	66.42	66.28	65.96	66.11	66.77	65.94	65.25	63.44	65.59	66.79	66.74
Ab	26.75	29.95	29.28	30.56	29.95	29.45	32.34	30.80	31.01	31.26	31.21	30.52	31.21	31.90	33.52	31.60	30.62	30.71
Or	2.25	2.62	2.62	2.63	2.52	2.48	2.86	2.78	2.71	2.78	2.68	2.71	2.85	2.85	3.05	2.81	2.59	2.55

Table E.1 ctd.: Fine glomerocryst traverse in flank trachybasalt AMB10.

	26 / 1	28 / 1	29 / 1	30 / 1	31 / 1	57 / 1	58 / 1	59 / 1
SiO_2	50.04	49.90	50.38	50.35	50.01	49.98	50.94	50.54
TiO_2	0.62	0.61	0.55	0.57	0.59	0.61	0.52	0.54
Al_2O_3	3.83	3.82	3.41	4.04	3.68	3.77	3.22	3.62
Cr_2O_3	0.16	0.12	0.13	0.21	0.14	0.11	0.07	0.12
FeO	8.50	8.21	8.13	8.11	8.10	8.63	8.29	8.33
MnO	0.19	0.20	0.20	0.18	0.19	0.23	0.22	0.20
MgO	15.14	15.11	15.33	15.23	14.99	14.82	15.17	14.91
CaO	20.10	20.04	20.27	20.21	20.12	19.96	20.40	20.41
Na_2O	0.37	0.36	0.37	0.38	0.36	0.38	0.35	0.34
Total	98.96	98.38	98.79	99.29	98.18	98.52	99.19	99.05
Cations on the basis of 6 oxygens								
Si	1.88	1.88	1.89	1.88	1.89	1.89	1.91	1.89
Ti	0.02	0.02	0.02	0.02	0.02	0.02	0.01	0.02
Al	0.17	0.17	0.15	0.18	0.16	0.17	0.14	0.16
Fe^{2+}	0.27	0.26	0.26	0.25	0.26	0.27	0.26	0.26
Mn	0.01	0.01	0.01	0.01	0.01	0.01	0.01	0.01
Mg	0.85	0.85	0.86	0.85	0.84	0.83	0.85	0.83
Ca	0.81	0.81	0.82	0.81	0.81	0.81	0.82	0.82
Na	0.03	0.03	0.03	0.03	0.03	0.03	0.03	0.02
Total	4.03	4.03	4.03	4.02	4.02	4.02	4.02	4.02
En	44.06	44.28	44.49	44.39	44.09	43.58	43.98	43.53
Wo	42.06	42.22	42.27	42.34	42.55	42.19	42.52	42.83
Fs	13.88	13.50	13.24	13.27	13.37	14.23	13.49	13.64
Mg#	76	77	77	77	77	75	77	76

Table E.2: Clinopyroxene phenocrysts in flank trachybasalt AMB10.

	Glomerocryst		Euhedral, embayed					Heavily embayed					
	24 / 1	25 / 1	32 / 1	33 / 1	53 / 1	54 / 1	55 / 1	56 / 1	64 / 1	65 / 1	66 / 1	67 / 1	68 / 1
SiO_2	39.02	38.97	38.85	38.63	39.29	39.88	39.57	39.15	38.92	38.77	39.20	39.35	39.47
TiO_2	0.01	0.02	0.01	0.01	0.01	0.01	0.01	0.01	0.01	0.01	0.02	0.00	0.02
Al_2O_3	0.03	0.03	0.03	0.02	0.03	0.03	0.02	0.01	0.02	0.02	0.03	0.02	0.02
FeO	20.12	19.48	19.84	20.22	18.83	19.23	16.75	18.32	19.93	18.97	19.93	18.19	17.82
MnO	0.39	0.41	0.38	0.41	0.41	0.40	0.40	0.43	0.37	0.41	0.42	0.40	0.40
NiO	0.12	0.13	0.10	0.15	0.14	0.15	0.17	0.13	0.13	0.14	0.15	0.15	0.14
MgO	40.62	40.60	40.66	40.19	41.94	40.83	43.51	41.57	40.42	40.77	40.90	41.88	41.90
CaO	0.27	0.27	0.28	0.28	0.25	0.21	0.20	0.28	0.28	0.27	0.27	0.24	0.23
Total	100.59	99.94	100.17	99.94	100.93	100.76	100.62	99.94	100.11	99.38	100.95	100.26	100.01
Cations on the basis of 4 oxygens													
Si	1.00	1.00	1.00	1.00	1.00	1.01	1.00	1.00	1.00	1.00	1.00	1.00	1.01
Fe^{2+}	0.43	0.42	0.43	0.44	0.40	0.41	0.35	0.39	0.43	0.41	0.42	0.39	0.38
Mn	0.01	0.01	0.01	0.01	0.01	0.01	0.01	0.01	0.01	0.01	0.01	0.01	0.01
Ni	0.00	0.00	0.00	0.00	0.00	0.00	0.00	0.00	0.00	0.00	0.00	0.00	0.00
Mg	1.55	1.56	1.56	1.55	1.59	1.55	1.63	1.58	1.55	1.57	1.55	1.59	1.59
Ca	0.01	0.01	0.01	0.01	0.01	0.01	0.01	0.01	0.01	0.01	0.01	0.01	0.01
Total	3.00	3.00	3.00	3.00	3.00	2.99	3.00	3.00	3.00	3.00	3.00	3.00	2.99
Fo	78.25	78.79	78.51	77.99	79.88	79.10	82.24	80.17	78.33	79.30	78.54	80.40	80.74

Table E.3: Olivine phenocrysts in flank trachybasalt AMB10.

Appendix F: Trachyandesite mineral analyses

	82/1	9 /1	8 / 1	62/1	45/1	83/1	84/1	29/1	15/1	46/1	91/1	28/1	80/1	16/1	57/1	56/1	90/1	61/1
SiO_2	49.28	51.67	52.42	52.59	52.91	53.14	55.77	53.01	53.54	52.97	53.70	53.57	54.38	54.13	54.93	55.59	55.18	55.61
TiO_2	0.03	0.03	0.03	0.03	0.04	0.04	0.06	0.03	0.03	0.03	0.02	0.03	0.04	0.03	0.03	0.03	0.03	0.03
Al_2O_3	30.62	29.34	28.91	28.87	28.31	28.04	26.92	28.24	28.36	28.21	28.04	27.78	27.64	28.06	27.70	27.25	27.09	27.74
FeO	0.80	0.75	0.61	0.68	0.69	0.94	0.98	0.60	0.60	0.70	0.55	0.62	0.73	0.60	0.57	0.63	0.62	0.52
MgO	0.11	0.10	0.08	0.09	0.09	0.12	0.08	0.07	0.08	0.10	0.06	0.06	0.10	0.07	0.07	0.08	0.08	0.06
CaO	15.17	13.38	12.62	12.50	12.26	12.22	9.83	12.15	11.80	11.77	11.57	11.53	11.25	11.22	10.97	10.55	10.52	10.42
Na_2O	2.78	3.71	4.10	4.19	4.32	4.39	5.50	4.51	4.50	4.44	4.77	4.80	4.84	4.84	5.08	5.36	5.28	5.36
K_2O	0.21	0.30	0.34	0.33	0.36	0.41	0.64	0.38	0.38	0.37	0.42	0.43	0.45	0.42	0.48	0.51	0.54	0.49
SrO	0.19	0.13	0.21	0.17	0.20	0.19	0.24	0.18	0.18	0.14	0.22	0.18	0.23	0.20	0.23	0.22	0.17	0.20
Total	99.20	99.42	99.31	99.47	99.19	99.51	100.04	99.18	99.46	98.74	99.36	99.02	99.68	99.61	100.06	100.23	99.52	100.42
Numbers of ions on the basis of 8 oxygens																		
Si	2.28	2.37	2.41	2.41	2.43	2.44	2.53	2.43	2.45	2.44	2.46	2.46	2.48	2.47	2.49	2.51	2.51	2.51
Al	1.67	1.59	1.56	1.56	1.53	1.51	1.44	1.53	1.53	1.53	1.51	1.50	1.49	1.51	1.48	1.45	1.45	1.47
Fe	0.03	0.03	0.02	0.03	0.03	0.04	0.04	0.02	0.02	0.03	0.02	0.02	0.03	0.02	0.02	0.02	0.02	0.02
Mg	0.01	0.01	0.01	0.01	0.01	0.01	0.01	0.00	0.01	0.01	0.00	0.00	0.01	0.01	0.00	0.01	0.01	0.00
Ca	0.75	0.66	0.62	0.61	0.60	0.60	0.48	0.60	0.58	0.58	0.57	0.57	0.55	0.55	0.53	0.51	0.51	0.50
Na	0.25	0.33	0.36	0.37	0.38	0.39	0.48	0.40	0.40	0.40	0.42	0.43	0.43	0.43	0.45	0.47	0.47	0.47
K	0.01	0.02	0.02	0.02	0.02	0.02	0.04	0.02	0.02	0.02	0.02	0.03	0.03	0.02	0.03	0.03	0.03	0.03
Total	5.01	5.01	5.00	5.01	5.01	5.01	5.01	5.01	5.00	5.00	5.01	5.01	5.00	5.00	5.01	5.01	5.01	5.00
An	74.21	65.43	61.72	61.04	59.81	59.17	47.86	58.50	57.86	58.15	55.89	55.60	54.75	54.79	52.91	50.59	50.81	50.35
Ab	24.58	32.85	36.29	37.03	38.09	38.48	48.44	39.31	39.95	39.66	41.68	41.94	42.63	42.77	44.33	46.51	46.11	46.86
Or	1.21	1.72	1.98	1.93	2.10	2.35	3.70	2.19	2.19	2.19	2.43	2.46	2.63	2.44	2.77	2.89	3.08	2.79

Table F1: 1986 trachyandesite plagioclase phenocryst compositions.

	53 / 1	77 / 1	58 / 1	76 / 1	22 / 1	2 / 1
SiO_2	53.34	55.46	56.45	56.63	57.99	58.37
TiO_2	0.04	0.04	0.04	0.05	0.12	0.04
Al_2O_3	28.57	26.86	26.57	26.44	25.03	25.30
FeO	0.85	0.87	0.69	0.78	0.98	0.70
MgO	0.12	0.09	0.07	0.07	0.15	0.07
CaO	12.18	10.35	9.73	9.58	9.35	8.15
Na_2O	4.35	5.16	5.59	5.67	5.87	6.35
K_2O	0.38	0.63	0.76	0.80	1.18	0.99
SrO	0.17	0.22	0.22	0.16	-	0.18
Total	100.00	99.69	100.13	100.20	101.66	100.16
Cations on the basis of 8 oxygens						
Si	2.43	2.52	2.55	2.56	2.61	2.63
Al	1.53	1.44	1.42	1.41	1.33	1.34
Fe	0.03	0.03	0.03	0.03	0.04	0.03
Mg	0.01	0.01	0.00	0.00	0.01	0.00
Ca	0.59	0.50	0.47	0.46	0.45	0.39
Na	0.38	0.46	0.49	0.50	0.51	0.55
K	0.02	0.04	0.04	0.05	0.07	0.06
Total	5.01	5.00	5.01	5.01	5.02	5.01
An	59.43	50.62	46.89	46.11	43.75	39.15
Ab	38.39	45.71	48.77	49.34	49.66	55.21
Or	2.18	3.66	4.34	4.56	6.59	5.65

Table F2 1986 trachyandesite plagioclase microphenocryst and groundmass compositions.

	3 / 1	17 / 1	10 / 1	11 / 1
SiO_2	50.04	49.19	49.01	49.90
TiO_2	0.80	0.94	1.04	0.90
Al_2O_3	2.94	3.70	4.31	3.27
FeO	12.56	12.06	12.05	12.04
MnO	0.57	0.51	0.45	0.54
MgO	13.72	13.59	13.42	13.34
CaO	17.90	18.19	18.59	18.72
Na_2O	0.32	0.32	0.37	0.32
K_2O	0.02	0.01	0.00	0.03
Total	98.89	98.52	99.25	99.08
Cations on the basis of 6 oxygens				
Si	1.91	1.88	1.86	1.90
Ti	0.02	0.03	0.03	0.03
Al	0.13	0.17	0.19	0.15
Fe	0.40	0.39	0.38	0.38
Mn	0.02	0.02	0.01	0.02
Mg	0.78	0.77	0.76	0.76
Ca	0.73	0.75	0.76	0.76
Na	0.02	0.02	0.03	0.02
Total	4.02	4.02	4.03	4.02
En	40.80	40.66	40.02	39.76
Wo	38.25	39.11	39.83	40.10
Fs	9.87	10.00	20.15	20.13

Table F3: 1986 trachyandesite clinopyroxene microphenocryst and groundmass compositions.

	52 / 1	34 / 1	43 / 1	55 / 1	54 / 1	51 / 1
SiO_2	51.80	50.15	51.87	51.85	51.13	48.85
TiO_2	0.48	0.94	0.44	0.41	0.56	0.96
Al_2O_3	2.04	4.24	1.63	1.67	2.16	4.74
FeO	10.73	11.00	10.08	10.26	10.98	10.86
MnO	0.46	0.46	0.51	0.60	0.52	0.33
MgO	15.56	13.60	15.00	14.73	14.07	13.67
CaO	18.20	19.08	19.08	19.17	19.49	19.63
Na_2O	0.20	0.32	0.25	0.30	0.33	0.32
Total	99.47	99.91	98.85	99.02	99.26	99.35
Cations on the basis of 6 oxygens						
Si	1.94	1.88	1.96	1.95	1.93	1.85
Ti	0.01	0.03	0.01	0.01	0.02	0.03
Al	0.09	0.19	0.07	0.07	0.10	0.21
Fe	0.34	0.35	0.32	0.32	0.35	0.34
Mn	0.01	0.01	0.02	0.02	0.02	0.01
Mg	0.87	0.76	0.84	0.83	0.79	0.77
Ca	0.73	0.77	0.77	0.77	0.79	0.80
Na	0.01	0.02	0.02	0.02	0.02	0.02
Total	4.01	4.01	4.01	4.01	4.02	4.03
En	44.88	40.61	43.64	43.00	41.10	40.35
Wo	37.75	40.96	39.90	40.20	40.92	41.66
Fs	17.37	18.43	16.46	16.80	17.99	17.98
Mg#	72	69	73	72	70	69

	64 / 1	63 / 1	44 / 1	74 / 1	47 / 1	81 / 1
SiO_2	51.31	51.55	52.36	51.23	48.12	50.88
TiO_2	0.55	0.49	0.42	0.54	0.90	0.58
Al_2O_3	2.14	1.93	1.85	2.09	5.65	2.94
FeO	11.01	10.85	9.40	10.76	10.87	8.70
MnO	0.58	0.58	0.35	0.57	0.28	0.30
MgO	13.84	13.75	15.27	13.82	13.05	14.24
CaO	19.69	19.93	19.97	20.24	20.32	21.15
Na_2O	0.32	0.28	0.30	0.33	0.35	0.27
Total	99.45	99.43	99.96	99.59	99.57	99.07
Cations on the basis of 6 oxygens						
Si	1.94	1.95	1.95	1.93	1.82	1.91
Ti	0.02	0.01	0.01	0.02	0.03	0.02
Al	0.10	0.09	0.08	0.09	0.25	0.13
Fe	0.35	0.34	0.29	0.34	0.34	0.27
Mn	0.02	0.02	0.01	0.02	0.01	0.01
Mg	0.78	0.77	0.85	0.78	0.74	0.80
Ca	0.80	0.81	0.80	0.82	0.82	0.85
Na	0.02	0.02	0.02	0.02	0.03	0.02
Total	4.01	4.01	4.01	4.02	4.04	4.01
En	40.50	40.25	43.76	40.16	38.66	41.49
Wo	41.42	41.93	41.13	42.29	43.27	44.29
Fs	18.08	17.82	15.11	17.54	18.06	14.22
Mg#	69	69	74	70	68	74

Table F4: 1986 trachyandesite clinopyroxene phenocryst compositions.

	35 / 1	25 / 1	68 / 1	72 / 1	24 / 1	71 / 1	31 / 1	86 / 1	87 / 1	32 / 1	6 / 1
SiO_2	36.10	35.23	35.75	35.81	35.20	35.63	35.29	35.28	35.28	35.28	35.16
TiO_2	0.06	0.02	0.02	0.01	-0.01	0.02	0.02	0.02	0.03	-	0.04
Al_2O_3	0.02	0.01	0.01	0.01	0.01	0.06	0.02	0.03	0.05	-	0.03
FeO	34.36	35.58	35.75	36.40	36.28	36.46	36.42	36.76	40.27	37.54	39.13
MnO	0.99	1.12	1.15	1.18	1.17	1.14	1.07	1.11	1.20	1.21	1.17
MgO	27.95	26.71	26.68	26.62	26.61	26.57	26.42	26.15	23.14	24.31	24.13
CaO	0.26	0.22	0.21	0.21	0.21	0.23	0.25	0.23	0.42	0.27	0.36
Na_2O	0.00	-	0.02	0.02	-	0.01	0.02	0.02	0.02	0.01	0.02
K_2O	0.01	-	0.00	0.01	-	0.00	0.01	0.01	0.03	0.05	0.02
Total	99.78	98.90	99.58	100.28	99.49	100.13	99.53	99.62	100.46	98.79	100.05
Cations on the basis of 4 oxygens											
Si	1.00	1.00	1.00	1.00	0.99	1.00	1.00	1.00	1.01	1.01	1.00
Fe^{2+}	0.80	0.84	0.84	0.85	0.86	0.85	0.86	0.87	0.96	0.90	0.93
Mn	0.02	0.03	0.03	0.03	0.03	0.03	0.03	0.03	0.03	0.03	0.03
Mg	1.16	1.13	1.12	1.11	1.12	1.11	1.11	1.10	0.98	1.04	1.02
Ca	0.01	0.01	0.01	0.01	0.01	0.01	0.01	0.01	0.01	0.01	0.01
Total	2.99	3.00	3.00	3.00	3.01	3.00	3.00	3.00	2.99	2.99	3.00
Fo	59.18	57.23	57.08	56.59	56.67	56.50	56.39	55.92	50.60	53.57	52.37

Table F5: Olivine phenocryst and glomerocryst crystal compositions, 1986 trachyandesite.

	21 / 1	5 / 1	59 / 1	78 / 1	75 / 1	18 / 1	Mean	Std Dev
SiO_2	34.85	35.02	34.47	36.01	34.68	33.92	34.83	0.69
TiO_2	0.04	0.03	0.05	0.03	0.04	0.04	0.04	0.01
Al_2O_3	0.09	0.03	0.04	0.33	0.18	0.15	0.14	0.11
FeO	39.69	39.98	40.64	37.90	40.18	41.08	39.91	1.10
MnO	1.33	1.21	1.27	1.29	1.30	1.27	1.28	0.04
MgO	23.33	23.07	22.16	21.96	21.69	21.22	22.24	0.82
CaO	0.31	0.30	0.29	0.51	0.72	1.89	0.67	0.62
Na_2O	0.02	0.01	0.02	0.40	0.09	0.01	0.09	0.15
K_2O	0.03	0.03	0.05	0.04	0.04	0.09	0.04	0.02
Total	99.68	99.70	99.04	98.45	98.92	99.69	99.25	0.52
Cations on the basis of 4 oxygens								
Si	1.00	1.01	1.00	1.04	1.01	0.99	1.01	0.02
Fe^{2+}	0.95	0.96	0.99	0.91	0.98	1.00	0.96	0.03
Mn	0.03	0.03	0.03	0.03	0.03	0.03	0.03	0.00
Mg	1.00	0.99	0.96	0.94	0.94	0.92	0.96	0.03
Ca	0.01	0.01	0.01	0.02	0.02	0.06	0.02	0.02
Total	3.00	2.99	3.00	2.97	2.99	3.01	2.99	0.01
Fo mol	51.17	50.71	49.29	50.80	49.04	47.93	49.82	1.27

Table F6: 1986 trachyandesite microphenocryst and groundmass olivine compositions.

Appendix G: Melt inclusion and matrix glass analyses

	Host	SiO_2	Al_2O_3	TiO_2	FeO	MnO	MgO	CaO	Na_2O	K_2O	P_2O_5	F ppm	Cl ppm	S ppm	Total
22 / 1	px	51.73	14.61	1.11	12.63	0.25	4.14	7.37	3.35	2.44	0.46	770	367	136	98.22
23 / 1	px	52.45	14.37	1.08	12.97	0.26	4.02	7.51	3.24	2.38	0.45	707	384	151	98.89
2 / 1	px	52.54	14.45	1.08	11.81	0.25	4.39	8.19	3.00	2.25	0.44	781	388	175	98.57
6 / 1	px	51.86	14.64	1.06	11.66	0.21	4.53	8.58	3.23	2.24	0.42	644	407	222	98.59
7 / 1	px	51.83	14.63	1.10	11.96	0.24	4.61	8.26	3.15	2.10	0.42	643	386	199	98.46
14 / 1	px	52.06	14.58	1.02	11.38	0.22	4.58	7.97	3.15	2.34	0.45	658	337	161	97.89
15 / 1	px	52.01	14.38	1.10	11.94	0.24	4.73	8.07	3.16	2.31	0.46	687	341	128	98.54
20 / 1	px	51.76	14.49	1.03	11.96	0.26	4.29	8.06	3.38	2.32	0.43	739	348	153	98.12
21 / 1	px	51.87	14.62	0.98	11.89	0.27	4.22	7.92	3.25	2.32	0.43	783	441	160	97.96
27 / 1	px	51.41	14.24	1.24	11.52	0.26	4.67	8.64	2.93	2.09	0.42	786	407	257	97.61
31 / 1	px	52.18	14.54	1.03	11.36	0.25	4.70	8.44	2.50	2.15	0.43	682	369	181	97.73
35 / 1	px	50.78	14.37	1.02	12.68	0.25	4.49	8.33	2.96	2.04	0.40	591	428	235	97.48
36 / 1	px	51.30	14.68	1.06	12.48	0.27	4.20	8.10	3.12	2.25	0.41	622	464	272	98.03
37 / 1	px	50.92	14.32	1.02	13.06	0.25	4.30	7.66	3.20	2.25	0.42	705	435	152	97.57
38 / 1	px	51.71	14.43	1.06	12.12	0.25	4.40	8.40	3.16	2.21	0.43	825	373	267	98.36
39 / 1	px	51.94	14.38	0.97	12.45	0.23	4.54	8.38	3.03	2.20	0.44	592	390	186	98.67
40 / 1	px	51.45	14.31	1.02	11.56	0.24	4.55	8.43	3.16	2.22	0.41	835	382	226	97.52
41 / 1	px	51.57	13.70	0.98	12.62	0.26	4.54	8.62	2.90	1.93	0.38	548	433	250	97.68
42 / 1	px	50.94	13.70	0.98	12.27	0.29	4.73	8.76	3.00	1.98	0.37	667	405	234	97.21
43 / 1	px	52.02	13.87	0.98	12.49	0.30	4.68	8.56	2.80	1.90	0.40	618	437	274	98.18

Table G1: Pyroxene-hosted melt inclusions from basaltic scoria AMB6, raw data (uncorrected for PEC).

	Host	SiO_2	Al_2O_3	TiO_2	FeO	MnO	MgO	CaO	Na_2O	K_2O	P_2O_5	F ppm	Cl ppm	S ppm	Total
44 / 1	px	51.96	14.11	0.55	12.41	0.26	4.85	9.41	2.84	1.67	0.30	693	408	747	98.63
45 / 1	px	51.68	14.39	0.61	12.81	0.28	4.92	9.26	2.75	1.70	0.29	672	419	715	98.94
7 / 1	px	52.09	14.55	1.03	11.49	0.28	4.04	7.89	3.13	2.44	0.46	702	388	150	97.55
9 / 1	px	50.93	15.18	1.09	13.32	0.22	4.17	7.77	3.19	2.21	0.41	733	417	264	98.66
11 / 1	px	52.73	14.79	1.04	12.04	0.27	4.36	7.82	3.07	2.28	0.44	764	355	189	99.00
12 / 1	px	52.14	15.02	1.07	11.87	0.22	4.34	8.00	3.24	2.39	0.44	654	338	139	98.87
13 / 1	px	52.34	14.75	1.04	11.85	0.26	4.46	8.01	3.20	2.29	0.43	752	346	154	98.78
20 / 1	px	52.28	14.70	1.02	11.64	0.26	4.64	8.48	3.11	2.26	0.44	581	372	207	98.97
21 / 1	px	52.98	11.92	1.48	13.83	0.33	3.76	8.42	2.24	1.55	0.32	466	490	213	97.01

Table G1 continued: Pyroxene-hosted melt inclusions from AMB6.

	Host	SiO_2	Al_2O_3	TiO_2	FeO	MnO	MgO	CaO	Na_2O	K_2O	P_2O_5	F ppm	Cl ppm	S ppm	Total
3 / 1	ol	51.79	14.87	0.79	12.19	0.26	3.89	9.42	3.45	1.91	0.36	699	525	1053	99.28
10 / 1	ol	52.84	14.69	1.08	12.14	0.24	4.35	8.14	3.16	2.38	0.45	627	333	192	99.61
11 / 1	ol	52.39	14.61	1.10	12.01	0.25	4.52	8.14	3.27	2.38	0.46	857	330	164	99.30
16 / 1	ol	51.47	14.50	1.00	12.24	0.23	4.37	8.37	3.24	2.21	0.42	710	396	232	98.22
17 / 1	ol	50.68	14.87	1.00	12.55	0.27	4.45	8.45	3.22	2.22	0.43	813	385	174	98.34
26 / 1	ol	50.78	14.58	1.02	12.67	0.24	3.51	10.26	3.26	1.66	0.46	802	731	1490	98.90
1 / 1	ol	51.77	14.35	1.05	11.77	0.25	4.13	8.78	3.04	2.26	0.44	621	433	180	98.01
5 / 1	ol	52.67	14.40	1.10	12.54	0.24	3.86	8.95	2.34	2.25	0.42	729	407	181	98.93
15 / 1	ol	52.24	14.73	1.10	10.92	0.25	3.39	8.54	2.91	2.49	0.45	668	510	251	97.19
17 / 1	ol	51.96	14.76	0.99	12.01	0.28	3.91	8.88	3.11	2.14	0.39	835	416	196	98.61
18 / 1	ol	51.72	14.91	1.09	11.98	0.27	4.19	8.72	3.25	2.22	0.42	907	409	232	98.97
19 / 1	ol	52.67	13.89	1.03	12.69	0.25	3.80	8.58	3.22	2.15	0.42	683	463	206	98.87
48 / 1	ol	52.39	14.78	0.58	10.94	0.27	4.00	9.81	2.87	1.63	0.31	946	411	533	97.85
49 / 1	ol	51.47	14.55	0.60	12.09	0.25	4.33	9.68	2.95	1.69	0.31	576	388	485	98.14
50 / 1	ol	51.17	14.93	0.95	11.78	0.27	3.45	10.56	3.17	1.10	0.32	693	646	980	98.05
21 / 1	ol	51.93	14.89	0.97	12.43	0.24	3.18	9.82	3.20	1.81	0.46	839	750	1486	99.41
22 / 1	ol	50.12	14.55	1.07	13.07	0.24	3.29	9.45	3.50	1.92	0.45	718	829	1469	98.12
23 / 1	ol	51.50	14.54	0.74	12.39	0.26	3.90	9.13	3.27	1.83	0.35	757	568	1036	98.27
24 / 1	ol	51.62	15.33	0.76	11.61	0.24	3.65	9.12	3.60	1.95	0.35	657	567	1100	98.61
27 / 1	ol	51.97	14.85	0.88	10.95	0.26	3.42	10.75	3.13	1.20	0.32	797	670	954	98.08
28 / 1	ol	51.98	15.22	0.88	12.04	0.25	3.40	10.56	3.35	1.21	0.31	989	636	989	99.57
12 / 1	sp	51.57	14.46	0.96	11.95	0.22	4.59	8.70	3.08	2.31	0.39	733	308	271	98.40
13 / 1	sp	51.52	14.68	0.93	12.01	0.22	4.74	8.56	3.07	2.29	0.39	643	410	277	98.67

Table G2: Olivine- and spinel-hosted melt inclusions from basaltic scoria AMB6, raw data (uncorrected for PEC). Ol=olivine, ox=spinel.

	Host	SiO_2	Al_2O_3	TiO_2	FeO	MnO	MgO	CaO	Na_2O	K_2O	P_2O_5	F ppm	Cl ppm	S ppm	Total
10 / 1	sp	51.53	14.83	1.12	12.93	0.28	5.07	8.91	3.09	2.12	0.75	851	457	175	100.85
12 / 1	sp	52.20	14.83	1.01	11.83	0.26	4.51	8.22	3.32	2.45	0.45	624	331	166	99.28
13 / 1	sp	52.42	14.81	1.10	11.92	0.24	4.33	8.07	3.33	2.46	0.42	611	348	133	99.27
14 / 1	sp	52.64	14.73	1.02	11.23	0.22	4.42	8.12	3.28	2.35	0.42	779	343	163	98.62
16 / 1	sp	52.34	14.72	1.08	12.05	0.21	4.17	8.61	3.19	2.22	0.41	566	370	153	99.12
18 / 1	sp	49.24	14.69	1.16	13.47	0.26	4.86	7.97	3.21	2.31	0.42	621	339	161	97.78
30 / 1	sp	52.78	14.84	1.10	12.70	0.22	4.56	8.18	3.26	2.22	0.40	796	350	145	100.50
31 / 1	sp	54.41	13.67	1.01	11.75	0.23	4.32	7.72	3.09	2.28	0.42	10984	328	145	100.07
32 / 1	sp	52.73	14.57	1.12	11.98	0.24	4.41	8.32	3.41	2.47	0.44	717	335	152	99.84
17 / 1	ol	51.58	13.81	0.64	12.79	0.30	5.05	9.72	2.80	1.48	0.31	725	426	684	98.76
19 / 1	ol	51.47	14.12	0.60	12.45	0.30	5.07	9.89	2.79	1.44	0.31	678	441	693	98.71
20 / 1	ol	51.44	14.08	0.58	12.61	0.24	5.00	9.62	2.74	1.43	0.29	706	441	702	98.34

Table G3: Olivine- and spinel-hosted melt inclusions from basaltic scoria AMB2007. Ol=olivine, sp=spinel.

	Host	SiO_2	Al_2O_3	TiO_2	FeO	MnO	MgO	CaO	Na_2O	K_2O	P_2O_5	F ppm	Cl ppm	S ppm	Total
60 / 1	ol	65.39	17.52	0.73	3.23	0.10	0.50	3.10	5.45	4.76	0.36	880	1180	288	101.42
61 / 1	ol	64.29	15.60	0.63	6.20	0.17	0.92	3.85	4.86	4.08	0.30	755	990	248	101.13
62 / 1	ol	64.82	15.56	0.72	5.99	0.15	0.88	3.62	4.49	3.87	0.40	866	1101	286	100.77
25 / 1	ol	65.24	16.19	0.61	5.91	0.21	0.85	3.80	4.59	3.91	0.32	648	1089	296	101.88
4 / 1	ol	64.04	17.25	0.61	4.45	0.13	0.65	4.16	4.99	4.83	0.42	902	1188	361	101.80
5 / 1	ol	64.02	17.01	0.66	4.61	0.14	0.71	3.89	4.98	4.81	0.41	920	1183	385	101.54
53 / 1	ox	64.33	14.97	0.64	7.13	0.24	1.52	3.52	4.23	4.37	0.27	800	1492	338	101.52
54 / 1	ox	64.73	14.80	0.65	6.94	0.22	1.45	3.48	4.22	4.35	0.27	845	1440	305	101.41
55 / 1	ox	64.76	15.01	0.66	6.66	0.19	1.46	3.26	4.30	4.45	0.27	863	1451	310	101.34
56 / 1	ox	64.02	15.02	0.64	7.18	0.24	1.58	3.36	4.33	4.17	0.33	845	1343	342	101.16
57 / 1	ox	64.32	14.73	0.61	6.76	0.23	1.43	3.36	4.36	4.31	0.34	873	1373	376	100.76
58 / 1	ox	63.61	15.00	0.63	7.55	0.22	1.50	3.36	4.49	4.35	0.31	916	1397	366	101.34
59 / 1	ox	65.03	14.91	0.60	6.91	0.25	1.41	3.50	4.31	4.39	0.33	918	1457	490	101.98
24 / 1	ox	63.81	14.91	0.62	7.47	0.24	1.53	3.39	4.24	4.30	0.32	881	1385	357	101.15
2 / 1	ox	64.99	15.92	0.62	6.45	0.18	1.33	4.54	2.66	4.86	0.36	1172	1354	385	102.24
9 / 1	ox	65.58	15.77	0.96	5.21	0.14	0.83	3.90	4.63	4.18	0.48	815	1004	257	101.91
23 / 1	ox	64.48	14.97	0.69	7.04	0.23	1.53	3.51	4.28	4.47	0.27	746	1468	296	101.76

Table G4: Olivine- and spinel-hosted melt inclusions from 1986 trachyandesite lava. Ol=olivine, sp=spinel.

	SiO_2	Al_2O_3	TiO_2	FeO	MnO	MgO	CaO	Na_2O	K_2O	P_2O_5	F ppm	Cl ppm	S ppm	Total
AMB6														
Analysed December 2009														
5 / 1	52.37	14.61	1.11	11.59	0.26	4.55	8.21	3.18	2.45	0.45	566	299	64	98.90
18 / 1	52.32	14.57	1.04	11.37	0.24	4.37	8.26	3.24	2.31	0.44	779	342	95	98.31
24 / 1	52.64	14.36	1.01	11.54	0.20	4.62	8.23	3.23	2.39	0.44	654	300	b.d.	98.77
25 / 1	52.37	14.33	1.07	11.87	0.26	4.40	8.27	3.26	2.39	0.44	638	272	82	98.79
32 / 1	52.83	14.39	1.13	11.30	0.25	4.44	8.20	3.31	2.38	0.45	712	279	b.d.	98.78
34 / 1	52.63	14.64	1.00	11.72	0.26	4.54	8.27	3.22	2.28	0.45	575	310	60	99.11
47 / 1	53.19	14.35	1.09	11.79	0.28	4.39	8.25	3.26	2.34	0.43	679	318	b.d.	99.48
Analysed March 2007														
58 / 1	52.60	14.51	1.15	11.95	0.24	4.13	8.60	3.12	2.40	0.43	471	364	51	99.24
59 / 1	53.13	14.81	1.13	10.86	0.21	4.62	9.07	3.40	2.57	0.42	529	315	b.d.	100.31
60 / 1	51.89	14.49	1.14	11.89	0.23	4.54	8.36	3.24	2.54	0.40	638	297	51	98.84
61 / 1	52.51	14.47	1.11	12.05	0.20	4.47	7.98	3.19	2.49	0.42	304	355	b.d.	98.95
62 / 1	52.55	14.53	1.16	11.91	0.21	4.41	8.57	3.07	2.38	0.44	208	364	55	99.30
63 / 1	52.47	14.68	1.16	11.38	0.24	4.42	8.49	3.04	2.51	0.41	467	383	b.d.	98.91
64 / 1	52.33	15.01	1.17	13.35	0.29	3.23	7.08	3.14	2.79	0.44	590	411	b.d.	98.94
65 / 1	52.77	14.81	1.07	11.92	0.25	6.26	6.40	3.46	2.90	0.43	299	276	b.d.	100.32
67 / 1	52.61	14.69	1.16	12.08	0.22	4.37	8.17	3.06	2.49	0.43	583	254	51	99.41
68 / 1	52.06	14.64	1.14	12.12	0.24	4.38	8.35	3.14	2.43	0.42	167	329	b.d.	98.97
69 / 1	52.14	14.44	1.12	11.79	0.24	4.41	8.21	3.23	2.43	0.41	422	299	b.d.	98.50
Analysed June 2006														
12 / 1	52.63	14.27	1.15	11.76	0.25	4.22	8.68	3.24	2.48	0.49	-	-	-	99.23
5 / 1	53.25	14.34	1.15	10.98	0.23	3.84	8.30	3.49	2.67	0.45	-	-	-	98.78
6 / 1	52.43	14.36	1.12	12.02	0.21	4.50	8.41	3.32	2.40	0.47	-	-	-	99.30
7 / 1	52.49	14.41	1.14	11.70	0.27	4.57	8.31	3.41	2.43	0.47	-	-	-	99.38
17 / 1	52.43	14.56	1.19	11.95	0.27	3.80	8.97	3.28	2.45	0.47	-	-	-	99.55

Table G5: Matrix glass compositions in AMB6. Data shown are from three separate analytical sessions, and demonstrate the stability of the electron probe performance over a period of several years, although secondary standards were not routinely analysed. The 2005 basaltic glass is reasonably homogeneous and there are no systematic differences between analytical sessions. Measurements below the detection limit are indicated by 'b.d.'.

	SiO_2	Al_2O_3	TiO_2	FeO	MnO	MgO	CaO	Na_2O	K_2O	P_2O_5	F ppm	Cl ppm	S ppm	Total
AMB2007 (basaltic scoria)														
51 / 1	52.61	14.42	1.06	11.44	0.21	4.44	8.53	3.29	2.30	0.43	620	350	151	98.87
52 / 1	52.77	14.45	1.06	11.88	0.26	4.63	8.20	3.35	2.32	0.42	632	306	127	99.49
110 / 1	52.45	13.99	1.16	11.71	0.24	4.55	8.54	3.30	2.45	0.40	780	333	77	98.91
98 / 1	52.04	14.38	1.08	11.20	0.22	4.70	8.74	3.31	2.50	0.46	625	297	103	98.76
104 / 1	52.15	14.15	1.21	11.45	0.22	4.48	8.42	3.27	2.43	0.45	560	321	106	98.34
1986 trachyandesite lava flow														
63 / 1	66.53	13.99	0.86	5.97	0.15	1.04	2.77	4.67	4.84	0.43	820	881	64	101.43
64 / 1	66.32	13.22	0.80	7.54	0.25	1.32	2.91	3.48	4.96	0.52	1026	1492	110	101.60
66 / 1	65.50	14.13	0.81	6.55	0.21	0.98	2.66	3.93	5.34	0.40	761	938	55	100.69
68 / 1	64.97	14.67	0.78	5.96	0.22	1.03	2.79	4.45	4.92	0.40	916	975	b.d.	100.38
88 / 1	65.78	0.79	15.01	5.19	0.18	1.61	2.09	5.10	5.06	0.44	1131	779	b.d.	101.45
30 / 1	64.11	0.67	13.96	6.40	0.17	1.16	2.52	3.59	6.15	0.44	818	1337	182	99.43
4 / 1	66.24	0.84	14.20	5.65	0.17	0.77	2.33	4.47	5.91	0.37	760	846	b.d.	101.14
19 / 1	68.10	0.83	13.73	5.13	0.12	0.63	2.00	4.53	5.78	0.34	727	849	b.d.	101.39
69 / 1	65.86	0.72	16.30	3.78	0.11	0.55	3.81	5.38	4.07	0.36	289	856	b.d.	101.05
89 / 1	68.00	0.83	15.27	4.18	0.12	0.54	2.63	4.76	5.28	0.27	436	732	b.d.	102.02
1 / 1	69.09	0.82	14.36	3.68	0.08	0.21	1.23	3.67	6.25	-	-	-	-	99.39
70 / 1	66.94	0.80	15.85	4.84	0.14	0.72	3.70	2.38	3.81	-	-	-	-	99.17

Table G6: Matrix glass compositions from AMB2007 and 1986 trachyandesite lava flow.

	88 / 1	30 / 1	4 / 1	70 / 1	19 / 1	69 / 1	1 / 1	**Mean**	**Stdev**
SiO_2	65.78	64.11	66.24	66.94	68.10	65.86	69.09	66.76	1.60
TiO_2	0.79	0.67	0.84	0.80	0.83	0.72	0.82	0.79	0.06
Al_2O_3	15.01	13.96	14.20	15.85	13.73	16.30	14.36	14.83	0.92
FeO	5.19	6.40	5.65	4.84	5.13	3.78	3.68	4.86	0.94
MnO	0.18	0.17	0.17	0.14	0.12	0.11	0.08	0.14	0.03
MgO	1.61	1.16	0.77	0.72	0.63	0.55	0.21	0.77	0.43
CaO	2.09	2.52	2.33	3.70	2.00	3.81	1.23	2.54	0.86
Na_2O	5.10	3.59	4.47	2.38	4.53	5.38	3.67	4.24	0.97
K_2O	5.06	6.15	5.91	3.81	5.78	4.07	6.25	5.29	0.93
P_2O_5	0.44	0.44	0.37	-	0.34	0.36	-	0.37	0.06
F	0.11	0.08	0.08	-	0.07	0.03	-	0.07	0.03
Cl	0.08	0.13	0.08	-	0.08	0.09	-	0.09	0.02
SO_2	0.00	0.04	0.00	-	0.00	0.01	-	0.01	0.01
Total	101.45	99.43	101.14	99.17	101.39	101.05	99.39	100.63	1.12
F ppm	1131	818	760	-	727	289	-	694	297
Cl ppm	779	1337	846	-	849	856	-	900	220
S ppm	10	182	12	-	23	39	-	50	65

Table G7: 1986 trachyandesite matrix glass compositions. Analyses missing P_2O5-F-Cl-SO_2 were inadvertently analysed using the olivine setup.

Appendix H: alkali adjustment of $K_D^{Fe\text{-}Mg}$ for olivine

Toplis (2005) uses the parameter Ψ to describe the offset, ΔSi, between actual SiO_2 content ($\%SiO_2$) and predicted SiO_2 content based on alkali-free systems ($\%SiO_2^{adj}$), where

$$\Psi = \frac{\Delta Si}{\%Na_2O + \%K_2O}$$

This parameter varies as a function of silica and alkali content, and has been constrained using experimental data to give the following expressions for its calculation:

$$\Psi = \left(0.46\left(\frac{100}{100 - \%SiO_2}\right) - 0.93\right)(\%Na_2O + \%K_2O) + \left(-5.33\left(\frac{100}{100 - \%SiO_2}\right) + 9.69\right)$$

for SiO_2 content ≤ 60 mol%, and,

$$\Psi = \left(11 - 5.5\left(\frac{100}{100 - \%SiO_2}\right)\right) \times e^{-0.13(\%Na_2O + \%K_2O)}$$

for SiO_2 ≥ 60 mol%.

The SiO_2 value adjusted for alkali content, here denoted$\%SiO_2^{adj}$, can then be calculated by rearranging the equation for Ψ, so that:

$\%SiO_2^{adj} = \%SiO_2 + \Psi \times (\%Na_2O + \%K_2O)$

where% denotes molar percentages.

Finally, this adjusted SiO_2 value is used to calculate a K_D value at given P, T, and olivine composition:

$$K_D = e^{\left(-\frac{6766}{RT}\right) - \frac{7.34}{R} + \ln\left(0.036 \cdot SiO_2^{adj} - 0.22\right) + 3000\left(\frac{1-2X_{Fo}}{RT}\right) + 0.035\left(\frac{P-1}{RT}\right)}$$

where T is temperature in Kelvin, P is pressure in bars, and X_{Fo} is the forsterite fraction of olivine. A reasonable temperature estimate is necessary in order to use this equation; a temperature estimate within ±50K will have an effect of less than ±0.01 on calculated K_D. Temperature values were calculated using Eq. 19 of Putirka (2008), and a pressure of 500 MPa was chosen, guided by clinopyroxene barometry results. The effect of P in this calculation is small; a change in K_D of approximately 0.01 per GPa. Calculations at 0 MPa are included for comparison.